

Numerical Simulation of Diesel Spray Combustion in an Automotive-Size Diesel Engine

Author:

Pasunurthi, Shyam Sundar

Publication Date:

2014

DOI:

<https://doi.org/10.26190/unsworks/18622>

License:

<https://creativecommons.org/licenses/by-nc-nd/3.0/au/>

Link to license to see what you are allowed to do with this resource.

Downloaded from <http://hdl.handle.net/1959.4/55350> in <https://unsworks.unsw.edu.au> on 2024-05-01

Numerical Simulation of Diesel-Spray Combustion in an Automotive-Size Diesel Engine



Shyam Sundar Pasunurthi

School of Photo Voltaic Renewable Energy Engineering

University of New South Wales

A thesis submitted for the degree of

Doctor of Philosophy

April 2014

COPYRIGHT STATEMENT

'I hereby grant the University of New South Wales or its agents the right to archive and to make available my thesis or dissertation in whole or part in the University libraries in all forms of media, now or here after known, subject to the provisions of the Copyright Act 1968. I retain all proprietary rights, such as patent rights. I also retain the right to use in future works (such as articles or books) all or part of this thesis or dissertation. I also authorise University Microfilms to use the 350 word abstract of my thesis in Dissertation Abstracts International. I have either used no substantial portions of copyright material in my thesis or I have obtained permission to use copyright material; where permission has not been granted I have applied/will apply for a partial restriction of the digital copy of my thesis or dissertation.'

Signed: 

Date: April 22, 2014

AUTHENTICITY STATEMENT

'I certify that the Library deposit digital copy is a direct equivalent of the final officially approved version of my thesis. No emendation of content has occurred and if there are any minor variations in formatting, they are the result of the conversion to digital format.'

Signed: 

Date: April 22, 2014

PLEASE TYPE

THE UNIVERSITY OF NEW SOUTH WALES
Thesis/Dissertation Sheet

Surname or Family name: Pasunurthi

First name: Shyam Sundar

Other name/s:

Abbreviation for degree as given in the University calendar: PhD

School: Photovoltaic and Renewable Energy Engineering

Faculty: Engineering

Title: Numerical Simulation of Diesel-Spray Combustion in an Automotive-Size Diesel Engine

Abstract 350 words maximum: (PLEASE TYPE)

Better knowledge of complex in-cylinder processes that affect emissions and limit the fuel efficiency in diesel engines would aid the development of low-emissions and more efficient engines. Two outstanding issues that are not properly addressed by current understanding are jet-wall and jet-jet interactions, which impact significantly the in-cylinder flow field, air-fuel ratio distribution, and temperature – and thus soot formation. Compared with older generations of engines, these interactions are much more important in modern and proposed future engines, due to trends of downsizing, higher injection pressures, and oxidiser dilution.

One way this knowledge may be gained is through numerical modelling. However, it is unclear the extent to which models can capture these interactions, due to few focussed studies which directly compared modelled jet-wall and jet-jet interactions with experimental in-cylinder optical measurements. This study aims to help bridge this gap. A pragmatic approach is taken to the modelling wherein standard and well understood spray and turbulence models are coupled with relatively detailed chemical kinetic models and, where possible, with a full cycle, full geometry model of the engine.

The modelling is comprehensively compared with experimental data. This requires going beyond the typical comparisons of pressure traces and engine-out emissions to examine the phenomena in detail as they happen inside the engine, which is achieved by comparisons to a suite of measurements in two optically accessible engines (one small-bore engine at UNSW and one heavy-duty engine at Sandia National Laboratories). After the usual comparisons of the heat release rate, comparisons of fuel-PLIF with modelled fuel mass fraction are used to understand the transient mixture formation process. Early-stage chemiluminescence and formaldehyde PLIF are compared with modelled fuel formaldehyde mass fraction to evaluate whether the simulations can predict cool flame, first-stage ignition. Chemiluminescence from OH and OH-PLIF is compared with the modelled OH and OH mass fractions, respectively, to assess the ability to predict the high temperature combustion regions. Finally PAH PLIF is compared with modelled single-ring aromatic mass fraction to evaluate the ability of the model to predict soot precursors.

In the small-bore engine, comparisons of model and experiment are first performed with a full cycle engine model for a single fuel-jet interacting with the bowl wall for a range of different injection pressures. The comparisons are first performed for a baseline injection pressure of 70 MPa, and then extended to study effects of higher injection pressures. Numerical experiments are then performed to study jet-jet interactions at different injection pressures using fuel injection through two jets. In the heavy duty engine, a sector mesh model is adopted due to the intake geometry being unavailable. Comparisons of model and experiment are performed for two bowl geometries, with the focus on predictions of aromatic compounds. Overall, these comparisons are shown to be quite successful. In all the considered cases a good agreement is obtained for the heat release rate, in-cylinder fuel-air mixing, and the timing and location of cool flame and high temperature combustion. The location and timing of aromatic species also agrees quite well in the heavy duty engine, but leaves room for improvement.

The numerical results are further analysed revealing features that are not obvious from the experiments alone. In particular they highlight that jet-wall and jet-jet interactions have a major and leading order influence on combustion in modern diesel engines. The flow-flame interactions involved during these phenomena are quite complex and quite geometry specific, highlighting the need for further development of conceptual models for diesel engine combustion affected by jet-jet and jet-wall interactions, which relative to older conceptual models of conventional diesel engine combustion are at a much less advanced stage.

Declaration relating to disposition of project thesis/dissertation

I hereby grant to the University of New South Wales or its agents the right to archive and to make available my thesis or dissertation in whole or in part in the University libraries in all forms of media, now or here after known, subject to the provisions of the Copyright Act 1968. I retain all property rights, such as patent rights. I also retain the right to use in future works (such as articles or books) all or part of this thesis or dissertation.

I also authorise University Microfilms to use the 350 word abstract of my thesis in Dissertation Abstracts International (this is applicable to doctoral theses only).


Signature


Witness


Date

The University recognises that there may be exceptional circumstances requiring restrictions on copying or conditions on use. Requests for restriction for a period of up to 2 years must be made in writing. Requests for a longer period of restriction may be considered in exceptional circumstances and require the approval of the Dean of Graduate Research.

FOR OFFICE USE ONLY

Date of completion of requirements for Award:

Declaration

Originality statement

'I hearby declare that this submission is my own work and to the best of my knowledge it contains no material previously published or written by another person, or substantial material which have been accepted for the award of any other degree or diploma at UNSW or any other educational institution, except where due acknowledgement is made in the thesis. Any contribution made to the research by others, with whom I have worked at UNSW or elsewhere, is explicitly acknowledged in the thesis. I also declare that the intellectual content of this thesis is the product of my own work, except to the extent that assitance from others in the project's design and conception or in style, presentation and linguistic expression is acknowledged.'

Signed

Shyam Sundar/Pasunurthi

April 22, 2014

To my beloved wife and son

Acknowledgements

I am grateful to Professor Evatt Hawkes for giving me an opportunity to work under his guidance. Apart from the guidance, his encouragement, patience, freedom and especially his immense combustion knowledge helped me a lot to learn and adapt to the expectations during the four years. Every time, in the fortnightly meetings, his questions and new ideas to a problem on the table helped to present the work in the current shape. The work is the first numerical insight into the Optical Engine in our Combustion Laboratory.

I acknowledge Associate Professor Shawn Kook for identifying me to numerically understand the combustion physics of the Optical Engine. Thankful to my experimental research colleagues Alvin Rusly, Minh Le and Bryan for providing the experimental data and making me to understand the data. I also thank Srinivas Padala who was always available for discussions about different aspects of the experiments.

Thankful to acumen of Professor Evatt Hawkes for recognizing OpenFOAM as a potential research tool for IC engine combustion CFD analysis and sending me to Politecnico di Milano, Milan for 6 months OpenFOAM training. Special thanks to Professor Tommaso Lucchini and Professor Gianluca D'Errico from Politecnico di Milano for OpenFOAM training and Lib-ICE engine simulation utilities without which my present work would have not been possible.

The combustion group in UNSW is friendly and at the same time one of the most research oriented groups I have ever seen in my life. I got benefited from many research related discussions with Shahram Karami, Obulesu Chatakonda, Michele Bolla, Fatemah Salehi, James

Behzadi, Mohsen Talei, Yuanjiang Pei, Haoyang Zhang, Shakil Ahmed, Nabeel Qazi and Aqib Chishti. Also, thankful to all of our experimental combustion researchers.

Never the least, I am very thankful to my wife VijayaLakshmi for understanding and being on my side in the difficult times. I never forget the cute moments of my son Srinandan, which helped me to cope with the difficult times during the four years. The time in Sydney has provided very essential lessons of life not only to me but to my wife. At the end, I am indebted to my family and friends for allowing me to realize my dream of doing research.

Abstract

Better knowledge of complex in-cylinder processes that affect emissions and limit the fuel efficiency in diesel engines would aid the development of low-emissions and more efficient engines. Two outstanding issues that are not properly addressed by current understanding are jet-wall and jet-jet interactions, which impact significantly the in-cylinder flow field, air-fuel ratio distribution, and temperature - and thus soot formation. Compared with older generations of engines, these interactions are much more important in modern and proposed future engines, due to trends of downsizing, higher injection pressures, and oxidiser dilution.

One way this knowledge may be gained is through numerical modelling. However, it is unclear the extent to which models can capture these interactions, due to few focussed studies which directly compared modelled jet-wall and jet-jet interactions with experimental in-cylinder optical measurements. This study aims to help bridge this gap.

A pragmatic approach is taken to the modelling wherein standard and well understood spray and turbulence models are coupled with relatively detailed chemical kinetic models and, where possible, with a full cycle, full geometry model of the engine.

The modelling is comprehensively compared with experimental data. This requires going beyond the typical comparisons of pressure traces and engine-out emissions to examine the phenomena in detail as they happen inside the engine, which is achieved by comparisons to a suite of measurements in two optically accessible engines (one small-bore

engine at UNSW and one heavy-duty engine at Sandia National Laboratories). After the usual comparisons of the heat release rate, comparisons of fuel-PLIF with modelled fuel mass fraction are used to understand the transient mixture formation process. Early-stage chemiluminescence and formaldehyde PLIF are compared with modelled fuel formaldehyde mass fraction to evaluate whether the simulations can predict cool flame, first-stage ignition. Chemiluminescence from OH^* and OH-PLIF is compared with the modelled OH^* and OH mass fractions, respectively, to assess the ability to predict the high temperature combustion regions. Finally PAH PLIF is compared with modelled single-ring aromatic mass fraction to evaluate the ability of the model to predict soot precursors.

In the small-bore engine, comparisons of model and experiment are first performed with a full cycle engine model for a single fuel-jet interacting with the bowl wall for a range of different injection pressures. The comparisons are first performed for a baseline injection pressure of 70 MPa, and then extended to study effects of higher injection pressures. Numerical experiments are then performed to study jet-jet interactions at different injection pressures using fuel injection through two jets. In the heavy duty engine, a sector mesh model is adopted due to the intake geometry being unavailable. Comparisons of model and experiment are performed for two bowl geometries, with the focus on predictions of aromatic compounds. Overall, these comparisons are shown to be quite successful. In all the considered cases a good agreement is obtained for the heat release rate, in-cylinder fuel-air mixing, and the timing and location of cool flame and high temperature combustion. The location and timing of aromatic species also agrees quite well in the heavy duty engine, but leaves room for improvement.

The numerical results are further analysed revealing features that are not obvious from the experiments alone. In particular they highlight that jet-wall and jet-jet interactions have a major and leading order

influence on combustion in modern diesel engines. The flow-flame interactions involved during these phenomena are quite complex and quite geometry specific, highlighting the need for further development of conceptual models for diesel engine combustion affected by jet-jet and jet-wall interactions, which relative to older conceptual models of conventional diesel engine combustion are at a much less advanced stage

Preface

This thesis deals with numerical simulation of diesel-spray combustion in an automotive-size diesel engine. It is based on the following papers published and planned to be published:

1. Pasunurthi, S. S., Hawkes, E. R., Joelsson, T., Rusly, A. M., Kook, S., Lucchini, T., and D'Errico, G., Numerical simulation of sprays and combustion in an automotive-size diesel engine under reacting and non-reacting conditions, *9th Asia-Pacific Conference on Combustion, Gyeongju Hilton, Gyeongju, Korea*, pp 308-311, 2013.
2. Pasunurthi, S. S., Hawkes, E. R., Talei, M., Kook, S., Lucchini, T., and D'Errico, G., Development of an n-heptane-aromatic hydrocarbon reaction mechanism for engine simulations, *Proceedings of the Australian Combustion Symposium, The University Club of Western Australia (ISSN 1839-8162 online)*, pp 210-213, 2013.
3. Pasunurthi, S. S., Hawkes, E. R., Talei, M., Kook, S., Lucchini, T., and D'Errico, G., Numerical simulation of the impact of wall on the flame zone in an automotive-size diesel engine, *Proceedings of the Australian Combustion Symposium, The University Club of Western Australia (ISSN 1839-8162 online)*, pp 396-399, 2013.
4. Pasunurthi, S. S., Hawkes, E. R., Minh, L., Kook, S., Lucchini, T., and D'Errico, G., A numerical study on the development of combustion in an automotive-size diesel engine: baseline condition, manuscript in preparation for Applied Energy.

5. Pasunurthi, S. S., Hawkes, E. R., Minh, L., Kook, S., Lucchini, T., and D'Errico, G., A numerical investigation of the effect of injection pressure and jet-jet interaction on the combustion development in an automotive-size diesel engine, manuscript in preparation for Applied Energy.
6. Pasunurthi, S. S., Hawkes, E. R., Talei, M., Kook, S., Lucchini, T., and D'Errico, G., A comprehensive n-heptane, n-dodecane and aromatic hydrocarbon reaction mechanism for engine simulations: validation and application, manuscript in preparation for Fuel.

Contents

Contents	x
List of Figures	xv
List of Tables	xxiv
1 Introduction	1
1.1 Objectives	4
2 Literature review	7
2.1 Conceptual models	7
2.1.1 Conventional diesel combustion	7
2.1.2 Partially premixed low-temperature combustion in a light-duty engine with EGR-dilution	11
2.2 Jet-wall interaction	13
2.3 Injection pressure	16
2.4 Jet-jet interaction	17
2.5 Motivation	18
3 Simulation tools and combustion models for CI engine simulation	20
3.1 Review of the available modelling tools	20
3.1.1 KIVA	20
3.1.1.1 Development story	21
3.1.1.2 Major contributors	21
3.1.1.3 Advantages and limitations	24

3.1.2	STAR-CD	25
3.1.2.1	About numerical methods	25
3.1.2.2	About models for flow, spray and combustion	25
3.1.2.3	Usage by different groups	26
3.1.3	Converge	26
3.1.3.1	About numerical methods	26
3.1.3.2	About models for spray and combustion	27
3.1.3.3	Usage by different groups	27
3.1.4	OpenFOAM	27
3.2	OpenFOAM: A detailed view	30
3.2.1	Finite volume discretisation	30
3.2.2	Solution algorithm	31
3.2.3	Moving mesh techniques	32
3.2.4	Specification and calculation of thermo-physical properties	33
3.2.5	Spray modelling and validation	34
3.2.5.1	Validation of the spray model	40
3.2.6	Turbulence closure model	43
3.2.7	Combustion model and validation	44
3.2.7.1	Chemical reaction mechanisms and physical properties	48
3.2.7.2	Validation of the combustion model	50
4	Automotive-size optical diesel engine and diagnostics	57
4.1	Engine setup	58
4.2	Diagnostics	59
4.2.1	Low-temperature natural flame chemiluminescence	59
4.2.2	OH* chemiluminescence	60
4.2.3	OH planar laser-induced fluorescence (OH PLIF)	61
4.2.4	Fuel planar laser-induced fluorescence (Fuel PLIF)	62
4.3	Measurements and processing of results	63
4.3.1	In-cylinder pressure and heat release rate	63
4.3.2	Image selection and processing for optical diagnostics	63

5	Comparison of modelling and optical diagnostics in an automotive-sized diesel engine – baseline condition	65
5.1	In-cylinder pressure and heat release rate comparison	66
5.2	Jet-tip penetration comparison	68
5.3	Cool-flame period	71
5.4	Main combustion period	74
5.5	Scalar dissipation rate study	80
5.6	Heat release rate study in mixture fraction space	84
5.7	Re-entrainment study	87
5.8	Emission of CO and un-burned hydrocarbons (UHC)	90
5.8.1	Un-burned hydrocarbons (UHC)	91
5.8.2	Carbonmonoxide (CO)	91
5.9	Development of combustion and comparison with conceptual models	93
5.10	Conclusions	95
6	Effect of injection pressure on the combustion development in an automotive-size diesel engine	100
6.1	Engine operating conditions and modelling	101
6.2	In-cylinder pressure and heat release rate comparison	102
6.3	Jet-tip penetration comparison	104
6.4	Cool-flame period	106
6.5	Main combustion period	110
6.5.1	Re-entrainment study	117
6.6	Combustion development study in mixture fraction space	118
6.7	Un-burned hydrocarbons (UHC) and CO emissions	120
6.7.1	Un-burned hydrocarbons (UHC)	120
6.7.2	Carbon monoxide(CO)	121
6.8	Development of combustion and comparison with conceptual models	123
6.9	Conclusions	125
7	Effect of jet-jet interaction on the combustion development in an automotive-size diesel engine	128
7.1	Operating conditions	128

7.2	Comparison of in-cylinder pressure and apparent heat release rate from simulations	129
7.3	Combustion during cool-flame period	133
7.4	Combustion during main combustion period	137
7.5	Formation and oxidation of soot precursors	141
7.6	Un-burned hydrocarbons (UHC) and CO emissions	144
7.7	Comparison with conventional and low temperature combustion (LTC)	148
7.8	Conclusions	150
8	Modelling of <i>n</i>-heptane aromatic hydrocarbon formation in an optically accessible heavy duty engine	152
8.1	Chemical mechanism	154
8.2	Validation of the mechanism	156
8.2.1	Ignition delay time	156
8.2.2	Premixed flat flame	157
8.2.3	Counter-flow diffusion flame	158
8.3	Engine simulation results	159
8.3.1	Numerical setup	162
8.3.2	In-cylinder pressure and heat release rate comparison . . .	162
8.3.3	Effects of jet-wall and jet-jet interactions on PAH formation	165
8.3.3.1	Interactions in the main combustion period . . .	166
8.3.3.2	Mixing-controlled period	171
8.3.3.3	Further discussion	173
8.4	Conclusions	174
9	Conclusions	179
9.1	Summary of the thesis	179
9.2	Recommendations for future work	183
A	Numerical simulation of the impact of wall on the flame zone in an automotive-size diesel engine	186
A.1	Abstract	186
A.2	Introduction	187

A.3	Experimental setup	189
A.3.1	Engine configuration	189
A.3.2	Engine operating conditions	189
A.4	Numerical setup	189
A.4.1	CFD code	189
A.4.2	Computational grids and initial conditions	190
A.5	Results and Discussion	191
A.5.1	Pressure and heat release rate comparison	191
A.5.2	OH* chemiluminescence comparison	192
A.5.3	CFD based reasoning for flame base height reduction	193
A.6	Conclusions	195
References		198

List of Figures

2.1	Schematic of Dec's conceptual model for conventional diesel combustion during the quasi-steady period of diesel combustion [45; 115].	9
2.2	Conventional diesel and other combustion processes in relation to NOx and soot-forming zones [109].	10
2.3	(a) Conceptual model of conventional, heavy-duty, direct injection diesel combustion [45; 115]. (b) Conceptual model of light-duty, late-injection, EGR-diluted, partially premixed low-temperature combustion [115].	14
3.1	Overview of OpenFOAM structure [3].	29
3.2	A geometric Field <Type> and its operators [2].	31
3.3	The inheritance list of hsPsiMixtureThermo class.	34
3.4	Comparison of axial penetration of n-heptane vapour.	41
3.5	Comparison of radial distribution of mixture fraction at 1.13 <i>ms</i> aSOI at 30 <i>mm</i> and 50 <i>mm</i> from the injector.	42
3.6	Comparison of radial distribution of mixture fraction at 6 <i>ms</i> aSOI at 30 <i>mm</i> and 50 <i>mm</i> from the injector.	42
3.7	Schematic representation of the integrated detailed chemistry model.	49
3.8	Comparison of transient temperature evolution in a homogenous combustion of n-heptane vapour using the LLNL reaction mechanism at $\phi = 0.5, 1$ and 1.5 . Black lines: from SENKIN. Red lines: using OpenFOAM without DAC. Green lines: using OpenFOAM with DAC.	51
3.9	Swirl ratio calculated using Eq.(3.45) in a mid axial plane at different crank angles.	52

LIST OF FIGURES

3.10	Computational grids used for the combustion model validation. . .	53
3.11	Velocity (m/s) contours with vectors showing the asymmetric swirl.	54
3.12	Motored pressure comparison.	54
3.13	Meshes used for mesh dependence study of the spray.	55
3.14	Iso-contours of fuel mass fraction with two meshes as shown in Fig.3.13.	55
3.15	Pressure and aHRR comparison with experimental data in C1 an C2 cases.	56
4.1	A schematic diagram of the optical engine with experimental setup. Schematic picture of piston and bowl shape after quartz window cuts (shown in bottom right corner) [17].	59
4.2	Relative positions of laser sheet levels, nominal spray axis and piston bowl geometry at top dead centre [17].	62
5.1	In-cylinder pressure and apparent heat release rate (aHRR) com- parison.	67
5.2	Relative position of jet of interest – top view of piston bowl. . . .	69
5.3	A schematic pictorial representation of calculation of jet-tip pene- tration length.	69
5.4	Jet-tip penetration length comparison.	71
5.5	Comparison of fuel penetration. (a) Fuel PLIF from the exper- iment in a plane at 7 mm from fire-deck. (b) n-heptane mass fraction contours in a plane at 7 mm from fire-deck from CFD. (c) n-heptane mass fraction contours in a plane along jet-axis from CFD.	72
5.6	Velocity vector plots in a plane at 7 mm from fire-deck at different crank angles.	73
5.7	(a) Cool flame chemiluminescence from the experiment. (b) Line of sight mass fraction contours of CH_2O from CFD. (c) Mixture fraction (Z) contours with stoichiometric mixture fraction line from CFD.	73
5.8	OH and CH_2O mass fraction contours from CFD at 7 mm from fire-deck at 8.5° CA aTDC.	75

LIST OF FIGURES

5.9	Comparison of line of sight chemiluminescence images of OH* from the experiment and mass fraction contours of OH* from the simulations at 9.5 °, 11.5 ° and 13.5 ° CA aTDC.	76
5.10	Comparison of ensemble averaged online OH PLIF from the experiment and mass fraction contours of OH from the simulations at 9.5 ° CA aTDC in planes at 5, 7 and 10 mm from fire-deck. . .	78
5.11	Comparison of ensemble averaged online OH PLIF from the experiment and mass fraction contours of OH from the simulations at 11.5 ° CA aTDC in planes at 5, 7 and 10 mm from fire-deck. .	79
5.12	Comparison of ensemble averaged online OH PLIF images from the experiment and mass fraction contours of OH from the simulations at 13.5 ° CA aTDC in planes at 5, 7 and 10 mm from fire-deck. .	80
5.13	First observation of second-stage OH chemiluminescence in experiment and simulation.	81
5.14	Scalar dissipation rate (χ) at 7 mm from fire-deck during cool-flame and main combustion periods. The black encircled regions represent regions of moderate χ	82
5.15	Scalar dissipation rate (χ) at jet-tip.	83
5.16	Scatter plots of heat release rate (J/s) in mixture fraction space and conditional average of heat release rate with respect to mixture fraction. First column: on up-swirl side; Second column: on down-swirl side.	85
5.17	Planes considered along the jet-axis to study re-entrainment effect.	87
5.18	Contours at 7°, 9°, 10° and 12° CA aTDC in the plane 1 as shown in Fig. 5.17. First row: velocity vectors; Second row: contours of ketohydroperoxyl (KET) and CO; Third row: contours of formaldehyde (CH ₂ O); Fourth row: contours of heat release rate (HRR) in J/s; Fifth row: contours of temperature in <i>kelvin</i>	89
5.19	Contours at 7°, 9°, 10° and 12° CA aTDC in the plane 2 as shown in Fig. 5.17. First row: velocity vectors; Second row: contours of formaldehyde (CH ₂ O); Third row: contours of temperature in <i>kelvin</i> ; Fourth row: contours of scalar dissipation rate (χ) in s ⁻¹	90

LIST OF FIGURES

5.20	Transient development of CO and un-burned hydrocarbons (UHC). First column: on up-swirl side; Second column: on down-swirl side.	92
5.21	3-D iso-contours of CO, un-burned hydrocarbons (UHC), mixture fraction (Z) and temperature in <i>kelvin</i> at 80° CA aTDC.	93
5.22	Combustion development in an automotive-size, direct injection diesel combustion (present case).	96
6.1	Comparison of pressure and apparent heat release rate at 100, 130 and 160 MPa of injection pressure.	103
6.2	Comparison of jet-tip penetration length at 100, 130 and 160 MPa of injection pressure.	105
6.3	Comparison of fuel mass fraction contours in a plane at 7 mm from fire-deck from CFD at 70, 100, 130 and 160 MPa of injection pressure.	106
6.4	Comparison of cool-flame period chemiluminescence from the ex- periment and line of sight CH_2O contours from CFD at 100 and 130 MPa of injection pressure.	107
6.5	Line of sight CH_2O contours from CFD at 160 MPa of injection pressure.	108
6.6	Schematic representation of zones for mass split study.	109
6.7	Contours of mixture fraction (Z) and scalar dissipation rate (χ) in a plane at 7 mm from fire-deck at 70, 100, 130 and 160 MPa injection pressure and at 4° CA aTDC.	111
6.8	First appearance of second-stage OH radical concentration from CFD at 100, 130 and 160 MPa injection pressure in a plane at 7 mm from fire-deck.	112
6.9	Comparison of OH PLIF and OH* chemiluminescence from exper- iment and OH and OH* mass fraction contours from simulations at 100 MPa injection pressure in planes at 5, 7 and 10 mm from fire deck at 9° and 11° CA aTDC.	113
6.10	Schematic representation of laser sheet attenuation.	115

LIST OF FIGURES

6.11	Comparison of OH PLIF and OH* chemiluminescence from experiment and OH and OH* mass fraction contours from simulations at 130 MPa injection pressure in planes at 5, 7 and 10 mm from fire deck at 9° and 10° CA aTDC.	116
6.12	OH and OH* mass fraction contours from simulations at 160 MPa injection pressure in planes at 5, 7 and 10 mm from fire deck at 8° and 11° CA aTDC.	117
6.13	Combustion heat release rate study in mixture fraction space from simulations at 3°, 7° and 11° CA aTDC with 100, 130 and 160 MPa injection pressures.	119
6.14	Comparison of transient development of un-burned hydrocarbons (UHC) and CO from the simulations with 70, 100, 130 and 160 MPa injection pressure at 55° CA aTDC.	122
6.15	Iso-contours of UHC, CO, temperature and mixture fraction from the simulations with 100 MPa injection pressure at 55° CA aTDC.	123
7.1	A schematic representation of relative position of two jets (viewed from top).	129
7.2	Comparison of in-cylinder pressure and apparent heat release rate from the simulations. (a) At 70 and 130 MPa injection pressure with two jets. (b) Comparison with single jet and two jets at 70 and 130 MPa injection pressure.	130
7.3	Top row: <i>n</i> -heptane mass fraction contours. Bottom row: Velocity vectors. Both the plots are from a plane at 7 mm from fire-deck with 70 MPa injection pressure.	132
7.4	Top row: <i>n</i> -heptane mass fraction contours. Bottom row: Velocity vectors. Both the plots are from a plane at 7 mm from fire-deck with 130 MPa injection pressure.	133

LIST OF FIGURES

7.5	Top row: Line of sight CH_2O contours. Bottom row: Mixture fraction contours in a plane at 7 mm from fire-deck. Both the plots are taken at 5° , 8° and 10° CA aTDC with 70 MPa injection pressure. Contours on top right corner are line of sight CH_2O contours along jet axes at 8° CA aTDC. 1-1 is along jet 1 and 1-2 is along jet 2.	134
7.6	Top row: Line of sight CH_2O contours. Bottom row: Mixture fraction contours in a plane at 7 mm from fire-deck. Both the plots are taken at 2° , 5° , 8° and 9° CA aTDC with 130 MPa injection pressure. Contours on top right corner are line of sight CH_2O contours along jet axes at 5° CA aTDC. 1-1 is along jet 1 and 1-2 is along jet 2.	135
7.7	Temperature (K) contours in a plane at 7 mm from fire-deck. Left: At 10° CA aTDC with 70 MPa injection pressure. Right: At 9° CA aTDC with 130 MPa injection pressure.	136
7.8	First three columns: Mass fraction contours of OH in three different planes at 5, 7 and 10 mm from fire-deck at 10° , 11° and 13.5° CA aTDC. Last column: Line of sight mass fraction contours of OH^* at 10° , 11° and 13.5° CA aTDC. All the contours are with 70 MPa injection pressure.	138
7.9	First three columns: Mass fraction contours of OH in three different planes at 5, 7 and 10 mm from fire-deck at 9° , 10° and 13° CA aTDC. Last column: Line of sight mass fraction contours of OH^* at 9° , 10° and 13° CA aTDC. All the contours are with 130 MPa injection pressure.	139
7.10	Scalar dissipation rate (χ) in a plane at 7 mm from fire-deck at 10° CA aTDC with 70 MPa injection pressure and at 9° CA aTDC with 130 MPa injection pressure.	140
7.11	Mass fraction contours of formaldehyde (CH_2O) and OH in a plane at 7 mm from fire-deck. First row: 70 MPa injection pressure at 12° CA aTDC. Second row: 130 MPa injection pressure at 10° CA aTDC.	142

LIST OF FIGURES

7.12	First row: Line of sight mass fraction contours of ($C_2H_2 + C_3H_3$). Second row: Line of sight mixture fraction (Z) contours. Both the plots are taken at 10° , 12° and 16° CA aTDC with 70 MPa injection pressure.	143
7.13	First row: Line of sight mass fraction contours of ($C_2H_2 + C_3H_3$). Second row: Line of sight mixture fraction (Z) contours. Both the plots are taken at 9° , 10° and 16° CA aTDC with 130 MPa injection pressure.	144
7.14	Comparison of transient development of UHC and CO with two jets at 70 and 130 MPa injection pressure from simulations.	145
7.15	First column: Mass fraction iso-contours of UHC and CO at 16° CA aTDC with 70 MPa injection pressure. Second column: Mass fraction iso-contours of UHC and CO at 16° CA aTDC with 130 MPa injection pressure.	146
7.16	First column: Mass fraction iso-contours of UHC and CO at 80° CA aTDC with 70 MPa injection pressure. Second column: Mass fraction iso-contours of UHC and CO at 80° CA aTDC with 130 MPa injection pressure. (A): Velocity vectors in a plane at 10 mm from fire-deck at 80° CA aTDC with 70 MPa injection pressure (viewed from top).	148
7.17	Comparison of transient development of UHC and CO with single and two jets configuration at 70 and 130 MPa injection pressure from simulations.	149
8.1	Comparison of predicted ignition delay times using LLNL-MAH and LLNL mechanisms with experimental data from Ciezki et al. [37].	157
8.2	Mole fractions of important species and soot precursors for the rich n-heptane/air premixed flat flame (dots: experiment from Bakali et al. [22]; blue lines: simulations using LLNL-MAH; green lines: simulations from Blanquart et al. [29]).	158

LIST OF FIGURES

8.3	Mole fractions of important species and soot precursors for the n-heptane/air counter-flow diffusion flame (dots: experiment from Berta et al. [24]; blue lines: simulations using LLNL-MAH; green lines: simulations from Blanquart et al. [29]).	160
8.4	Comparison of in-cylinder pressure and aHRR with the experimental pressure trace [56] for 70% and 80% bowl geometries.	163
8.5	Top row: Formaldehyde (CH_2O) and equivalence ratio (non-combustion condition) comparison with the experiment [56] at 7° CA aTDC and in a plane at 12 mm from firedeck for the 70% bowl geometry. Bottom row: formaldehyde (CH_2O) and equivalence ratio (non-combustion condition) comparison with the experiment [56] at 7° CA aTDC and in a plane at 10 mm from firedeck for the 80% bowl geometry.	165
8.6	Transient formation of PAH from simulations for both 70% and 80% bowl geometries.	166
8.7	Comparison of equivalence ratio in non-combustion condition and $\text{CH}_2\text{O}/\text{PAH} + \text{OH}$ with combustion at 12° CA aTDC. The planes are taken at 7, 12 and 18 mm from fire-deck for the 70% bowl geometry.	167
8.8	Comparison of $\text{CH}_2\text{O}/\text{PAH} + \text{OH}$ at 14° CA aTDC. The planes are taken at 7, 12 and 18 mm from fire-deck for the 70% bowl geometry. Laser beam width is shown by black rectangle.	169
8.9	Comparison of equivalence ratio in non-combustion condition at 12° CA aTDC and $\text{CH}_2\text{O}/\text{PAH} + \text{OH}$ with combustion at 14° CA aTDC. The planes are taken at 7, 10 and 14 mm from fire-deck for the 80% bowl geometry.	170
8.10	Comparison of $\text{CH}_2\text{O}/\text{PAH} + \text{OH}$ at 19° CA aTDC. The planes are taken at 7, 12 and 18 mm from fire-deck for the 70% bowl geometry. Laser beam width is shown by black rectangle.	172
8.11	Comparison of $\text{CH}_2\text{O}/\text{PAH} + \text{OH}$ at 24° CA aTDC. The planes are taken at 7, 10 and 14 mm from fire-deck for the 80% bowl geometry. Laser beam width is shown by black rectangle.	173

LIST OF FIGURES

8.12	Comparison of simulated equivalence ratio (ϕ) with velocity vectors in non-combustion condition (first column), temperature with combustion (second column) and MAH mass fraction contours with velocity vectors (third column). The plane is taken at 18 mm from firedeck for the 70% bowl geometry and 14 mm from firedeck for the 80% bowl geometry. The crank angle position considered is 14° CA aTDC.	175
8.13	Comparison of model predicted mass fraction contours of CH ₂ O/C ₂ H ₂ + OH (second column) and CH ₂ O/MAH + OH (third column) using LLNL-MAH mechanism at 14° aTDC with PLIF images (first column) from the experiment at 7 mm, 10 mm and 14 mm planes from the fire-deck and simulations (fourth column) from Ref. [58].	177
8.14	Model predicted temporal evolution of total mass of C ₂ H ₂ in kg per kg of fuel using LLNL-MAH and LLNL mechanisms [40] and total mass of MAH in kg per kg of fuel using LLNL-MAH mechanism. .	178
A.1	A top view schematic of the modified piston and jet trajectory of a single jet bisecting into a simultaneous free-jet and wall-jet [144].	188
A.2	Computational grids.	191
A.3	In-cylinder pressure and apparent heat release rate comparison. .	192
A.4	OH* chemiluminescence comparison. Experiment (left), with the LLNL mechanism (right).	193
A.5	Comparison of flame base heights.	194
A.6	Iso-surfaces of CO and $\phi = 1$ and temperature (K) contours with velocity vectors from the simulations at 8, 9 and 10° CA aTDC. .	195
A.7	Averaged velocity magnitude (m/s) contours from the simulations at 8 and 9° CA aTDC.	196

List of Tables

3.1	RNG $k - \epsilon$ model constants [66].	44
3.2	Selected operating conditions.	53
4.1	Important engine and injector specifications	60
5.1	Important operating conditions for baseline case.	66
5.2	ppm values of CO and UHC at 80° CA aTDC.	93
6.1	Important operating conditions for 100, 130 and 160 MPa injection pressure cases.	101
6.2	Percentage split of evaporated fuel between different zones at 4° CA aTDC.	110
6.3	ppm values of UHC and CO at 55° CA aTDC.	124
6.4	Percentage of fuel/UHC mass escaped into squish region at differ- ent injection pressures at 13° CA aTDC.	124
7.1	Important operating conditions for 70 and 130 MPa injection pres- sure cases.	129
8.1	Engine operating conditions.	161

Nomenclature

Roman Symbols

B	Normalised mass fraction of evaporated fuel at droplet surface
B_0	a constant in KH wave instability theory
B_1	a constant in KH wave instability theory
C_{RT}	a constant in RT wave instability theory
C_τ	a constant in RT wave instability theory
C_d	drag co-efficient
D	diameter of a droplet
D_v	diffusivity of fuel
\mathbf{g}	acceleration due to gravity
h_d	sensible enthalpy of droplet
h_s	sensible enthalpy of the gas phase
$H_{f,i}$	heat of formation of species i
h_v	sensible enthalpy of fuel vapour
k	turbulent kinetic energy
K_{RT}	wave number of a breaking RT wave

LIST OF TABLES

m_d	mass of a droplet
Nu	Nusselt number
Oh	Ohnesorge number
Pr	Prandtl number
Q	net adiabatic chemical energy released at a crank angle position during combustion
r	radius of a droplet
r_{AB}	a normalised factor in DRG
r_c	radius of smaller drops
Re_d	Reynolds number of a droplet
$c_{p,v}$	specific heat of fuel vapour
Sc	Schmidt number
Sc_t	turbulent Schmidt number
Sh	Sherwood number
T	temperature of gas phase
T_g	Taylor number
T_d	temperature of a droplet
\mathbf{U}_d	velocity vector of a droplet
V	cylinder volume as a function of crank angle
We_d	Weber number of a droplet
We_g	Weber number of gas phase
\dot{Y}_i	rate of production or consumption of species i

LIST OF TABLES

Y_i	mass fraction of species i
$Y_{f,\infty}$	mass fraction of fuel far away from droplet
$Y_{f,s}$	mass fraction of fuel at droplet surface
Z	mixture fraction
a_p	central co-efficient in discretised equations
\mathbf{F}^s	momentum source term due to evaporation of injected fuel
p	pressure
S_{evap}	mass source term due to evaporation of injected fuel
$S_{evap,h}$	energy source term due to evaporation of injected fuel
\mathbf{U}	velocity vector
\mathbf{u}_p	vertex velocity vector of a vertex in a finite volume cell
a_N	co-efficient related to the neighbouring grid points in discretised equations
\mathbf{U}_N	velocity vector at the neighbouring grid points
\mathbf{U}_p	velocity vector at the chosen computational point

Greek Symbols

α	thermal diffusivity
α_t	turbulent thermal diffusivity
χ	scalar dissipation rate
ϵ	turbulent rate of dissipation of kinetic energy
γ_p	diffusion co-efficient of diffusion of the vertex velocity
γ	adiabatic process exponent
κ	thermal conductivity of fuel vapour

LIST OF TABLES

Λ_{KH}	wavelength of a KH wave with maximum growth rate
μ	dynamic viscosity of the gas phase
μ_d	dynamic viscosity of a droplet
μ_v	dynamic viscosity of fuel vapour
Ω_{KH}	frequency of a breaking KH wave
Ω_{RT}	frequency of a breaking RT wave
ρ	density of the gas phase
ρ_d	density of a droplet
ρ_v	density of vapour fuel
σ	surface tension of a droplet
τ_b	boiling relaxation time
τ_e	evaporation relaxation time
τ_{KH}	droplet break-up time in KH wave instability theory
τ_{RT}	droplet break-up time in RT wave instability theory
μ_t	turbulent viscosity

Other Symbols

$ $	magnitude of a vector
$\text{tr}(\)$	trace of a square matrix

Acronyms

aHRR	apparent heat release rate
CR	compression ratio
EVO	exhaust valve open

LIST OF TABLES

IVC	intake valve closure
LTC	low temperature combustion
ppm	parts per million
SIBS	Semi-Implicit Bulirsch-Stoer
TDC	top dead centre
UHC	unburned hydrocarbons
aSOI	after start of injection
aTDC	after top dead centre
BFS	breadth first search
CA	crank angle
CI	compression ignition
DAC	dynamic adaptive chemistry
DRG	direct relation graph
EGR	exhaust gas recirculation
KH	Kelvin-Helmholtz wave instabilty theory
LES	large eddy simulation
PAH	poly-cyclic aromatic hydrocarbon
PLIF	planar laser induced fluorescence
PM	particulate matter
PPC	partially premixed combustion
RANS	Reynolds averaged Navier-Stokes
RT	Rayleigh-Taylor wave instabilty theory

LIST OF TABLES

SCR selective catalytic reactor

SOI start of injection

Chapter 1

Introduction

The high thermal efficiency and the associated high power density of direct injected diesel engine combustion are the driving features that lead to its wide application in the automobile industry despite high NO_x and particulate matter (PM) emissions. The industry has been investing constantly in research and development in developing new technologies that can suppress NO_x and PM emissions because of the enforcement of stringent emission laws worldwide. The technologies include post-combustion emissions control such as selective catalytic reduction (SCR) or diesel particulate filters (DPF) and during-combustion emissions-control such as partially premixed combustion (PPC) or low-temperature combustion using high rates of exhaust gas recirculation (EGR) [72; 114]. Post-combustion measures can add to the vehicle cost of an already expensive diesel engine, so avoiding these measures would be preferred by manufacturers and consumers.

Better knowledge of the in-cylinder processes that affect emissions and limit the fuel efficiency for new in-cylinder combustion regimes would aid the development of low-emissions and more efficient diesel engines. One way this knowledge may be gained is through observations using in-cylinder imaging diagnostics. For instance, data obtained using multiple laser-based and imaging diagnostics was distilled into a conceptual model of conventional diesel combustion by Dec [45]. A summary of this work is depicted in Fig. 2.3a. The model explains that liquid fuel vaporises due to hot charge-gas entrainment and mixing, fuel and air react in a fuel-rich mixture leading to soot formation at the jet head, and high-temperature diffusion flame exists at the jet periphery leading to nitrogen monoxide (NO) for-

mation. Dec's model changed the paradigm of engine research that was largely driven by performance tests and trial and error approaches towards fundamentals-driven research using advanced diagnostics and computational modelling. Later, this paradigm became the basis to develop new conceptual models that are applicable to advanced combustion regimes such as high exhaust gas recirculation (low oxygen intake air) based low temperature combustion (LTC) for simultaneous reduction of soot and NO [115]. Further examples of involving techniques like chemiluminescence and laser diagnostics to understand diesel combustion processes may be found in Refs. [46; 91; 113; 127].

One outstanding issue that is not fully addressed by these models is flame-wall interaction, which impacts significantly the in-cylinder flow field, air-fuel ratio distribution, and temperature, and thus soot formation [52; 54; 127]. Compared with diesel engine technology at the time of development of Dec's model, several technology changes have caused the wall to become much more important than it was in the past. Injection pressures have increased considerably, leading to higher jet momentum, and thus flame lift-off length (the lift-off length is the distance from the fuel nozzle to the location of high temperature chemical reactions). Reduced oxygen concentration to achieve low emissions LTC also significantly increases the lift-off length. At the same time, with downsizing trends, particularly in the automotive market, the wall is now closer to the injector. All these factors lead to an increased importance of flame-wall interactions.

In particular, combustion development in automotive-size, direct injection diesel engines under normal oxygen conditions (21% by volume) takes place differently compared to heavy duty engines under similar operating conditions. However, while conceptual models for conventional diesel combustion in heavy duty engines [45] and low-temperature combustion with EGR in heavy and light duty engines have been proposed [115], such efforts have been very few for small bore engines under normal oxygen conditions (21% by volume). Moreover, effect of inter-dependent processes like injection pressure, injection timing, jet-wall and jet-jet interactions are not fully understood on the combustion development in small bore engines. In this direction, Rusly et al. [143] studied experimentally to understand combustion and pollutants formation with short injection duration leading to positive ignition dwell and with long injection duration with an aim to

investigate engine knock and re-entrainment phenomenon. These experimental insights have been useful in unfolding diesel combustion in different regimes and for development of computational fluid dynamics (CFD) based tools.

Another way to gain knowledge about the in-cylinder combustion processes is by multi-dimensional CFD modelling. Multi-dimensional simulation tools are now routinely used for the prediction and analysis of combustion development and post combustion emissions in engines. Numerical models can significantly reduce time and cost of research and development. Once validated they can be used in a number of ways, for example by what-if scenario analysis, or to guide designers by deliver insight into the phenomena involved more rapidly and more cost effectively than an experimental approach. All models, and particularly complex models such as those needed to simulation engine combustion, are usually valid only over a certain range of operating conditions and in a specific regimes because of assumptions and approximations made in the model. The valid range and the errors committed needs to be well understood before the model can be a useful tool in practical engine design.

Recently, many engine specific CFD tools have come into existence both from universities and commercial companies to predict engine performance and emissions [6; 12; 14; 88]. However, prediction capability of any CFD tool depends on the accuracy of implemented sub-models related to turbulence, diesel spray and diesel combustion. Furthermore, better prediction of global parameters like in-cylinder pressure and exhaust emissions does not guarantee that in-cylinder combustion processes are correctly predicted. In particular, there are relatively few direct assessments of whether the available models can predict the details of the influence of jet-wall and jet-jet interactions on combustion development inside a running engine. While there have obviously been many numerical studies which involved these interactions, for example [151; 160], they mostly considered only coarse experimental measures such as pressure traces and engine-out emissions. To establish greater confidence of in the modelling, more detailed comparisons are clearly needed.

1.1 Objectives

The main objectives of the work are as follows:

- To develop a multi-dimensional modelling methodology which is capable of predicting spray, mixture formation, and combustion development in jet-wall and jet-jet interactions in diesel engines.
- To comprehensively validate this model against in-cylinder experimental data in selected operating conditions which expose jet-wall and jet-jet interactions, with emphasis on optical measurements that span the phases of mixture formation, first- and second-stage combustion, and formation of key pollutants.
- To comprehensively examine the observed jet-wall and jet-jet interactions using the model and thereby learn more about the role of these interactions on combustion development and emissions formation.

The thesis is organised as follows:

- Chapter 2 presents a short literature review related to the work. A conceptual model of conventional diesel combustion in heavy duty engines proposed by Dec [45] is first reviewed. It is compared to a conceptual model of low-temperature combustion with exhaust gas recirculation (EGR) proposed for heavy and light duty engines proposed by Musculus et al. [115]. Later in the thesis, the combustion development in an automotive-size, optical diesel engine will be compared to these conceptual models. Chapter 2 then briefly covers outcomes from various diesel engine experiments pertaining to effects of jet-wall interactions, injection pressure and jet-jet interactions. Finally, it covers conclusions from certain relevant numerical simulations.
- Chapter 3 briefly reviews the available multi-dimensional modelling packages for engine combustion, discussing the reasons for the selection of OpenFOAM in this project. It then discusses details of the spray, turbulence, and combustion models adopted in this project. Two models of optical

engines were considered. A full geometry, full cycle model, including the intake and exhaust stroke, was developed for a small bore engine, while a sector-mesh geometry was used for a heavy duty engine. Relatively detailed chemical kinetic models were also considered, while well-known and well understood spray and turbulence models, and a simplified direct-integration turbulence-chemistry model was adopted.

- In chapter 4, the in-house automotive-size, optical diesel engine, which is modelled in chapters 5-7 is described. The experimental measurements were performed by others, but need to be recounted for completeness of the thesis. The measurements included natural flame chemiluminescence during the cool flame period, OH* chemiluminescence during the main combustion period, planar laser induced fluorescence (PLIF) of fuel and OH.
- In chapter 5, a numerical study of combustion development in the small bore engine with a single jet injection of fuel at 70 MPa injection pressure (baseline condition) is presented. The available experimental data is used to validate the numerical results at different stages of the combustion development. The numerical analysis is then extended to further understand the jet-wall interaction effect on the combustion development and relevance to the conceptual models.
- In chapter 6, the effect of injection pressure on the combustion development is studied in the small bore engine. The same configuration of a single jet as used at baseline condition is presented. The injection pressures considered were 100, 130 and 160 MPa. Comparisons of model and experiment are performed before further numerical analysis of the fuel injection pressure effects.
- In chapter 7, a numerical study of effect of jet-jet and jet-wall interactions between two jets on the combustion development is carried out for two injection pressures. No experimental data were available for this study.
- Chapter 8 is mainly devoted to studying aromatic hydrocarbon formation. No data on aromatics were available from the small bore engine, so a heavy

duty engine was considered instead. The heavy duty engine was operated in a low-temperature combustion mode where jet-wall and jet-jet interactions were significant so that these data could still contribute usefully to the thesis as a whole. The development steps, validation, and application of a combined *n*-heptane and single ring aromatic compounds reaction mechanism is first presented. Comparisons to various optical measurements in the heavy duty engine are then considered and discussed.

- In chapter 9, overall conclusions of the work and recommendations for the future work are highlighted.

Chapter 2

Literature review

Combustion in a direct injected, diesel spray, compression ignition engine depends on many inter-dependent parameters like common-rail injection pressure, injection timing and duration, nozzle included angle and orifice diameter, amount of fuel injected, ambient temperature and density and geometry of the engine. Many experimental studies have been done [46; 91; 113; 127; 143] and will be done to understand and optimally manage the inter-dependent parameters to improve combustion efficiency and at the same time aim for less undesirable exhaust emissions. As the focus of the current work is on the effect of injection pressure and engine geometry in a small bore, automotive-size, diesel engine, the review is limited to those two effects concluded from experiments and numerical simulations. In the beginning, highlights from conceptual models of conventional diesel combustion [45] and low-temperature diesel combustion with exhaust gas recirculation [115] are covered.

The following section has been added in response to comments from Examiner-1

2.1 Conceptual models

2.1.1 Conventional diesel combustion

In conventional diesel engines, diesel is injected shortly before TDC with a little or no EGR. Fuel injection is long enough for ignition to

start before the end of injection and much of the fuel burns in mixing-controlled combustion mode. Dec [45] proposed a conceptual model for conventional direct injection diesel-spray combustion based on laser-sheet imaging conducted on an optically accessible heavy-duty diesel engine installed in Sandia National Laboratories [115].

Evaporation stage: The injected diesel liquid from each hole of the injector breaks into droplets and develops into a roughly conical shape. The high jet velocity due to relatively high injection pressure (~ 100 MPa) causes natural entrainment of surrounding hot (~ 1000 K) [48] in-cylinder gases towards fuel droplets. The thermal energy provided by entrained hot gases causes vapourisation of fuel droplets. The entrainment increases with downstream distance and causes equivalence ratio to decrease approximately inversely with downstream distance, which has been and is observed experimentally in direct fuel vapour measurements [96]. The fuel vapour penetration rate scales as $\rho_a^{-0.35}$ [116], where ρ_a is the ambient density. This conveys that higher density slows down the evaporated fuel jet penetration rate. Similarly, the liquid length varies with $\rho_a^{-0.7}$ [51].

Combustion stage: After a certain distance from the point of injection, only vaporised fuel exists and because of sustained jet momentum, the vapour fuel further entrains hot in-cylinder gases. The first-stage combustion reactions start at the tip of the liquid length across the jet, which is indicated by weak chemiluminescence and fluorescence of intermediate species such as formaldehyde [35]. A short duration after the start of the first-stage combustion, the reactions progress into the second-stage combustion releasing considerable heat, leading to the high temperature premixed burn phase of diesel combustion. The fuel-air mixture is usually rich in the premixed burn stage with an equivalence ratio around 2. The hot temperatures (~ 1600 - 2000 K) with rich conditions trigger formation of polycyclic aromatic hydrocarbon (PAH) soot-precursor species and followed by soot formation that fills the entire downstream jet cross section. Combustion products of the premixed burn reach further downstream and a thin diffusion flame

forms on the periphery, reaching upstream till the premixed burn region. Nitrogen oxides form in the hot, near-stoichiometric mixtures over the diffusion flame. The long injection duration enables the co-existence of all the stages of the conventional diesel spray combustion in a quasi-steady state jet. Over this, hot partial combustion products leaving the premixed burn zone combined with hot products entrained from the diffusion flame increase the temperature of the hot core region, which results in continuous formation of soot. Most of the formed soot is oxidised near the diffusion flame in the presence of OH radicals. A schematic sketch of the quasi-steady state burning jet is shown in Fig. 2.1.

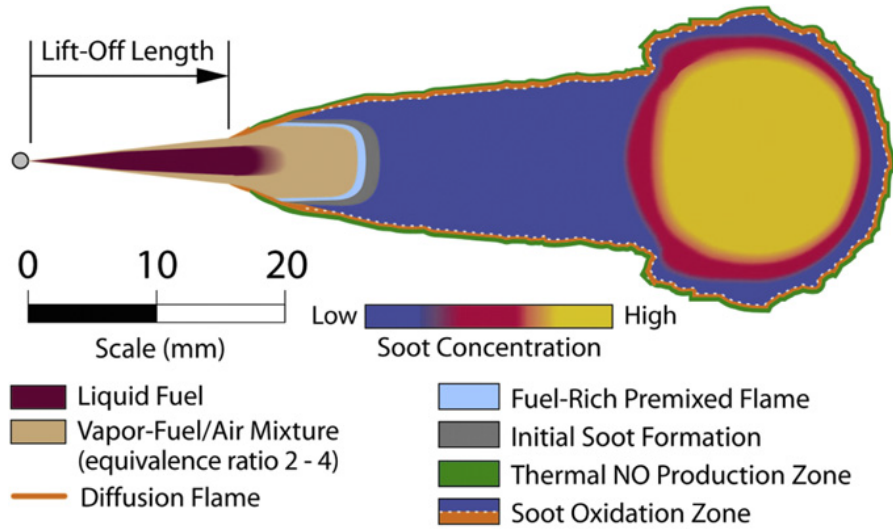


Figure 2.1: Schematic of Dec's conceptual model for conventional diesel combustion during the quasi-steady period of diesel combustion [45; 115].

The soot formation in the core region depends on the magnitude of the lift-off length. The more is the lift-off length, the more is the entrained oxygen to the premixed burn region making the mixture leaner. Below a threshold equivalence ratio of 2, no soot forms in the jet [96]. The lift-off length that effects soot formation is influenced by a combination of parameters like ambient gas temperature, density,

oxygen concentration, injection pressure, nozzle orifice size, and fuel properties [148].

According to this conceptual model, different zones within the flame are responsible for the generation of different pollutants, and in conventional diesel engines, the flame spans both hot, near stoichiometric regions, which are responsible for NO_x formation as well as medium-temperature, fuel-rich regions, which are responsible for soot formation. These features have been conveniently represented on equivalence ratio temperature maps, such as shown in Fig. 2.2, reproduced from Ref. [109], which nominally suggest regions of high pollutant formation. As shown in Fig. 2.2, advanced combustion strategies, which are discussed in more detail later, such as premixed charge compression ignition (PCCI), homogeneous charge compression ignition (HCCI), and low-temperature combustion (LTC) have been proposed to operate in regimes that avoid these pollutant-forming regions of equivalence ratio temperature space.

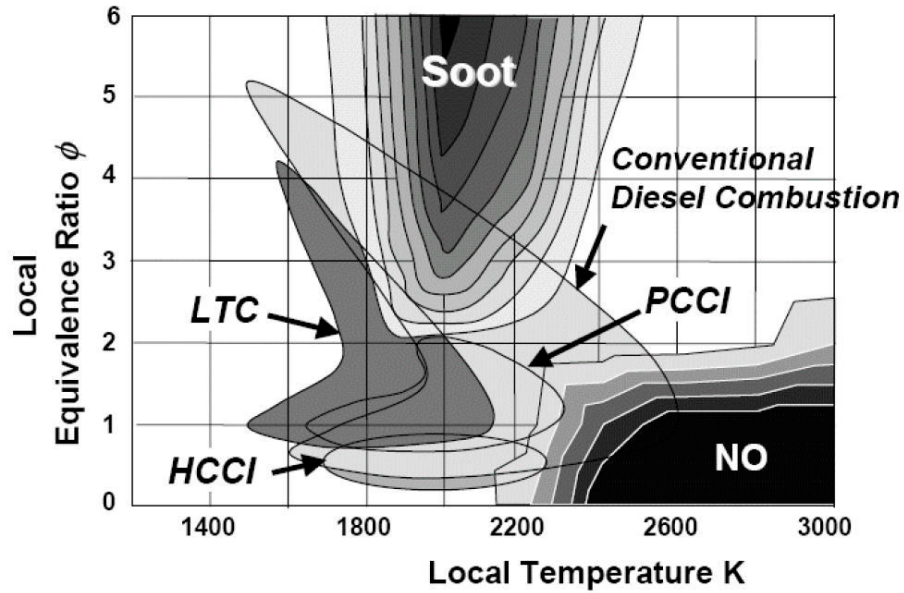


Figure 2.2: Conventional diesel and other combustion processes in relation to NO_x and soot-forming zones [109].

Effect of jet-wall and jet-jet interactions on emissions: In the presence of diesel jet-wall interactions, the above said combustion evolution is disturbed and emissions are affected by the wall interaction. Soot deposition takes place at the point of impingement and escapes oxidation. This deposited soot leads to potential particulate matter engine-out emissions [10]. Also, because of jet-wall interaction, flame surface area reduces, reducing the rate of combustion and the rate of formation of NO_x [49]. Jet injection direction and bowl shape also influence emissions based on how the burning jet impinges on the bowl-wall and re-enters into oxygen rich regions [85]. On the other hand, the jet-jet interaction region leads to locally rich mixtures, which can lead to high soot formation during the combustion and eventually oxidises. If the jet-jet interaction is combined with jet-wall interaction, the high quantity of soot formed may escape oxidation and deposit as particulate matter on the walls. In this case, an optimal bowl design plays a crucial role in controlling the emissions [59; 168].

2.1.2 Partially premixed low-temperature combustion in a light-duty engine with EGR-dilution

Engine out emissions reduction has become an uphill task for engine research community to meet increasingly stringent emission regulations worldwide. Even though after-treatment methods to reduce emissions have matured enough to meet current emission regulations, their usage is limited by higher costs, durability issues, fuel economy penalties and greater space requirements compared to engines without after-treatment [81]. Consequently, in-cylinder strategies to reduce emissions are gaining importance and are now being considered as essential to meet anticipated even more stringent standards.

In diesel combustion, NO_x is formed mainly by thermal (Zel'dovich) mechanism, wherein production rates increase exponentially with temperature. Therefore, low temperature combustion (LTC) methods have taken lead over after-treatment methods. In all LTC strategies,

combustion temperature is reduced either by making the combustible mixture leaner than stoichiometric or using EGR. In both the cases, the combustion temperature is reduced and consequently NO_x formation is also.

Besides slowdown of NO_x formation reactions, rate of soot formation kinetics also decreases with reduced combustion temperature. But, at the same time soot oxidation also slows down with decrease in temperature and oxygen concentration sometimes resulting into a net increase of PM emissions. In the cases with high enough EGR, soot formation rates become so slow that PM emissions reduce even with reduced oxidation [76]. On the other hand, with high EGR levels, reduced combustion efficiency leads to high unburned hydrocarbon (UHC) and CO emissions [38]. To enhance combustion efficiency, with moderate EGR levels, pre-combustion mixing is increased to address PM emissions. Increased pre-combustion mixing is effective because it avoids soot-forming fuel rich pockets [62].

There are many low temperature combustion (LTC) strategies, which can be broadly classified as homogeneous-charge compression ignition (HCCI) and partially premixed compression ignition (PPCI). HCCI can be achieved either by having a relatively uniform premixed vaporized fuel-air mixture which is lean or highly diluted with EGR. All HCCI strategies use either early direct injection of fuel externally to the combustion chamber or direct early injection to allow enough time for mixing of evaporated fuel and air prior to combustion. Combustion of the premixed fuel and air in HCCI is mostly kinetically controlled and independent of time of injection. On the other hand, PPCI uses direct injection of fuel with moderate mixing times. The main difference between HCCI and PPCI is that in PPCI the mixture is more heterogeneous with fuel lean and rich mixtures. Low temperature during combustion is achieved with EGR.

Musculus et. al. [115] developed conceptual models for different types of PPCI combustion strategies through extensive optical diagnostics. The relevant PPCI conceptual model that can be correlated

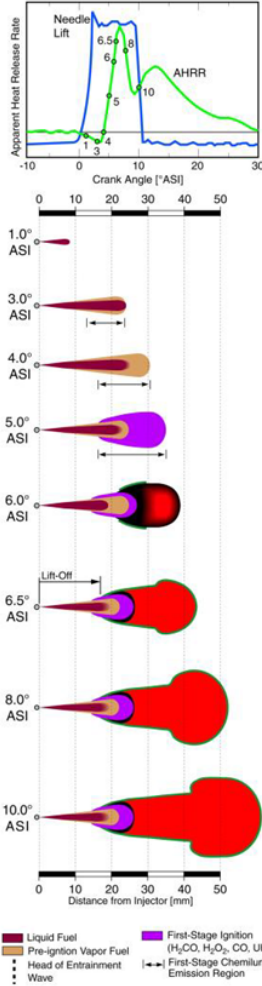
to the diesel spray combustion studied in this thesis is the one formulated for light-duty, late-injection, EGR diluted low temperature combustion.

The light-duty engine considered in Musculus et. al. [115] for the light-duty PPCI combustion conceptual model has closely dimensions as that one studied in this thesis apart from the bowl-shape. A re-entry bowl with a curved bottom profile was used whereas in the present engine, the bowl has a flat bottom surface. The combustion development is shown in Fig. 2.3b. The late fuel-injection is short, spanning around 5° CA. Because of small bowl-diameter, the evaporated fuel impinges on the bowl-wall before the end of injection. The first-stage combustion starts almost after the end of the injection, which is termed as positive ignition dwell. This provides enough time for the entire evaporated fuel to become premixed with air before the start of the combustion. The first-stage combustion starts over the entire partially premixed fuel and the second stage combustion starts over a broad area covering the leading edge of the jet. CO, UHC and the first-stage combustion products are observed in the squish region at 50° CA aTDC, which conveys that the fuel escaped into the squish region has not undergone complete combustion. The conceptual model developed for light-duty engines covers the jet-wall interaction effect on the evolution of low-temperature combustion [115]. In the experimental and numerical study by [56] in a heavy-duty engine, the effect of jet-jet and jet-wall interactions on PAH formation with two different bowl-geometries has been studied. In the jet-jet interaction situation, rich fuel-air mixture forms in the interaction zone and results in the formation of more soot compared to the case in which only jet-wall interactions are present.

2.2 Jet-wall interaction

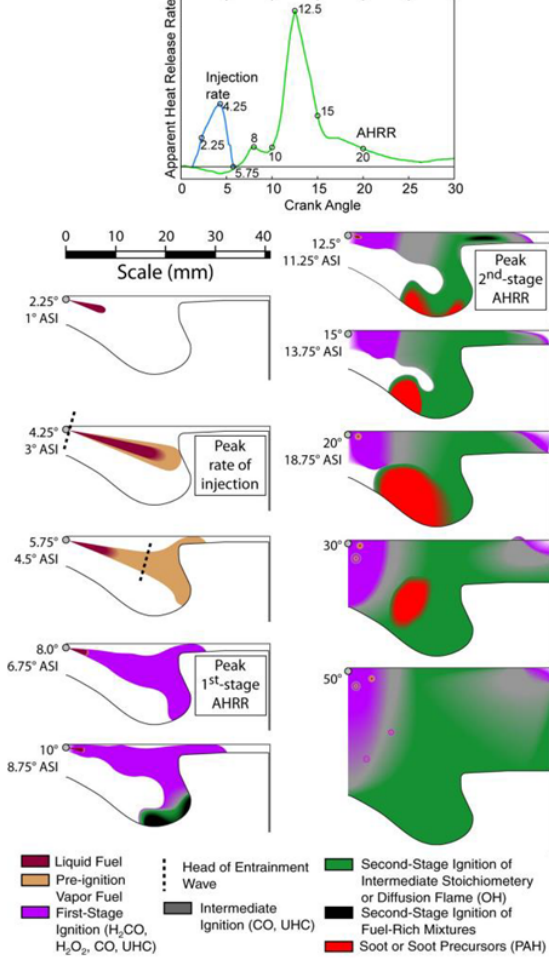
Many experimental studies were done to understand the effect of jet-wall interaction on combustion and pollutants formation. In that direction, Docquier [52]

Conventional heavy-duty, direct-injection diesel combustion



(a)

Light-duty, late-injection, low-load, EGR-diluted partially premixed low-temperature combustion



(b)

Figure 2.3: (a) Conceptual model of conventional, heavy-duty, direct injection diesel combustion [45; 115]. (b) Conceptual model of light-duty, late-injection, EGR-diluted, partially premixed low-temperature combustion [115].

in an experiment on a small-bore optical engine with late injection of fuel showed that soot emissions will be less if the fuel-jet impinges on the bowl-wall nearer to squish volume, which finds a way into squish space and the soot formed can oxi-

dise easily. In another experiment by Bruneaux [34], compared level of mixing of evaporated fuel and air in a free-jet and a perpendicular wall-jet configurations at two different injection pressures. The experiments revealed a significant increase in mixing levels at an injection pressure of 200 MPa due to wall-vortex formation in the wall-jet case compared to the free-jet case at the same injection pressure. However, at 150 MPa injection pressure, observed no net increase in mixing levels with the wall-jet configuration compared to the free-jet configuration as the drop in natural entrainment mixing is compensated by wall-vortex induced mixing. Genzale et al. [56] studied the effects of jet-wall and jet-jet interactions on mixing and pollutants formation processes of a late-injected low-temperature combustion in a heavy-duty diesel engine using three different bowl-diameters of a flat-bowl configuration. The studies provided information that in a smaller bowl-diameter case, the fuel-jet impinges on the bowl-wall before ignition and merges with adjacent jets forming fuel-rich regions, where soot can form. When the bowl-diameter was larger, jet impingement prior to ignition was reduced and delayed and mixtures were lean everywhere. In the upstream portion of the jet, mixtures were too lean for complete combustion. In the third configuration with the smallest bowl-diameter of all the three, caused early impingement and reflected the rich regions to the upstream portion of the jet, where mixtures were predominantly lean. This brought the upstream portion of the jet into combustible regime and reduced the net soot formation.

Some experiments were also devoted to the study of variation of flame lift-off length and affected combustion development under the influence of jet-wall interaction. The study by Pickett et al. [128] showed that in a confined jet environment, redirected combustion gases on to the incoming jet, where the flame exists could actually reduce the flame lift-off length and increase soot formation in the region. According to their study, this effect can be avoided if the fuel injection ends prior to the significant interaction of redirected combustion gases. The experimental investigation of low-soot and soot-free combustion strategies in heavy-duty engines by Polonowski et al. [132] found that sustaining soot-free combustion during the entire combustion period is limited by jet-wall and jet-jet interactions with re-entrainment of hot combustion products towards the flame lift-off length region. Even increase of ambient density and temperature

can reduce the flame lift-off length [112; 115].

In all the above studies, the reported flame lift-off length for heavy-duty engines is in the order of 20 mm to 35 mm from the nozzle centerline. On the other hand, in small-bore engines, because of small bore diameter, lifted flame along the jet-axis may not be seen and instead flame may appear in post jet-wall interaction regions. Besides this, low ambient conditions in small-bore engines compared to heavy-duty engines can further move the flame along the bowl-wall. Additionally, direct injected diesel combustion is characterised by inhomogeneous fuel-air mixtures and high variation of in-cylinder velocity field during fuel injection, which is further effected by jet-wall and jet-jet interactions. These velocity variations induce velocity gradients that impose diffusion rate or mixing rate, which is commonly referred to as the strain rate. As a generalised representation of strain rate in any geometry, scalar dissipation rate is used which measures the gradient of mixture fraction [27] in the domain. According to a fundamental numerical study by Liu et al. [95] in a counterflow diffusion flame configuration under diesel engine like conditions, for low to moderate strain rates, first- and intermediate-stages of diesel combustion were not much effected, but second-stage was delayed compared to pure homogeneous combustion. At high strain rates, diffusive losses of heat and intermediate radicals from the reaction zone further inhibited second-stage combustion. Moreover, scalar dissipation rate along jet-axis of a diesel jet influences the location of the flame-base or in other words flame lift off length. Venugopal et al. [163] found that the laminar flamelet based extinction scalar dissipation rate correlates lift-off length. In the cases of small-bore engines like in the present study, the situation may arise for a given injection pressure that the scalar dissipation rate along the jet-axis may not fall below extinction value before the jet impinges on the wall, which means the flame may not exist along the jet-axis at all and the combustion only starts after jet-wall interaction, where scalar dissipation rate or mixing rate is in combustible limits.

2.3 Injection pressure

Injection pressure strongly influences jet-wall interaction as the jet velocity increases with the increase of injection pressure [173] and in fact can reduce soot

formation in the impingement zone as fuel rich regions can be avoided with the increase of jet-momentum [56; 167]. On the other hand, jet penetration after wall impingement can increase with the increase of injection pressure and increases the chances of jet-jet interaction depending on the proximity of neighbouring jets. This would enhance the re-entrainment effect in heavy-duty engines and increase soot formation in the flame lift-off region. However, as observed by Polonowski et al.[132], for a fixed mass of injected fuel, the reduced fuel injection duration with the increase of injection pressure has actually reduced the net soot formed as there was no intact fuel jet by the time combustion products re-entrained towards the jet-axis. Furthermore, increase of fuel injection pressure increases entrainment of hot ambient air and increases mixing of evaporated fuel and air [138]. This helps in reducing equivalence ratio in rich premixed combustion region, which can reduce soot formation. Also, increased jet velocity due to the increased injection pressure reduces soot residence time, which can reduce the net soot formed combining with small nozzle orifice diameter [129].

2.4 Jet-jet interaction

Jet-jet interaction is an unavoidable interaction after jet-wall interaction for a multi-hole fuel injection condition and even increases re-entrainment of combustion products from the interaction zone to flame lift-off region, which ultimately decreases the flame lift-off length as more evaporated fuel along the jet-axis undergoes combustion in the presence of more hot re-entrained combustion products [155]. Similar observation was also made by Musculus [112] along with jet-wall interaction effect when number of fuel injection holes were increased from 3 to 8. All the mentioned studies were done on heavy-duty engines. Whereas in small bore engines, the effect of jet-jet interaction on the combustion development is not well understood. Therefore, a numerical study of isolated two jets with two different injection pressures is devoted to the jet-jet interaction effect in the current work.

Certain numerical studies have also provided valuable information on effects of jet-wall and jet-jet interactions on diesel combustion. Diwakar et al. [50] performed numerical studies varying start of injection (SOI) of fuel from -30°

to -12° CA aTDC and jet included angle from 120° to 158° to study the jet-wall impingement effects in a medium-duty engine under premixed-charge compression ignition (PCCI) conditions. The engine has re-entrant bowl geometry that can assist in mixing of fuel and air after wall-impingement. The studies showed that with 158° spray included angle and with all SOIs, soot and CO emissions reach minimum because of splitting of fuel-air mixture between the bowl and the squish regions that efficiently get oxidised during the expansion stroke. This observation is in similar lines with the experimental observation made by Docquier [52]. For the other spray included angles $< 120^\circ$, soot emissions decreased monotonically with the advancement of SOI beyond -15° CA aTDC, but there was no splitting of fuel observed between the bowl and the squish volumes after impingement on the wall. In this case, the early SOI caused early ignition and the re-entrant bowl shape assisted in the oxidisation of soot during expansion stroke. In another numerical study by Luckhchoura et al. [102] on a similar kind of geometry but with a smaller bore at different SOIs ranging from -7° to 1° CA aTDC with a spray included angle of 158° concluded similarly as observed by Diwakar et al. [50]. Genzale et al. [56] have also performed numerical studies of their experimental observations [58]. After initial validation of the results, studied the source of UHC emissions and found that the origin was from lean upstream portion of the fuel-jet. The net UHC reduced in the smallest-bowl configuration that has seen re-entrainment of fuel-rich mixtures to the upstream portion of the jet.

2.5 Motivation

Lack of thorough understanding of effect of jet-wall and jet-jet interactions on the combustion development in small-bore engines under no exhaust gas circulation is a motivation for the current work to do thorough numerical analysis beyond validation of some results with the available experimental data. The numerical study besides validation with the experimental data is done with an isolated single fuel jet to understand jet-wall interaction effect on the combustion development with different fuel injection pressures. Then numerical study alone is done with isolated two fuel-jets with two different fuel injection pressures that simultane-

ously captured the effects of jet-wall and jet-jet interactions on the combustion development. In each study, the combustion development is compared with the conceptual model of conventional diesel combustion in heavy-duty engines and the conceptual model of low-temperature combustion in small-bore engines with exhaust gas recirculation.

Chapter 3

Simulation tools and combustion models for CI engine simulation

Numerical models that can simulate complex spray-combustion in diesel engines are needed to reduce time and cost in engine research and development time but overall development cost involved in a project. A numerical tool with thoroughly validated models can provide insight into the combustion phenomenon that is not possible through experiments. Many tools exist for 3D numerical simulation of compression ignition (CI) engines. This chapter first reviews some of the leading including KIVA, STAR-CD, Converge, and OpenFOAM, outlining the reasons this work selected OpenFOAM. This will be followed by a detailed description about OpenFOAM in general and specifically about its spray and combustion models. The validation results of spray and combustion models from OpenFOAM used for diesel-spray combustion in an automotive-size diesel engine will also be presented in the final section of the chapter.

3.1 Review of the available modelling tools

3.1.1 KIVA

KIVA is one of the most widely used 3-D computational fluid dynamics tools in engine research community and also one of the first tools for engine simulations. The code was first released by Los Alamos National Laboratories (LANL), US in

1985 [21]. KIVA was specifically developed to simulate thermo-fluid processes in internal combustion engines.

3.1.1.1 Development story

The first version of the code in KIVA family was only able to simulate relatively simple geometries of engines. In the series, by KIVA-3 version, a $k - \epsilon$ turbulence model was added and included a feature of block-structured mesh to generate a mesh by patching multiple blocks of cells. The code was also improved to tackle piston movement by a procedure of adding and removing cells called snapping [19]. In the next version, KIVA-3V, many advanced features of turbulence modelling and Lagrangian based spray models were implemented [20]. Many improvements were due to its open-source distribution to universities and industry [141]. Throughout all versions of the KIVA code, an arbitrary Lagrangian-Eulerian (ALE) methodology on staggered grid with finite volume based discretisation of governing equations was used to couple different physical models (spray, turbulence, combustion) and moving boundaries [36]. The recent version of KIVA is KIVA-4. The major changes in KIVA-4 were generalisation of discretisation procedure to handle unstructured meshes, a multi-component fuel vaporisation algorithm and parallelisation of the code using Message Passing Interface (MPI) library [43; 44; 161].

3.1.1.2 Major contributors

Engine Research Center (ERC), the University of Wisconsin

Many of the new sub-models in KIVA were implemented by Engine Research Center (ERC) from the University of Wisconsin. In the series of improvements for spray modelling using Lagrangian particle approach, the current and the most accurate model was based on Kelvin-Helmholtz (KH) instability theory to predict the primary break-up of intact liquid core of a diesel jet and this was combined to another instability model called Rayleigh-Taylor (RT) accelerative instability model to predict secondary break-up of individual drops. Furthermore, a Rosin-Rammler distribution theory was used to determine the sizes of smaller drops resulting from RT break-up [139]. In the area of turbulent flow modelling using

Reynolds average approach, Han and Reitz [66] implemented variable-density formulation of RNG $k - \epsilon$ model, which was originally developed by Yakhot [170] for incompressible flows. The same authors also extended the variable-density formulation to much needed temperature wall function treatment [67] to model heat losses across engine walls.

The ERC group considerably contributed in the domain of combustion models for diesel combustion in engines. Based on work of Abraham et al. [18], Kong and Reitz [88] developed a hybrid eddy-breakup (EBU) model called in KIVA as characteristic time combustion (CTC) model. According to the model, the time at which the considered species reach their chemical equilibrium value is the longest of a characteristic chemical time scale and a characteristic turbulent time scale. Only some important species like *fuel*, O_2 , N_2 , CO_2 , H_2 , H_2O and CO were considered in the model. Even though the CTC model is simple, the results are acceptable in many conventional-diesel combustion conditions, where combustion is mixing-controlled [87]. The ability to model detailed chemistry during the combustion was introduced by combining CHEMKIN solver for homogeneous reactor with KIVA. This approach is termed as KIVA-CHEMKIN model [90]. In this model, turbulent-chemistry interaction is not considered in sub-grid scale (*i.e.* mixture is assumed to be homogeneous in each computational cell). The KIVA-CHEMKIN model and even the CTC model are suitable when auto-ignition of combustion controls chemical energy release of the fuel. Another combustion model, which is an extension of KIVA-CHEMKIN model called as KIVA-CHEMKIN-G combustion model [152] was incorporated to simulate combustion in the cases of dual-fuel combustion, where diesel fuel is injected into premixed natural gas/ethanol and air. The letter ‘G’ represents level-set method of tracking flame front generated in multiple locations of premixed natural gas/ethanol and air.

Soot model was also implemented in KIVA based on Hiroyasu soot formation model for formation of soot and the Nagle-Strickland-Constable (NSC) model was used to predict the oxidation of the soot [68]. In the CTC combustion model, fuel itself was used as soot initiating species whereas in the KIVA-CHEMKIN and the KIVA-CHEMKIN-G combustion models, acetylene (C_2H_2) was used as soot formation species. Recently, a detailed soot model was implemented by adding

chemistry of aromatic soot precursors up to pyrene to the fuel chemistry and also considered practical surface growth of soot through acetylene and benzene, soot coagulation and oxygen radical and hydroxyl (OH) induced soot oxidation processes [165]. NO_x was also modelled by adding GRI NO_x mechanism [162] to the fuel chemistry.

The ERC group has also extended the KIVA code for large eddy simulation (LES) of engines. Four LES models were implemented. These include - the zero equation Smagorinsky model [154]; the dynamic Smagorinsky model [60; 93]; one equation Menon model [84]; and the dynamic structure model [133]. The combustion model, the KIVA-CHEMKIN model was extended to LES and turbulence-chemistry interaction was considered through flamelet time scale (FTS) model. More details of the approach are provided in [80]. All the mentioned developments were incorporated in KIVA-3V version of the code.

Institute of Energy and Powerplant Technology (EKT), TU-Darmstadt

The group has mainly concentrated on simulations of gasoline direct injection (GDI) engines using KIVA-3V. The classical Smagorinsky model based LES turbulence model was used for capturing unsteady effects of in-cylinder charge motion and cycle-to-cycle variations due to initial conditions. A kind of pseudo parallelisation method was used in which 5 different simultaneous simulations with different initial conditions were run on 5 processors and each simulation was run for 10 cycles. The approach provided results for 50 cycles and results from each cycle being statistically independent of the other cycle [41]. The Lagrangian spray was modelled by the linear instability sheet atomisation (LISA) model [42] for primary break-up and the secondary break-up of spray droplets was modelled by Taylor analogy break-up (TAB) model. A simple single step reaction mechanism based combustion model with Arrhenius reaction rates was used to simulate combustion [42].

Institute for Combustion Technology, RWTH Aachen University

The main contribution from this group was implementation of reference interactive flamelet (RIF) model in KIVA-3V. The flamelet concept is based on an

assumption that the smallest turbulent length and time scales are greater than the largest chemical time scale and chemical reactions can occur in unperturbed laminar sheets called flamelets [125; 126]. With this assumption, all reacting scalars can be uniquely expressed as a function of a single passive scalar called mixture fraction and diffusing with a numerically defined diffusivity in terms of scalar dissipation rate in mixture fraction space. This separation of flow and chemistry is possible with unity Lewis number assumption and considerable reduction of chemistry computational time is attained. Besides this, flamelet equations consider sub-grid scale turbulence-chemistry interaction. Details about the implementation of RIF model in KIVA-3V are given in [23; 83]. As highlighted by Singh [149], RIF model could successfully predict global parameters like in-cylinder combustion pressure rise, heat release rate and exhaust emissions like NO_x , but failed to capture in-cylinder combustion development details like flame lift-off length.

3.1.1.3 Advantages and limitations

Advantages:

- The users will have access to the full-code to be able to modify an existing sub-model or implement a new sub-model.
- A text file based block-mesh generator and also has an interface to accept a mesh generated by a third-party mesh generating tool like ICEM-CFD.
- KIVA generates output files that are readable in Tecplot.

Limitations:

- The major drawback of the popular KIVA-3V code is that the code is not parallelised. Even though parallel version of KIVA-4 was released, there is no literature available suggesting that the code is in use.
- Numerical schemes are first-order in time and up to second-order in space. Numerical accuracy of the schemes were not improved when LES was implemented. Only coarse grid LES simulations called ‘engineering LES’ can be simulated.

-
- Different advanced models developed by different groups are not available with the base code when someone buys KIVA.

3.1.2 STAR-CD

3.1.2.1 About numerical methods

STAR-CD is a 3-D computational fluid dynamics (CFD) tool for simulating thermo-fluid processes in IC engines. STAR-CD was developed by CD-Adapco [14]. The tool is based on finite-volume discretisation with pressure implicit with splitting of operator (PISO) algorithm for solving discretised Navier-Stokes equations [1]. A conjugate-gradient (CG) method combined with algebraic multigrid method was used for solving system of linearised governing equations. Like in KIVA, arbitrary Lagrangian-Eulerian (ALE) algorithm of moving boundaries was used to tackle moving surfaces associated with piston and valves movement.

3.1.2.2 About models for flow, spray and combustion

STAR-CD offers different Reynolds-averaged Navier-Stokes (RANS) two-equation turbulence models. Out of that, the suitable model for engine simulations is RNG $k - \epsilon$ model. Two LES models available for engine simulation are simple Smagorinsky model [154] and one equation sub-grid scale kinetic energy equation model [84]. Three different spray models are available to model Lagrangian diesel-spray. The models are - Reitz and Diwakar model [140], Pilch and Erdman model [130] and Hsiang and Faeth model [75].

STAR-CD has different combustion models to model diesel spray combustion. The simplest of all is the eddy break-up (EBU) model [105]. This model is similar to the characteristic time combustion (CTC) model in KIVA. Another combustion model in which four different in-built reaction mechanisms for C_7H_{16} - O_2 are provided with varying number of reactions and species based on the work of Müller and Peters [108]. Like in KIVA-CHEMKIN, each cell is assumed as a homogeneous reactor and a set of ordinary differential equations are solved for a reaction source term of a species. A feature to alter reaction coefficients to match the cetane number of considered diesel fuel is also provided. This model

was extended further to consider any detailed reaction mechanism in CHEMKIN format by an add-in called STAR/KINetics [15]. The other mode of the model takes in DigAnaRS [7] developed reaction mechanisms.

3.1.2.3 Usage by different groups

Combustion group in Pennsylvania state university used LES of STAR-CD for simulating cold flow in an axi-symmetric, central open-valve, flat piston geometry. As published, the comparison of different parameters with the experimental data was good [94]. The group has also used STAR-CD to study cycle to cycle variations using proper orthogonal decomposition (POD) in a transparent combustion chamber (TCC) engine [70]. The Institute of Energy and Power-Plant Technology (EKT), TU-Darmstadt has made a similar kind of LES based cycle-to-cycle variation study in a 4-valve pent-roof engine [63]. The University of Modena, Italy used the tool for LES-CFM (coherent flamelet model) based combustion simulation of a high-speed, turbo-charged, 4-valve, pent-roof engine [63]. Many automobile industries also use STAR-CD as an important tool in their design improvement cycles.

3.1.3 Converge

3.1.3.1 About numerical methods

The foremost point to be made about Converge is that it is an automatic mesh generating 3-D CFD tool for simulating thermo-fluid processes in IC engines. Automatic mesh generation in Converge means the solver itself generates the mesh with no user intervention in the mesh generation process, just the user need to provide a flawless geometry file to the solver. This means very minimal man-hours in the mesh generation process. Converge was developed by Convergent Science Inc [6]. An automatic high quality volume mesh is generated in every time step using a patented cut-cell Cartesian meshing technique [4]. Adaptive mesh refinement technique was implemented to auto-refine the mesh in the necessary locations. Pressure-velocity coupling was accomplished by PISO algorithm. All solvable variables are defined at the centre of the cell and to avoid resulting checker-board distribution of pressure and velocity, Rhie-Chow interpolation

scheme was used [142]. Like in STAR-CD, Converge has similar turbulent flow models both by RANS and LES approach.

3.1.3.2 About models for spray and combustion

Converge has a wide variety of spray sub-models for simulating diesel spray. Namely improved Kelvin-Helmholtz break-up and Rayleigh-Taylor break-up models, LISA sheet break-up model and traditional TAB break-up model. Like in KIVA and STAR-CD, Converge also has the simple characteristic time combustion model. SAGE detailed chemical kinetics model [147], which is similar to KIVA-CHEMKIN combustion model was also implemented. To reduce the computational time for kinetics, *in situ* adaptive tabulation (ISAT) algorithm [135] was coupled to SAGE combustion model.

3.1.3.3 Usage by different groups

Converge is used in the combustion research group of the University of Illinois for characterisation of diesel-spray, studies leading to the effects of primary break-up modelling and effect of geometry of spray-nozzle orifice [157]. The tool is also used in Argonne National Laboratory for diesel-spray studies [156]. In Wayne State University, Converge was used for spray characterisation of ethanol-gasoline blends [106]. It is worthwhile to mention that because of its automatic mesh generation features and improved spray models, the tool is also being used extensively in major automobile industries.

3.1.4 OpenFOAM

OpenFOAM (Open Source Field Operation and Manipulation) is a set of C++ libraries from [12] used to create executables called applications for CFD. The tool has the following advantages over other CFD tools from turbulent combustion simulation point of view.

- It is an open source code with pre-coded many of RANS and LES turbulent flow models. This means in most of the cases, users do not need to develop a new turbulent flow model. In case, if a necessity arises, a new flow model

implementation is easy. In the case of other CFD tools that are in use for engine simulations as mentioned in the earlier sections, few turbulent flow models are implemented and a new model implementation is not an easy task as code accessibility to users is limited. However, with KIVA, an user can have access to the source code for a new model implementation, but the code has other inherent problems that are highlighted in section 3.1.1.3.

- Has different Lagrangian spray models with full access for modification and improvement.
- Has in-built parallelisation. An user in the phase of implementation of a new model, does not need to bother about incorporating any MPI commands in the code. Parallelisation was done right in the core of preliminary classes and all inherited classes and objects defined thereon are automatically parallelised.
- It is possible to give thermal and transport properties of different species as function of temperature whether in standard NASA polynomials format or in the format of OpenFOAM. Even it has a chemkin format reader for properties.
- Has in-built hexahedral mesh generators. Also has a post-processing tool based on Paraview [13]. This means, OpenFOAM is a complete package for CFD simulations. At the same time accepts meshes from third-party mesh generators like Gambit and ICEM-CFD [5] and generates output data to be readable in Tecplot, Enight and Fieldview [9; 10; 16].
- Has different ordinary differential equation (ODE) solvers from explicit to implicit methods [12] and some basic combustion models based on Chalmers partially stirred reactor combustion model [119].
- Additionally, the object-oriented framework of C++ [159] allows the code development to be easily manageable with lower maintenance, code re-usability and fewer bugs. The main features of the language as highlighted in [79] can be summarised as *data abstraction*, allowing the designer to introduce new data types appropriate for the problem, *object orientation*, i.e.

bundling of data and operations into classes, protecting the data from accidental corruption and creating class hierarchies, *operator overloading*, which provides natural syntax for newly defined classes and *generic programming*, allowing code re-use for equivalent operations on different types.

OpenFOAM mainly contains *src* folder where all C++ libraries called source files necessary to create applications are present and *applications* folder where all created applications are present. The applications can be classified into two categories, namely: *solvers* and *utilities*. *Solvers* are used to solve a specific problem in continuum mechanics and *utilities* are used to perform data manipulation and supplement. There are pre- and post-processing *utilities* in OpenFOAM. For computation fluid dynamics usage, OpenFOAM comes with many finite volume based *solvers* and *utilities*, which are helpful for an user to develop new applications upon them. In the present work, OpenFOAM was used for the simulation of diesel-spray combustion in an automotive-size diesel engine. The overall structure of OpenFOAM is shown in Figure 3.1.

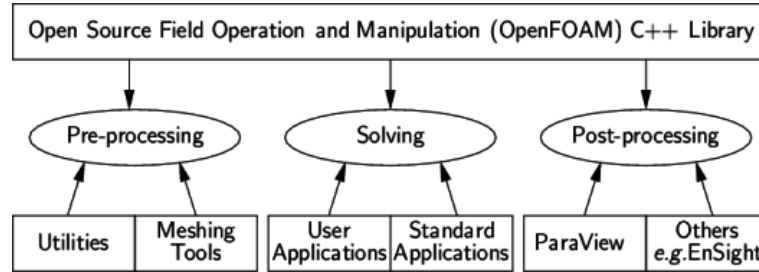


Figure 3.1: Overview of OpenFOAM structure [3].

In view of the above advantages with OpenFOAM, it was an obvious choice to go with the tool in the current work for simulating diesel spray combustion in compression ignition engines. Also, OpenFOAM has become a prominent CFD tool in research works in universities and some industries are using for regular product design improvements. Some more details related to relevant numerical methods, C++ classes and solution algorithm followed by governing equations and validation of the spray and combustion models used in the current study are covered in the next section.

3.2 OpenFOAM: A detailed view

3.2.1 Finite volume discretisation

Any physics related to fluids can be mathematically represented by partial differential equations. For instance, the conservation of momentum in a flow can be represented by Eq. (3.1). The finite volume discretisation of the equation results in a linearised equation and the system contains as many equations as the number of grid points in a computational domain.

$$\frac{\partial \rho \mathbf{U}}{\partial t} + \nabla \cdot (\rho \mathbf{U} \mathbf{U}) - \nabla \cdot (\mu \nabla \mathbf{U}) = -\nabla p \quad (3.1)$$

where \mathbf{U} is the velocity vector; p is the pressure; ρ is the density of the gas phase and μ is the dynamic viscosity. The implicit form of the linearised equation can be written as shown in Eq. (3.2).

$$a_p \mathbf{U}_p + \sum_N a_N \mathbf{U}_N = r_p \quad (3.2)$$

where a_p is the central co-efficient; \mathbf{U}_p is the velocity vector at the chosen computational point; \mathbf{U}_N is the velocity vector at the neighbouring grid points; a_N is the co-efficient related to the neighbouring grid points; r_p is the explicit term at the chosen computational point. To represent the implicit form of the linearised equations, OpenFOAM uses two classes **fvm** and **fvc** that take in data types from a template class, **geometricField<Type>** covering scalars, vectors and tensors at cell centres accessed by a class **volField<Type>**, at cell surfaces accessed by a class **surfaceField<Type>** and at cell vertices accessed by a class **pointField<Type>**. The schematic representation is shown in Figure 3.2. As shown below, OpenFOAM representation of solving Eq. (3.1) implicitly resembles actual partial differential equation.

```
solve
(
    fvm :: ddt(rho, U)
+ fvm :: div(phi, U)
```

```

- fvm :: laplacian( $\mu$ , U)
==
- fvc :: grad(p)
)

```

ddt(), **div()** and **laplacian()** are member functions of **fvm** class, which consider the passed objects as part of system of implicit linearised equations after discretisation. **grad()** is a member function of **fvc** class considers explicitly the passed object, p . The detailed description about different classes used for different purposes in the code is provided in [2; 11].

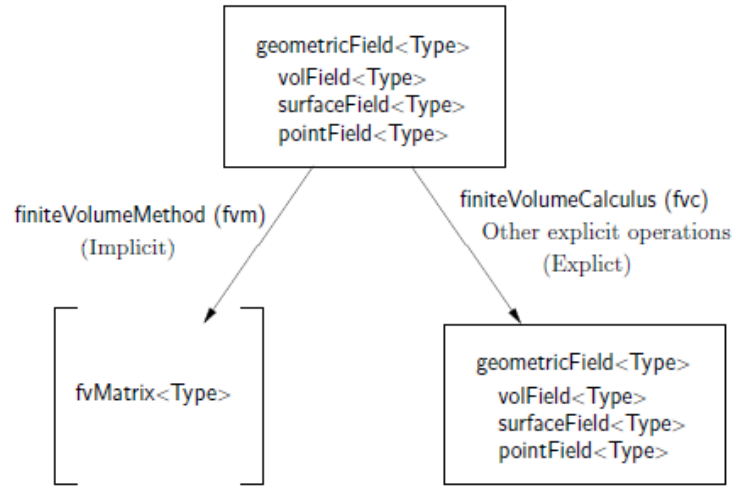


Figure 3.2: A geometric Field <Type> and its operators [2].

3.2.2 Solution algorithm

The discretised momentum equation was solved satisfying continuity by following either SIMPLE (Semi-Implicit Method for Pressure-Linked Equations) or combined SIMPLE and PISO (Pressure Implicit with Splitting Operators) called as PIMPLE algorithm [77]. Whatever may be the algorithm followed, in the first step, predicted velocities are computed with pressure taking at previous time-

step, which do not satisfy continuity. Corrector velocities are determined from a continuity satisfying pressure corrector Poisson equation. From the corrector values of velocities and pressure, new time step velocities and pressure are computed. In PIMPLE algorithm one more PISO corrector loop is done for pressure corrector Poisson equation before updating the next time step values. In the present work, PIMPLE algorithm was followed. The checker-board distribution of pressure and velocity when pressure and velocity are taken at cell centroids i.e. collocated grid approach is prevented by following Rhie and Chow [142] interpolation technique. This technique is also known as momentum-interpolation technique. The other combustion governing equations were also solved along with the flow equations. The details about the combustion model will be discussed in section 3.2.7.

3.2.3 Moving mesh techniques

The movement of mesh boundaries because of movement of piston and valves in an engine mesh is achieved by two different methods. One is polyhedral vertex-based motion method proposed by Jasak and Tukovic [78] and the other one is the method of topology changes proposed by Lucchini [99]. In the polyhedral vertex-based motion method, a Laplacian equation with constant or varying diffusion coefficient as shown in Eq. (3.3) is solved for vertex motion velocity with boundary conditions from the moving and the fixed boundaries of an engine mesh. The new locations of the vertices are updated by using Eq. (3.4).

$$\nabla \cdot (\gamma_p \nabla \mathbf{u}_p) = 0 \quad (3.3)$$

$$\mathbf{x}_{new} = \mathbf{x}_{old} + \mathbf{u}_p \Delta t \quad (3.4)$$

where \mathbf{u}_p is the vertex velocity vector of a vertex in a finite volume cell of an engine mesh; \mathbf{x} is the position co-ordinate vector of a vertex. In the topology change method to preserve the quality of the moving mesh, the implemented topology changes are attach/detach boundaries, cell layer addition/removal and sliding mesh interfaces [99]. These are called as mesh modifiers. The combination of both the methods was used for the engine motion simulation. A series of

geometrical and topological tests were performed to ensure the quality of the mesh during the mesh motion.

3.2.4 Specification and calculation of thermo-physical properties

In a combustion simulation involving computation of different thermo-physical properties like specific heat at constant pressure (c_p), sensible enthalpy (h_s), heat of formation (h_f) and temperature (T) of participating species requires the access of different template classes from thermophysicalModels module of *src* folder. The user need to specify the inheritance list while running a case using a combustion model by an alias name ***thermoType*** called typedef in C++. For the combustion model used in the present study, which will be discussed in section 3.2.7, the list of classes is

thermoType hsPsiMixtureThermo<reactionMixture<gasThermoPhysics>>

gasThermoPhysics is again a typedef for a list of classes.

gasThermoPhysics sutherlandTransport<specieThermo<janafThermo<perfectGas>>>

As shown in Fig.3.3, **hsPsiMixtureThermo** class further inherits different other classes basically to give access to the calculated values of sensible enthalpy, heat of formation, heat capacity at constant pressure and temperature of the combustion mixture. **reactionMixture** class inherits **chemistryReader**, **speciesTable**, **mutliComponentMixture** and **Reaction** classes to read species list, reactions and thermo data coefficients (of c_p , entropy(s) and enthalpy(h)) from the user provided Chemkin files (chem.inp and therm.dat). Furthermore, **sutherlandTransport** class calculates and gives access to dynamic viscosity (μ) of the mixture, **specieThermo** calculates temperature from sensible enthalpy by the Newton-Raphson iterative method and **janafThermo** actually calculates c_p , s and h of all the species from the stored thermo coefficients.

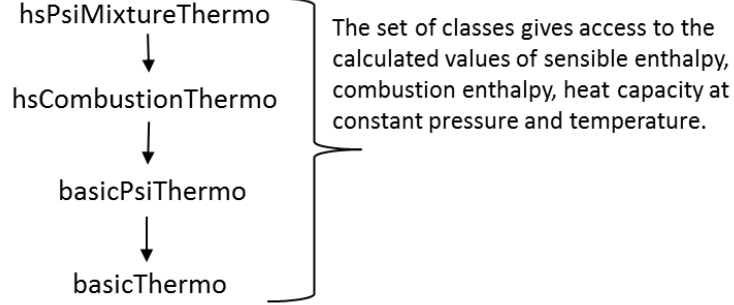


Figure 3.3: The inheritance list of **hsPsiMixtureThermo** class.

3.2.5 Spray modelling and validation

Diesel spray is modelled by Lagrangian approach in OpenFOAM and the interaction between Eulerian mass, momentum and energy is done by different spray sub-models. OpenFOAM comes with already implemented different spray sub-models and all the classes related to diesel spray modelling are available in *src\lagrangian\dieselSpray*. A copy of all these sub-models are implemented in Lib-ICE library developed by Lucchini [101] to improve the sub-models and at the same time not to disturb the original OpenFOAM spray sub-models. The improvement efforts were mainly concentrated on reducing the computational time and the grid dependency, which are discussed in [100]. The gas phase Eulerian equations of mass, momentum and energy are solved for a compressible, multi-component gas flow with combustion using the Reynolds averaged Navier-Stokes (RANS) approach. The details about the combustion model will be discussed in the next section [3.2.7](#).

Conservation of mass:

$$\frac{\partial \rho}{\partial t} + \nabla \cdot (\rho \mathbf{U}) = S_{evap} \quad (3.5)$$

Conservation of momentum:

$$\begin{aligned} \frac{\partial \rho \mathbf{U}}{\partial t} + \nabla \cdot (\rho \mathbf{U} \mathbf{U}) = & -\nabla p + \nabla \cdot [(\mu + \mu_t) (\nabla \mathbf{U} + (\nabla \mathbf{U})^T)] \\ & - \nabla \cdot \left[(\mu + \mu_t) \left(\frac{2}{3} \text{tr}(\nabla \mathbf{U})^T \right) \right] + \rho \mathbf{g} + \mathbf{F}^s \end{aligned} \quad (3.6)$$

Conservation of species mass fractions:

$$\frac{\partial \rho Y_i}{\partial t} + \nabla \cdot (\rho \mathbf{U} Y_i) - \nabla \cdot \left[\left(\mu + \frac{\mu_t}{Sc_t} \right) \nabla Y_i \right] = S_{evap,i} + \rho \dot{Y}_i \quad (3.7)$$

Conservation of energy:

$$\frac{\partial \rho h_s}{\partial t} + \nabla \cdot (\rho \mathbf{U} h_s) - \nabla \cdot [(\alpha + \alpha_t) \nabla h_s] = \frac{Dp}{Dt} + S_{evap,h} + \sum_i \rho \dot{Y}_i h_{f,i} \quad (3.8)$$

where \mathbf{U} is the ensemble average velocity vector; Y_i is the ensemble average mass fraction of species i ; h_s is the ensemble average sensible enthalpy of the gas phase; $\frac{Dp}{Dt}$ is the total derivative of the pressure, which is important in internal combustion engines; \dot{Y}_i is the rate of production or consumption of species i provided by a combustion model (see section 3.2.7); \mathbf{g} is the acceleration due to gravity; ρ is the density of the gas phase; $h_{f,i}$ is the heat of formation of species i ; Sc_t is the turbulent Schmidt number taken a value of 0.7; μ_t is the turbulent viscosity obtained from RNG $k - \epsilon$ model [66] and α_t is the turbulent thermal diffusivity taken equal to μ_t . The source terms S_{evap} , $S_{evap,i}$, \mathbf{F}^s and $S_{evap,h}$ are due to mass, momentum and energy exchange between the gas and the liquid phases. The Lagrangian governing equations of droplets for mass, momentum and energy conservation are solved to account for mass added or removed, position change, velocity and temperature of droplets.

Droplet mass conservation:

$$\frac{dm_d}{dt} = -\frac{m_d}{\tau_e}, \quad \frac{dD}{dt} = -\frac{D}{3\tau_e} \quad (3.9)$$

$$\frac{dm_d}{dt} = -\frac{m_d}{\tau_b}, \quad \frac{dD}{dt} = -\frac{D}{3\tau_b} \quad (3.10)$$

where τ_e is the evaporation relaxation time; τ_b is the boiling relaxation time; m_d is the mass of a droplet and D is the diameter of a droplet. Eq.(3.9) is valid under standard evaporation conditions and Eq.(3.10) is valid under standard boiling conditions. τ_e is further expressed in terms of the Sherwood number (Sh) as

$$\tau_e = \frac{m_d}{\pi D D_v \rho_v Sh [\ln(1 + B)]} \quad (3.11)$$

Sh is provided by Ranz-Marshall correlation [39] as

$$Sh = 2.0 + 0.6Re^{1/2}Sc^{1/3} \quad (3.12)$$

while D_v is the diffusivity of fuel; ρ_v is the density of fuel vapour and B , the Spalding transfer number is expressed as

$$B = \frac{Y_{f,s} - Y_{f,\infty}}{1 - Y_{f,s}} \quad (3.13)$$

where $Y_{f,s}$ is the mass fraction of fuel at droplet surface; $Y_{f,\infty}$ is the mass fraction of fuel far away from droplet. τ_b is expressed in terms of the Nusselt number, Nu as

$$\tau_b = \frac{D^2 \rho_d c_{p,v}}{2\kappa Nu \left[\ln \left(\frac{c_{p,v}}{h_v} (T - T_d) + 1 \right) \right]} \quad (3.14)$$

Nu is given by a correlation as suggested by Gosman [64] as

$$Nu = 2.0 + 0.6Re_d^{1/2}Pr^{1/3} \quad (3.15)$$

where the Prandtl number(Pr) is defined as

$$Pr = \mu_v \frac{c_{p,v}}{\kappa} \quad (3.16)$$

where μ_v is dynamic viscosity of fuel vapour; ρ_d is the density of a droplet; $c_{p,v}$ is the specific heat of fuel vapour; κ is the thermal conductivity of fuel vapour; h_v is

the sensible enthalpy of fuel vapour; T is the temperature of the gas phase; T_d is the temperature of a droplet and Re_d is the Reynolds number of a droplet, which is defined below in momentum conservation section of a droplet. When $\tau_b > \tau_e$ and the saturation pressure is close to the surrounding pressure, only droplet vaporisation due to evaporation is considered as provided in Eq. 3.9. The net rate of vaporisation of all droplets due to evaporation and boiling goes as a source term to the mass conservation equations of the gas phase.

Droplet momentum conservation:

$$m_d \frac{d\mathbf{U}_d}{dt} = -\frac{\pi D^2}{8} \rho_d C_d |\mathbf{U}_d - \mathbf{U}| (\mathbf{U}_d - \mathbf{U}) + m_d \mathbf{g} \quad (3.17)$$

where \mathbf{U}_d is the velocity vector of a droplet; C_d is the drag co-efficient. The first part of r.h.s of Eq.(3.17) is due to drag force and the second part is due to gravity, which is usually neglected. C_d is defined as suggested by Nordin [119].

$$C_d = \begin{cases} \frac{24}{Re_d} \left(1 + \frac{1}{6} Re_d^{2/3}\right) & Re_d < 1000 \\ 0.424 & Re_d > 1000 \end{cases} \quad (3.18)$$

The Reynolds number of a droplet is defined as

$$Re_d = \rho_d \frac{|\mathbf{U}_d - \mathbf{U}| D}{\mu_d} \quad (3.19)$$

where μ_d is the dynamic viscosity of a droplet. The calculated drag force goes as a source term to the gas phase momentum equation.

Droplet energy conservation:

The liquid fuel droplets receive heat energy from the gas which is used to increase the liquid temperature and overcome the latent heat of evaporation fuel droplets. The energy conservation of a droplet is given as

$$m_d \frac{dh_d}{dt} = \dot{m}_d h_v(T_d) + \pi D \kappa Nu (T - T_d) f \quad (3.20)$$

where h_d is the sensible enthalpy of liquid droplet; h_v is the sensible enthalpy of fuel vapour and is function of droplet temperature, T_d ; \dot{m}_d is the evaporation rate of a liquid droplet and f is a factor defined as

$$f = \frac{z}{e^z - 1}, \quad z = -\frac{c_{p,v}\dot{m}_d}{\pi D \kappa Nu} \quad (3.21)$$

The net energy calculated using Eq.(3.20) in a CFD finite volume cell goes as a source term to the energy equation of the gas phase. In addition to the above mass, momentum and energy exchange between the Lagrangian liquid phase and the Eulerian gas phase, the liquid droplets which are injected as blobs with diameter equal to the effective nozzle hole diameter also undergo a series of break-up phenomena under the influence of aerodynamic forces from the gas phase and surface tension force of droplets. The break-up of droplets is modelled by the Kelvin-Helmholtz Rayleigh-Taylor (KH-RT) break-up model proposed by Reitz [139]. The KH-RT model has two distinct steps: primary and secondary break-up. The primary break-up of the intact liquid core of a diesel jet is modelled by the Kelvin-Helmholtz instability model and the secondary break-up of the individual drops is modelled by the Kelvin-Helmholtz instability model in conjunction with the Rayleigh-Taylor accelerative instability model. According to the KH model, the parent drop injected from the nozzle hole breaks to form smaller drops and radius r_c of smaller drops is given by

$$r_c = B_0 \Lambda_{KH} \quad (3.22)$$

where Λ_{KH} is the wavelength of a KH wave with maximum growth rate and B_0 is a constant with a value of 0.61. The rate of change of the radius of a droplet is given by

$$\frac{dr}{dt} = \frac{r - r_c}{\tau_{KH}} \quad (3.23)$$

where τ_{KH} is the break-up time defined as

$$\tau_{KH} = \frac{3.726 B_1 r}{\Omega_{KH} \Lambda_{KH}} \quad (3.24)$$

where B_1 is a constant that can take values between 10 and 60; Ω_{KH} is the frequency of a breaking KH wave.

$$\Omega_{KH} = \frac{0.34 + 0.38We_g^{1.5}}{(1 + Oh)(1 + 1.4T_g^{0.6})} \sqrt{\frac{\sigma}{\rho_d r^3}} \quad (3.25)$$

$$\Lambda_{KH} = \frac{9.02r(1 + 0.45\sqrt{Oh})(1 + 0.4T_g^{0.7})}{(1 + 0.865We_g^{1.67})^{0.6}} \quad (3.26)$$

where We_g is the Weber number of the gas; Oh is the Ohnesorge number; T_g is the Taylor number and σ is the surface tension of the liquid droplet. They are defined as

$$We_g = \frac{\rho|\mathbf{U} - \mathbf{U}_d|^2 r}{\sigma} \quad (3.27)$$

$$Oh = \frac{\sqrt{We_d}}{Re_d} \quad (3.28)$$

$$T_g = Oh\sqrt{We_g} \quad (3.29)$$

where We_d is the Weber number of a liquid droplet defined in the similar lines as We_g and Re_d is the Reynolds number of a liquid droplet as defined in Eq.(3.19). The RT wave instability theory introduced by Su et al. [160] predicts break-up of droplets that grow until a certain characteristic break-up time. The frequency of a fast growing RT wave is given by

$$\Omega_{RT} = \sqrt{\frac{2}{\sqrt{27}\sigma} \frac{|g_t(\rho_d - \rho)|^{3/2}}{(\rho_d + \rho)}} \quad (3.30)$$

where g_t is the acceleration in the direction of travel of a droplet, which is defined by $g_t = \mathbf{g} \cdot \mathbf{j} + \mathbf{a} \cdot \mathbf{j}$, where \mathbf{g} is the acceleration due to gravity as defined earlier; \mathbf{a} is the droplet acceleration and \mathbf{j} is the unit vector tangent to the droplet trajectory. The wave number of the breaking wave is given as

$$K_{RT} = \sqrt{\frac{-g_t(\rho_d - \rho)}{3\sigma}} \quad (3.31)$$

The wavelength corresponding to the fastest wave growth rate is $2\pi C_{RT}/K_{RT}$. This value is compared to the radius of the droplet and the RT wave is allowed to grow until the wavelength is greater than the radius of the droplet. The tracked time during the growth of the wave is compared to the break-up time, which is defined as

$$\tau_{RT} = \frac{C_\tau}{\Omega_{RT}} \quad (3.32)$$

where C_{RT} and C_τ are model constants usually taken as 0.1 and 1 respectively. If the break-up time is greater than the tracked time, the droplet is assumed to break-up and the radius of the new smaller droplet is given by

$$r_c = \frac{\pi C_{RT}}{K_{RT}} \quad (3.33)$$

During the break-up period, the droplets are subjected to the conservation of mass, momentum and energy and radii are corrected accordingly. The implementation of coupling between the Eulerian gas phase and the Lagrangian liquid phase in OpenFOAM is discussed in detail in [100; 119].

3.2.5.1 Validation of the spray model

Lagrangian spray models contain multiple constants in different sub-models and the values of those constants need to be tuned for different ambient pressure and temperature of diesel spray combustion. A parametric study of varying model constants of KH-RT break-up model was done in the simulation of spray-H in non-combustion conditions in a constant volume combustion chamber under diesel engine like ambient conditions. The spray-H data was taken from the Engine Combustion Network (ECN) [8]. A uniform mesh with 1 mm cell size was considered. The predicted axial penetration of n-heptane vapour and radial distribution of mixture fraction at different axial distances were compared with the experimental data. A slight variation of values for constants B_0 , C_{RT} and C_τ from the suggested values (refer Eqs. 3.22, 3.33 and 3.33) has resulted in a big deviation in the predicted distribution of n-heptane vapour compared to the experimental data and so retained the suggested values. Finally, only B_1 constant used in Eq.(3.24) was changed from 10 to 40 and the results were comparable with

the experimental data for the values of 15 and 40. The axial penetration of n-heptane vapour is shown in Fig.3.4. The axial penetration distance as defined in [116] is the distance from the injector tip to the point on the jet-axis where n-heptane mass fraction is 0.1%. As shown in Fig.3.4, the penetration distance

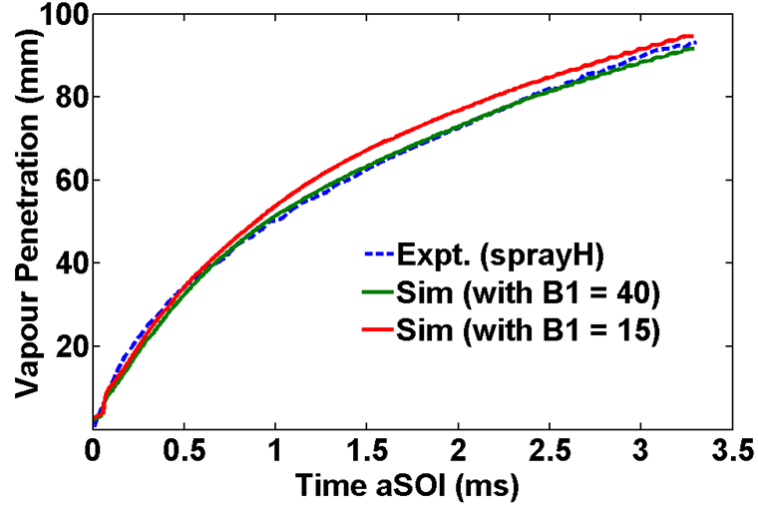


Figure 3.4: Comparison of axial penetration of n-heptane vapour.

is compared after start of injection (aSOI) in milliseconds (ms). The penetration distance is under-predicted up to around $0.6 ms$ with both $B_1 = 15$ and 40 . From $0.6 ms$ onwards there is a consistent over-prediction up to around $3 ms$ with $B_1 = 15$ and the prediction is better matched with the experimental data with $B_1 = 40$ in the period.

The comparison of radial penetration of n-heptane vapour in terms of mixture fraction (mass fraction) at $1.13 ms$ and $6 ms$ aSOI is shown in Fig.3.5 and Fig.3.6 respectively. At $30 mm$ distance and at $1.13 ms$ aSOI, the peak concentration is under-predicted with both $B_1 = 15$ and 40 , but the extent of radial distribution is comparable with the experimental distribution whereas at $6 ms$ the predictions are good over the entire radial distribution at this distance of $30 mm$. At $50 mm$ distance and at both the times, the predictions are fairly good with both the values of B_1 considered. Overall, the spray predictions are better with $B_1 = 40$ compared to $B_1 = 15$ with respect to the axial penetration distance and the radial distribution of n-heptane vapour. In the automotive-size

diesel engine considered in the present work, the bowl diameter is 55 *mm* and the impingement of evaporated fuel-jet on the bowl-wall occurs at around 1.0 *ms* aSOI. The prediction capability shown by the spray-model with $B_1 = 40$ and with a grid cell size of 1 *mm* is good enough to properly capture the evaporated fuel distribution in an engine and so maintained maximum grid cell size of 1 *mm* even in the engine meshes used for the diesel-spray combustion simulations using the considered spray sub-models with $B_1 = 40$.

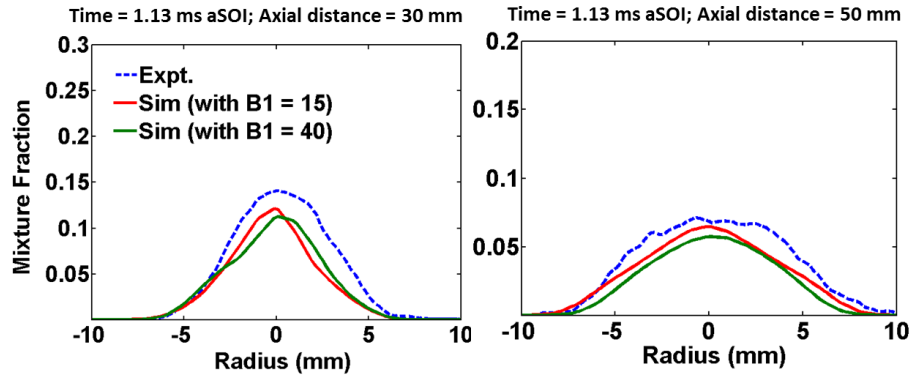


Figure 3.5: Comparison of radial distribution of mixture fraction at 1.13 *ms* aSOI at 30 *mm* and 50 *mm* from the injector.

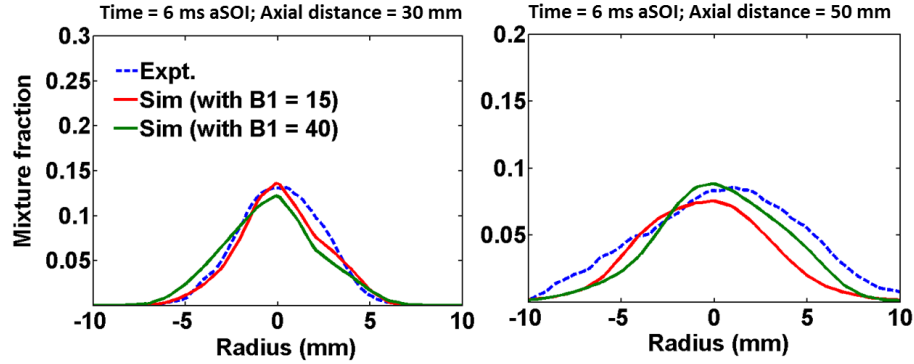


Figure 3.6: Comparison of radial distribution of mixture fraction at 6 *ms* aSOI at 30 *mm* and 50 *mm* from the injector.

3.2.6 Turbulence closure model

The turbulent viscosity (μ_t) that appears in ensemble averaged momentum equation shown in Eq. (3.6) is modelled in terms of ensemble averaged turbulent kinetic energy (k) and rate of dissipation of turbulent kinetic energy (ϵ) as shown in Eq. (3.36). The turbulent viscosity is the modelling term after expressing Reynolds stress tensor [136] in terms of gradient of ensemble averaged velocities using eddy-viscosity hypothesis [66]. Further, transportation equations of k and ϵ are solved by compressible, variable density formulation of RNG $k - \epsilon$ model as proposed by Han and Reitz [66] applicable for reciprocating engine simulations based on the original RNG $k - \epsilon$ model developed by Yakhot and Smith [170]. The final modelled equations of k and ϵ are

$$\frac{\partial \rho k}{\partial t} + \nabla \cdot (\rho \mathbf{U} k) = -\frac{2}{3} \rho k \nabla \cdot \mathbf{U} + \tau : \nabla \mathbf{U} + \nabla \cdot (\alpha_k \mu \nabla k) - \rho \epsilon + \dot{W}^s \quad (3.34)$$

$$\begin{aligned} \frac{\partial \rho \epsilon}{\partial t} + \nabla \cdot (\rho \mathbf{U} \epsilon) = & - \left[\frac{2}{3} C_1 - C_3 + \frac{2}{3} C_\mu C_\eta \frac{k}{\epsilon} \nabla \cdot \mathbf{U} \right] \rho \epsilon \nabla \cdot \mathbf{U} + \nabla \cdot (\alpha_\epsilon \mu \nabla \epsilon) \\ & + \frac{\epsilon}{k} \left[(C_1 - C_\eta) \tau : \nabla \mathbf{U} - C_2 \rho \epsilon + C_s \dot{W}^s \right] \end{aligned} \quad (3.35)$$

where C_η is a model constant calculated based on Eq. (3.37), C_3 is a constant given by Eq. (3.38), \dot{W}^s is a turbulence source term due to interaction between the gas and the spray and τ is a modelled Reynolds stress tensor as shown in Eq. (3.39). All other model constants are given in Table 3.1.

$$\mu_t = \rho C_\mu \frac{k^2}{\epsilon} \quad (3.36)$$

$$C_\eta = \frac{\eta(1 - \frac{\eta}{\eta_0})}{1 + \beta \eta^3} \quad (3.37)$$

$$C_3 = \frac{-1 + 2C_1 - 3m(n-1) + (-1)^\delta \sqrt{6} C_\mu C_\eta \eta}{3} \quad (3.38)$$

$$\tau \equiv \tau_{ij} = \frac{2}{3}k\delta_{ij} - \frac{\mu_t}{\rho}2S_{ij} \quad (3.39)$$

where $\eta = S_\epsilon^k$ is the ratio of the turbulent to mean-strain time-scale, $S = (2S_{ij}S_{ij})^{1/2}$ is the magnitude of the mean strain $S_{ij} = \frac{1}{2}\left(\frac{\partial u_i}{\partial x_j} + \frac{\partial u_j}{\partial x_i}\right)$, $m = 0.5$ is a constant (Bird et al. [28]), n is a polytropic process index, which ranges between 1.3 and 1.4 for engines [72], δ_{ij} is the Kronecker delta, $\eta_0 = 4.38$ is a model constant and δ is the Kronecker delta takes either 0 or 1 based on velocity dilatation (if $\nabla \cdot \mathbf{U} > 0$, $\delta = 0$).

Table 3.1: RNG $k - \epsilon$ model constants [66].

C_μ	C_1	C_2	α_k	α_ϵ	β	C_s
0.0845	1.42	1.68	1.39	1.39	0.012	1.5

3.2.7 Combustion model and validation

The challenging part in any combustion model with turbulence is treating the reaction source time. As shown in Eq. (3.41) for fuel mass fraction conservation, after ensemble average, the reaction source term contains an unclosed term, which is a function of temperature and species mass fraction fluctuations. Here, to differentiate a Favre ensemble average variable from an instantaneous variable, $\widetilde{(-)}$ ¹ is used for average variable and $(-)^{\prime\prime}$ is used for fluctuating part. If fuel species transport equation is considered

$$\frac{\partial \rho \tilde{Y}_F}{\partial t} + \nabla \cdot (\rho \mathbf{U} \tilde{Y}_F) - \nabla \cdot \left[\left(\mu + \frac{\mu_t}{Sc_t} \right) \nabla \tilde{Y}_F \right] = S_{evap,i} + \rho \tilde{Y}_F \quad (3.40)$$

¹For simplicity, $\widetilde{(-)}$ over all ensemble average variables in equations in other sections is removed.

Averaged reaction source given by Arrhenius law is further expanded by Taylor's expansion as shown by Veynante et al. [164]

$$\begin{aligned} \tilde{\dot{Y}}_F = & -A\rho\tilde{T}^b\tilde{Y}_F\tilde{Y}_O\exp\left(-\frac{T_A}{\tilde{T}}\right) \\ & \times \left[1 + \frac{\widetilde{Y_F''Y_O''}}{\tilde{Y}_F\tilde{Y}_O} + K_1\left(\frac{\widetilde{Y_F''T''}}{\tilde{Y}_F\tilde{T}} + \frac{\widetilde{Y_O''T''}}{\tilde{Y}_O\tilde{T}}\right) + \text{higher order terms}\right] \end{aligned} \quad (3.41)$$

where \tilde{Y}_F is the Favre ensemble average fuel mass fraction, \tilde{Y}_O is the Favre ensemble average oxidiser mass fraction, Y_F'' and Y_O'' are fluctuating parts of fuel and oxidiser mass fractions, \tilde{T} is the Favre ensemble average temperature, T'' is the fluctuating part of temperature, T_A is the activation temperature, A is the pre-exponential constant and K_1 is the Taylor's series expansion constant.

The unknown fluctuating terms in Eq. (3.41) need to be closed using algebraic expressions or transport equations in terms of averaged values, which is difficult as higher order terms are there. Moreover, this method of expansion is very complex for realistic chemical reaction mechanisms. Therefore, combustion models are rather derived following physical analysis considering turbulence-chemistry interaction. The foremost and simple combustion model in the list is characteristic time combustion (CTC) model developed by Kong and Reitz [89] and is described briefly in section 3.1.1.2. The other improved combustion model in use for diesel engine combustion simulations is flamelet model. First introduced by Peters [125] for diffusion flames. Later, for premixed and diffusion flames, the flamelet concept was reviewed by Peters [126] and Bray and Peters [33]. Basically, in the flamelet concept, all species concentrations and temperature are evaluated in a mixture fraction space that diffuse with a scalar dissipation rate. The scalar dissipation rate accounts the mixing rate of fuel-air mixture in the CFD domain. The calculated instantaneous values are mapped to the CFD domain by using some probability density function (pdf) averaging. The flamelet concept was implemented for diesel combustion in internal combustion engines by Barths et al. [23]. The other advanced turbulence-chemistry interaction models that are in use for combustion simulations other than internal combustion engines are statistical approaches like joint probability density function (pdf) of velocity and composi-

tion variables (species mass fraction and enthalpy) [134] and conditional moment closure (CMC) [86].

However, all models of turbulence-chemistry interaction have their own uncertainties and limitations. The other simplest approach is assuming fuel and air are perfectly mixed and turbulence-chemistry interaction can be neglected. This assumption will make all fluctuating terms in Eq. (3.41) zero and average reaction source term is only function of average temperature and species concentrations, which does not require any model. However, the combustion or chemical time scales span over a vast range from very small to large scales depending on the type of reactions involved. For instance, the initial fuel decomposition and heat release reactions are relatively faster compared to the post NO_x and soot formation reactions. Usually, for a bi-molecular reaction, the chemical time scale is inversely proportional to the initial concentration of reactants and the value of rate co-efficient [162]. Moreover, the CFD time step considered in an implicit solver is always more than the largest chemical time scale. In this situation, an effort to solve species transport equations with convection, diffusion and the average reaction source term along with momentum equations will involve internal time looping of species transport equations with a smallest possible time step dictated by a smallest chemical time scale and is computationally expensive. The increase in computational cost limits the number of species to be considered in the simulations. Consequently, this method is usually avoided for combustion simulations.

In the current study, an integrated detailed chemistry model implemented in Lib-ICE code developed by Lucchini et al. [101] in OpenFOAM was used. In the approach, convection and diffusion terms were dropped from Eq. (3.40) and the set of ordinary differential equations (ODEs) as represented in Eq. (3.42) was solved in each CFD time step using a Semi-Implicit Bulirsch-Stoer (SIBS) solver [158]. Recent comparisons of similar models with diesel ignition in constant volume chambers and also for engine simulations demonstrate that this simple approach is at least capable of predicting general trends with geometry and kinetic effects [69; 151]. The integrated detailed chemistry model used in this study is very similar to KIVA-CHEMKIN model implemented in KIVA-3V (see in section 3.1.1). As highlighted by Singh [149], KIVA-CHEMKIN combustion model was

able to predict well the in-cylinder combustion development and flame lift-off length compared to KIVA-RIF and KIVA-CTC models from KIVA-3V. So, the model can also be used to study the combustion development in the in-house, optically accessible diesel engine (see in chapter 4).

$$\frac{dY_i}{dt} = \dot{Y}_i = f_i(T, p, Y_1, \dots, Y_n) \quad (3.42)$$

where $\frac{dY_i}{dt} = \dot{Y}_i$ is the rate of change of mass fraction of species i as defined earlier in section 3.2.5 and Y_1 to Y_n are the mass fractions of species 1 to n . The computed \dot{Y}_i in each CFD computational cell was used as a source term for further updating species mass fractions and enthalpy as shown in Eqs. (3.7) and (3.8). Mixture fraction (Z) equation shown in Eq.(3.43) was also solved with S_{evap} (defined in section 3.2.5) as a source term.

$$\frac{\partial \rho Z}{\partial t} + \nabla \cdot (\rho \mathbf{U} Z) - \nabla \cdot \left[\left(\mu + \frac{\mu_t}{Sc_t} \right) \nabla Z \right] = S_{evap} \quad (3.43)$$

When a detailed chemical mechanism with a large number of species and chemical reactions is used, the Jacobian matrix of the implicit ODE solver becomes prohibitively big and computationally expensive. To reduce the computational time, a dynamic adaptive chemistry (DAC) methodology as developed by Liang et al. [92] was used. The DAC method develops the on-the-fly skeletal mechanism based on the local thermo-chemical conditions. According to the method

- A direct relation graph (DRG) developed by Lu and Law [97] of all the species of the mechanism is generated. Each vertex in the graph represents a species and each direct edge represents the immediate dependence of one species on the other. This dependence is quantified by a normalised factor r_{AB} representing contribution of species B to A and is defined as

$$r_{AB} = \frac{\sum_{i=1}^N |\nu_{A,i} \omega_i \delta_{B,i}|}{\sum_{i=1}^N |\nu_{A,i} \omega_i|}, \quad \delta_{B,i} = \begin{cases} 1 & \text{if reaction } i \text{ involves } B \\ 0 & \text{otherwise} \end{cases} \quad (3.44)$$

where i is the reaction index ($i = 1, \dots, N$), $\nu_{A,i}$ is the stoichiometric coefficient of species A in the i^{th} reaction, ω_i is the rate coefficient of reaction

i. r_{AB} basically quantifies error introduced in the production/consumption rate of A because of elimination of all the reactions that contain B . In the DRG, a direct edge between species A and B only exists if r_{AB} is greater than a user specified threshold value, e , which is taken a value of 10^{-4} .

- A search procedure is then initiated along the directed edges starting from a initial set of species. This initial set is chosen as $\{fuel, HO_2$ (hydroperoxyl radical), $CO\}$ as suggested in [92]. Fuel represents hydrocarbon decomposition, HO_2 represents water production ($H_2 - O_2$ system) and CO represents CO oxidation reactions. The search is carried out by a searching algorithm called breadth-first search (BFS) algorithm [74].
- The depth of search along the each path originating from an initiating species from the set is controlled based on one more threshold value, R taken as a product of r_{AB} values in the path. The value of R is taken as 10^{-4} in this study. This method controlled the number of species to be included in the search path. The union of such paths of species and the reactions involving the species will become a working skeletal mechanism for the local thermo-chemical conditions in a CFD computational cell. Only system of ODEs of such active species is solved and for the other in-active species, the concentrations from the old time step are retained. Thus, the computational time of the implicit ODE solver is reduced in each CFD computational cell. The schematic representation of the integrated detailed chemistry model with DAC is shown in Fig.3.7.

The following section has been updated in response to comments from Examiner-1

3.2.7.1 Chemical reaction mechanisms and physical properties

Ultra-low sulphur diesel used in the experiments has a cetane number of 46. In the simulations, *n*-heptane is used as a surrogate fuel to simulate diesel combustion used in the experiment. N-heptane with cetane number of 56 shows reactivity very close to diesel used in the experiments, which is mainly assessed by the ignition delay times [71]. In

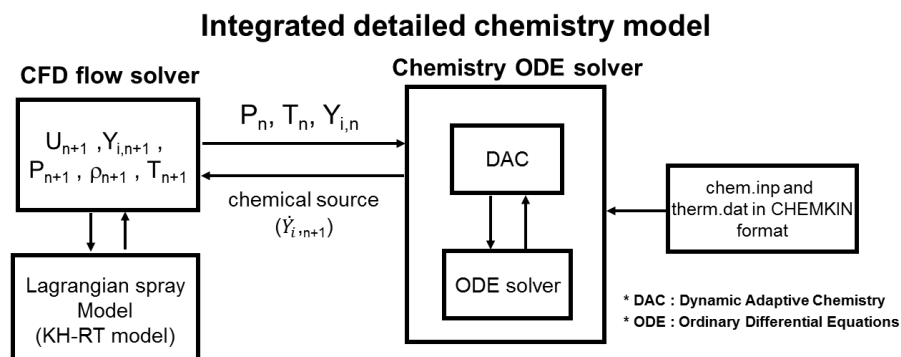


Figure 3.7: Schematic representation of the integrated detailed chemistry model.

the present simulations, two reaction mechanisms are used. The first reaction mechanism considered was a detailed one from the Lawrence Livermore National Laboratories (LLNL) with 159 species and 1540 reactions [146] and the second reaction mechanism was a skeletal mechanism developed by Lu [171] and has 88 species and 397 reactions. During the validation stage, as discussed in section 3.2.7.2, both n -heptane mechanisms captured the time of start of combustion for the range of operating conditions considered in the study. Therefore, n -heptane was considered as a reasonable chemical surrogate for diesel fuel.

OH^* reaction steps developed by Hall et al. [65] were added to the mechanisms for qualitatively predicting OH^* concentration in the flame region, thus enabling a more direct comparison with experimental OH^* chemiluminescence images. It is believed that the present work offers the first direct comparison between modelled and experimental OH^* chemiluminescence. OH^* is used experimentally because its chemiluminescence is believed to correspond well with high temperature chemical reactions, and it also be isolated from other broadband luminescence sources due to a strong peak in its luminescence spectrum (see chapter 4 for further discussion of OH^* chemiluminescence measurements). An alternative may be suggested to use the modelled ground state OH for comparisons with experimental OH^* chemiluminescence; however

the ground state OH is a major component of product gases and, as shown recently by Pei et al.[124] does not peak in the region of high heat release rate in diesel spray flames but instead peaks much further downstream. An examination of the mechanism by Hall et al. [65] shows that OH* is generally not produced from OH, but instead from reactions involving other species. Clearly, therefore, a direct comparison of experimental OH* chemiluminescence of to modelled OH* is expected to be superior to comparing the modelled ground state OH.

The physical properties of *n*-heptane were also used. It is noted that *n*-heptane has different physical properties compared with diesel in terms of volatility, density, and surface tension. These quantities would be expected to result in some differences between *n*-heptane and diesel sprays in the liquid region; however, these effects are not expected to result in large differences to the evaporated fuel distributions, which is what is mainly relevant in the reported cases since the fuel is completely evaporated well before ignition occurs. Moreover, the prediction of evaporation during spray injection is comparable as observed in the two experimental data considered for the validation. Therefore, both physical and chemical properties of *n*-heptane are used without attempting to model physical properties of heavier hydrocarbons.

3.2.7.2 Validation of the combustion model

The integrated detailed chemistry model was first validated using a simple cube domain with 4 x 4 x 4 uniform grid under homogenous mixture conditions using the LLNL *n*-heptane reaction mechanism. The homogenous mixture of *n*-heptane vapour and air at three different equivalence ratios ($\phi = 0.5, 1$ and 1.5) was considered and spray sub-model was switched off to verify the performance of the combustion model alone. The transient evolution of the temperature was compared with the results from the SENKIN [104] at $\phi = 0.5, 1$ and 1.5 . As shown in Fig.3.8, the black lines are from the SENKIN, the red lines are from using the integrated detailed chemistry model without DAC and the green lines are from

using the integrated detailed chemistry model with DAC. Start of the first-stage and the second-stage combustion predicted by the combustion model with and without DAC at three different equivalence ratios matches well with the SENKIN predictions. Also, overall temperature evolution and peak values compare well with the SENKIN results. In the second validation study, combustion in an optical diesel engine under two different injection conditions was simulated using the combustion model.

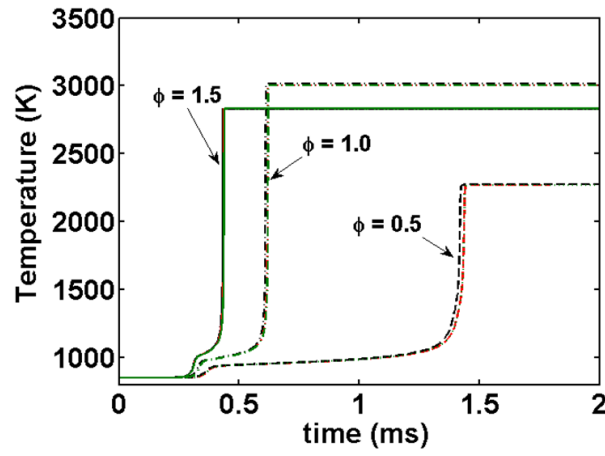


Figure 3.8: Comparison of transient temperature evolution in a homogenous combustion of n-heptane vapour using the LLNL reaction mechanism at $\phi = 0.5, 1$ and 1.5 . Black lines: from SENKIN. Red lines: using OpenFOAM without DAC. Green lines: using OpenFOAM with DAC.

The selected operating conditions for the combustion simulation in an automotive-size, optical diesel engine are shown in Table 3.2. More details about the engine geometry and the experimental setup are discussed in chapter 4. The computational grids used for the simulations are shown in Fig. 3.10. The mesh with valves and ports (see Fig. 3.10a) contains a combination of hexahedral and tetrahedral cells, 2.5 million cells at Bottom Dead Centre (BDC) and 0.7 million cells at Top Dead Centre (TDC). This mesh was used for a motored simulation of one complete cycle to capture the asymmetric swirl induced by intake ports and is shown in Fig. 3.11. The swirl ratio (SR) defined as the ratio of axial component of momentum caused by the swirling flow to the axial component of engine speed swirl was calculated in a mid axial plane at different crank angles using the formula

shown in Eq.(3.45). As shown in Fig.3.9, the calculated swirl ratio gradually decreases with piston movement during the compression stroke as some fraction of tangential velocity of the flow changes to axial velocity and after TDC, there is a sharp drop in the swirl ratio during the expansion stroke. Around TDC, the swirl ratio is around 1.5 and being asymmetric can effect evaporated fuel-air distribution before and during the combustion. This swirl effect is further discussed in the study devoted to the effect of jet-wall and jet-jet interactions on the combustion development in chapters 5, 6 and 7.

$$SR = \frac{\int \rho(\mathbf{r} \times \mathbf{U}) \cdot \mathbf{k} dV}{\omega \int \rho(\mathbf{r} \times (\mathbf{k} \times \mathbf{r})) \cdot \mathbf{k} dV} \quad (3.45)$$

where \mathbf{r} is the radius vector from the cylinder axis, \mathbf{k} is the unit vector in the direction of cylinder axis and ω is the engine angular velocity. The motored pressure simulated using the mesh in Fig.3.10a compared with the motored pressure from the experiment. The comparison is shown in Fig.3.12. The unavoidable crevice flow leakages were accounted for by increasing crevice volume that gave an effective compression ratio (CR) of 17.1.

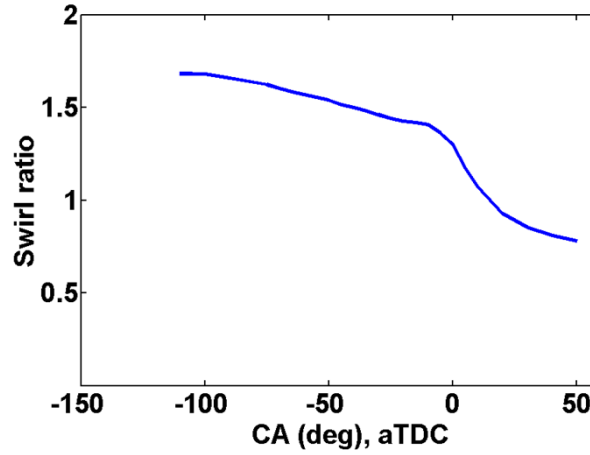


Figure 3.9: Swirl ratio calculated using Eq.(3.45) in a mid axial plane at different crank angles.

The mesh used for the spray and combustion simulations was a mesh without valves and ports using a spider web type hexahedral arrangement with 0.5 million

cells at BDC and 100000 cells at TDC (see Fig.3.10b). The initial condition for the spray and combustion simulation was mapped from fields from the motored simulation after Intake Valve Closure (IVC) (-142° after Top Dead Centre (aTDC)). This approach provided a good quality hexahedral mesh and reduced computational time for the spray and combustion simulations. The LLNL *n*-heptane reaction mechanism was used for the diesel spray combustion simulation.

Table 3.2: Selected operating conditions.

parameters	case, C1	case, C2
Injected fuel mass	11 mg	1.45, 3.8 mg
Number of holes of the injector	7	7
Start of injection (aTDC)	1°	$-20^\circ, -10^\circ$
Injection duration (Crank Angle)	6.5°	$2^\circ, 3^\circ$
Geometrical compression ratio (CR)	17.7	17.7
Motored TDC temperature ¹	849 K	815 K
Motored TDC pressure	4.2 MPa	4 MPa
Motored TDC density	17.16 kg/m^3	17 kg/m^3
Intake oxygen % (vol.)	21	21

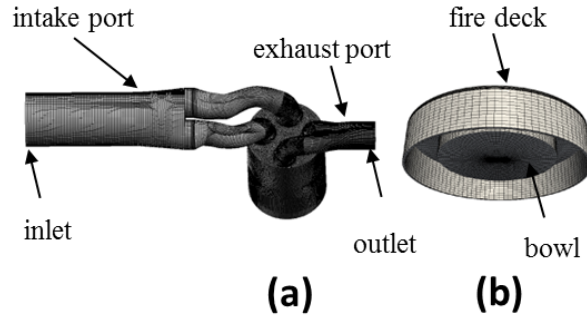


Figure 3.10: Computational grids used for the combustion model validation.

Before arriving at using a suitable hexahedral mesh for diesel spray combustion simulation as shown in Fig.3.10b, a mesh dependence study of the spray was done using two different meshes as shown in Fig.3.13. In the study, a non-combustion spray simulation was done with a concentric cylindrical swirl with swirl ratio of

¹Motored values are reported from motored CFD simulations.

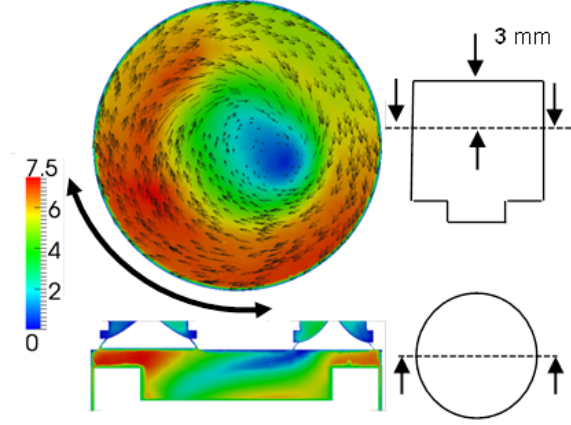


Figure 3.11: Velocity (m/s) contours with vectors showing the asymmetric swirl.

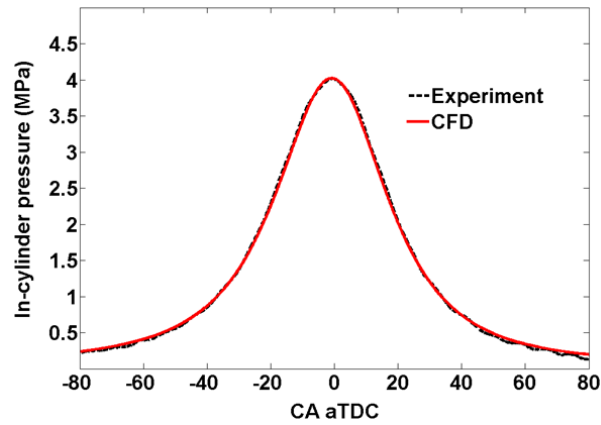


Figure 3.12: Motored pressure comparison.

1.5 using the conditions of the case, C1 as shown in Table 3.2. As all the 7 holes of the injector inject the fuel at the same flow rate and the evaporated fuel from all the holes see similar swirl flow, exactly similar distribution is expected from each of the hole. The iso-contours of the fuel mass fraction 4° after start of injection (aSOI) as shown in Fig.3.14a show that the fuel distribution from all the injector holes with mesh Fig.3.13a is not similar. The iso-contours from the holes that see elongated mesh are elongated and in the other regions the iso-contours are short compared to the elongated contours. This effect is avoided with the mesh shown

in Fig.3.13b as each of the spray sees exactly similar kind of the mesh.

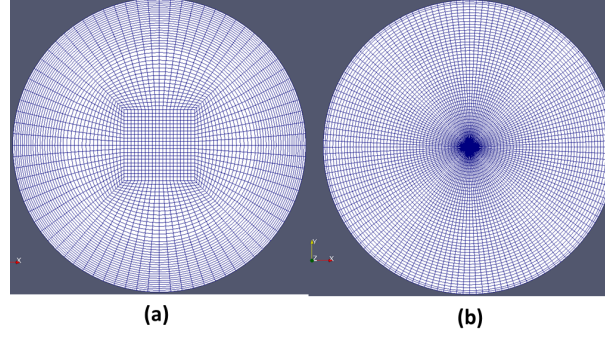


Figure 3.13: Meshes used for mesh dependence study of the spray.

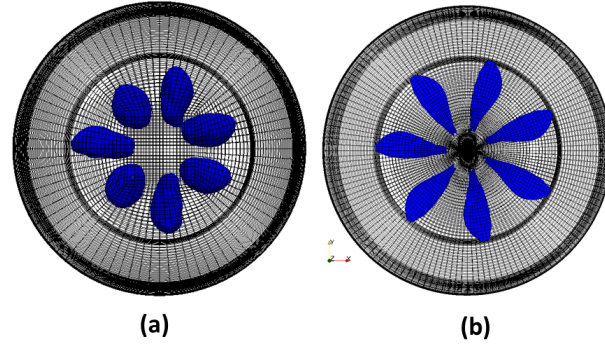


Figure 3.14: Iso-contours of fuel mass fraction with two meshes as shown in Fig.3.13.

The model predicted in-cylinder pressure and calculated apparent heat-release rate, (aHRR) are compared with experimentally measured pressure and aHRR in Fig. 3.15 for C1 and C2 cases. The aHRR in the experiment and simulations were calculated based on the pressure data and cylinder volume by using the first law of thermodynamics with an adiabatic assumption [72] using Eq.(3.46).

$$\frac{dQ}{d\theta} = \frac{\gamma}{(\gamma - 1)} p \frac{dV}{d\theta} + \frac{1}{(\gamma - 1)} V \frac{dp}{d\theta} \quad (3.46)$$

where Q is the net adiabatic chemical energy released at a crank angle position during combustion in *joules*, p is the instantaneous in-cylinder pressure in *pascal*,

V is the volume as a function of crank angle in m^3 , θ is the crank angle in *degrees* and γ is the adiabatic exponent with a value of 1.35.

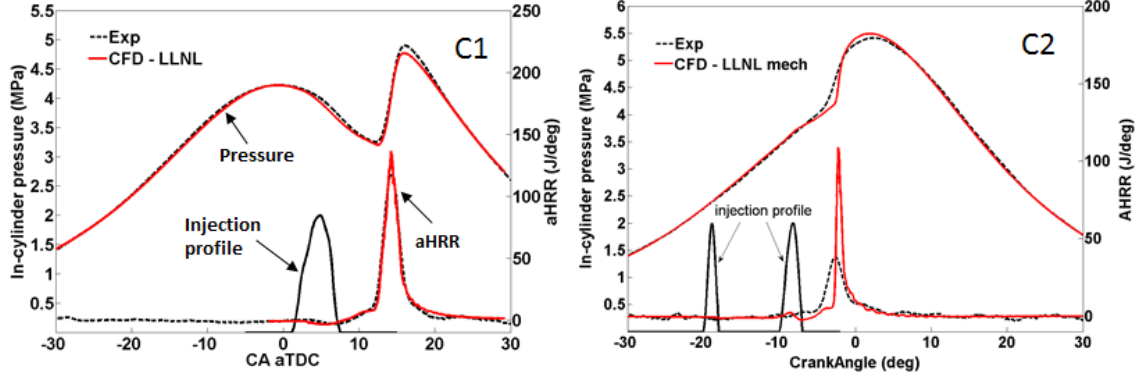


Figure 3.15: Pressure and aHRR comparison with experimental data in C1 and C2 cases.

In the case C1, the major heat releases from 12.5 CA aTDC indicating the premixed combustion is going on [56]. The start and pressure rise during this combustion phase are well captured by the LLNL mechanism and the combustion model. The experimental aHRR plot shows there is no heat gain during the cool-flame ignition that usually happens near the end of injection. In both the experiment and in the simulation, the heat released may have been nullified by evaporative cooling of the injected fuel. In the case C2, the peak aHRR occurs around -3 CA aTDC in the experiment and in the simulation. The combustion heat release in the simulation with the LLNL mechanism is steep and sharp. This trend is not observed in the experiment; however, the area under the aHRR curve between -5 and 3 CA aTDC from both the experiment and the simulation is almost same suggesting the total heat release from the combustion is same.

Chapter 4

Automotive-size optical diesel engine and diagnostics

Diesel spray combustion in an automotive-size diesel engine sees a series of interconnected processes starting from the fuel injection, mixture formation and combustion development influenced by jet-wall and jet-jet interactions, and burn-out to form combustion products and pollutants such as NO_x , CO and UHC. Optically accessible engines provide an opportunity through advanced laser diagnostics and high speed cameras to understand the involved processes and improve the design features for better performance of the engine. Data from these engines can also be extremely valuable for validating a combustion model, which can in turn provide additional insight into the combustion process that is not always possible through the experiments alone. In this chapter, setup of an in-house automotive-size, optical diesel engine is first described. Details about the optical diagnostics that were used for the combustion model validation and analysis are then covered.

The experimental work reported in this chapter was conducted at the University of New South Wales by Minh K. Le and Sanghoon Kook [17]. It is not an original contribution of this thesis, but needs to be recounted for completeness.

4.1 Engine setup

A simplified schematic of the optical engine is shown in Fig. 4.1. The selected engine and injector specifications are summarised in Table 4.1. To allow optical access into the combustion chamber, certain parts of the piston top and the cylinder liner were replaced by quartz pieces, effectively turning them into optical windows. The piston-top quartz window provided a field of view of 43 mm, slightly smaller than the piston-bowl diameter (55 mm). To avoid experimental difficulties with refraction, the piston bowl had to be flat as opposed to a conventional dome-in-bowl piston geometry. A portion of the piston-bowl rim (33 mm wide), in line with one of the liner quartz windows, was removed to allow laser access for laser-based diagnostic techniques.

Earlier experimental studies were also done without laser access in which the piston-bowl rim cut was not needed [145]. In those studies, only natural soot luminosity and chemiluminescence images were acquired optically using a high speed camera through the piston-top quartz window, along with the in-cylinder combustion pressure trace. Pressure data from such two different injection conditions was used in section 3.2.7.2 of Chapter 2 to validate the combustion model.

In this study, the engine was naturally aspirated and has a fixed nominal swirl ratio of around 1.4 during the intake stroke. The intake air and wall temperatures were controlled by cooling water and oil to mimic normal operating conditions of an automotive diesel engine. A conventional ultra-low sulphur (ULSD) diesel fuel (cetane number 51) was used throughout the study. To ensure repeatability and stability between the experiments as well as to reduce the thermal loading on optical quartz windows, fuel injection was executed for every 10th cycle (skip-firing mode).

¹Bowl-cut is for laser access for laser-based diagnostic techniques

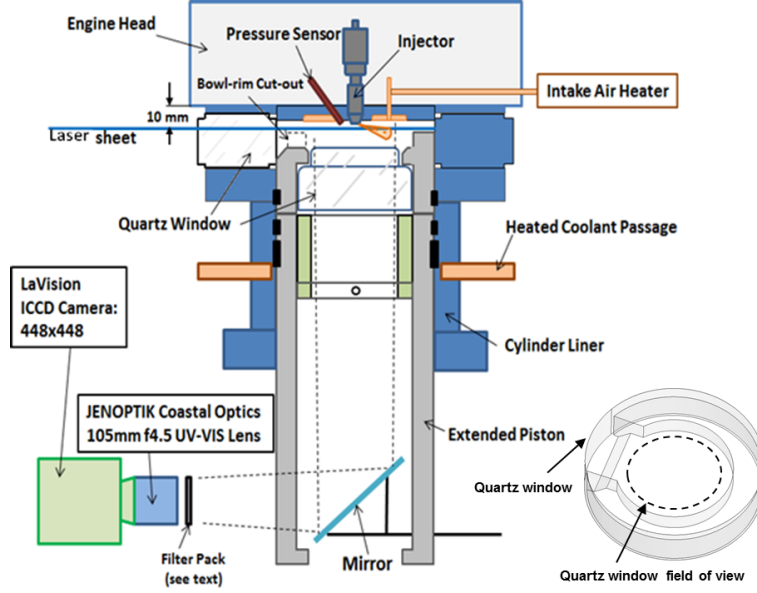


Figure 4.1: A schematic diagram of the optical engine with experimental setup. Schematic picture of piston and bowl shape after quartz window cuts (shown in bottom right corner) [17].

4.2 Diagnostics

4.2.1 Low-temperature natural flame chemiluminescence

Naturally occurring chemiluminescence during the combustion of a diesel jet comes from a range of species during different stages of the combustion. These include early reactions during the first-stage produce species such as CH , CO and formaldehyde (CH_2O) from the breaking down of ketohydroperoxide (KET) species [46; 47; 115] and high temperature second-stage reactions that produce hydroxyl radical (OH) and soot. The chemiluminescence signal was captured by an intensified charge-coupled device (ICCD) camera (LaVision NanoStar) equipped with an ultraviolet lens. Previous studies [46; 127; 150] have demonstrated that the chemiluminescence of early reactions is very weak and is emitted over a broad wavelength ranging from 360 to 560 nm. Hence, the camera gate was kept at 100 μs with 100 % ICCD gain without any optical filter throughout the early reaction stages until the signal becomes significantly stronger (a few order of magnitude

Table 4.1: Important engine and injector specifications

Engine speed	1200 rpm
Displacement (single-cylinder)	497.5 cm ³
Bore	83 mm
Stroke	92 mm
Geometrical compression ratio (without bowl-cut)	17.7
Geometrical compression ratio (with bowl-cut) ¹	15.2
Swirl ratio (nominal)	1.4
Wall (coolant) temperature	363 K
Intake air temperature	303 K
Injector type	Second-generation Bosch common-rail
Number of holes in the injector	7
Nozzle type	Hydro-grounded, K1.5/0.86
Nozzle diameter	134 μ m
Included angle	150°

stronger), which signifies the commencement of high temperature reactions. Natural chemiluminescence images were captured at various crank angle locations until the high temperature reactions start, from where the OH* chemiluminescence diagnostic was applied instead. Twenty images were captured at each location from twenty firing cycles.

4.2.2 OH* chemiluminescence

Electronically excited hydroxyl (OH*) radicals are formed from high-temperature exothermic reactions of hydrocarbons at near stoichiometric condition (e.g. $\text{CH} + \text{O}_2 \rightarrow \text{CO} + \text{OH}^*$) [47]. Therefore, OH* radicals are good indicators of high-temperature, high heat release reaction zone. As these excited OH* radicals return to their ground state, a chemiluminescence signal is emitted, particularly dominating the 306–310 nm range. To isolate the emission range of the OH* signal (unlike natural chemiluminescence), an optical filter pack including a WG-

305 glass filter and a 300 nm band-pass filter (FWHM 40 nm) was placed in front the ICCD camera. The ICCD gate was set at 70 μ s (the duration of half a crank angle) with the gain set at 25 % of the maximum gain value. Similar to the other optical diagnostic techniques applied in this study, 20 OH* chemiluminescence images were captured at each crank location.

4.2.3 OH planar laser-induced fluorescence (OH PLIF)

The excitation laser wavelength chosen for OH PLIF is near 284 nm (vacuum wavelength) which is the overlapping Q1(9) and Q2(8) lines of the (1,0) band of $A \leftrightarrow X$ transition of OH fluorescence. The resulting fluorescence emissions due to the vibrational and rotational transitions fall in the 308 - 320 nm range and were imaged using ICCD camera equipped with a UV lens (similar to the chemiluminescence experiments). To isolate the OH PLIF emission range and to avoid fluorescence and interference from other species (such as from aromatic compounds and soot), a 300 nm band-pass filter (40 nm FWHM with around 70% maximum transmission in the range) was used, coupled with a WG305 long-wave-pass glass filter to reject the scattering from the excitation wavelength. A Rhodamine 6G filled dye laser (Sirah Cobra-stretch) was pumped by a frequency-doubled Nd:YAG laser (Quanta-ray PRO) to produce a fundamental emission at 568 nm and then frequency doubled by a beta-barium-borate (BBO) crystal to achieve the desired OH excitation wavelength.

In the 308 - 320 nm range, under UV excitation, other species such as formaldehyde, polycyclic aromatic hydrocarbons (PAH), fuel aromatics additives, etc., also fluoresce. Together with soot incandescence, these signals can produce unwanted interferences to the OH fluorescence signal in the OH PLIF diagnostic. However, unlike most of these species, OH, being a diatomic molecule, has a unique, fine-scaled and well-defined rotational-vibrational structure in its fluorescence excitation spectrum. Hence, OH fluorescence absorption and emission changes drastically with very small changes in the excitation wavelength. By comparing images taken under the wavelength tuned to the OH excitation fluorescence line: ‘online’ images and off the excitation line: ‘offline’ images, the location and intensity of the interferences as well as that of the OH radicals can be identified

and assessed. Both ‘online’ and ‘offline’ OH PLIF images were taken at three different planes in the engine as shown in schematic Fig. 4.2, with 20 images taken for each setting at each engine crank location. Only ensemble averaged ‘online’ images were used to compare with corresponding images from the simulations.

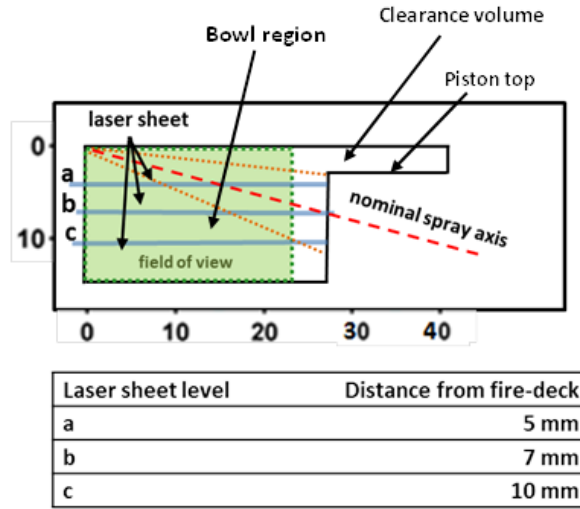


Figure 4.2: Relative positions of laser sheet levels, nominal spray axis and piston bowl geometry at top dead centre [17].

4.2.4 Fuel planar laser-induced fluorescence (Fuel PLIF)

Conventional diesel fuel such as the ULSD used in this study contains many aromatic hydrocarbons additives such as naphthalene and alkyl benzenes which under UV light become excited and undergo fluorescence. Unlike OH, excitation of these aromatics produce fluorescence spectrum over a broad band which overlaps with the OH emission range [113; 150]. Therefore, the fluorescence from these sources will not show much difference in terms of intensity between online and offline images with respect to the OH excitation scheme. Although this will create problematic interferences during the jet reaction period, it can provide valuable information on the development and penetration of fuel in a wall-interacting jet prior to heat release occurring. In this study, images that do not show major

differences between online and offline OH excitation scheme before the reaction period (deduced from aHRR curve: aHRR below or equal to 0) will be used as fuel fluorescence images to gain information on jet penetration. The capturing process for fuel PLIF is identical to OH PLIF with the same camera system and filter pack.

4.3 Measurements and processing of results

4.3.1 In-cylinder pressure and heat release rate

In-cylinder pressure was acquired through a piezoelectric transducer (Kistler type 6056A) installed as a replacement to the glow plug unit in the engine head compartment. The face of the sensor was exposed at an angle near the centrally-located injector nozzle as shown schematically in Fig. 4.1. Data were recorded using a data acquisition system (MCC USB-1616HS-BNC). The in-cylinder pressure was ensemble-averaged over 20 firing cycles. After going through the ensemble-averaging process, the averaged pressure data were smoothed using an in-house developed filtering software [143]. The filtering software removes the acoustic ringing and noise in the pressure data and hence, the resulting apparent heat release rate calculated from smoothed pressure and instantaneous in-cylinder volume using Eq. (3.46) under adiabatic condition was also smoothed. The filtered results do not differ much from the original data in terms of the information provided, such as the rises and peaks of the pressure and heat release rate.

4.3.2 Image selection and processing for optical diagnostics

Effect of cycle-to-cycle variations on captured images: Under the high compression ratio, in-cylinder swirl flow and changing ambient condition during the injection event, the fuel air mixing process will be affected and the resulting combustion event will be highly turbulent. This is the main cause for the cycle-to-cycle variations observed in diesel engine, especially in this study of a single wall-interacting jet flame. Due to this, the shape and development of the flame

between each firing cycles will be slightly different. When ensemble-averaging is applied to the captured images, the resulting averaged image is smeared out in comparison to individual images captured at each cycles and the details of turbulence effect at each cycles will be lost. While this is not always desirable in experimental engine research, it is necessary to compare the ensemble averaged images to the images generated by using RANS approach in the simulations. Brightness of all the images was artificially improved to reduce the smearing effect.

Image presentation: For each optical diagnostic, the grayscale of the images was converted into false colours: Low-temperature natural flame chemiluminescence was converted to false colour brown, OH* chemiluminescence to false colour cyan, Fuel PLIF and online OH PLIF to false colour blue. The images were also rotated so that the axis of the jet of interest is vertical. Red circular curves representing the field of view were also added to the images, with the imaging crank location after top-dead-centre (aTDC) on the top left corner and crank location after start-of-injection (aSOI) on the top right. The scale attached to the bottom and left side of the images displayed the distance to nozzle in mm. All the images captured using laser-based diagnostics were put through a low-pass filter for noise reducing.

Chapter 5

Comparison of modelling and optical diagnostics in an automotive-sized diesel engine – baseline condition

The combustion development in the in-house automotive-size, direct injected compression ignition engine with a baseline 70 MPa injection pressure was numerically studied and compared with the experimental data during the first-stage and the second-stage of combustion. The objective is to go beyond the typically reported comparisons of pressure traces by performing comparisons against optical measurements of key combustion indicators and thus learn more about the ability of the model to capture details of the combustion process. First, the modelled and measured pressure trace and apparent heat release rate are compared to establish a basis for further comparisons. Fuel penetration and distributions were compared based on fuel PLIF to understand mixture formation. First stage chemiluminescence was compared to the modelled formaldehyde to understand the timing and locations of low temperature, first stage ignition. Hydroxyl radical chemiluminescence and PLIF were compared to understand the timing and locations of second stage ignition and the main heat releasing events.

After these comparisons, the numerical analysis was extended to better un-

derstand the observed combustion phenomena. The effect of scalar dissipation rate on the combustion development, re-entrainment effect, transient development of CO and un-burned hydrocarbons (UHC) were all examined. Finally, a comparison of the combustion development in the present engine to conceptual models for conventional diesel combustion [45] and the low-temperature partially premixed diesel combustion [115] was done. The agreement between model and experiment is generally quite good, suggesting that the overall combustion and mixing behaviours are reasonably well captured by the model. In the present study, a single isolated fuel-injection as shown in Fig. 5.2 was used to specifically understand the effect of jet-wall interaction on the combustion development. In the numerical simulations, diesel chemistry was captured using a skeletal reaction mechanism for n-heptane developed by Lu [171] appended with OH* reaction steps developed by Hall et al. [65] (see in section 3.2.7.1). The combustion model used was an integrated chemistry model and the details are covered in section 3.2.7. The important operating conditions of the study are given in Table 5.1 in addition to the general engine specifications listed in Table 4.1.

Table 5.1: Important operating conditions for baseline case.

Number of injector holes used	1
Injected fuel mass	10 mg
Rail pressure	70 MPa
Actual start of fuel injection	-7° CA aTDC
End of injection	10° CA aTDC

5.1 In-cylinder pressure and heat release rate comparison

A comparison of the predicted in-cylinder pressure trace and apparent heat release rate (aHRR) with the experimental data is shown in Fig.5.1. The aHRR in the experiment and simulations were calculated based on the pressure data and cylinder volume by using the first law of thermodynamics with an adiabatic assumption [72] using Eq. (3.46). The simulated pressure trace during the combustion compares well with the ensemble averaged experimental pressure trace,

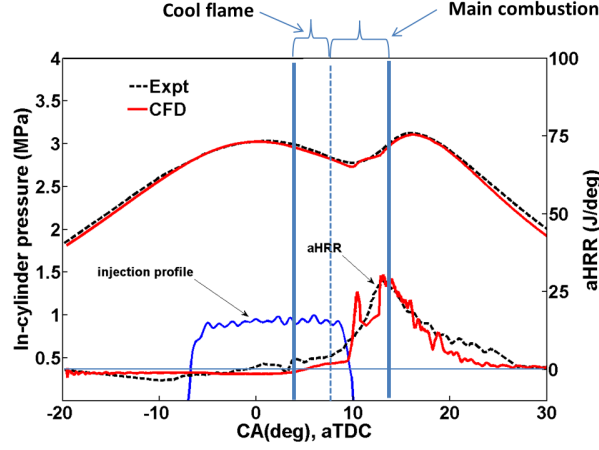


Figure 5.1: In-cylinder pressure and apparent heat release rate (aHRR) comparison.

which is taken from 20 fired cycles. In the simulation, the aHRR begins at a small negative value. From the start of fuel injection, the aHRR becomes more negative due to evaporation of fuel. Around 5° CA aTDC, the aHRR becomes positive and starts increasing, indicating that the first stage combustion has started. The period up to around 8.5° CA aTDC is called cool-flame period as only first stage combustion goes on everywhere in the cylinder. After 8.5° CA aTDC as observed from a strong localised concentration of OH mass fraction from the simulation (Fig. 5.8), the second stage combustion starts. However, this is not immediately evident in net heat release rate as fuel injection is active up to 10° CA aTDC and the fuel heat of evaporation partly cancels the heat released in combustion. As postulated in [115; 116], the rate of evaporation increases during the last stage of fuel injection because of generation of an entrainment wave. After the cool-flame period, the period up to around 13.5° CA aTDC is called the premixed burn of main combustion period.

The below paragraph has been added in response to comments from Examiner-1

A dip in the heat release rate in the simulation is observed around 12° CA aTDC which is not observed in the experimental data. As

will be explained later, the dip, which results in two distinct peaks of HRR, does not correspond to an overall transition between a premixed burn to a mixing-controlled burn but actually to a staging of the combustion events between different sides of the cylinder according to the influence of swirl. It will be shown later that both sides each undergo a distinct premixed and mixing-controlled burn, albeit at slightly different times. There are two likely reasons why this dip is not observed in the experiments. First, the experimental result is the ensemble of many cycles, and there is a level of natural cycle-to-cycle variability such that different cycles ignite at slightly different times, resulting in the smoothing of the initial HRR spike. In contrast, the CFD has no way of accounting for cycle-to-cycle fluctuations. Another possible reason is that the experiments involve a multi-component fuel where each component has a slightly different ignition delay, which may also result in smoothing relative to the CFD where there is only one fuel component.

5.2 Jet-tip penetration comparison

In the present study as mentioned in the experimental setup section 4.1, only a single jet of fuel was injected into the cylinder to study the effect of jet-wall interactions on combustion progress. The bowl diameter in this engine is relatively small compared to that in heavy-duty diesel engines which have been more widely studied. This small bowl has results in evaporated fuel impinging on the bowl-wall and penetration of the fuel vapour jet along the bowl-wall before the start of combustion. (Note that Mie scattering [143] indicates however that the fuel is completely vaporised before impinging upon the wall.) As shown in a schematic representation of the jet in Fig. 5.2, the region of the wall-bounded fuel-air mixture on the upstream side of swirl is denoted the up-swirl side and the opposite side region is denoted the down-swirl side.

The experimental penetration was estimated using fuel PLIF in a plane at 7 mm from fire-deck. To define a boundary of the jet, a threshold was applied to the fuel PLIF image using Otsu's method [120]. In the simulations, a threshold fuel

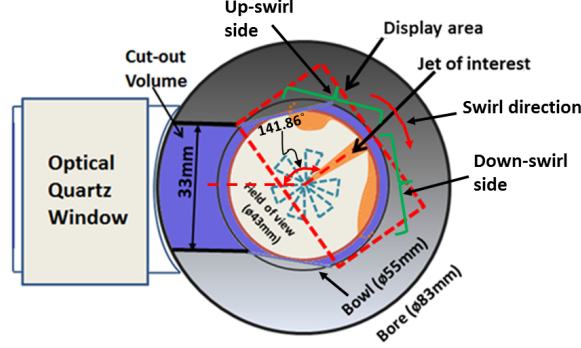


Figure 5.2: Relative position of jet of interest – top view of piston bowl.

mass fraction of 0.0001 was used. Previous studies have shown that penetration lengths obtained in this way are not sensitive to the threshold value as long as it is sufficiently small [69]. Before wall impingement, the jet-tip was located as the point of furthest location from the injector having a signal greater than the threshold on either side of the jet (up-swirl side and down-swirl side). The penetration length was defined as the projection of this length onto the jet-axis (angle of 15° from fire-deck as included angle of the injector is 150°). After impingement, the arc length of the jet along the bowl-wall from jet-axis to the jet-tip is also added. A schematic pictorial representation of the method is shown in Fig. 5.3. In the simulations, the jet-tip penetration calculations replicated the experimental approach and the comparison is shown in Figs. 5.4 and 5.5.

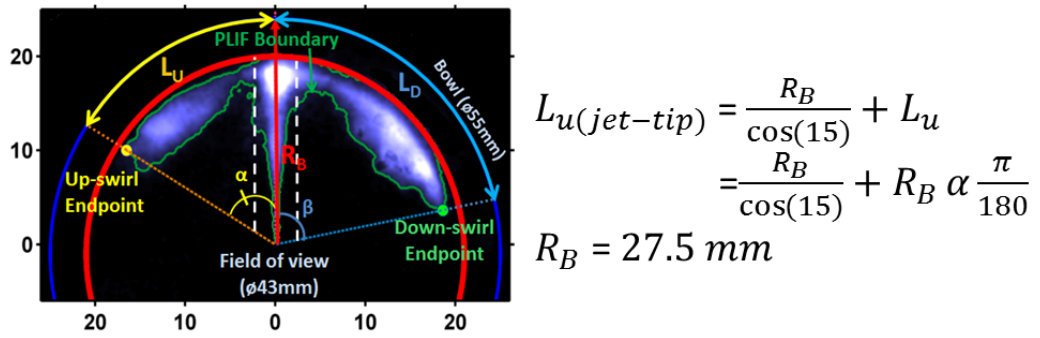


Figure 5.3: A schematic pictorial representation of calculation of jet-tip penetration length.

As shown in Fig. 5.4, simulated jet-tip penetration length is compared with jet-tip penetration length from the experiment. In the experiment, the penetration length was calculated for multiple runs to see the range of variation and so a standard-deviation at each considered crank angle along with the mean is also shown in the plot. In the simulations, before impingement, the penetration lengths from the up-swirl and the down swirl-sides are same and after impingement the down-swirl length has become slightly longer than on the up-swirl side. The differences between the two sides are more apparent in the experiments, the down-swirl length being longer compared to the up-swirl side length right from the beginning of evaporation of fuel. Despite this difference, overall the quantitative agreement between the modelling and experiment is quite good, suggesting that the fuel jet-wall interaction is reasonably well captured by the model.

In Fig. 5.5, fuel PLIF from the experiment and n-heptane mass fraction contours from the simulations in a plane at 7 mm from fire-deck are compared at different crank angles up to 8° CA aTDC and in column ‘c’, mass fraction contours of n-heptane from the simulations along the jet-axis in the direction as shown by section line A-A are also shown. The dotted yellow arc in all the images in the column ‘b’ of Fig. 5.5, and in other figures appearing afterwards, represents the field of view boundary in the experiment. As seen in the experiment in fuel PLIF images, the location of first observation of evaporated fuel at -6° CA aTDC is predicted correctly in the simulations and the further penetration and distribution of evaporated fuel before and after impingement are also captured well in the simulations. As mentioned earlier, because of small bowl diameter, the evaporated fuel impinges on the bowl-wall at around -3° CA aTDC, where around 24% of fuel was injected into the system.

The difference in jet-tip penetration lengths between up-swirl side and down-swirl side can be better explained with the help of velocity vector plots from the simulations taken in a plane at 7 mm from fire-deck at -8° , 0° and 8° CA aTDC. The plots are shown in Fig. 5.6. At 0° and 8° CA aTDC, vector plots are super-imposed with mass fraction contours of n-heptane. At -8° CA aTDC before the start of injection of fuel, the eccentric swirl induced by intake ports (in clock-wise direction viewed from top) exists undisturbed, but swirl-ratio is in the order of 1.0, which is a moderate swirl. At 0° CA aTDC, the evaporated

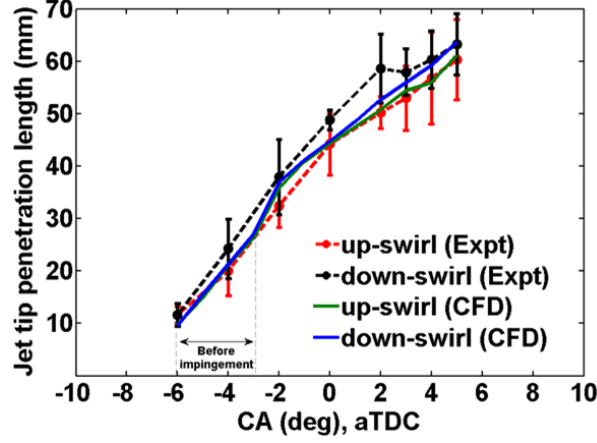


Figure 5.4: Jet-tip penetration length comparison.

fuel after impinging on the bowl-wall starts spreading along the bowl-wall sees opposing low velocity swirl-flow (≈ 5 m/s) on the up-swirl side and favouring swirl-flow (≈ 7 m/s) on the down-swirl side and this phenomenon exists even at 8° CA aTDC. Because of opposing swirl-flow on the up-swirl side, the spread of evaporated fuel is hindered and the jet-tip penetration length on the up-swirl side is slightly shorter after impingement compared to that on the down-swirl side, which is favoured by the swirl-flow.

5.3 Cool-flame period

As explained in the diagnostics section 4.2.1, during first-stage combustion, species that include CH, C_2 and formaldehyde (CH_2O) emit weak naturally occurring luminous emission over a broadband of wavelength from about 360 nm to about 560 nm [46; 47]. Such line of sight chemiluminescence images from the experiment at 5° , 6° , 7° and 8° CA aTDC are compared with formaldehyde line of sight mass fraction contours from the simulations in Fig. 5.7 to qualitatively compare the regions of cool flame reactions between the model and the experiments. As earlier mentioned, formaldehyde is a stable intermediate that is formed during the low-temperature first stage ignition phase. In the simulations, line of sight images were obtained by summing-up equally-spaced planar data in the bowl re-

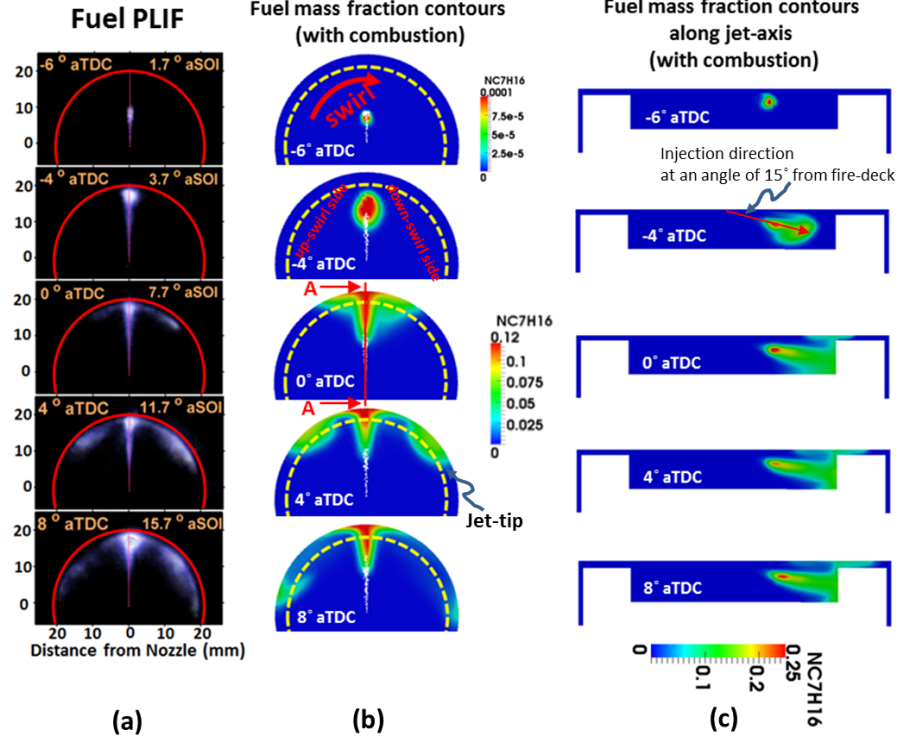


Figure 5.5: Comparison of fuel penetration. (a) Fuel PLIF from the experiment in a plane at 7 mm from fire-deck. (b) n-heptane mass fraction contours in a plane at 7 mm from fire-deck from CFD. (c) n-heptane mass fraction contours in a plane along jet-axis from CFD.

gion into a single plane. The dotted yellow arc in all the images in the column ‘b’ represents field of view boundary in the experiment. In column (c) of Fig. 5.7, plots of mixture fraction in a plane at 7 mm from fire-deck are also shown. Mixture fraction contours show that in the locations either side of the impingement point outside of the cone of the pre-impingement fuel jet, rich mixtures exist from the stoichiometric line ($Z = 0.0621$) to the bowl-wall with a maximum mixture fraction of around 0.085 ($\phi = 1.4$), i.e. the mixture is relatively well premixed in these regions.

The first appearance of weak chemiluminescence assumed to be from the mentioned first-stage species is seen on the either side of the jet at 5° CA aTDC in the experiment. Similarly, CH_2O is observed over a broad region on either side

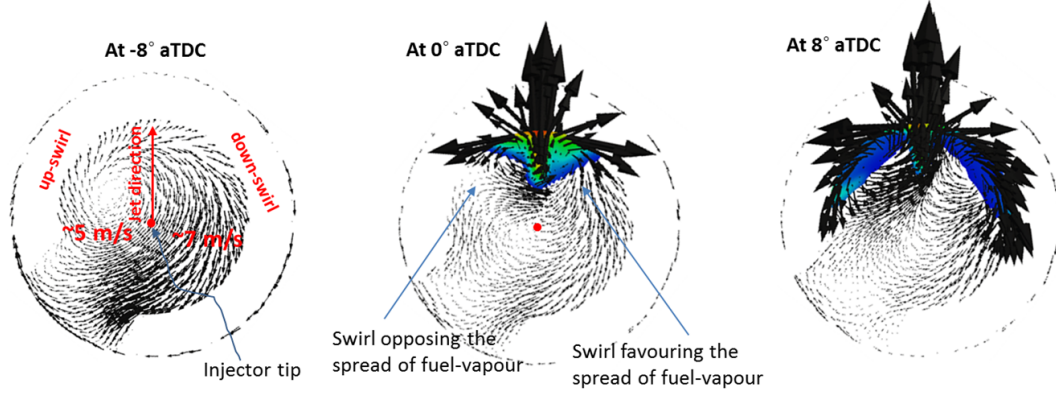


Figure 5.6: Velocity vector plots in a plane at 7 mm from fire-deck at different crank angles.

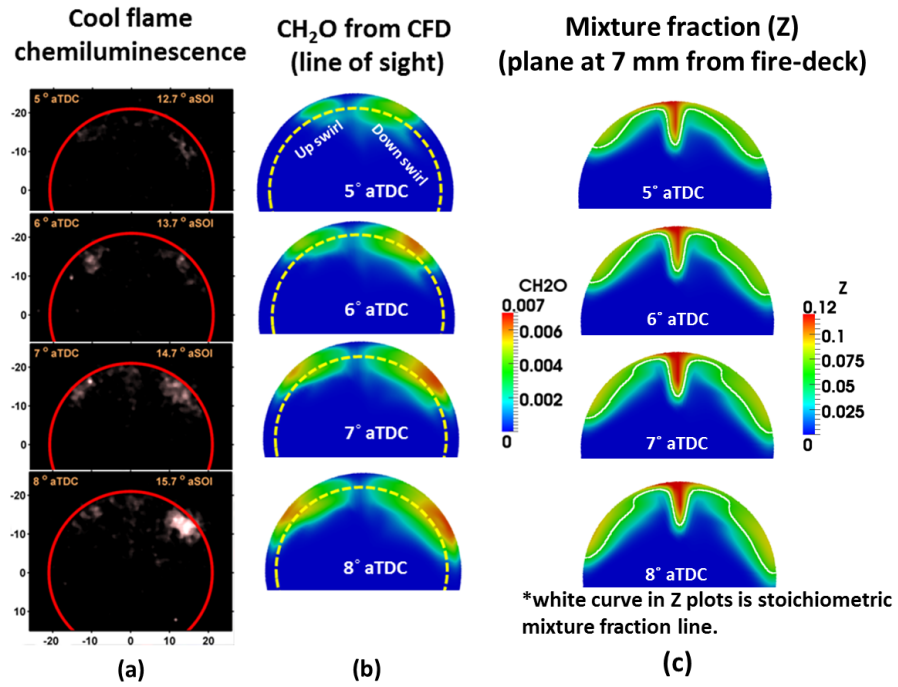


Figure 5.7: (a) Cool flame chemiluminescence from the experiment. (b) Line of sight mass fraction contours of CH_2O from CFD. (c) Mixture fraction (Z) contours with stoichiometric mixture fraction line from CFD.

of the jet at this time in the simulations. Over the crank angles shown, the first-stage combustion region broadens on both sides of the jet in the simulations and experiments, suggesting the first-stage ignition is qualitatively captured by the modelling. Comparison of the regions of localised high concentration of CH_2O shows they occur in rich mixtures ($Z \approx 0.085$). The coincidence of rich regions with high concentration of CH_2O is in accordance with the experimental observations made by Dec [45] in his experimental studies of the conventional heavy duty diesel combustion.

Another primary observation in both the simulations and experiments is that the first-stage combustion progresses slightly faster and in a larger area on the down-swirl side compared to the up-swirl side. This will be explained with the help of a scalar dissipation rate study in section 5.5.

A weak chemiluminescence signal is also seen along the jet axis in the experiments and not in the simulations - this could be because of natural luminosity from the diesel fuel constituent species.

5.4 Main combustion period

The start of main combustion period in the simulations is taken from the crank angle where high concentration of OH due to the second-stage combustion is observed. As shown in Fig. 5.8, such high concentration of OH is first seen at 8.5° CA aTDC on the down-swirl side. The consumption of CH_2O in the same location confirms this and also the maximum temperature in the region is around 2360 K.

The main combustion period is first investigated by comparing the measured line of sight OH^* chemiluminescence images with the modelled OH^* mass fraction. The simulated mass fraction of OH^* is in the order of $1\text{e-}12$. To the best of our knowledge, this is the first such comparison in a running engine. Fig. 5.9 shows the comparison at 9.5° , 11.5° and 13.5° CA aTDC. At 9.5° CA aTDC, the experimental images show that high temperature ignition occurs off the jet axis significantly on the down-swirl side of the jet, thus pointing to the strong impact of the wall in this small bore engine.

The below paragraph has been updated in response to comments from Examiner-1

The modelling shows a similar location for the high OH* region, but it is slightly larger suggesting that the ignition occurs slightly earlier in the model. Note that the experiments and model concur that for 9.5° CA aTDC, combustion is only occurring on the down-swirl side. This supports the earlier claim with respect to Fig. 5.1 that the double peak in the cylinder HRR observed in the model is due to a spatial staging of the combustion event in different parts of the cylinder rather than a transition from premixed to mixing-controlled burning over the whole cylinder.

It is worth noting that the filtered OH* chemiluminescence (see section 4.2.2) may also contain natural luminosity from PAH and soot in 306 - 310 nm range. Nevertheless, it is expected that PAH and soot can only form in the rich regions, which according to the model (which corresponded well with fuel PLIF and experimental penetration data), exist in this case from stoichiometric mixture line to the bowl wall as observed in the mixture fraction contours in Fig. 5.7. The field of view boundary in all the images is 6 mm from the bowl wall, and according to the model this misses the near wall rich regions (Fig. 5.7), and so the observed signal is probably not due to soot or PAH.

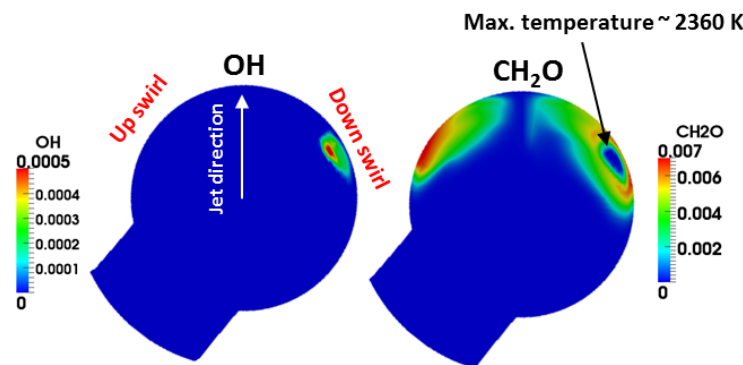


Figure 5.8: OH and CH₂O mass fraction contours from CFD at 7 mm from fire-deck at 8.5° CA aTDC.

The progress of the main combustion period is further analysed by comparing

OH mass fraction contours from the simulations and the online ensemble averaged OH PLIF images from the experiment in three different planes at 5, 7 and 10 mm from fire-deck. The comparison at 9.5° , 11.5° and 13.5° CA aTDC is shown in Figs. 5.10, 5.11 and 5.12 respectively. The bottom row in all figures is from the simulations and the top row is from the experiments. The stoichiometric mixture fraction line ($Z = 0.0621$) is also superimposed in all the OH mass fraction contours from the simulations.

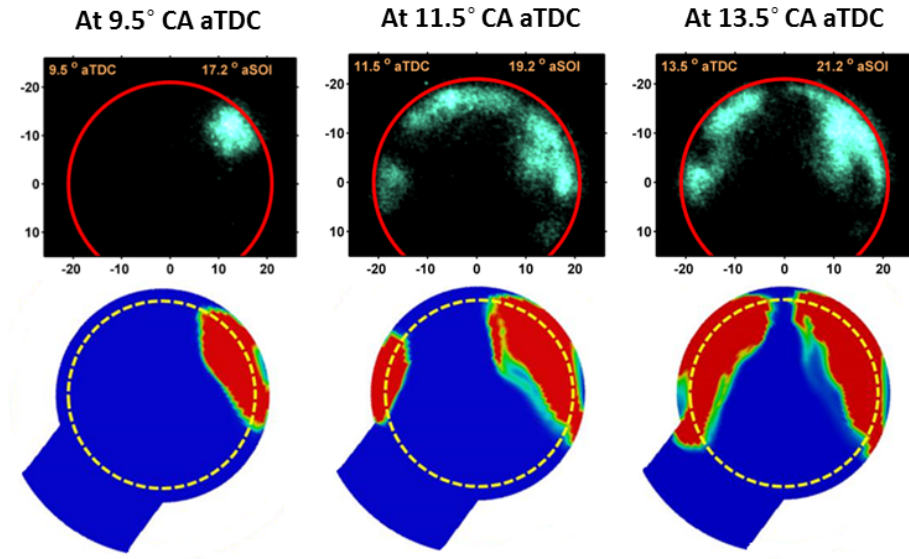


Figure 5.9: Comparison of line of sight chemiluminescence images of OH^* from the experiment and mass fraction contours of OH^* from the simulations at 9.5° , 11.5° and 13.5° CA aTDC.

At 9.5° CA aTDC: The experimental OH PLIF shows a signal in some areas consistent with the modelled OH PLIF at the 5 mm and 10 mm planes, noted by the green ellipses in Fig. 5.10. The OH PLIF in the experiments however shows signals on the jet axis at the 5mm and 10mm plane, and on the up-swirl side on the 10mm plane, which are not observed in the modelling. These differences are further discussed in the following.

The OH contours from the simulations at 9.5° CA aTDC (see Fig. 5.10) suggest that the second-stage combustion has only started on the down-swirl side at this crank angle and the presence of OH in all the planes signifies that the com-

bustion spans the bowl in the region. This was confirmed also in the experiments via the OH* chemiluminescence Fig. 5.9, suggesting that the fluorescence on the jet axis observed in all three planes in the experiments (most strongly at 7 mm) and on the up-swirl side (most strongly at 7 mm) are from another source. (The signal on the down-swirl side may also be partly from other sources, though the consistency with OH* suggests that at least in part this should be due to the existence of OH.)

As mentioned in section 4.2.3, online OH PLIF also contains fluorescence from CH₂O, diesel fuel constituent aromatic compounds, and aromatic compounds that form during combustion and soot. As mentioned in relation to the OH* images, the model suggests that PAH and soot are unlikely to contribute, since the mixture-fractions in the imaged region are too lean for strong formation of these compounds. Formaldehyde also fluoresces in this range but it is a broadband low-level signal and therefore unlikely to be significant. It is therefore likely that along the jet-axis and on the up-swirl side the fluorescence is almost certainly from fuel constituent aromatic compounds, particularly at the 7mm plane. It is also likely that a part of the signal on the up-swirl side is due to these fuel components.

On the 5 mm and 10 mm planes, the fluorescence on the down-swirl side is distinctly lower than at the 7 mm plane. A possible explanation for this is that the first stage ignition is more advanced in 5 mm and 10 mm planes, which are at the hot periphery of the jet than it is in the 7mm plane, which is more towards the cooler inner core of the jet. During the first stage ignition, some of the aromatic components may break down, which could lead to a reduced fluorescence signal.

At 10 mm, the OH PLIF image shows that there is hardly any fluorescence on the down-swirl side. This suggests that there is no second-stage combustion near the bowl bottom wall in the experiments (see Fig. 4.2 for bowl geometry). In contrast, the modelling indicates that combustion is occurring in this location, suggesting once again that the ignition process is slightly advanced in the modelling.

At 11.5° CA aTDC: A more clear interpretation of the experimental images can be made at 11.5° CA aTDC, when much of the fluorescing fuel components have been consumed. The comparison of OH images is shown in Fig. 5.11. In

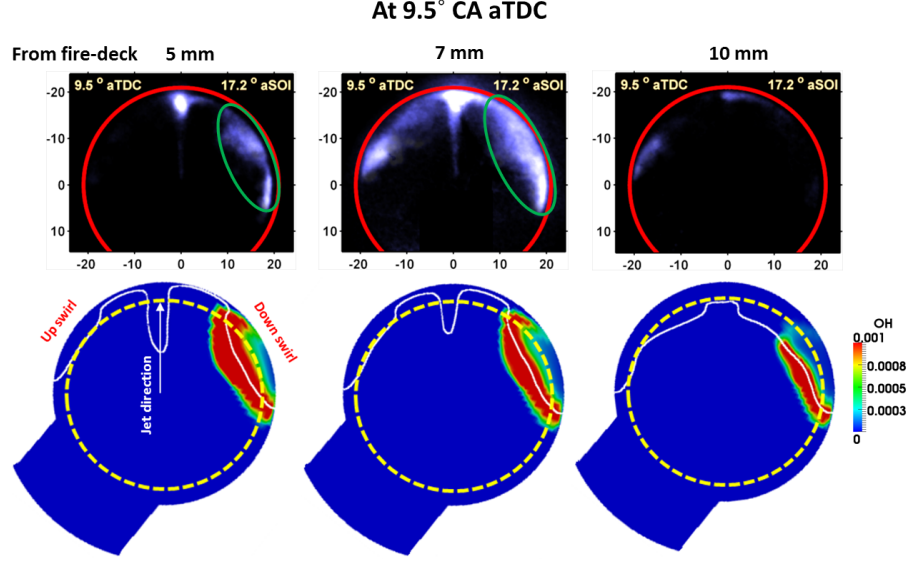


Figure 5.10: Comparison of ensemble averaged online OH PLIF from the experiment and mass fraction contours of OH from the simulations at 9.5° CA aTDC in planes at 5, 7 and 10 mm from fire-deck.

the simulations, it is observed that the second-stage combustion has now also started on the up-swirl side in planes at 5 and 7 mm from fire-deck, is away from the jet-axis near the jet-tip. On the down-swirl side, the spread of strong OH concentration over a broad region conveys that the second-stage combustion is in an advanced stage. In the experiment, green encircled regions represent probable OH fluorescence, as judged by the regions with OH^* in Fig. 5.9. The locations and size of these regions in the bowl, and the relatively stronger intensity on the down-swirl side, is very consistent between the modelling and experiment, suggesting that at this time in the simulation, the high temperature combustion is well captured.

Some differences are noted, however. The simulations exhibit a fairly narrow region of high OH, while the experiments show a broader more diffuse region. This difference is probably because the model ignores turbulence-chemistry interactions. As has been discussed by Pei et al. [121; 122; 123], Bhattacharjee and Haworth [25], and Bolla et al. [32], the well-mixed model considerably underestimates the thickness of species profiles compared to other models that account

for turbulence-chemistry interactions.

Additionally, in the experiment at 10 mm, the ensemble averaged OH fluorescence is also seen on the up-swirl side. This shows that the second-stage combustion has started on the up-swirl side in the experiment throughout the entire bowl in this region, whereas in the simulations, the combustion is prevalent only from the middle to upper part of the bowl (the 5 mm and 10 mm planes).

The fluorescence along the jet-axis near the wall impingement point is still probably from aromatic compounds from the considered diesel fuel. However, it is noted that for the 7 mm plane, the fluorescence signal on the up-swirl side of the jet, but before the region circled in green, is much lower than in the same region at 9.5° CA aTDC. This is consistent with that region having gone through the first stage ignition which destroyed some of the aromatic components in the fuel.

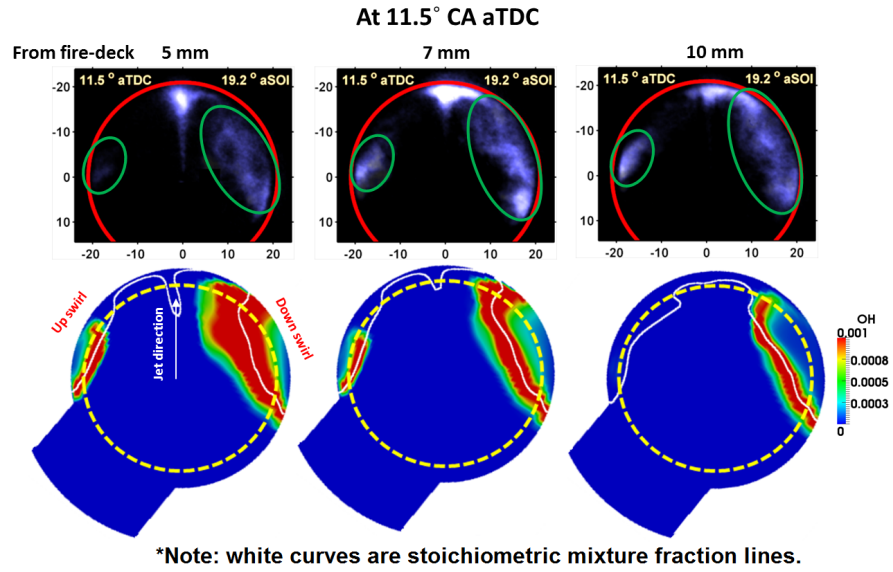


Figure 5.11: Comparison of ensemble averaged online OH PLIF from the experiment and mass fraction contours of OH from the simulations at 11.5° CA aTDC in planes at 5, 7 and 10 mm from fire-deck.

At 13.5° CA aTDC: At this angle, the comparison of OH PLIF images is

shown in Fig. 5.12. The comparison of OH images shows that the second-stage combustion is in an advanced stage on both sides of the jet in the simulations whereas in the experiment, the second-stage as observed in the simulations is spread over a broad area on the down-swirl side, but localised on the up-swirl side. Once again this is consistent with slightly advanced combustion progress in the modelling.

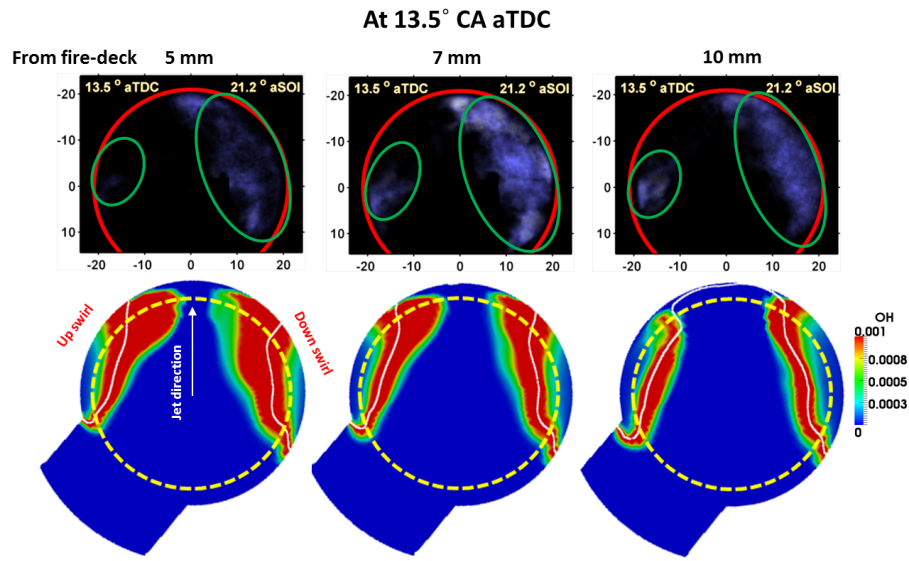


Figure 5.12: Comparison of ensemble averaged online OH PLIF images from the experiment and mass fraction contours of OH from the simulations at 13.5 ° CA aTDC in planes at 5, 7 and 10 mm from fire-deck.

5.5 Scalar dissipation rate study

If the development of combustion is observed on both sides of the jet right from 5° CA aTDC, where the first appearance of formaldehyde (CH_2O) is seen both in the experiment and in the simulations (see Fig. 5.7), the first-stage combustion starts on both sides of the jet, but the progress of combustion is slightly faster and occurs in a broader area on the down-swirl side compared to the up-swirl side. In the second-stage, the combustion starts first on the down-swirl side at around 8.5° CA aTDC in the simulations, while on the up-swirl side, the start of

the second-stage is observed at around 11° CA aTDC in the simulations and at around 10.5° CA aTDC in the experiment, (Fig. 5.13). The delay of around 0.5° CA in the start of second-stage combustion in the simulations on the up-swirl side compared to the experiment might have also resulted a dip in heat release rate between 10° and 13° CA aTDC as shown in Fig. 5.1. The delay in the start of the second-stage combustion on the up-swirl side compared to the down-swirl side is explained with the help of scalar dissipation rate in this section. The

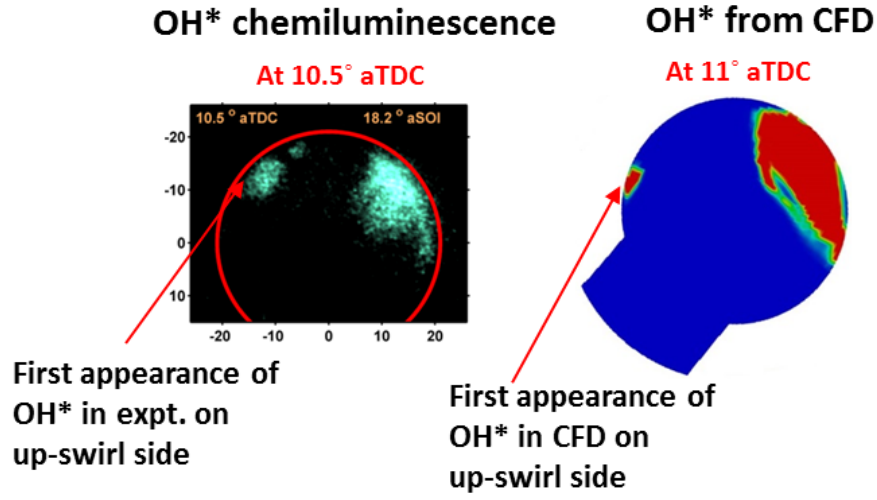


Figure 5.13: First observation of second-stage OH chemiluminescence in experiment and simulation.

scalar dissipation rate represents mixing rate or turbulent diffusion rate. It was calculated as shown in Eq. 5.1, where $D_t = \frac{\nu_t}{Sc_t}$ is the turbulent mass diffusivity, Z is the mixture fraction, $|\nabla Z|$ is the magnitude of the gradient of mixture fraction, ν_t is the turbulent viscosity and $Sc_t = 0.7$ is the turbulent Schmidt number.

$$\chi = D_t |\nabla Z|^2 \quad (5.1)$$

The scalar dissipation rate in a plane at 7 mm from the fire-deck at 7° and 8° CA aTDC during the cool-flame period and at 9.5° and 11.5° CA aTDC during the main combustion period is shown in Fig. 5.14. The calculated peak value of χ at 7°, 8° and 9.5° CA aTDC is 1.9 s^{-1} and at 11.5° CA aTDC, 0.7 s^{-1} . The

peak value occurs along the jet-axis because of high fuel-jet velocity, and thus high turbulence intensity, as expected. The preceding sections on combustion development comparison during the cool-flame and the main combustion period show that there is no combustion along the jet-axis up to 11.5° CA aTDC, which highlights the fact that χ value of around $\geq 0.7s^{-1}$ is high enough to prevent ignition (Eq. 5.1).

During the cool-flame period (7° and 8° CA aTD), Fig. 5.14 shows that in regions downstream of the jet impingement point and away from the jet-tip, χ is in the order of $0.2 - 0.3 s^{-1}$, which are moderate values, both on the up-swirl side and the down-swirl side (highlighted by black encircled regions). At the jet-tip on the up-swirl side, however, the value is higher, around $0.6 s^{-1}$. This higher value is due to strain caused by the opposing swirl-flow. In the moderate χ regions, the first-stage combustion can start and is seen in the regions as shown in Fig. 5.7. Furthermore, the area span of the moderate χ region is larger on the down-swirl side compared to the up-swirl side because of favouring swirl-flow on the down-swirl side and opposing swirl-flow on the up-swirl side. At 9.5° CA aTDC,

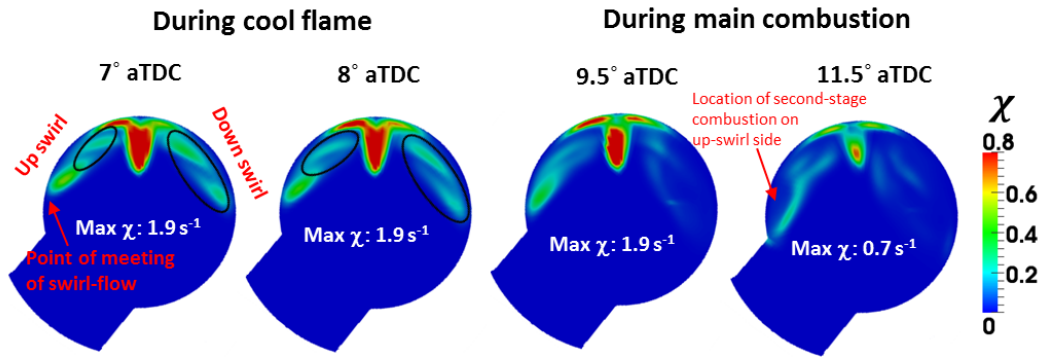


Figure 5.14: Scalar dissipation rate (χ) at 7 mm from fire-deck during cool-flame and main combustion periods. The black encircled regions represent regions of moderate χ .

where the second-stage combustion has only started on the down-swirl side (see Fig. 5.10) low χ values order $\leq 0.1s^{-1}$ are observed everywhere downstream of the impingement point except in the up-swirl side jet-tip region, where χ is order $0.2s^{-1}$. By 11.5° CA aTDC, the second-stage combustion has started at the

7mm plane on the up-swirl side where χ reached a range of low value $\leq 0.1s^{-1}$. Overall based on the observed trends at 9.5° and 11.5° CA aTDC a dissipation rate around $0.1s^{-1}$ seems to be sufficient to cause a significantly delayed ignition.

The temporal trend of the scalar dissipation rate is investigated further in Fig. 5.15, which shows the maximum scalar dissipation rate at the jet-tip region on the up-swirl and the down-swirl sides versus CA aTDC. The maximum value plotted is considered from the entire axial span of the jet-tip. As expected, because of the opposing swirl-flow effect on the up-swirl side, maximum χ at jet-tip is consistently a factor 2-4 higher than the maximum value on the down-swirl side. The maximum value is around $0.35 s^{-1}$ at 11.5° CA aTDC, which according to the previously suggested criterion for a critical value of $0.1s^{-1}$ is sufficient to prevent ignition at the location of maximum χ . Nonetheless the ignition is observed to occur at the 7 mm plane. However, the observed second-stage combustion at 7 mm on the up-swirl side at 11.5° CA aTDC is in fact slightly inside from the jet-tip where dissipation rate is lower. On the other hand, on the down-swirl side, from 9.5° CA aTDC, the maximum χ across the whole jet is $\leq 0.1s^{-1}$, which is low enough to allow the second-stage combustion in the entire axial span.

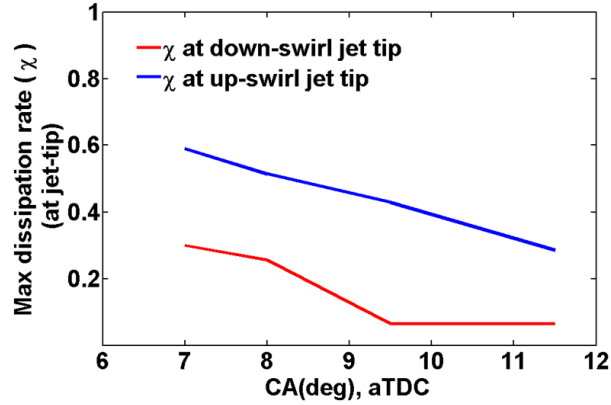


Figure 5.15: Scalar dissipation rate (χ) at jet-tip.

As mentioned earlier in the chapter 2, according to a fundamental study by Liu et al. [95], even moderate strain rates or scalar dissipation rates can delay the second-stage combustion compared to a homogeneous combustion. The Liu et al. study therefore supports a hypothesis that higher dissipation rates, caused

by interactions of the wall-jet flow with the opposing swirl flow, result in the observed delay in the start of the second-stage combustion on the up-swirl side.

5.6 Heat release rate study in mixture fraction space

The advantage of looking at heat release rate in the mixture fraction space is that it gives heat release rate information from the entire domain and reveals the range of mixture fraction where the major heat release rate or combustion is taking place. Fig. 5.16, shows such scatter plots at 7°, 9° and 12° CA aTDC separately for the up-swirl side and down-swirl side regions with the conditionally average values superimposed as red curves. The conditionally averaged heat release rate is symbolically represented as $\langle Q|Z \rangle$. The up-swirl side region is defined as the entire region of the in-cylinder domain on the up-swirl side from the jet-axis and the opposite side is the down-swirl side. The selected crank angles cover the cool-flame period i.e. at 7° CA aTDC, initial start of the second stage combustion i.e. at 9° CA aTDC and the advanced second-stage period, where the second-stage combustion was observed on both sides of the jet i.e. at 12° CA aTDC.

At 7° CA aTDC, the maximum heat release rate is around 50 J/s and the conditional value peaks in rich mixtures at around $Z = 0.1$ ($\phi = 1.7$) on both sides of the jet. This confirms that the high concentration regions of formaldehyde CH_2O as observed in Fig. 5.7 also correspond to the regions of heat release rate during the cool-flame period. In other words, it can be mentioned that heat release in the first-stage preferentially happens in rich regions. This is as expected and is in line with the observations made by other numerical and experimental studies [45; 58]. To further explain this point, it is known from understanding of the kinetics of n-alkane ignition [40] that the first stage ignition timing exhibits a monotonically decreasing trend with increasing temperature. It therefore occurs first in lean mixtures which are hotter. However, these very lean ignitions have temperatures close to the crossover point for the forwards and reverse reaction of alkyl radicals with molecular oxygen to form peroxy alkyl radicals, which is a key step in path to the low-temperature chain branching, so only a small amount

of heat release causes the reaction to proceed in the reverse direction thus ending the first stage heat release. Richer mixtures, however, are cooler and this allows a greater amount of heat release to occur before the first stage ends. This explains the larger first-stage heat release and larger amounts of formaldehyde in the rich regions.

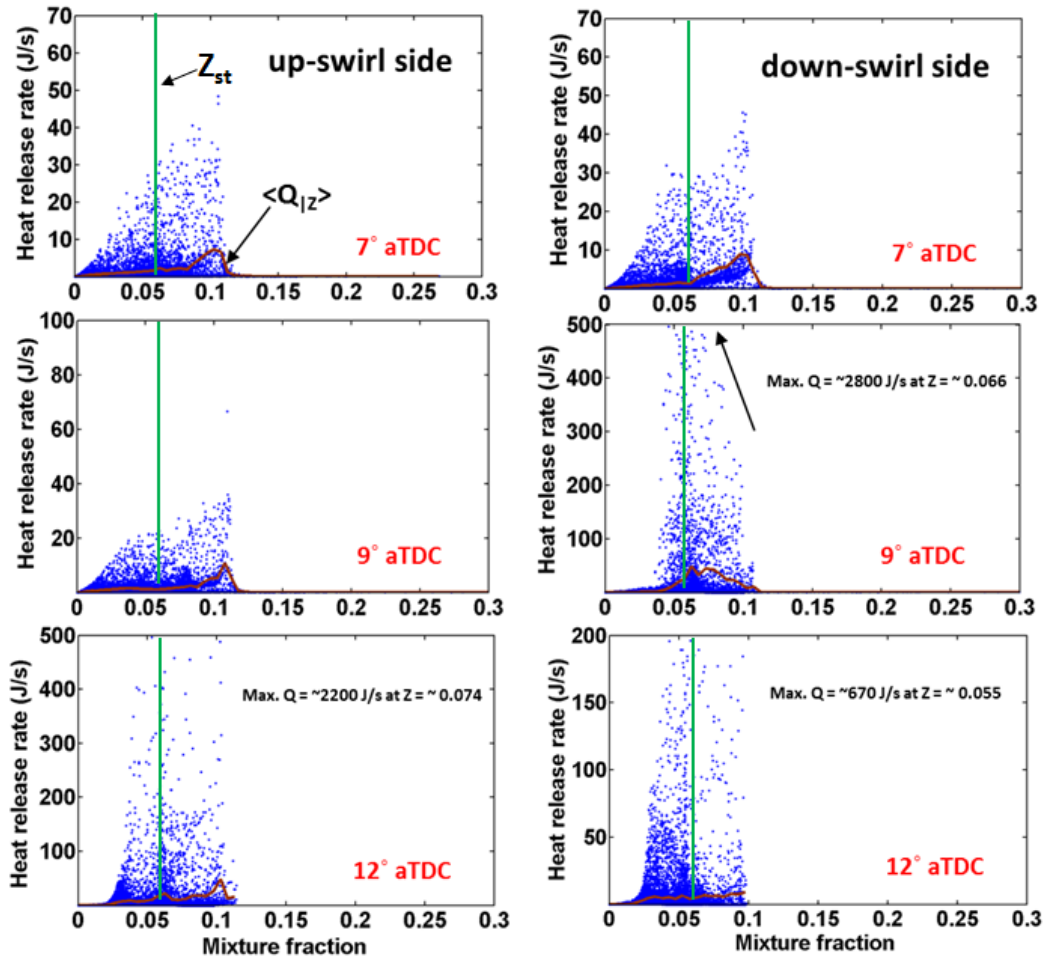


Figure 5.16: Scatter plots of heat release rate (J/s) in mixture fraction space and conditional average of heat release rate with respect to mixture fraction. First column: on up-swirl side; Second column: on down-swirl side.

At 9° CA aTDC, where the second-stage combustion was only observed on the down-swirl side (see Figs. 5.8 and 5.10), the main heat release rate with a peak value of around 2800 J/s occurs around stoichiometric mixtures and somewhat

on the rich side. These high values of the heat release suggest that the down-swirl side is undergoing the premixed burn phase of ignition. It also confirms that the high concentrations of OH around stoichiometric mixtures (see Fig. 5.10) are the high heat release rate regions during the second-stage of combustion. On the other hand, on the up-swirl side, the main heat release rate is still from the rich mixtures and the values are low compared to the heat release rate from the down-swirl side, which shows that the first-stage combustion is still going on.

At 12° CA aTDC, on the up-swirl side, the conditional average value has two local peaks, one is around stoichiometric mixture fraction ($\langle Q|Z \rangle \sim 30 J/s$) and the other one is around mixture fraction of 0.1 in rich mixtures ($\langle Q|Z \rangle \sim 60 J/s$). However, the total amount of the heat release around stoichiometric conditions is larger because these regions are more probable. The peak value of heat release rate around 2200 J/s is seen at around $Z = 0.074$ ($\phi = 1.2$), which is consistent with the up-swirl side entering the premixed burn phase of the second-stage of combustion. On the down-swirl side, the conditional average heat release rates are lower than they were at 9° CA aTDC. The peak value of heat release rate is around 670 J/s (which occurs at around $Z = 0.054$ i.e. $\phi = 0.86$) which is also less than the peak values observed at 7° and 9° CA aTDC. This suggests that the down-swirl side is entering the mixing-controlled burn phase (Fig. 5.1). The conditional mean is also no longer sharply peaked at stoichiometric conditions. This is consistent with those regions having burned most of the reactants with the combustion now being limited by mixing of fresh reactants into the stoichiometric region.

The below paragraph has been added in response to comments from Examiner-1

In summary, both the up-swirl and down-swirl sides go through distinct phases of first stage combustion, followed by a premixed burn and a mixing-controlled burn. These stages are phased slightly differently on each side, which as discussed earlier is a result of the effect of swirl.

5.7 Re-entrainment study

As discussed in chapter 2, the re-entrainment of combustion products into the fuel jet has been proposed in heavy duty engines to cause shortening of the lifted length and an increase of soot emissions. Although the present small bore engine does not feature a clear lifted flame, it is still possible that combustion products are re-entrained into the fuel jet which may advance the flame location towards the flame impingement point and thus result in less premixing prior to combustion.

The fuel injection starts at -7° CA aTDC and ends at 10° CA aTDC with a flat injection profile (see Fig. 5.1), which means the injection velocity will be almost constant during the injection period. The injection velocity is in the order of 150 m/s . As discussed in the above sections, the first-stage combustion starts at around 5° CA aTDC both on the up-swirl side and the down-swirl side, which is well before the end of fuel-injection. Even the second-stage combustion starts on the down-swirl side before the end of fuel injection. So, there is a definite chance of re-entrainment of combustion products towards the high-velocity fuel jet during the injection period. To study this effect, the combustion development is analysed from 7° to 12° CA aTDC spanning the cool-flame period and the main combustion period in two different planes along the jet-axis as shown in Fig. 5.17.

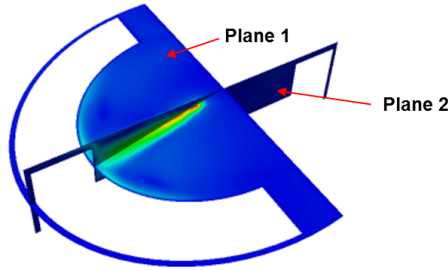


Figure 5.17: Planes considered along the jet-axis to study re-entrainment effect.

In plane 1 along the jet-axis, Fig. 5.18 shows: in the first-row, velocity vector plots; in the second row, contours of mass fraction of ketohydroperoxide (KET) superimposed with CO contours and the $\phi = 1$ line of unburnt fuel; in the third row, mass fraction contours of CH_2O with $\phi = 1$ line of unburnt fuel; in the fourth

row, heat release rate (HRR) in J/s and in the fifth row, temperature contours. The velocity vectors at 7° CA aTDC show that there is a strong entrainment of flow from both the directions towards the jet which is considerably enhanced by vortices formed on either side of the jet as a result of the flow redirection after wall impingement. At 9° and 10° CA aTDC, the rise in temperature above 2000 K on the down-swirl due to the second-stage combustion induced a strong dilatation flow, which further enhanced the entrainment effect. After the end of injection at 12° CA aTDC, the flow looks rather random as there is combustion induced dilatation flow from both the directions and there is no high-velocity jet to cause entrainment.

The distribution of ketohydroperoxide, which forms at the beginning of the first stage ignition via oxygen addition and hydrogen abstraction, and the distributions of CO and CH_2O , which form during the first-stage and get consumed during the second-stage shows that the species come towards the periphery of the jet carried by the entrainment flow, and it is clear that some amount of re-entrainment of these species is occurring, which may accelerate the ignition of newly injected fuel. However, none of these species are able to significantly penetrate the core of the jet and cause its ignition, perhaps because the dissipation rate is too high in this region or the residence time is too low. Any effect of re-entrainment of these first stage intermediates appears to be limited to regions downstream of the impingement point.

As to the re-entrainment of high temperature products, it may be noticed that the regions of heat release rate and temperature, and regions of low CH_2O and low CO, are away from the jet-axis and the $\phi = 1$ surface of unburned fuel. The $\phi = 1$ surface also remains intact along the jet-axis prior to the impingement point at least up to 10° CA aTDC. Together these facts suggest that re-entrainment of high temperature combustion products is not occurring over the injection duration considered here.

The combustion development is similarly studied in the plane 2 along the jet-axis (see Fig. 5.17). As shown in Fig. 5.19, the view of the plane from cylinder axis towards the jet is only considered. The first-row shows the velocity vectors, the second-row shows the mass fraction contours of CH_2O with $\phi = 1$ line of unburnt fuel, the third-rows shows the temperature and the fourth-row

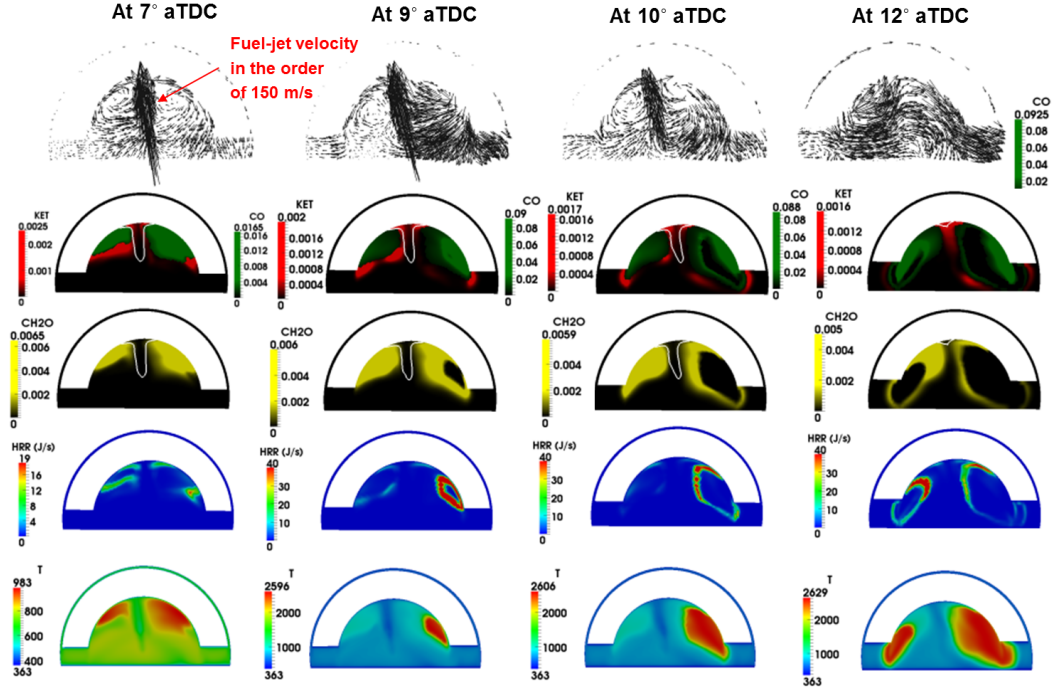


Figure 5.18: Contours at 7°, 9°, 10° and 12° CA aTDC in the plane 1 as shown in Fig. 5.17. First row: velocity vectors; Second row: contours of ketohydroperoxyl (KET) and CO; Third row: contours of formaldehyde (CH_2O); Fourth row: contours of heat release rate (HRR) in J/s ; Fifth row: contours of temperature in *kelvin*.

shows the scalar dissipation rate. The velocity vectors at different crank angles show that the close proximity of the bowl-wall at the bottom and the fire-deck wall on the top of the jet creates wall-vortices and consequently amplifies the entrainment flow. Also, there is an escape of fuel into the squish volume. On the bottom side of the jet, formaldehyde is observed suggesting first stage ignition has occurred. Similarly as for plane 1, it is clear that the intermediate products from the first stage, which have somewhat higher than ambient temperature, can be re-entrained into the main fuel jet, thus accelerating the ignition of newly injected fuel. Once again, however, ignition does not occur until after the wall impingement. Interestingly, the peak temperature in plane 2 is around 930 K, which shows that the combustion has not progressed beyond the first-stage at least up to 12° CA aTDC. This is due to high scalar dissipation rate in the order

of 6.5 s^{-1} up to 10° CA aTDC . By 12° CA aTDC , after fuel injection has finished, the maximum value is around 0.7 s^{-1} which is then low enough for the combustion to progress as evidenced by the growth of the formaldehyde-containing region.

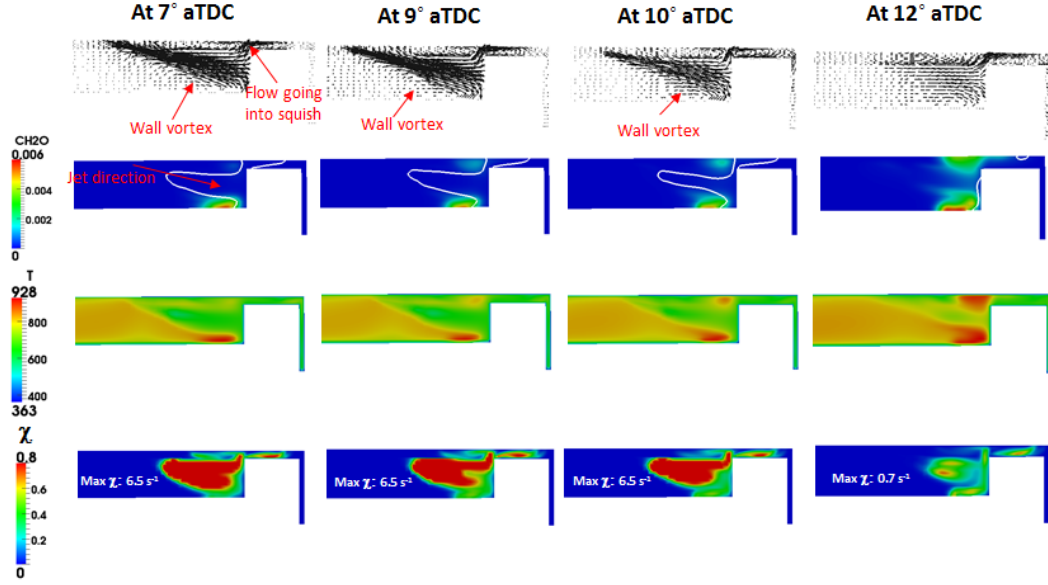


Figure 5.19: Contours at 7° , 9° , 10° and 12° CA aTDC in the plane 2 as shown in Fig. 5.17. First row: velocity vectors; Second row: contours of formaldehyde (CH_2O); Third row: contours of temperature in *kelvin*; Fourth row: contours of scalar dissipation rate (χ) in s^{-1} .

5.8 Emission of CO and un-burned hydrocarbons (UHC)

The escape of CO and UHC after the end of combustion is detrimental to combustion efficiency and emissions. The considered UHC constitute all the species that contain hydrogen and carbon elements. The sources of these emissions are therefore further investigated in this section. In the present small-bore engine with a single injection of fuel, transient development of CO and UHC are plotted separately in three ranges of mixture fraction for the up-swirl side and the

down-swirl side as shown in Fig. 5.20. The up-swirl side and the down-swirl side regions are the regions as defined in section 5.6.

5.8.1 Un-burned hydrocarbons (UHC)

Unburned hydrocarbons peaked around 10° CA aTDC on the up-swirl, whereas on the down-swirl side, they peaked slightly earlier. This is probably because of the earlier combustion on the down-swirl side. On both the up-swirl and the down-swirl sides, UHC is completely consumed by 20° CA aTDC in the range of mixture fraction $0.05 < Z \leq 0.1$. This is because the temperature was sufficient in these near-stoichiometric and moderately rich regions to enable complete conversion to combustion products. UHC in the range $Z \geq 0.1$ is also completely consumed in this case it is because very rich mixtures no longer exist after 20° CA aTDC.

In lean mixtures, $Z \leq 0.05$, a considerable fraction of UHC is left-over on the down-swirl side and some remains on the up-swirl side even at around 80° CA aTDC, where the combustion is almost finished. The UHC in this range does not change from around 30° CA aTDC, showing that the combustion is essentially frozen after this point.

5.8.2 Carbonmonoxide (CO)

The carbonmonoxide trend is similar to the one seen for UHC on both the sides. The peak values are seen around 15° CA aTDC on the up-swirl side and around 14° CA aTDC on the down-swirl side. In the usual two-stage combustion of diesel fuel, CO is first seen in the first-stage and gradually grows up to the second-stage, where it reaches peak values and thereafter is oxidised into CO_2 . Similar to the case for UHC, the earlier timing peak values ($\sim 14^\circ$ CA aTDC) and higher peak values on the down-swirl side signifies the earlier beginning of the second-stage combustion on that side. However, unlike for *UHC*, considerable CO is seen around 80° CA aTDC on both the sides in lean mixtures ($Z \leq 0.05$). CO is frozen in the range ($Z \leq 0.05$) from around 50° CA aTDC. To further understand the locations of lean mixtures ($Z \leq 0.05$) which have high CO and UHC values, 3-D iso-contours of UHC, CO, mixture fraction and temperature are examined at 80° CA aTDC. The contours are shown in Fig. 5.21. The un-consumed CO and

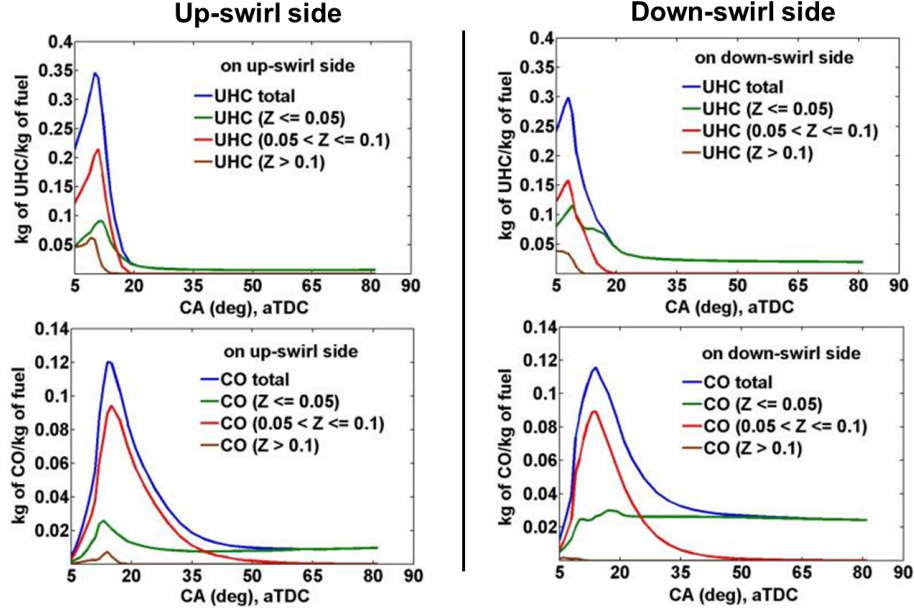


Figure 5.20: Transient development of CO and un-burned hydrocarbons (UHC). First column: on up-swirl side; Second column: on down-swirl side.

UHC are present in the upper part of the cylinder mostly in the squish volume, and because of the influence of the swirl-flow, seen mostly on the down-swirl side. The mixture fraction is less than 0.05 everywhere in the domain and the peak temperature is around 1450 K . At these conditions, the left-over UHC is not expected to undergo further combustion. Throughout the combustion event, due to larger heat transfer rates to the wall, the temperatures were significantly lower in the squish volume as compared to the main cylinder region, which led to combustion not fully proceeding to the main ignition. As discussed by Sjöberg and Dec [153], around 1500K is the minimum temperature required to achieve complete conversion of CO to CO_2 at typical engine speeds before expansion cooling prevents further cooling. Adding to this, as discussed in the section 5.7 and shown in Fig. 5.19, high strain rate experienced by the fuel-air mixture up to 12° CA aTDC exacerbates this effect by delaying the ignition of fuel in the squish volume to well after TDC when expansion cooling is becoming more rapid. The ppm (parts per million) values of CO and UHC on both the sides at 80° CA aTDC is shown in Table 5.2.

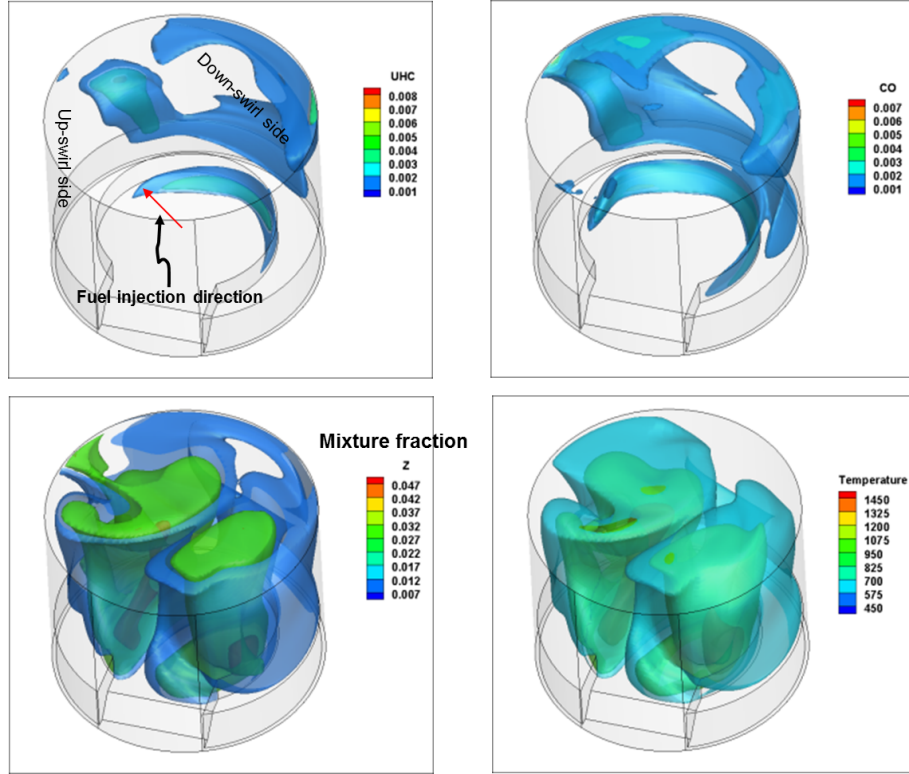


Figure 5.21: 3-D iso-contours of CO, un-burned hydrocarbons (UHC), mixture fraction (Z) and temperature in *kelvin* at 80° CA aTDC.

Table 5.2: ppm values of CO and UHC at 80° CA aTDC.

species	up-swirl side	down-swirl side	total
<i>UHC</i>	122	362	484
<i>CO</i>	175	443	618

5.9 Development of combustion and comparison with conceptual models

As outlined in Chapter 2, a conceptual model of light duty diesel engine combustion without EGR dilution does not appear to have been developed. It is therefore valuable to discuss similarities and differences between the available conceptual models and the observed phenomena in the present engine. As discussed in Chapter 2, the two most relevant conceptual models are the conventional heavy duty

engine model developed by Dec [45] and the low-temperature EGR-diluted late-injection light-duty model developed by Musculus et al. [115]. A brief description about the two conceptual models is given in section 2.1 of a chapter on literature review.

Before proceeding, it is important to note some differences between this optically accessible research engine and a conventional production engine used in passenger cars. First, the considered condition is at quite a low load. Second, there is no boost, the compression ratio is reduced because of the optical cut-out, and blow-by losses may be larger because metal rings are not used. All of these differences imply that the pressures, densities, and temperatures in the cylinder are lower than in a typical passenger car engine - these will cause the ignition delay to be longer and the flame to be located farther from the injector. Finally, there is only one nozzle hole rather than several, implying that the fuel injection is significantly longer. These are significant differences; however it is still valuable to discuss the observed combustion in the present engine.

The combustion development in the present automotive-size engine is shown in Fig. 5.22. As shown in the figure, the contours at -6° and 0° CA aTDC show the mass fraction of evaporated fuel ($\text{N-C}_7\text{H}_{16}$) in a plane at 7 mm from the fire-deck, at 5° and 8° CA aTDC; the line of sight contours of formaldehyde mass fraction (CH_2O) are shown and at 9.5° and 13.5° CA aTDC, the contours of hydroxyl radical mass fraction (OH) with superimposed stoichiometric mixture fraction line in a plane at 7 mm from the fire-deck are shown.

As shown in the fuel mass fraction contours, the evaporated fuel impinges on the bowl-wall before 0° CA aTDC, well before the first stage ignition has commenced around 5° CA aSOI, and certainly well before the second stage ignition commences around 8.5° CA aSOI. Also, both the first stage ignition and the second stage ignition occur off the jet axis, downstream of the impingement point. These features are similar to the light-duty EGR-diluted conceptual model, and rather different from the conceptual model for heavy duty engines. Another similarity between the present situation and the light-duty model is that the combustion occurs in regions that are already relatively well mixed, with $\phi < 2$; in contrast most of the heat release occurs in richer mixtures $2 < \phi < 4$ in a conventional heavy duty engine. However, there are also differences between the present

situation and the light-duty model and similarities between the present situation and the conventional diesel model. First, there is a negative ignition dwell, i.e. injection ends after ignition begins. Second, that a distinct peak in the aHRR corresponding to the first stage ignition is not observed. It is either obscured by the fuel heat of evaporation or the first stage heat release is spread out over more crank angles due to a lower level of mixedness. Finally, the present aHRR trace clearly shows a premixed burn phase followed by a slower mixing-controlled burn.

It is important to note, however, that all of the above conclusions could be influenced by the particular thermochemical conditions and fuel injection regime in the optical engine. The thermochemical conditions of pressure, temperature and density are lower than in a production engine, which could result in earlier ignition and flame stabilisation upstream of the wall impingement point in a production engine. A negative ignition dwell and mixing-controlled burn phase may also not occur because the fuel injection event is much shorter as more nozzle holes are available.

Another phenomenon that is happening in the present situation is the delay of start of the second-stage combustion between the up-swirl and the down-swirl sides because of the different strain rate experienced by these regions. This effect was not considered in the engines for which the conceptual models were developed which had lower swirl ratios. Whether this remains an important feature in cases that have jet-jet interactions would need further study.

5.10 Conclusions

The numerical model was compared with several experimental measurements in a small bore, optically accessible engine, to assess how well the model captures the experimentally observed phenomena, and to provide more insight into the combustion development. The following conclusions can be drawn.

- The pressure and aHRR traces generally agreed well between the experiment and model. The model showed a considerable dip in the heat release rate during the main combustion period, which was found to be due to a delay in the start of the second-stage combustion by around 0.5° CA on the

Direct, single –injection diesel combustion in a small-bore engine (present case)

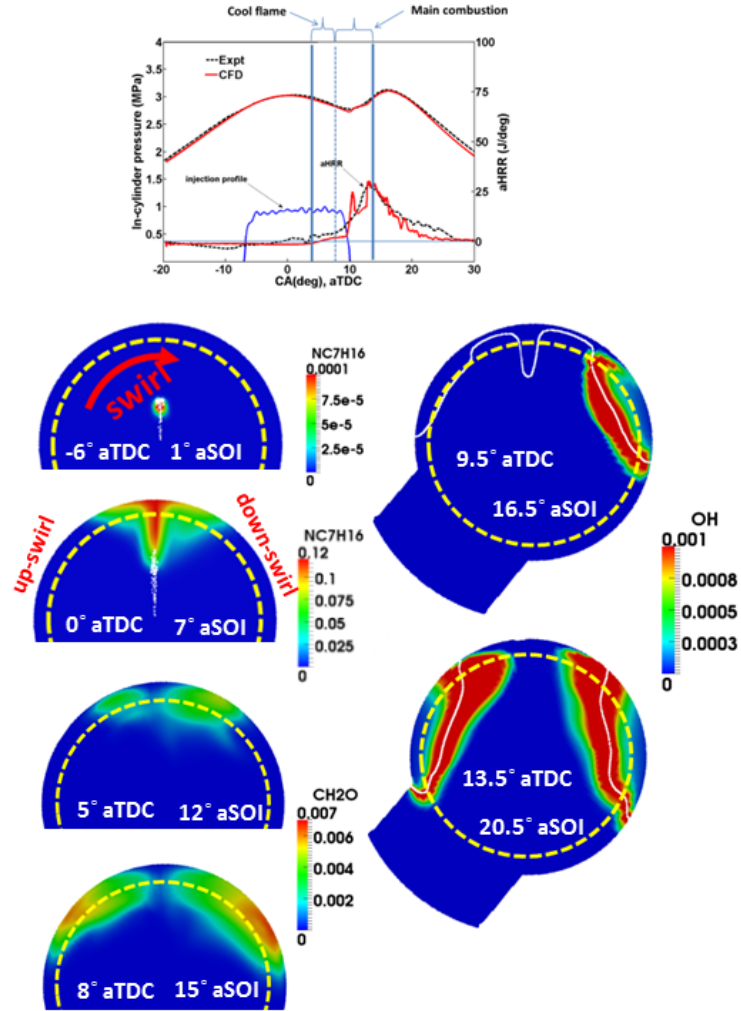


Figure 5.22: Combustion development in an automotive-size, direct injection diesel combustion (present case).

up-swirl side in the simulations as compared to the experiment.

- The agreement between model and experiment for the jet-tip penetration length was good, even after the wall impingement, which is encouraging particularly in this relatively complex, moving geometry. The experiments did however show a slightly greater effect of the swirl on the penetration on

different sides of the jet; however the agreement is acceptable as predictions fall within the standard deviation band of the experiment on both the sides.

- The experiment and model qualitatively agreed for the timing and location of the first stage cool-flame ignition, in particular showing that the cool flame initiates off the jet axis downstream of the wall impingement point, and has a somewhat faster progress on the down-swirl side of the jet. The model showed that the cool-flame activity occurred mainly in rich mixtures.
- During the main combustion period, modelled OH* was compared to experimental OH* chemiluminescence for the first time in a running diesel engine. The comparison revealed a good qualitative agreement between for the timing and location of these experimental signals and the modelled OH*, suggesting that the high temperature heat release was overall well captured. Second stage combustion was shown to occur off the jet axis, downstream of the fuel impingement point, and to occur earlier and more strongly on the down-swirl side compared with the up-swirl side. OH PLIF were also compared to the modelled OH. Interference of fluorescence from other sources, most probably fuel constituent aromatic compounds, affected the interpretation of these comparisons. In particular the experiments showed some signals in areas where the model indicated there was no OH. Nevertheless, the model rarely showed OH where there was no experimental signal, and agreement was notably better at 11.5° CA aTDC and afterwards, when the fuel aromatic compounds may have already been consumed during the first stage ignition or in the dwell between ignitions.
- The model and experiment agreed that combustion started earlier on the down-swirl side. This was further examined in the model by analysing the scalar dissipation rate. The down-swirl side was shown to have a significantly lower dissipation rate than the up-swirl side, consistent with a lower strain rate for a jet penetrating into a co-flowing swirl as compared with a jet penetrating into a counter-flowing swirl. It was therefore proposed that the strain rate in the jet head region caused the delayed ignition on the up-swirl side. Careful analysis of the local dissipation rates suggested that

combustion was delayed in regions with χ larger than about $0.1s^{-1}$.

- Whether the wall confinement of the jet caused re-entrainment of combustion products was examined. It was found that re-entrainment of first stage combustion products could be occurring. However, it was not significant enough to cause first stage ignition to occur along the jet axis. It is suggested that either strain rates were too high in this region or the residence time was insufficient. Nonetheless, re-entrainment of the first stage combustion products could have affected the combustion of fuel downstream of the wall impingement point. However, the products of the second stage, high temperature combustion remained far from the fuel jet and high temperature combustion was never initiated along the jet axis until after the fuel injection had finished.
- The unconsumed CO and UHC after almost completion of combustion at 80° CA aTDC were seen mainly in the upper part of the cylinder above the squish volume. These resulted from incomplete combustion in the squish volume where the peak combustion temperatures were less than 1450 K, insufficient to allow CO to CO₂ conversion before expansion cooling rendered the composition frozen. In fact, the temperatures were so low in this region that the second stage combustion never occurred, resulting in significant formaldehyde emissions.
- The numerical analysis showed that the combustion in the considered automotive size engine under the considered conditions was similar in some respects to a conceptual model of light-duty EGR diluted diesel combustion in that combustion occurred in mixtures of intermediate stoichiometry ($\phi \leq 2$) downstream of the wall impingement point, but similar in other respects to a conventional (not EGR diluted) heavy duty diesel engine, in that there was a negative ignition dwell and a mixing controlled burn. The results in general highlight the need to develop a conceptual model for combustion in light-duty not EGR-diluted diesel engines, and makes some progress in this direction. One feature that appears essential to understand combustion in this regime is that the effect of the jet-wall and flame-wall

interactions are significant, and the resulting flow and structures are significantly more complicated than the simple free jet concept of Dec's original conceptual model [45; 115].

Chapter 6

Effect of injection pressure on the combustion development in an automotive-size diesel engine

One of the key trends in development of diesel engines is the continuing increase of fuel injection pressure [31]. Fuel injection pressure can substantially influence combustion development and emissions in a number of ways. Most importantly, higher pressures increase rates of fuel evaporation and fuel-air mixing, leading to lower soot and NO_x emissions. Higher pressures also result in higher fuel jet velocities and lower Damköhler numbers, and thus longer lifted-lengths, which also leads to more fuel-air premixing prior to combustion. For these reasons, many experimental studies have been carried out to understand injection pressure effects [34; 54; 132; 148]. Further details about some related experimental and numerical studies are given in Chapter 2.

Fuel-injection pressure effects become particularly complicated in small-bore engines due to the presence of the wall, which as shown in Chapter 5, results in complex jet-wall interacting flows which significantly influence combustion development and emissions but are not particularly well understood. It is unclear at this stage how well CFD models can capture these features. Therefore, in this chapter, the effect of injection pressure is modelled and compared with experimental data from the in-house optical engine. Similarly to Chapter 5, the

modelled pressure traces are first compared with the experimental data. This is followed by comparisons and analysis of the optically measured in-cylinder data, including the first stage chemiluminescence and second-stage OH chemiluminescence and PLIF as compared with the experiments, and further analysis of the modelling results focussed on understanding the effect of injection pressure on the combustion development.

6.1 Engine operating conditions and modelling

The effect of injection pressure was studied experimentally. The start of fuel injection and total injected fuel-mass of 10 mg were held fixed. This resulted in reduced the injection duration and increased the fuel flow rate with the increased injection pressure. The higher flow rate and shorter injection duration affects the rate of mixing of the evaporated fuel and then the development of combustion. The injection pressures considered in the experiment were 100 and 130 MPa, in addition to the baseline injection pressure of 70 MPa studied in Chapter 5. The numerical study was also extended to 160 MPa injection pressure, for which only in-cylinder pressure and heat release rate data from the experiment were available. In all cases, the experimentally measured injection profile was used in the modelling. A single hole of the injector was used, as in the baseline condition, and the relative position of the jet was also same as shown in Fig. 5.2. The modelling used the same reaction mechanism and combustion model as used for the baseline case in Chapter 5. The important operating conditions are given in Table 6.1.

Table 6.1: Important operating conditions for 100, 130 and 160 MPa injection pressure cases.

Number of injector holes used	1
Injected fuel mass	10 mg
Rail pressure	100, 130, 160 MPa
Actual start of fuel injection	-7° CA aTDC
End of injection with 100 MPa	7.5° CA aTDC
End of injection with 130 MPa	6.5° CA aTDC
End of injection with 160 MPa	5.5° CA aTDC

6.2 In-cylinder pressure and heat release rate comparison

The comparisons of in-cylinder pressure and apparent heat release rate calculated using Eq. (3.46) at injection pressures of 100, 130 and 160 MPa are shown in Fig. 6.1. As shown in Table 6.1, the injection of fuel ends at 7.5, 6.5 and 5.5° CA aTDC, with injection pressures of 100, 130 and 160 MPa, respectively.

The predicted in-cylinder pressure during combustion compares remarkably well with the experimental pressure trace at all injection pressures. As shown in Fig. 6.1d, the crank angle position of start of combustion pressure rise shifts towards the top dead centre (TDC) with the increase of injection pressure. This crank angle position almost coincides with the end of injection for all injection pressures.

In the simulations, a small drop in heat release rate may be observed from the start of fuel injection (see Fig. 6.1d) up to a crank angle where the heat release rate due to the first-stage combustion overcomes the heat absorbed during the evaporation of fuel. The point of start of positive heat release rate is around 3° CA aTDC for all of the considered injection pressures. There is a trend towards slightly earlier and larger cool flame heat release towards higher injection pressures. This will be later shown to be consistent with cool flame chemiluminescence in the experiments and formaldehyde in the modelling. This heat release trend would be more pronounced but for the larger fuel evaporation rates and thus more evaporation cooling offsetting a larger cool flame heat release at higher injection pressures. In the simulations, a small dip in the heat release rate for injection pressures of 100, 130 and 160 MPa was also observed due to the so-called “negative temperature coefficient” effect after the local peak due to the first-stage combustion and before the start of rise in heat release rate due to the second-stage combustion. This was not very obvious in the baseline case because of relatively longer injection duration. The effects of evaporation cooling and low temperature heat release are less evident in the experiments. This may be a result of the required smoothing or the small sample size of 20 cycles. The evaporation cooling is certainly smaller than the observed fluctuations of the AHRR in the experiments before ignition. The low temperature heat release is

somewhat larger, and it is possible that the model does not capture the effects of cycle to cycle variations for this, which may spread out the heat release resulting in a less distinct low temperature heat release peak.

The experiments and models both show that as the injection pressure is increased, the crank angle position of peak heat release rate moves towards the TDC, the peak heat release rate becomes higher, and the total burn duration becomes shorter. These features are consistent with an earlier and more intense premixed burn and a reduced importance of mixing-controlled combustion as injection pressure is increased.

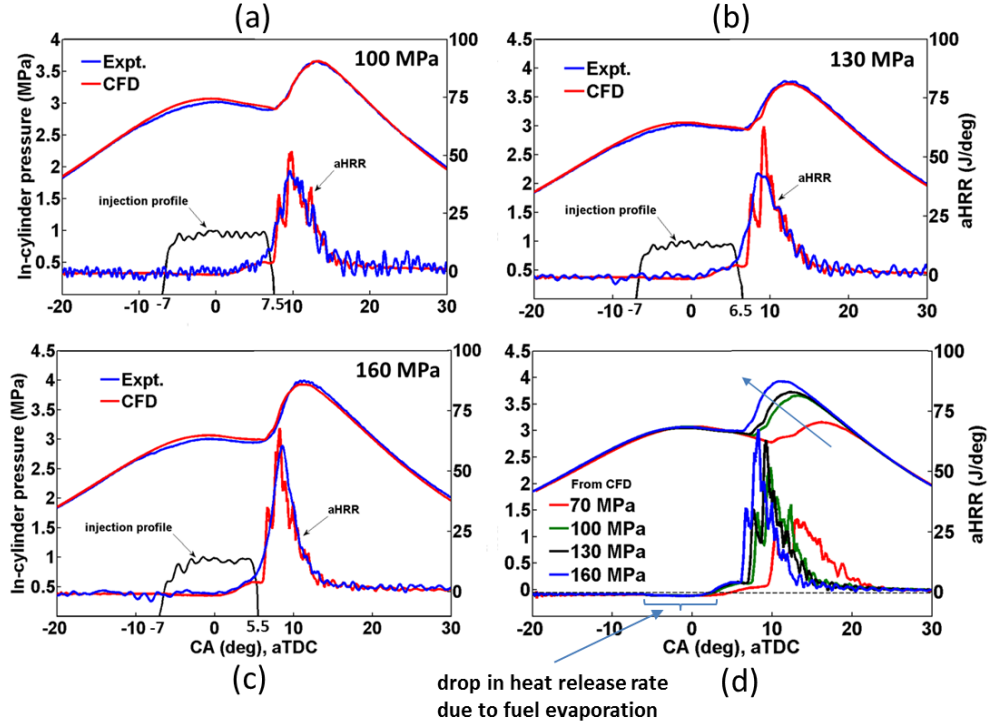


Figure 6.1: Comparison of pressure and apparent heat release rate at 100, 130 and 160 MPa of injection pressure.

6.3 Jet-tip penetration comparison

The calculated jet-tip penetration lengths as defined in section 5.2 from the simulations are compared with the experimental penetration lengths from fuel PLIF in Figs. 6.2a and b. The definition that demarcates the regions of the up-swirl side and the down-swirl side as used in section 5.2 is also used here. The jet-tip penetration length from the experiment is only available for 100 and 130 MPa injection pressures. In Figs. 6.2c and d, penetration lengths from the simulation on the up-swirl and the down-swirl sides are compared between the modelled results for different injection pressures.

As shown in Figs. 6.2a and b, the model shows only a small difference between the two sides and the model results generally fall between the experimental results on the up-swirl and down-swirl side. The averaged penetration over both sides is reasonably well captured. However, in the experiment, at the both 100 and 130 MPa injection pressures, and for 70 MPa in Chapter 5, Fig. 5.1, there is a clear and considerable difference between the penetration lengths on the up-swirl side that sees opposing swirl and the down-swirl side, which sees favouring swirl. This effect was not captured in the modelling. On the up-swirl side the penetration length is over-predicted in the simulations at both the injection pressures. For 130 MPa injection pressure it lies within the standard deviation band calculated from 20 firing cycles. On the down-swirl side, the calculated penetration length from the simulations is under-predicted at 130 MPa injection pressure while the predictions are fairly good at 100 MPa injection pressure. As mentioned in section 3.2.7.2 of Chapter 3, as opposed to the conventional practice of specifying a nominal swirl number, the modelling resolved the intake ports in an attempt to better capture the flow inside the engine. Despite this, it appears that the swirl effect is underestimated by the modelling. Further investigations on this point in the future would be interesting, particularly if velocity data were available in the experiments.

The increase of injection pressure (with same mass of injected fuel) increases jet velocity and thus jet-tip penetration length. This increase of penetration length, as shown in Figs. 6.2c and d, is captured well in the simulations both on the upswirl and the down-swirl sides. However, with 160 MPa injection pressure,

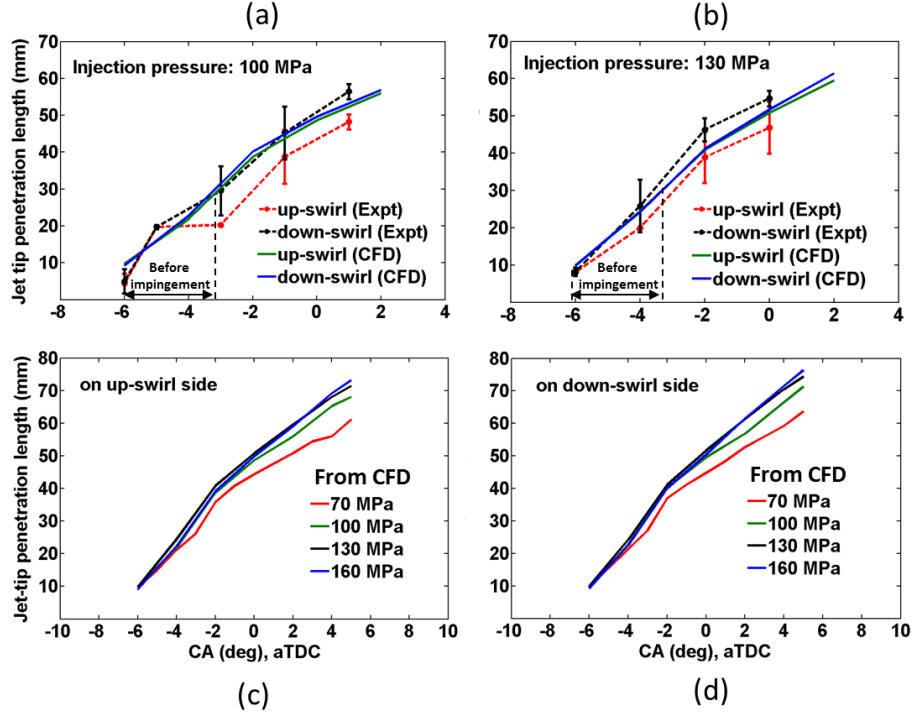


Figure 6.2: Comparison of jet-tip penetration length at 100, 130 and 160 MPa of injection pressure.

the jet-tip penetration length is initially slightly less than the length with 130 MPa injection pressure. This is due to the low rate of injection during the first few crank angles in 160 MPa injection pressure case compared to the other injection pressure cases (see Fig. 6.1c).

The difference in penetration lengths with injection pressures is also seen in fuel mass fraction contours taken in a plane at 7 mm from fire deck as shown in Fig. 6.3 at -4, 0 and 4° CA aTDC for all the injection pressures. The yellow dotted arc in all the images is the field of view margin in the experiment. The third row of the figure shows the extent of fuel consumption in the first-stage of combustion near the jet-axis after the impingement on the bowl-wall at 4° CA aTDC (shown in encircled black regions). The area of the region where first-stage combustion occurs increases with the injection pressure, corresponding to the larger amount of fuel injected up to the given crank angles in each image,

and the faster mixing rate of the evaporated fuel with air. The advancement of the first-stage combustion is further analysed with the help of cool-flame period chemiluminescence images from the experiment in the next section.

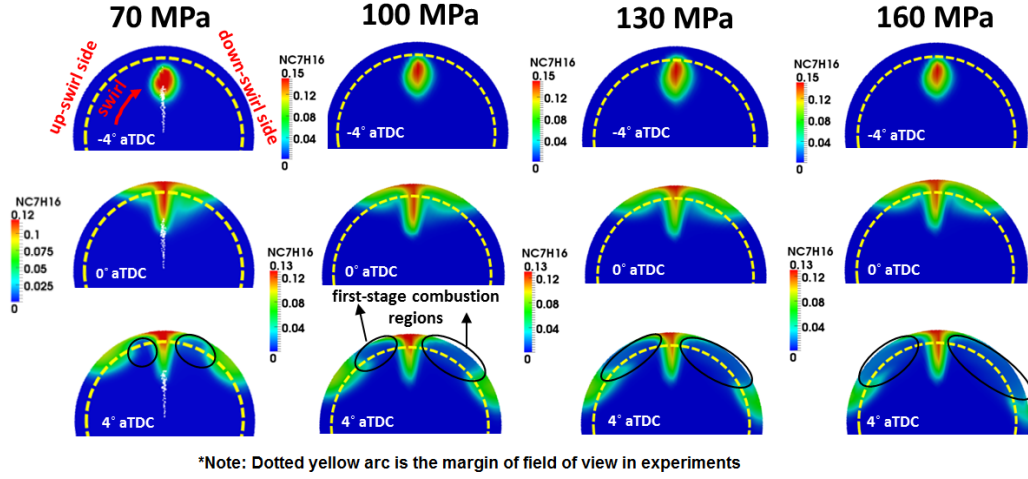


Figure 6.3: Comparison of fuel mass fraction contours in a plane at 7 mm from fire-deck from CFD at 70, 100, 130 and 160 MPa of injection pressure.

6.4 Cool-flame period

The cool-flame period is the period of the first-stage combustion. In the experiment, this period is identified by chemiluminescence of the first-stage species such as CH, CO and formaldehyde (CH_2O) emitted over a broad wavelength ranging from 360 nm to 560 nm (see in section 4.2.1). These line of sight chemiluminescence images from the experiment at 3°, 5° and 7° CA aTDC with the injection pressures of 100 and 130 MPa are compared with corresponding line of sight images of CH_2O mass fraction from the simulations in Fig. 6.4. In Fig. 6.5, line of sight images of CH_2O from the simulations at the same crank angles with 160 MPa injection pressure are also presented. In Fig. 6.4, the top two rows are with 100 MPa injection pressure and the two bottom rows are with 130 MPa injection pressure. The white curve in all the images is the stoichiometric mixture fraction contour and the yellow dotted line is the field of view margin in the experiment.

As can be seen, at 3° CA aTDC, very weak luminosity is seen on both sides of the jet with 100 MPa injection pressure which signifies that the first-stage combustion has just started whereas with 130 MPa injection pressure, the chemiluminescence is brighter on both the sides. This shows that the first-stage combustion has started marginally earlier at 130 MPa injection pressure compared to 100 MPa injection pressure. The simulations agree well with the experiments in this respect, as they show a similar increase in the concentration of CH₂O at 3° CA aTDC going from 100 to 130 MPa injection pressure. The chemiluminescence and formaldehyde for 70 MPa injection pressure shown in Chapter 5, Fig. 5.7 are lower than for 100 MPa, suggesting that the model captures the effect of injection pressure on the onset of cool flame activity well. The simulations suggest these trends would continue to 160 MPa injection pressure.

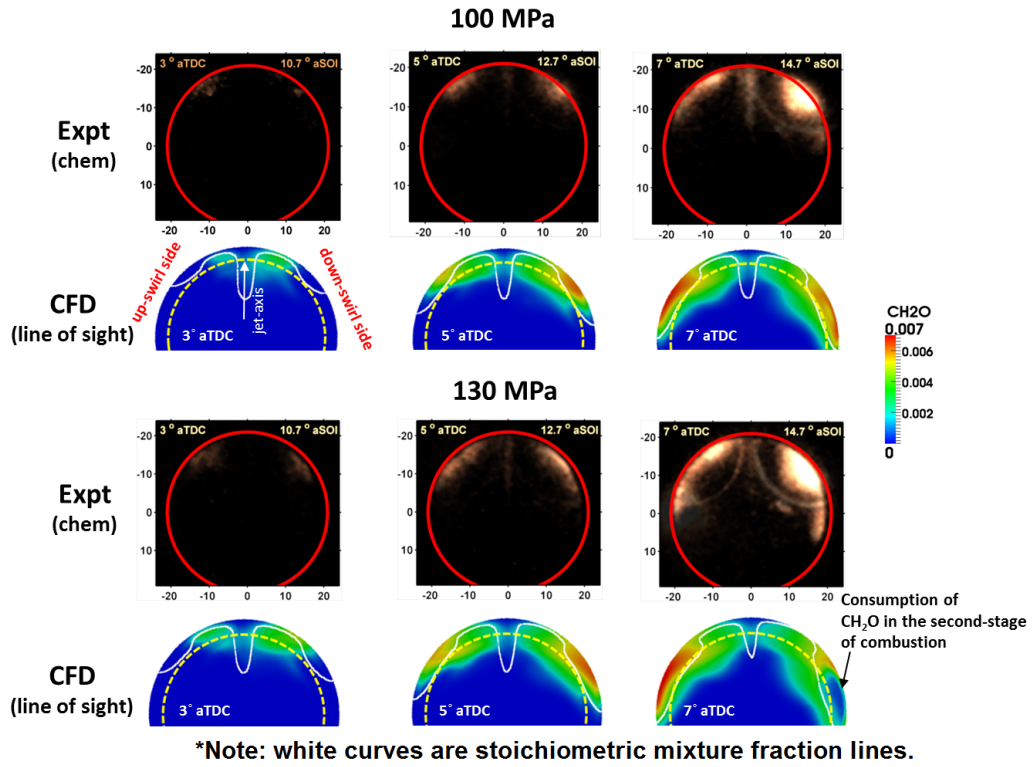


Figure 6.4: Comparison of cool-flame period chemiluminescence from the experiment and line of sight CH₂O contours from CFD at 100 and 130 MPa of injection pressure.

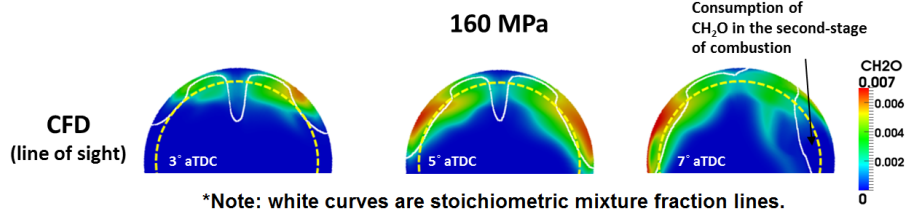


Figure 6.5: Line of sight CH_2O contours from CFD at 160 MPa of injection pressure.

By 7° CA aTDC, the increase in the brightness of chemiluminescence in the experiment and CH_2O concentration in the simulations shows the progress of the first-stage combustion at all injection pressures. Consumption of CH_2O in the simulations on the down-swirl side is noticeable at 160 MPa injection pressure and to a lesser extent at 130 MPa, conveying that the second-stage combustion has also started by 7° CA aTDC in the model. As can be seen, in both the model and experiments, the first-stage combustion has only started in the regions of the fuel jet that are downstream of the bowl-wall impingement point and along the bowl wall, similar to what was observed in the baseline case (70 MPa injection pressure shown in Fig. 5.7). It is noted that that in both model and experiment, for all the injection pressures, the cool flame activity is more advanced on the down-swirl side. The model and experiment also agree well with the observed that higher injection pressure causes a more advanced cool flame activity. In summary the model can capture the timing, location, and effect of fuel injection pressure on the cool flame activity reasonably well.

The relative advancement of combustion with the injection pressure is further analysed with the help of a mass split study between the jet-axis region and the post wall impingement regions on the up-swirl and the down-swirl sides, as shown in the schematic in Fig. 6.6, representing the division of the domain into four zones which will be analysed separately. In the schematic, the zone labels with sub-script '*u*' represent zones on the up-swirl side while labels with the '*d*' sub-script represent zones on the down-swirl side. The zones with letter '*A*' label cover the evaporated fuel near the jet-axis up to a normal distance of 8.5 mm from the jet-axis on either side of the jet and the other two zones with label '*B*'

cover the evaporated fuel along the bowl-wall on both sides of the jet away from the jet-axis.

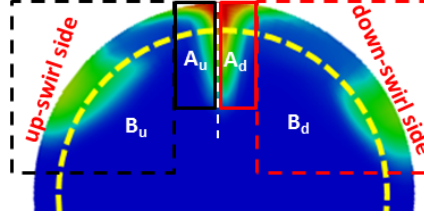


Figure 6.6: Schematic representation of zones for mass split study.

The percentage mass of the mixture corresponding to elemental mass originating in the fuel, calculated from the local mixture fraction (which accounts for partly burned fuel), is distributed into four zones of the combustion chamber at 4° CA aTDC as shown in Table 6.2. The percentages are shown as fractions of the total injected fuel mass, 10 mg. The chosen crank angle of 4° CA aTDC is chosen as representative of the first-stage combustion period for all the injection pressures. The observations made can be extended to the other crank angles in the cool flame period. As can be seen, with the increase of injection pressure from 70 MPa to 160 MPa, the percentage mass of total evaporated fuel increases from 64 % to 87.5 %, as expected. The percentage of the evaporated fuel near the jet-axis in ‘A’ zones almost remains same, which is also expected downstream of the liquid region in high Reynolds number jets. It is around 18 % on the up-swirl side and around 15 % on the down-swirl side. The increased evaporated fuel for higher injection pressures moves into the ‘B’ zones where the first-stage combustion starts for all the injection pressures as discussed above for 100, 130 and 160 MPa and in section 5.3 for 70 MPa injection pressure. Furthermore, mixture fraction and scalar dissipation rate contours as shown in Fig. 6.7 at 4° CA aTDC suggest the penetration of the moved evaporated fuel into the bowl-wall regions (in ‘B’ zones) increased with the injection pressure as injection velocity increased. Also, the regions of moderate scalar dissipation rate ($\chi \leq 0.2$ as discussed in section 5.5 and shown as encircled black regions in Fig. 6.7) broaden with the increase of injection pressure, which corresponds to the creation of larger mixed regions in which the first-stage combustion can begin. Moreover,

the first-stage combustion is more active in rich regions ($Z \approx 0.085$ or $\phi \approx 1.4$) for all the injection pressures. Similar observations were also made for baseline 70 MPa injection pressure case (see in Fig. 5.7).

Effectively, the increased availability of more evaporated and mixed fuel mass and larger regions of favourable scalar dissipation rate in ‘ B ’ zones with the increase of injection pressure increased the rate of progress of the first-stage combustion. It also advanced the start of the first-stage combustion with respect to the start of the fuel injection (i.e. -7° CA aTDC), which is evident in cool-flame period chemiluminescence and line of sight CH_2O images in Figs. 6.4 and 6.5. This is consistent with the increase of average temperature at 4° CA aTDC with injection pressure (see Table 6.2), confirming the increase of rate of progress of the first-stage combustion. This further influences the early start of the second-stage combustion as discussed in the next section.

Table 6.2: Percentage split of evaporated fuel between different zones at 4° CA aTDC.

Inj. pressure	Total evapo- rated fuel	¹	A_u	B_u	A_d	B_d	Avg. temper- ature (K)
70 MPa	64 %		17.5 %	12.6 %	15.3 %	18.6 %	769.4
100 MPa	76 %		18.2 %	18.8 %	15.0 %	24.0 %	790.4
130 MPa	82.3 %		18.4 %	22.3 %	14.4 %	27.2 %	795.6
160 MPa	87.5 %		19.2 %	24.2 %	15.1 %	29.0 %	801.2

6.5 Main combustion period

The main combustion period in the simulations is taken from the point where first appearance of high concentration of is seen. Such first appearance of second-stage OH on the up-swirl and the down-swirl sides from the simulations in a plane at 7 mm from fire deck is shown in Fig. 6.8. As can be seen, the first row corresponds to the first appearance of OH on the down-swirl side and the second row gives the first appearance of OH on the up-swirl side at different injection pressures. The crank angle position of each contour is shown in the bottom portion of every image. As highlighted in section 5.5 for baseline case

¹All percentages are expressed in terms of total injected fuel mass (10 mg).

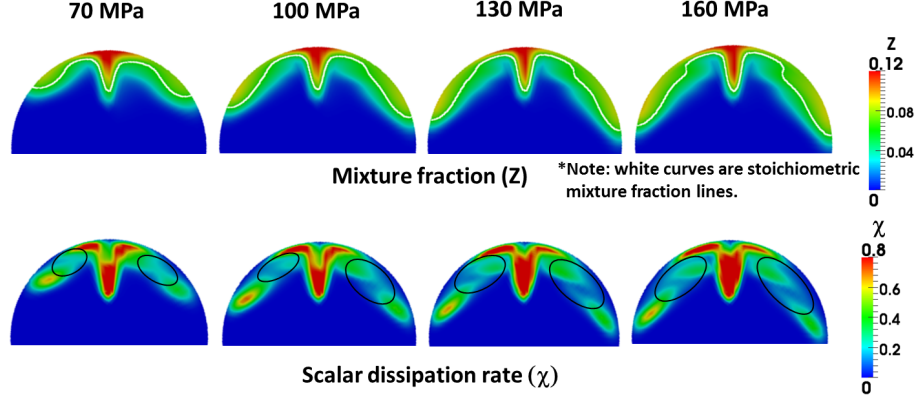


Figure 6.7: Contours of mixture fraction (Z) and scalar dissipation rate (χ) in a plane at 7 mm from fire-deck at 70, 100, 130 and 160 MPa injection pressure and at 4° CA aTDC.

at 70 MPa injection pressure, due to the effect of scalar dissipation rate, the second-stage combustion has not started simultaneously on both sides of the jet for all injection pressures. Instead it started first on the down-swirl side and then with a delay on the up-swirl side. As shown in the first row of Fig. 6.8, at 100 MPa injection pressure, the combustion starts at around 7.5° CA aTDC at 100 MPa and is advanced by 0.5° CA towards TDC with the 30 MPa increases of injection pressure. This advancement is due to a greater progress of the fuel jet along the bowl wall, creating larger regions of favourable equivalence ratios and scalar dissipation rate. These effects directly impact the second stage ignition but also advanced the progress of the first-stage, which obviously has influenced the second-stage too (section 6.4). After a delay of almost 1.5° CA at all injection pressures, the second-stage combustion starts on the up-swirl side (shown in the second-row of Fig. 6.8).

As mentioned in chapter 4, the fuel used in the experiment was diesel and because of fluorescence interference from other species, second-stage PLIF images were taken from 9° CA aTDC at injection pressures of 100 and 130 MPa. Online ensemble averaged OH PLIF images are used for comparison. The comparison is done in planes at 5, 7 and 10 mm from fire-deck with the corresponding OH mass fraction contours from the simulations. As shown in Fig. 6.9, at 100 MPa

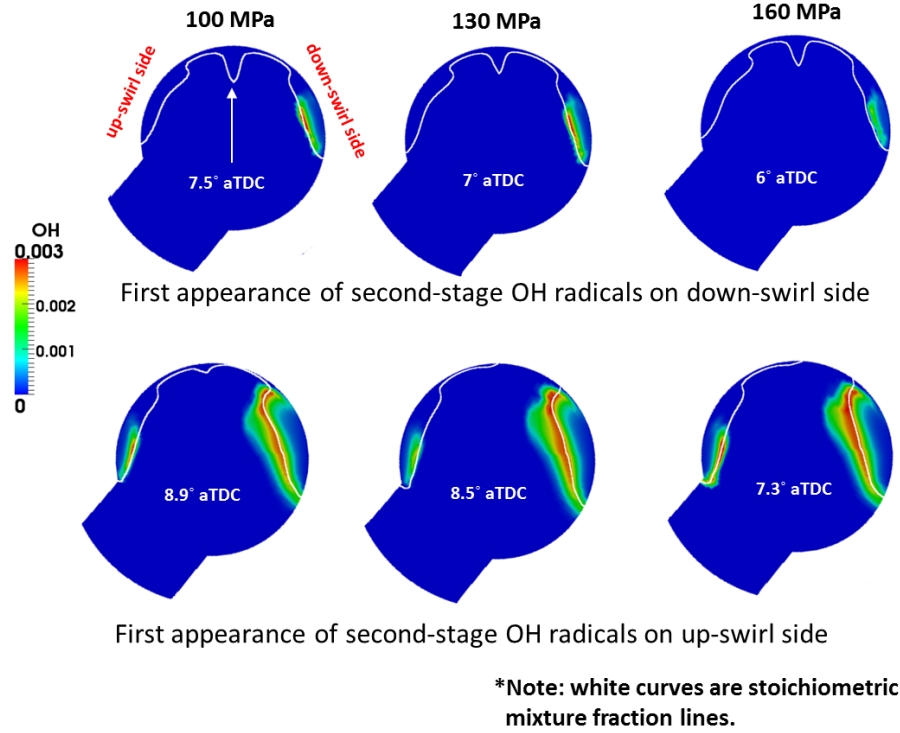


Figure 6.8: First appearance of second-stage OH radical concentration from CFD at 100, 130 and 160 MPa injection pressure in a plane at 7 mm from fire-deck.

injection pressure, the comparison is done at 9° CA aTDC in top two rows and 11° CA aTDC in bottom two rows. The last column shows the comparison of ensemble average OH* chemiluminescence from the experiment and line of sight OH* mass fraction contours from the simulations.

In the model, the OH* images are shown in Fig. 6.9 for 100 MPa injection pressure suggest that second stage combustion is well underway on the down-swirl side and just beginning on the up-swirl side, both well off the jet axis. For the information, the simulated mass fraction of OH* is in the order of 1e-12 at all the injection pressures. The experimental OH* is generally consistent with these points, with a much brighter signal on the down-swirl side and a dimmer but still noticeable signal on the up-swirl side. The experimental and model OH* at 11° CA aTDC show significantly expanded regions of combustion occurring on both sides of the jet.

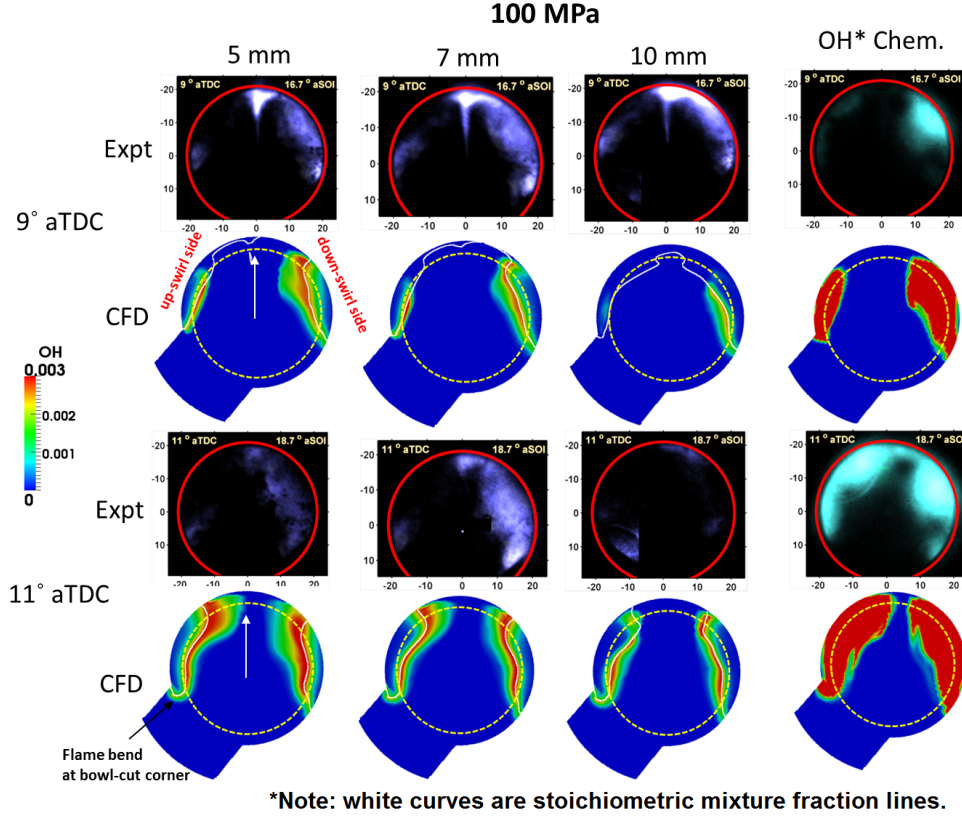


Figure 6.9: Comparison of OH PLIF and OH* chemiluminescence from experiment and OH and OH* mass fraction contours from simulations at 100 MPa injection pressure in planes at 5, 7 and 10 mm from fire deck at 9° and 11° CA aTDC.

Looking at the OH mass fraction images, at 9° CA aTDC in the simulations, a strong concentration of OH is seen on the down-swirl side in all the planes. On the up-swirl side the region of high concentration is much smaller across all planes and hardly present at the 10 mm plane. The experimental OH PLIF also exhibits strong signals on the down-swirl side across all planes, consistent with the modelling. The strong signals near the jet axis are however probably due to fuel fluorescence, as discussed in Chapter 5. On the up-swirl side, the experiments show a region of no signal between the jet impingement point and a brighter region towards the jet head along the wall. The interpretation of the brighter re-

gion as high temperature combustion is not clear, as it could also be fluorescence from fuel at the jet head in the high scalar dissipation region which may have not yet undergone the first stage ignition. Recall that the modelling shows that the first stage ignition, which may break down fuel aromatic components, proceeded initially in the lower dissipation region behind the jet head, thus possibly explaining the region of a low fluorescence signal between the bright spot and the jet impingement point. This region of no signal seems to correspond with the dim chemiluminescence region in the experimental OH*, suggesting this region could still be still undergoing first stage ignition and the chemiluminescence is not due to OH* but species involved in the first stage.

By 11° CA aTDC, the second-stage combustion becomes strong even on the up-swirl side in both the experiments and modelling. The model OH* mass fraction and experimental OH* chemiluminescence are consistent in terms of the regions of high values. Notably, the model and experiment agree that combustion mainly occurs off the jet axis. The model is also generally consistent with the experimental OH PLIF on the 5mm and 7mm planes and on the down-swirl side, while the model seems to over predict the combustion progress near the bottom of the bowl on the 10mm plane, which is possibly due to errors in the heat transfer prediction owing to its proximity to the wall. The experimental OH PLIF images show a region of low signal on the up-swirl side for all planes. The reason for low signal on the up-swirl side could be due to laser sheet attenuation caused by combustion products entering into bowl-cut region. Schematic representation of laser sheet attenuation problem with signal attenuated area is shown in Fig. 6.10. The existence of predicted OH and OH* concentration near bowl-cut entry on the up-swirl side at 11° CA aTDC in all the planes confirms that the combustion products in the region can cause laser sheet attenuation and in turn low signal in the effected area.

Along similar lines, for 130 MPa injection pressure case the images from the experiment and the simulations are presented at 9° and 10° CA aTDC in Fig. 6.11. In the fourth column from OH* distribution comparison, line of sight OH* mass fraction contours from the simulations compare well with OH* chemiluminescence images from the experiment at both the angles and convey that the second-stage combustion is strongly going on both sides of the jet-axis. Compar-

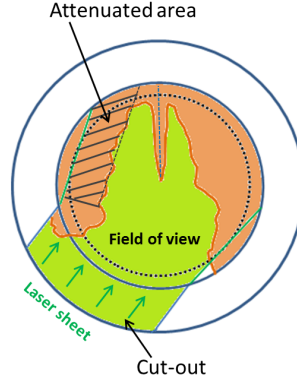


Figure 6.10: Schematic representation of laser sheet attenuation.

ing to Fig. 6.9, the second stage combustion is more advanced for 130MPa and this sensitivity is captured well by the model. These observations are supported by the presence of OH in the simulations in all the planes both on the up-swirl and the down-swirl side at both the angles. In the ensemble average OH PLIF images, fluorescence due to OH is seen in a broad area on the down-swirl side at both the angles which are consistent with the modelling. On the up-swirl side, similar to the 100MPa case, there is a region of low signal between the fuel impingement point and a bright patch which is near the leading edge of the jet according to the modelling. The model predicts there should be OH in this region. However, once again the lack of OH in the experiments is inconsistent with the OH* chemiluminescence. Again the reason for this could be laser sheet attenuation effect as seen with 100 MPa injection pressure.

At 160 MPa injection pressure, experimental PLIF and chemiluminescence data are not available, so the numerical simulations only are analysed. This is considered reasonable since the comparisons with the optical data at 100 and 130 MPa injection pressure were fairly good, and a good comparisons of the heat release profile was also confirmed. Fig. 6.12 shows the modelled OH and OH* at 8° CA aTDC and at 11° CA aTDC. The presence of strong concentrations of OH on either side of the jet-axis indicates that the second-stage combustion is in advanced stage at both the considered angles. Interestingly, high concentrations of OH on both sides of the jet are seen even at 8° CA aTDC, as the first appearance

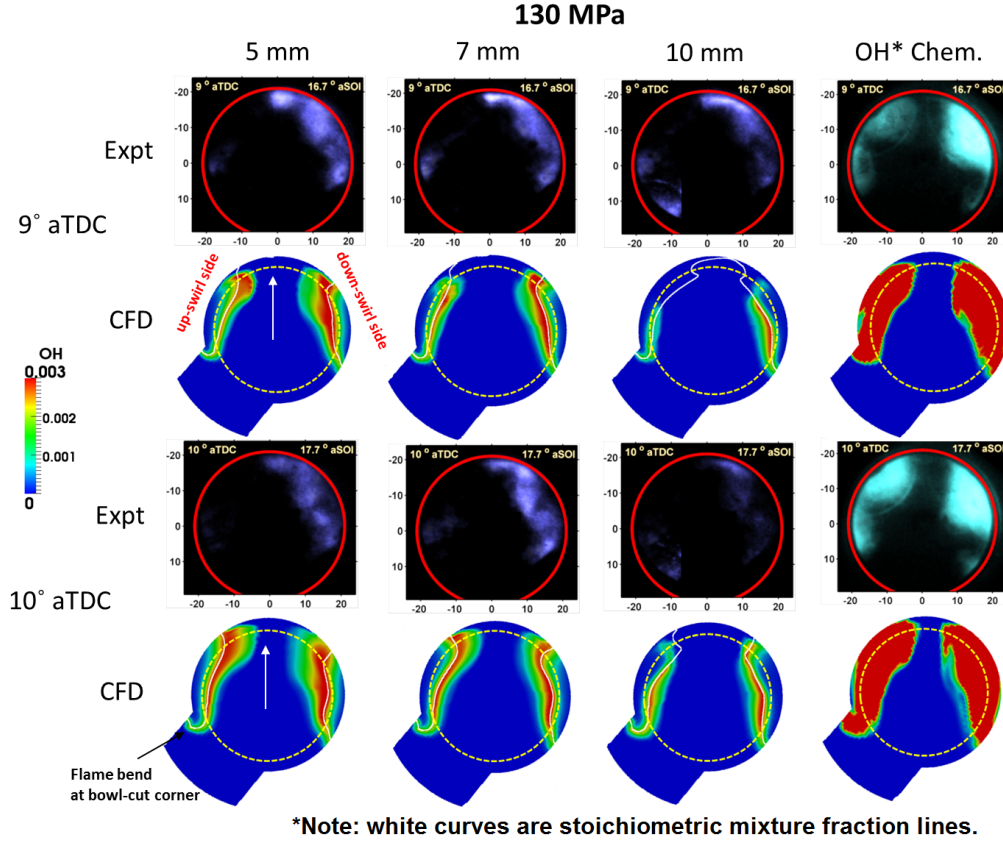


Figure 6.11: Comparison of OH PLIF and OH* chemiluminescence from experiment and OH and OH* mass fraction contours from simulations at 130 MPa injection pressure in planes at 5, 7 and 10 mm from fire deck at 9° and 10° CA aTDC.

of second-stage OH concentration is seen at 6° and 7.3° CA aTDC on the down-swirl and the up-swirl sides respectively (see Fig. 6.8). The modelling results for 160 MPa further support a continuing trend of earlier combustion phasing with increasing injection pressure, as compared with the earlier results for 70–130 MPa.

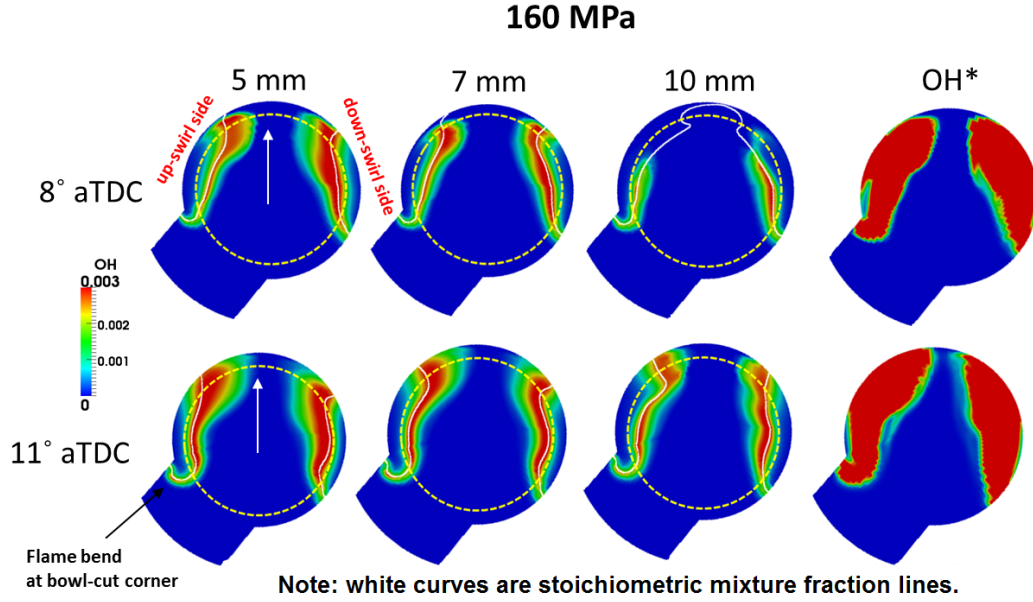


Figure 6.12: OH and OH* mass fraction contours from simulations at 160 MPa injection pressure in planes at 5, 7 and 10 mm from fire deck at 8° and 11° CA aTDC.

6.5.1 Re-entrainment study

The increase of injection pressure reduced the fuel injection period for the same amount of fuel mass injected. As a result, for 100, 130 and 160 MPa injection pressures, the start of the second-stage combustion was observed after the end of injection (see Table 6.1 for injection periods and c.f. Fig. 6.8). Furthermore the combustion occurred away from the jet-axis. So, the re-entrainment of hot combustion products is not possible during the second-stage of combustion at 100, 130 and 160 MPa injection pressures. Re-entrainment of first-stage combustion products may be occurring in the cool-flame period. However, even during this period, as shown in Fig. 6.4, there is no sign of initiation of combustion along the jet-axis. This is probably due to the high fuel-jet velocity and strain rate/scalar dissipation rate will be high along the jet-axis. Combustion eventually proceeded towards the jet-axis only after the end of the fuel injection at all injection pressures.

6.6 Combustion development study in mixture fraction space

Combustion development from the entire domain is studied with the help of heat release rate (Q J/s) scatter plots in mixture fraction space. As shown in Fig. 6.13, the scatter plots are presented for injection pressures of 100, 130 and 160 MPa at 3°, 7° and 11° CA aTDC, representing the timings spanning the first-stage and the second-stage combustion. Also, heat release rate conditionally averaged with respect to mixture fraction ($\langle Q|Z \rangle$ J/s) is shown to identify the main regions in which combustion occurs. The first row corresponds to 100 MPa injection pressure, the second and the third correspond to 130 and 160 MPa injection pressure, respectively. In all plots, green dots represent heat release rate from the up-swirl side while blue dots represent the down-swirl side. Red lines show the conditional average values on the up-swirl side and black lines show them on the down-swirl side.

As can be seen in Fig. 6.13, at 3° CA aTDC, heat release is predominantly happening around rich mixtures ($Z \approx 0.1$) at all the injection pressures. The maximum Q and $\langle Q|Z \rangle$ values increase with injection pressure and the peak Q is not greater than 100 J/s. These features signify that the first-stage combustion is going on at 3° CA aTDC at all the injection pressures and is predominantly occurring in rich regions on both sides of the jet-axis. Furthermore, as observed from the earlier plots (see in Fig. 6.4), the progress of the first-stage combustion increases with injection pressure. The maximum heat release rate (Q) on the down-swirl side is greater than on the up-swirl side at all the injection pressures, which as discussed earlier is because of favouring swirl that provided broad area of favourable equivalence ratios and moderate scalar dissipation rate ($\chi \approx 0.2\text{s}^{-1}$) as shown in Fig. 6.7.

At 7° CA aTDC, different combustion regimes are seen at the different injection pressures. At 100 MPa injection pressure, peak values of Q are 54.0 and 200 J/s on the up-swirl and the down-swirl sides respectively and the main heat release rate is happening around rich mixtures. This shows that the first-stage combustion is mainly going on. At 130 MPa injection pressure, on the down-swirl side, the peak Q and $\langle Q|Z \rangle$ values are 3000 and 70 J/s respectively, and

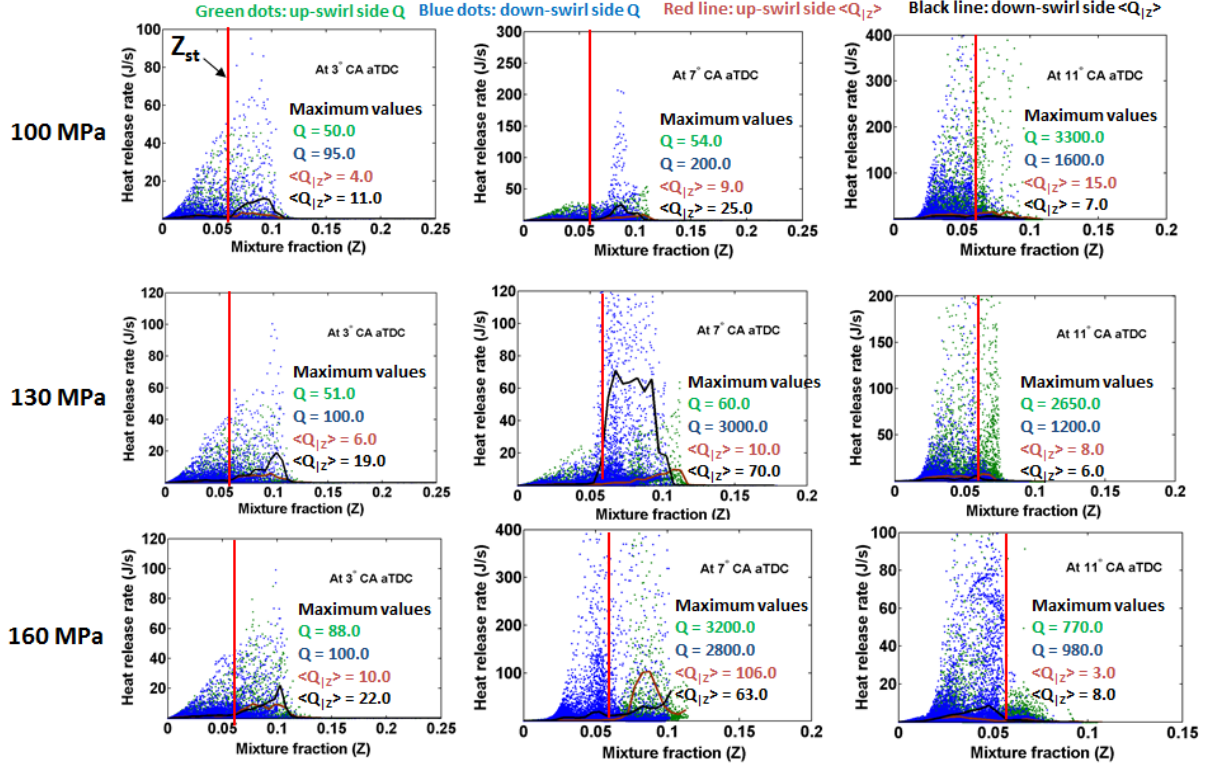


Figure 6.13: Combustion heat release rate study in mixture fraction space from simulations at 3°, 7° and 11° CA aTDC with 100, 130 and 160 MPa injection pressures.

these are occurring in the range of stoichiometric to rich mixtures. The values on the up-swirl side are lower, with peak Q and $\langle Q|Z \rangle$ values are 60 and 10 J/s , respectively, with the conditional heat release peaking on the rich side. This shows that the premixed-burn phase of the second-stage combustion is going on the down-swirl side whereas on the up-swirl side the first-stage combustion is still active. At 160 MPa injection pressure, the peak values of Q and $\langle Q|Z \rangle$ are 3200 J/s and 106 J/s respectively on the up-swirl side, and the burning mixtures are of intermediate stoichiometry $1 < \phi < 2$, suggesting that the premixed burn phase is underway. In contrast the heat release values are lower on the down swirl side suggesting that the peak release during the premixed burn is over on that side.

At 11° CA aTDC, at all the injection pressures, even though peak Q values are high and occurring around stoichiometric mixtures, the low conditional values show that in most of the locations the combustion is in the mixing-controlled phase (see in Fig. 6.1). Also, the drop in conditional values on either side of the jet-axis from 100 to 160 MPa injection pressure suggests that the entire combustion process has completed at faster rate in the 160 MPa injection pressure case.

The below paragraph has been added in response to comments from Examiner-2

In summary, similar to the case of 70 MPa in chapter 5, the up-swirl and down-swirl sides go through distinct phases of first stage combustion, followed by a premixed burn and a mixing-controlled burn. Similar to chapter 5, these stages are phased slightly differently on each side, which as discussed earlier is a result of the effect of swirl. The effect of injection pressure is mainly to increase the importance of the premixed burn relative to the mixing-controlled burn.

6.7 Un-burned hydrocarbons (UHC) and CO emissions

Any escaping CO and UHC after the end of combustion is detrimental to combustion efficiency as well as being undesirable in their own right. All the species that contain both hydrogen and carbon elements are considered as part of UHC. The transient development of UHC and CO from the simulations with 70, 100, 130 and 160 MPa injection pressure up to 55° CA aTDC are compared separately for the up-swirl side and the down-swirl side in Fig. 6.14. The up-swirl side and the down-swirl side regions are the regions as defined in section 6.6.

6.7.1 Un-burned hydrocarbons (UHC)

As can be seen in the first row of Fig. 6.14, both on the up-swirl and the down-swirl sides, the crank angle position of peak values of UHC moves towards top dead centre (TDC) with increasing injection pressure. This is principally because

the fuel injection period reduces for the same amount of total fuel injected (10 mg). After peak, there is a rapid fall in the mass of UHC on both sides of the jet-axis corresponding to UHC consumption in the second-stage of combustion [115; 146] and by 30° CA aTDC with all the injection pressures, the masses reach flat levels and there is no further consumption of UHC. These minimum masses generally reduce with increasing injection pressure on both sides of the jet-axis, which means the fuel burning efficiency increased with the increase of injection pressure. The earlier combustion timing as discussed in the last section, and shorter combustion duration implies the combustion happens closer to TDC when temperatures are higher, thus both allowing more time for UHC conversion and increasing its rate. (The exception to this general trend is that at 130 MPa injection pressure, the left over UHC mass is slightly higher compared to the one at 100 MPa injection pressure. This is presumably connected with slightly different flow structures at these two pressures.)

As shown in Fig. 6.15 for 100 MPa injection pressure, the left over UHC is seen in the squish region where mixture fractions are in the order of 0.01 and temperature is around 1000 K. This conveys that combustion is almost frozen and there will be no further reduction of UHC. A greater mass of UHC was left on the down-swirl side compared to the up-swirl side owing to more fuel and intermediates being diverted towards the down-swirl side due to favouring swirl. The same conclusions can be drawn from the UHC and temperature iso-contours for the other injection pressures.

6.7.2 Carbon monoxide(CO)

As presented in the second row of Fig. 6.14, the crank angle position of peak mass of CO shifts towards TDC with the increase of injection pressure on both sides of the jet-axis as seen for UHC. CO reaches a peak value towards the end of the second-stage of combustion and its consumption starts after the start of consumption of UHC when a pool of OH radicals are produced after H₂O₂ decomposition [115]. For this reason, the start of consumption of CO is delayed compared to UHC. By 50° CA aTDC, the masses reach almost constant levels which reduce with increasing injection pressure, as seen for UHC for the same

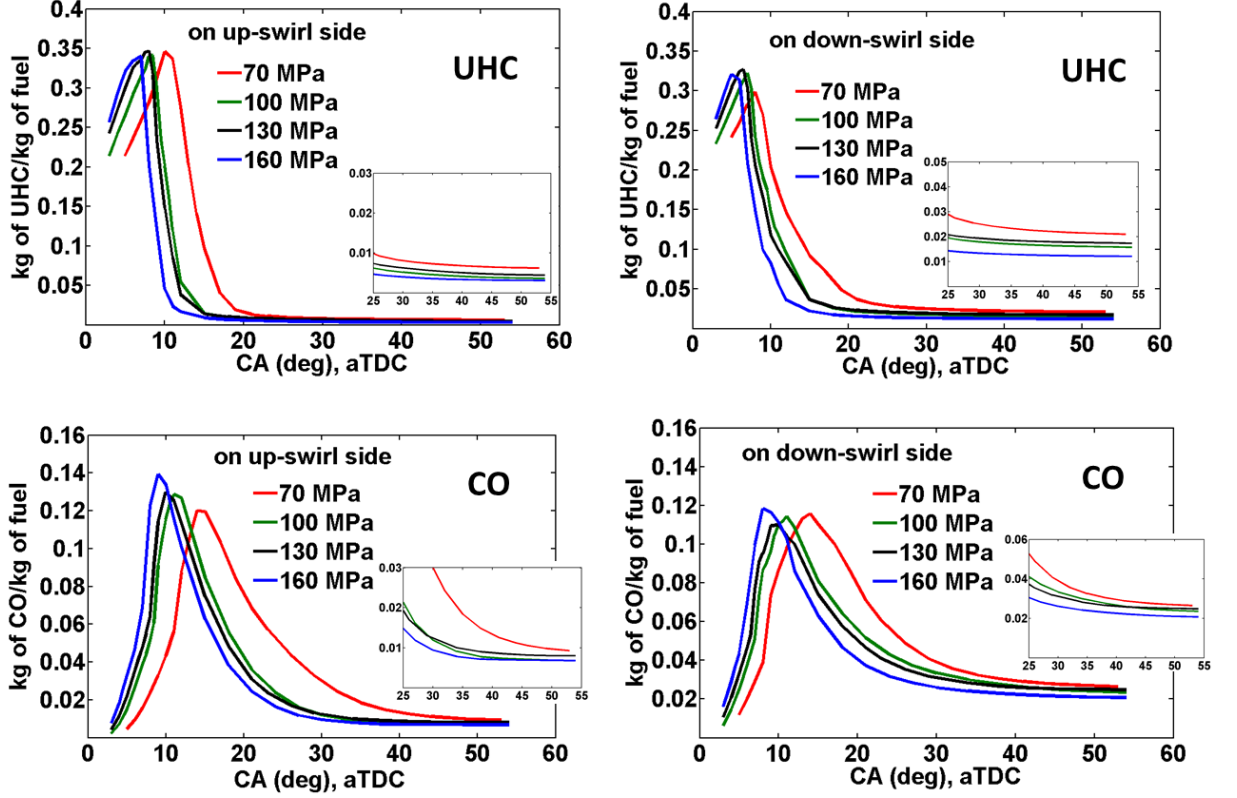


Figure 6.14: Comparison of transient development of un-burned hydrocarbons (UHC) and CO from the simulations with 70, 100, 130 and 160 MPa injection pressure at 55° CA aTDC.

reasons. The minimum values are higher on the down-swirl side compared to the up-swirl side as more mass of fuel goes towards the down-swirl side because of the favouring swirl. The iso-contours presented in Fig. 6.15 show that the left over CO at 55° CA aTDC exists in the squish region where mixtures are very lean ($Z \approx 0.01$) and temperature is in the order of 1000 K which will not support for further progress of combustion into the second-stage.

Parts per million (ppm) values of UHC and CO based on mass fraction are provided in Table 6.3. As shown in Table 6.4, the percentage mass of fuel that is entering into squish region (i.e. the volume above bowl region) out of the total fuel injected (10 mg) calculated using mixture fraction is almost same around 40% for all the injection pressures at 13° CA aTDC. This escaped mass of fuel

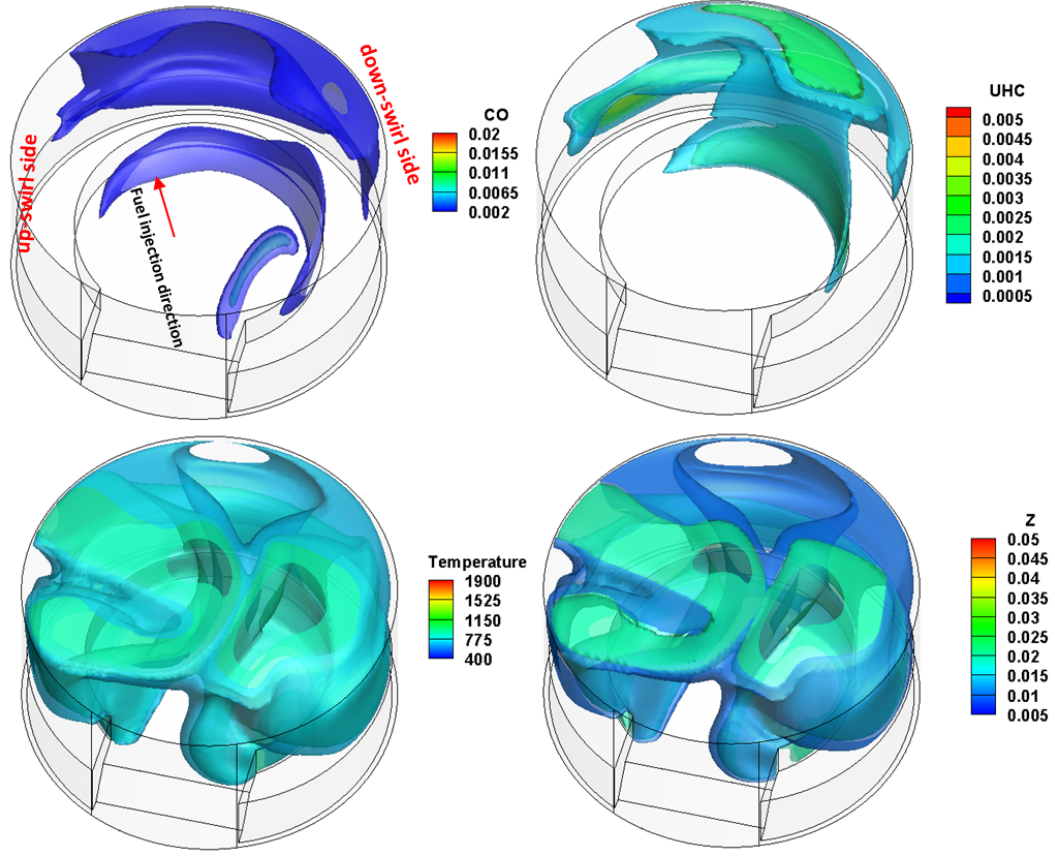


Figure 6.15: Iso-contours of UHC, CO, temperature and mixture fraction from the simulations with 100 MPa injection pressure at 55° CA aTDC.

should not increase further as fuel injection ends for all the injection pressure far before 13° CA aTDC. The increase in the rate of combustion progress with injection pressure has reduced the net UHC and CO left over in the squish region even though the fraction of fuel mass that escaped into the region is the same.

6.8 Development of combustion and comparison with conceptual models

The combustion development at 100, 130 and 160 MPa injection pressure is compared to the conceptual model of the conventional, direct injection diesel com-

inj. pressure	species	up-swirl side	down-swirl side	total
70 MPa	UHC	114	387	501
	CO	171	480	651
100 MPa	UHC	66	277	343
	CO	125	424	549
130 MPa	UHC	81	314	395
	CO	147	461	608
160 MPa	UHC	55	221	276
	CO	123	369	492

Table 6.4: Percentage of fuel/UHC mass escaped into squish region at different injection pressures at 13° CA aTDC.

Inj. pressure	Fuel mass split
70 MPa	44%
100 MPa	41%
130 MPa	41.2%
160 MPa	41.2%

Note: Percentage of squish mass of fuel/UHC expressed as a fraction of total injected fuel (10 *mg*)

bustion in a heavy-duty engine proposed by Dec [45] and the conceptual model of light-duty, late-injection, EGR-diluted, partially premixed low-temperature combustion proposed by Musculus et al. [115]. The two conceptual models are briefly described in section 2.1.

As mentioned in section 5.9, the operating conditions and geometrical parameters in the present optically accessible research engine are different from the actual production engine in passenger cars. Nonetheless it is worthwhile to highlight similarities and differences compared to the conceptual models at the different injection pressures considered here.

- Like in the baseline case, the combustion in the first-stage and the second-stage occurs in the post jet-wall impingement regions along the bowl-wall off the jet-axis where the fuel-air mixture is relatively well mixed with $\phi < 2$. The regions of well mixedness broaden with the injection pressure as a greater fraction of evaporated is available in these regions. The premixed

burn phase becomes more prevalent, with higher heat release rates and shorter burn duration, as injection pressure is increased. This occurrence of premixed combustion is similar to the one observed in EGR-diluted low-temperature combustion. However, it is noted that these conclusions could be affected by differences between the optical engine and a production engine. In production small-bore engines, ambient pressure, temperature and density are higher than observed in the optical engine at all the injection pressures while the injection period may be shorter with multi-hole fuel injection. This could lead to a flame stabilised on the jet axis and closer to the injector, similar to that observed in conventional heavy duty engines.

- Like in the low-temperature combustion model, two distinct heat release rate peaks were observed with a drop in between because of the negative temperature coefficient effect. However, the ignition dwell is very small in all the cases considered, placing it between a high EGR engine which usually has a large positive ignition dwell, and a conventional heavy duty engine which has a large negative ignition dwell.
- A phenomena that is not discussed in either of the conceptual models is that the start of the second-stage combustion is delayed by around 1.5° CA on the up-swirl side compared to the down-swirl side (see in Fig. 6.8) with all the injection pressures. It is argued with occurs because of different turbulent scalar dissipation rate experienced by the up-swirl and the down-swirl sides. Clearly, this is a feature that could be substantially different when multi-hole injectors where jet-jet interactions would probably dominate over swirl effects.

6.9 Conclusions

The effects of fuel injection pressure were studied using CFD modelling of a small bore diesel engine, with the following findings:

- The model was able to reproduce the experimental pressure traces at different injection pressures remarkably well, without any ad hoc adjustments of

the model parameters between the different injection pressures. Increased injection pressure was found to advance the start of combustion, advance the timing of the peak heat release rate, increase the magnitude of the peak heat release rate, and decrease the combustion duration.

- The model was able to reproduce the experimental fuel jet penetration reasonably well if averaged over both sides of the jet. The model could predict the effect of fuel injection pressure on increasing the fuel jet penetration length. However, the model could not reproduce the experimentally observed effect of swirl on the jet penetration, which caused lower penetration on the up-swirl side as compared to the down-swirl side. It is possible that the model under-predicts the magnitude of the swirl flow. This question is left for future investigations.
- In cool-flame period, where the first-stage combustion occurs, the line of sight CH_2O contours from the simulations followed the trend seen with chemiluminescence images from the experiment in terms of the timing and locations of cool flame activity. Both the experiment and simulations confirmed the increase of rate of progress of the first-stage combustion with the injection pressure. Additionally, simulations provided new information that more evaporated fuel was available at higher injection pressures in the regions away from the jet-axis downstream of the wall impingement point, where scalar dissipation rate was low enough ($\chi \approx 0.2\text{s}^{-1}$) for the first-stage combustion to start. Also, as seen in baseline case, the first-stage combustion was strongest in rich regions for all the injection pressures.
- The model and experiment agreed well on the timing and location of regions of high temperature heat release as judged by regions of high OH^* mass fraction from the model and chemiluminescence signal from the experiments. The model was able to capture the effect of pressure advancing the onset of high temperature combustion. Comparisons of the model OH and experimental OH PLIF were less clear, in part because the experimental images contained interference from fuel fluorescence, especially at earlier stages. At later stages in the combustion, the model OH mass fraction and

experimental OH PLIF agreed well on the down-swirl side, but on the up-swirl side there was a lack of experimental signal in some regions where OH was expected based on the model and on the presence of OH* chemiluminescence in the experiments. During the second-stage combustion period, the simulations showed the first observation of second-stage OH radical on the down-swirl side advanced by 0.5-1.0° CA with 30 MPa increases of injection pressure. In contrast to the 70 MPa case, the second-stage combustion was found to start after the end of fuel-injection for injection pressures of 100 MPa to 160 MPa. Also, from the simulations, the delay time of 1.5° CA between the second-stage ignition on the up-swirl side compared to the down-swirl side remained same with different injection pressures.

- There was no re-entrainment of hot second stage combustion products into the fuel jet for all the injection pressures considered. There may have been re-entrainment of first stage combustion products, but it was insufficient to cause first stage ignition upstream of the impingement point.
- The increased rate of progress of combustion with injection pressure reduced the net CO and UHC left un-consumed in the region above bowl, even though same fraction of evaporated fuel escaped into the squish region for all the injection pressures.
- The combustion development for all the injection pressures was more similar to a conceptual model developed for EGR-diluted, low-temperature combustion in light duty engines than it was for to a conceptual model for conventional, heavy duty combustion, except for the near-zero ignition dwell.

Chapter 7

Effect of jet-jet interaction on the combustion development in an automotive-size diesel engine

The previous two chapters studied jet-wall-flame interactions in a small bore engine. In addition to these wall interactions, jet-jet interactions are also important in small bore engines, as discussed in the introduction to this thesis, chapter 1. In this chapter, a numerical study of the effect of jet-jet interactions on the combustion development of two diesel fuel jets is covered. At the time of writing, experimental data were not available for comparison. Nonetheless, the good correspondence of the numerical results with the experimental data for the single fuel jet configuration at different injection pressures encouraged a purely numerically study of the jet-jet interaction effect.

7.1 Operating conditions

Two jets of diesel fuel separated by an angle of 102.86° as shown in Fig. 7.1 were considered. The study was carried out with injection pressures of 70 and 130 MPa. To maintain consistency with the single jet studies, the total injected fuel mass was fixed at 10 mg and the start of injection was -7.0° aTDC. In the two-jet cases, the total fuel of 10 mg was equally distributed between the jets (i.e. 5 mg

to the each jet). The important operating conditions are given in Table 7.1. The same modelling approach as in the previous chapters was adopted, including the skeletal mechanism for *n*-heptane combustion developed by Lu et al. [171], the direct-integration combustion model (see section 3.2.7) and the spray model (see section 3.2.5).

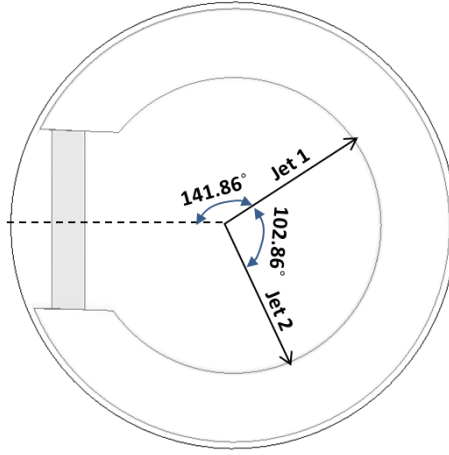


Figure 7.1: A schematic representation of relative position of two jets (viewed from top).

Table 7.1: Important operating conditions for 70 and 130 MPa injection pressure cases.

Number of injector holes used	2
Injected total fuel mass	10 <i>mg</i>
Rail pressure	70, 130 MPa
Actual start of fuel injection	-7° CA aTDC
End of injection with 70 MPa	4.5° CA aTDC
End of injection with 130 MPa	1.0° CA aTDC

7.2 Comparison of in-cylinder pressure and apparent heat release rate from simulations

The simulated combustion in-cylinder pressure rise and apparent heat release rate (aHRR) calculated using Eq. 3.46 under adiabatic conditions are shown in Fig.

7.2. The plots for the two-jet cases at 70 and 130 MPa injection pressure are shown in Fig. 7.2a and the comparison of single-jet and two-jet cases at the same injection pressures from the simulations is shown in Fig. 7.2b. As can be seen, the two-jet injection durations are shorter than all the injection durations with a single jet of fuel (see in Tables 5.1 and 6.1) for the same total mass of injected fuel (10 mg).

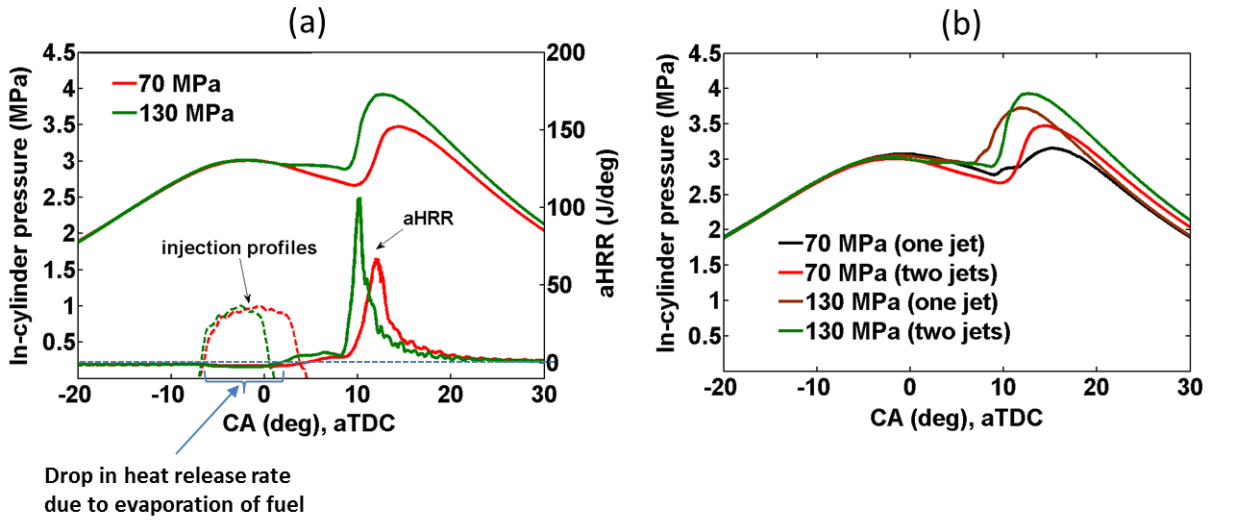


Figure 7.2: Comparison of in-cylinder pressure and apparent heat release rate from the simulations. (a) At 70 and 130 MPa injection pressure with two jets. (b) Comparison with single jet and two jets at 70 and 130 MPa injection pressure.

As shown in Fig. 7.2a, from the start of fuel injection for both the cases (i.e. at 70 and 130 MPa injection pressure with two jets) there is a small drop in the heat release rate due to evaporation of fuel. The drop lasts longer with 70 MPa injection pressure corresponding to the longer injection duration. After this drop, the heat release rate becomes positive due to the first-stage ignition. This occurs just after the end of fuel injection in both cases, while in the single jet cases, the first stage combustion phase overlapped with the later stages of the fuel injection. In principle this allowed more time for mixing before the first stage in the two-jet cases. The first stage period is considerably elongated for the two-jet cases as compared to the single jet cases, (c.f. Figs. 5.1 and 6.1). This is consistent with

burning in generally leaner mixtures, which ignite earlier in the first stage than rich mixtures, but have a longer dwell between ignitions [115]. Furthermore, a clear dip in the heat release rate at the end of the first stage due to the negative temperature coefficient effect is seen after the first-stage heat release for both the cases, as per the single jet cases at 100, 130 and 160 MPa injection pressures, suggesting that most of the cool flame activity is over by the time of the second stage ignition. Another observation comparing the single and two jets cases is that the crank angle position of the start of the first-stage combustion is almost same for the corresponding cases.

The peak heat release timing is retarded in the two-jet 130 MPa case as compared with the corresponding single jet case, while the peak heat release timing for the 70 MPa two-jet case occurs between the peaks of heat release corresponding to ignition the up-swirl and down-swirl sides in the single jet case. The combustion duration is significantly shorter in the two-jet cases for both pressures. The shorter combustion duration leads to higher peak pressures in the two-jet cases compared to the corresponding cases with a single jet. These features are generally consistent with greater premixing in the two-jet cases. Because of the earlier end of injection and elongated first-stage period in the two-jet cases, more mixing occurs, which promotes a larger fraction of rapid premixed burning. The ignition however occurs slightly later because of the overall leaner mixtures. (In the 70 MPa two-jet case ignition occurs later than the down-swirl side in the single-jet case only. This will be investigated further later in the chapter.)

Contours of mass fraction of *n*-heptane and velocity vectors in a plane at 7 mm from the fire-deck are shown in Fig. 7.3 for 70 MPa injection pressure and in Fig. 7.4 for 130 MPa injection pressure. The contours are shown at 1°, 3° and 5° CA aTDC for 70 MPa injection pressure and at -1°, 0° and 1° CA aTDC for 130 MPa injection pressure. The first row in both the figures shows mass fraction contours of *n*-heptane and the second row shows velocity vectors. As shown at 1° CA aTDC in Fig. 7.3, jet 1 is the fuel jet on the left-hand side and the jet 2 is the right hand side jet, when viewed from top. The same terminology is maintained throughout the chapter.

As can be seen, at 70 MPa injection pressure, by 1° CA aTDC, evaporated fuel from both the jets impinges on the bowl-wall and by 5° CA aTDC, jet-jet

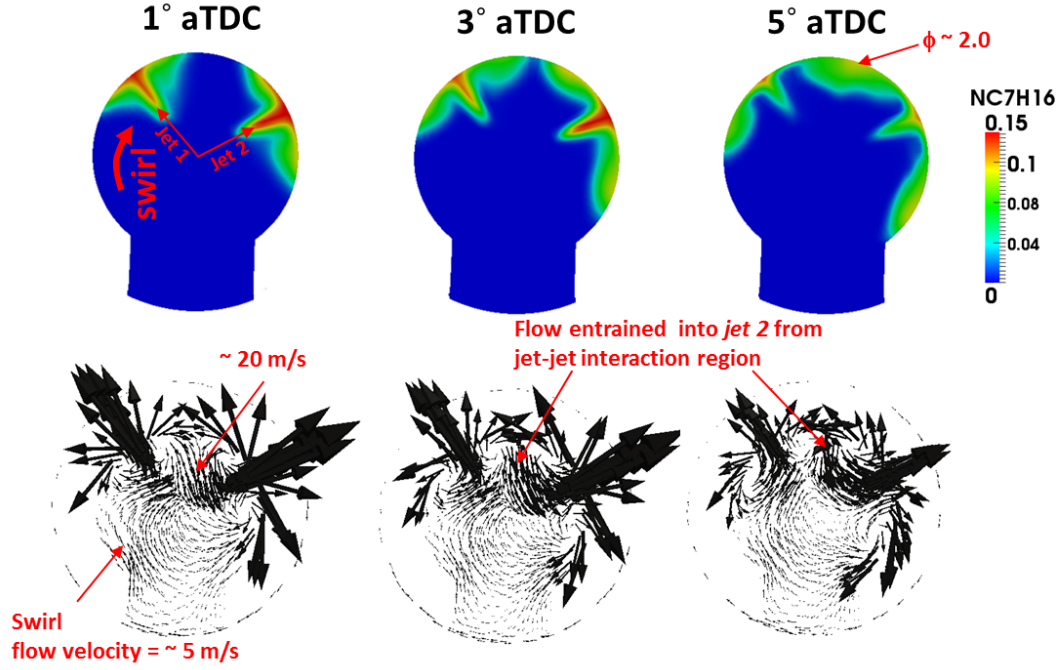


Figure 7.3: Top row: *n*-heptane mass fraction contours. Bottom row: Velocity vectors. Both the plots are from a plane at 7 mm from fire-deck with 70 MPa injection pressure.

interaction takes place and affects the local fuel concentrations. The maximum equivalence ratio (ϕ) in the interaction zone is around 2. The fuel injection ends at 4.5° CA aTDC and by 5° CA aTDC, most of the injected fuel has evaporated. Similar distributions of evaporated fuel are seen at the earlier timings of -1°, 0° and 1° CA aTDC at 130 MPa injection pressure with maximum ϕ of 2.0 in the jet-jet interaction zone. This shows the jet-jet interaction occurs earlier with 130 MPa injection pressure due to the faster jet penetration. In both the cases, the observed jet-jet interaction zone occurs at the end of fuel injection.

The structure of the velocity vector fields is similar in both cases at the shown crank angles as shown in the second row. The velocity fields are complex and feature a region of strongly opposing flow in the middle of the jets along the bowl wall, which redirects the flow back towards the centre of the bowl. There is substantial asymmetry to the flow. The redirected flow is entrained preferen-

tially into jet 2, which may be a result of a coupling with the swirl flow, which is redirected around get jet 1. Further analysis will be done whether this phenomenon brings combustion products towards jet 2 during combustion in the jet-jet interaction zone.

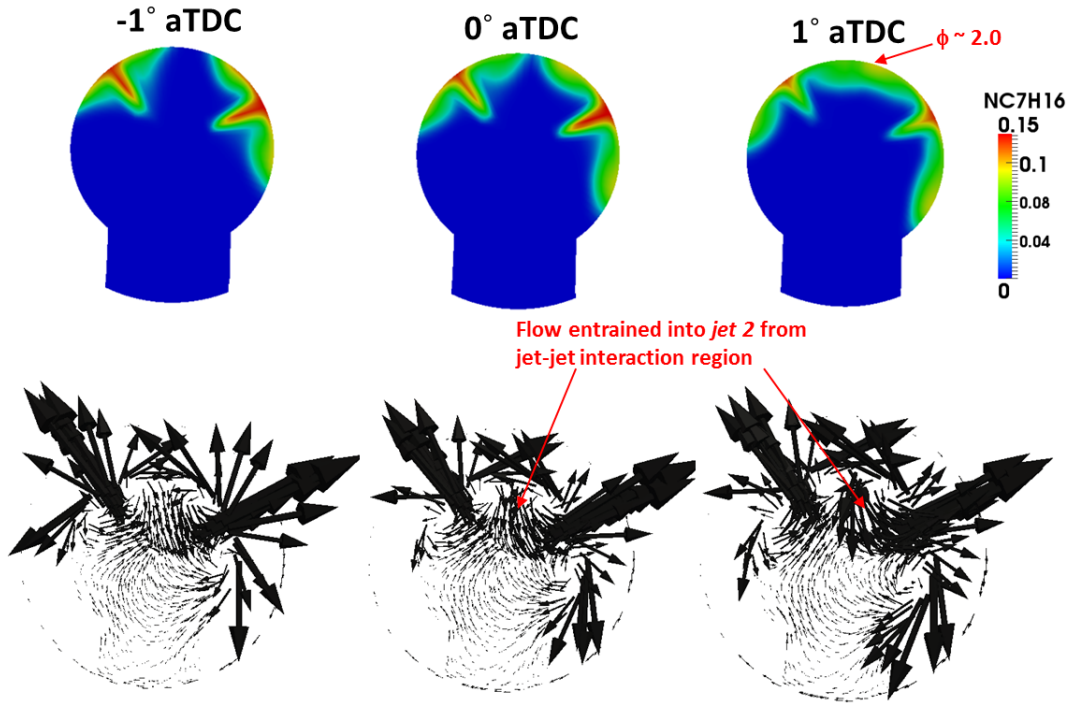


Figure 7.4: Top row: *n*-heptane mass fraction contours. Bottom row: Velocity vectors. Both the plots are from a plane at 7 mm from fire-deck with 130 MPa injection pressure.

7.3 Combustion during cool-flame period

The cool-flame period is taken from the crank angle where the first considerable concentrations of formaldehyde (CH_2O) due to the first-stage combustion are seen, up to the crank angle where the second-stage combustion starts, i.e. when high concentrations of OH radical appear. The cool-flame period is studied with the help of line of sight CH_2O mass fraction contours and mixture fraction contours for both the injection pressures. In Fig. 7.5, such contours for 70 MPa

injection pressure are shown at 5°, 8° and 10° CA aTDC and in Fig. 7.6, the same contours are shown for 130 MPa injection pressure at 2°, 5°, 8° and 9° CA aTDC. The first row in both the figures presents line of sight contours of the CH₂O mass fraction and second row gives the mixture fraction contours in a plane at 7 mm from the fire-deck. The contours on the top right corner in both the figures are line of sight CH₂O contours along the jet axes at 8° CA aTDC with 70 MPa injection pressure and at 5° CA aTDC with 130 MPa injection pressure.

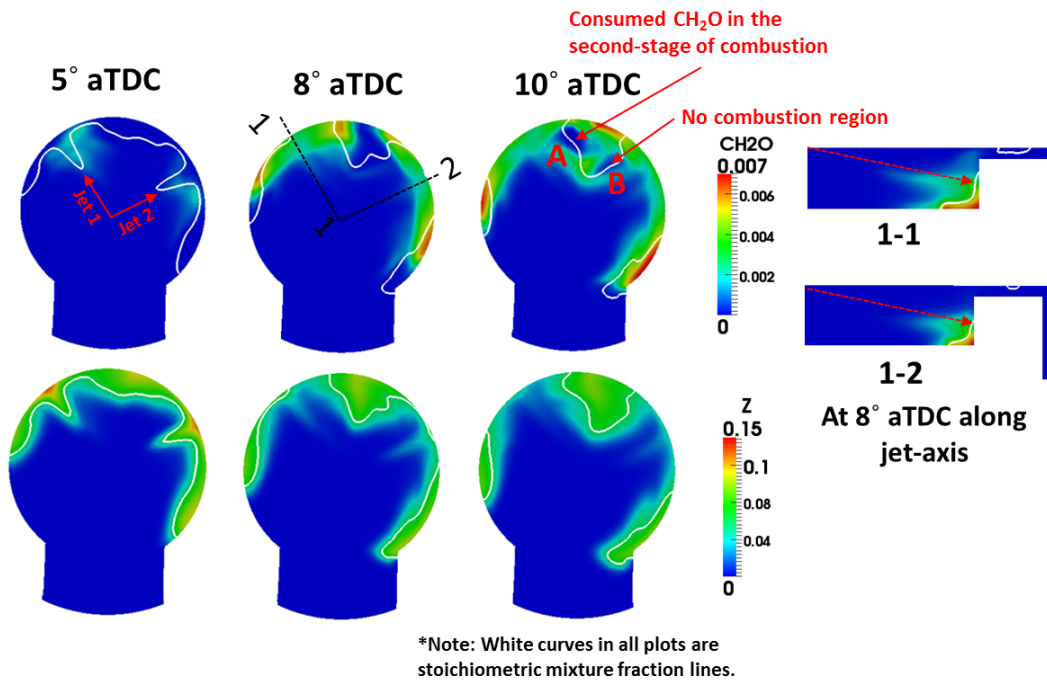


Figure 7.5: Top row: Line of sight CH₂O contours. Bottom row: Mixture fraction contours in a plane at 7 mm from fire-deck. Both the plots are taken at 5°, 8° and 10° CA aTDC with 70 MPa injection pressure. Contours on top right corner are line of sight CH₂O contours along jet axes at 8° CA aTDC. 1-1 is along jet 1 and 1-2 is along jet 2.

As can be seen at 70 MPa injection pressure (see Fig. 7.5), CH₂O is seen around the jet axes at 5° CA aTDC, which is after the end of fuel injection (4.5° CA aTDC) as highlighted in the in-cylinder pressure and heat release rate plot in Fig. 7.2a. By 8° CA aTDC, the injected fuel has entirely evaporated and first-stage combustion may be observed in almost all regions along the bowl-wall

wherever the evaporated fuel has penetrated except in the fuel rich region of jet-jet interaction, where the mixture fraction is around 0.1 ($\phi = 1.7$). Another observation is the occurrence of combustion along the jet axes. This is evident from contours of CH_2O mass fraction along the jet axes designated as '1-1' and '1-2'. By 10° CA aTDC, consumption of CH_2O in the region labelled 'A' signifies the second-stage combustion has started. However, in the region 'B', even the first-stage combustion has not started, which could be because of high scalar dissipation rate in this region. This will be further analysed with the help of scalar dissipation later in the chapter. As shown in Fig.7.7, temperature is in the order of 2500 K in the region 'A', which is far higher than the other first-stage combustion regions, confirming that second stage combustion has started in the region.

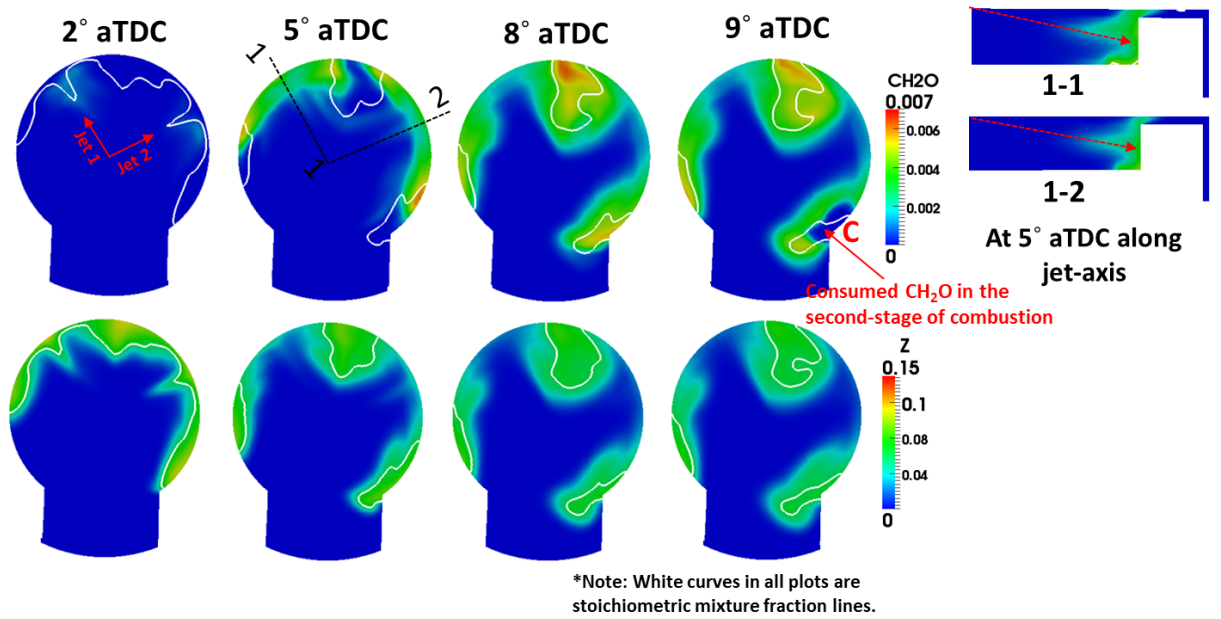


Figure 7.6: Top row: Line of sight CH_2O contours. Bottom row: Mixture fraction contours in a plane at 7 mm from fire-deck. Both the plots are taken at 2° , 5° , 8° and 9° CA aTDC with 130 MPa injection pressure. Contours on top right corner are line of sight CH_2O contours along jet axes at 5° CA aTDC. 1-1 is along jet 1 and 1-2 is along jet 2.

For the 130 MPa injection pressure, combustion is more advanced. The first

significant concentrations of CH_2O are seen earlier at 2° CA aTDC around the jet-axes. By 5° CA aTDC, similar combustion regions are seen as observed with 70 MPa injection pressure at 8° CA aTDC. First-stage combustion is observed along the jet axes as shown in CH_2O contours along jet axes in ‘1-1’ and ‘1-2’. Moreover, the mixture fraction contour at 5° CA aTDC shows that in the jet-jet interaction region, the fuel-air mixture is leaner compared to the mixture in the region with 70 MPa injection pressure at 8° CA aTDC. By 8° CA aTDC, first-stage combustion is seen across all mixtures. The mixture fraction contour shows that by this time, much of the evaporated fuel has moved away from the jet axes. Consumption of CH_2O in the region labelled as ‘C’ at 9° CA aTDC and temperature in the order of 2600 K in this region shows the second-stage combustion has started, but in a different location as seen with 70 MPa injection pressure. Consequently, the combustion is concentrated in three regions away from the jet axes. One is the jet-jet interaction zone and the other two regions result from penetration of the jets along the bowl wall. In comparison, in the single jet cases at 70

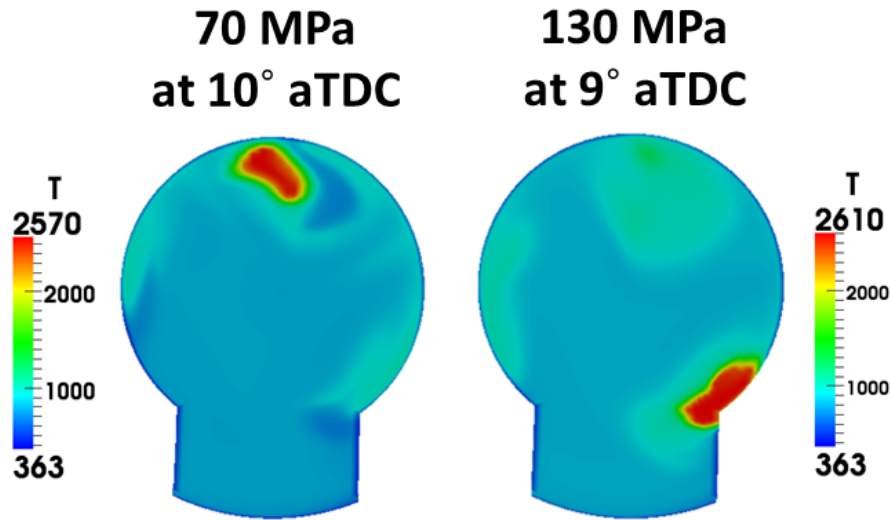


Figure 7.7: Temperature (K) contours in a plane at 7 mm from fire-deck. Left: At 10° CA aTDC with 70 MPa injection pressure. Right: At 9° CA aTDC with 130 MPa injection pressure.

and 130 MPa injection pressure, there was no appreciable first-stage combustion

happening along jet axis before the start of the second-stage combustion. This was due to the fact that fuel injection was ongoing and there was a strong high velocity jet in this region which prevented combustion occurring (see in Figs. 5.7 and 6.4). This high velocity and low residence time region implies that a part of the fuel was not available for combustion. In addition, the reduced time for mixing in the single jet cases implies that a reduced quantity of fuel could reach a combustible mixing state. Both effects lead to a less homogeneous combustion in the single jet cases as compared to the two-jet cases.

In Figs. 7.3 and 7.4 flow redirection from the jet-jet interaction zone towards the entrainment region of jet 2 was observed. There was an intact high velocity jet up to 5° CA aTDC with 70 MPa injection pressure and up to 1° CA aTDC with 130 MPa injection pressure. However, the first-stage combustion has not started in the jet interaction zone in both the cases (see in Figs. 7.5 and 7.6) at the mentioned crank angles. Therefore these flows did not recirculate combustion products towards jet 2, although fresh fuel-air mixture may be entrained, which would result in less global mixing than the entrainment of pure air. By 8° CA aTDC with 70 MPa injection pressure and 5° CA aTDC with 130 MPa injection pressure, there is no intact jet seen along the jet axes and so further entrainment effects will not be present.

7.4 Combustion during main combustion period

The start of the main combustion period is taken from a crank position where the first significant concentrations of OH due to the second-stage of combustion are observed. Contours of OH mass fraction and line of sight mass fraction OH* with 70 MPa injection pressure are shown in Fig. 7.8. The first row corresponds to 10° CA aTDC, the second and third row correspond to 11° and 13.5° CA aTDC respectively in planes at 5, 7 and 10 mm from the fire-deck (see Fig. 4.2 for relative position of the planes). Similar contours with 130 MPa injection pressure are shown in Fig. 7.9 at 9°, 10° and 13° CA aTDC.

As shown, the first significant OH is seen at 10° CA aTDC with 70 MPa injection pressure in all the three planes in the jet-jet interaction region where scalar dissipation rate (χ) as shown in Fig. 7.10 is less than 0.1 s^{-1} and second-stage

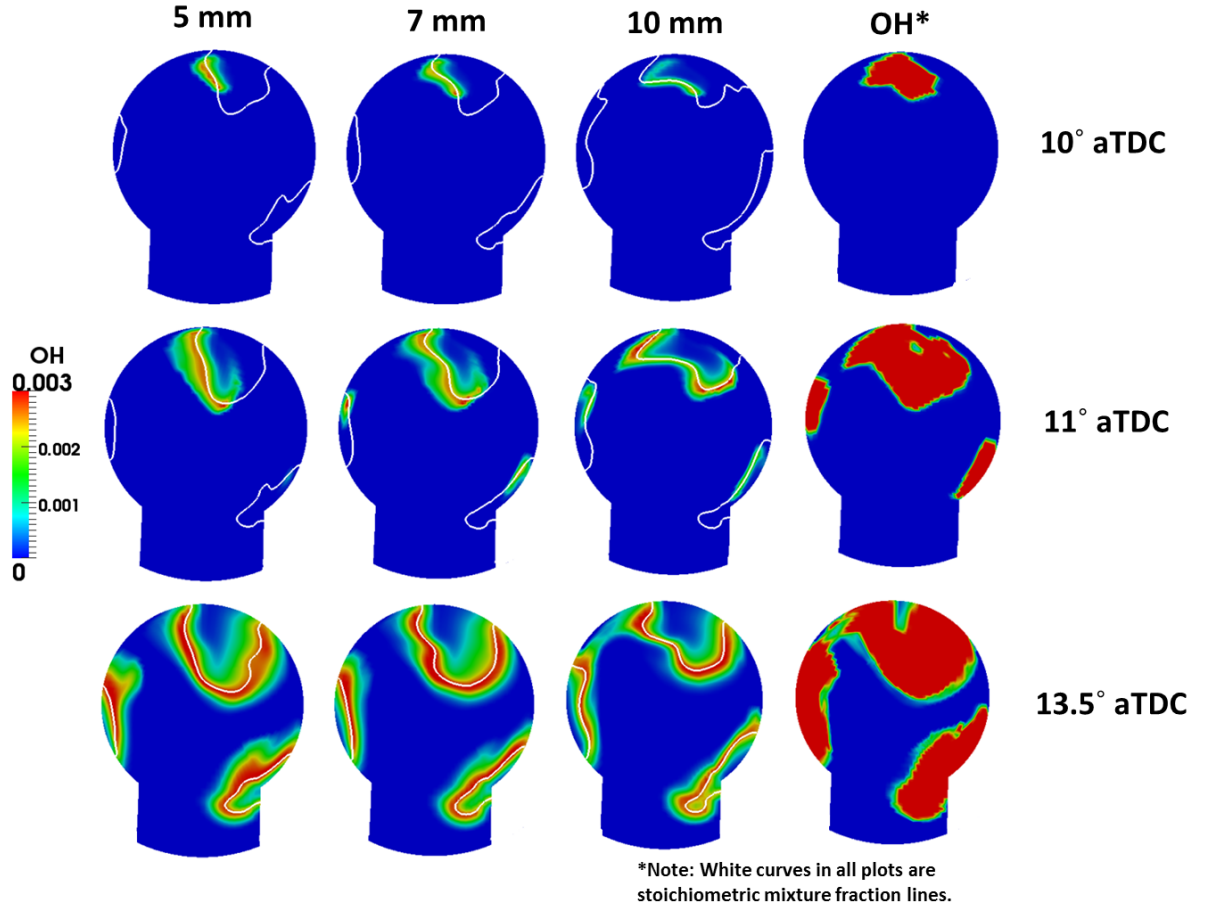


Figure 7.8: First three columns: Mass fraction contours of OH in three different planes at 5, 7 and 10 mm from fire-deck at 10°, 11° and 13.5° CA aTDC. Last column: Line of sight mass fraction contours of OH* at 10°, 11° and 13.5° CA aTDC. All the contours are with 70 MPa injection pressure.

combustion can take place as discussed in section 5.5. In the 130 MPa injection pressure case, significant OH is first observed at 9° CA aTDC in all the three planes, which is advanced by 1° crank angle compared to the 70 MPa injection pressure case. The location is just behind the head of the jet 2 penetrating along the bowl wall, where χ is less than 0.1 s^{-1} . The appearance of line of sight OH* contours in the similar locations for both the pressures further confirms the start of second-stage combustion in the locations highlighted by OH concentrations.

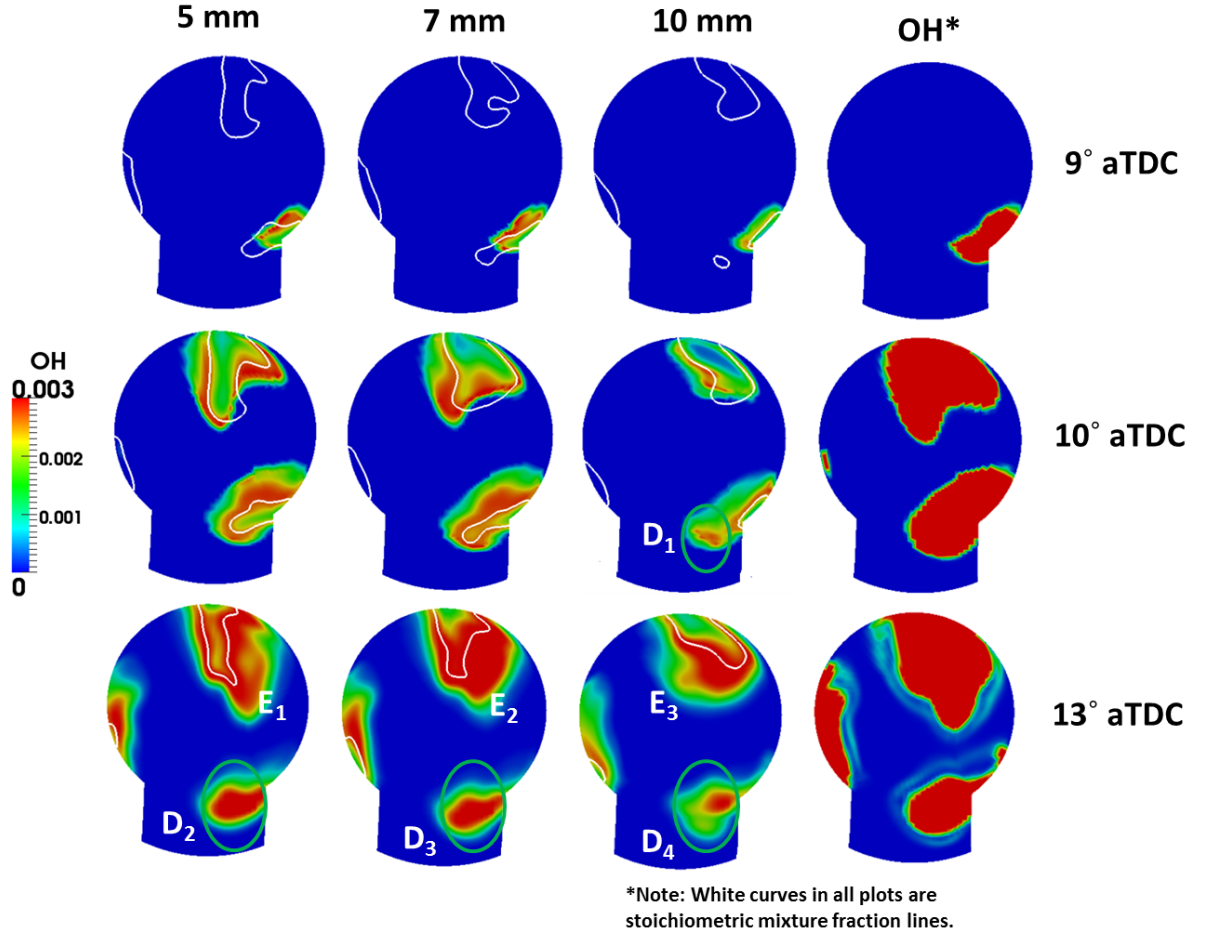


Figure 7.9: First three columns: Mass fraction contours of OH in three different planes at 5, 7 and 10 mm from fire-deck at 9°, 10° and 13° CA aTDC. Last column: Line of sight mass fraction contours of OH* at 9°, 10° and 13° CA aTDC. All the contours are with 130 MPa injection pressure.

By 11° CA aTDC with 70 MPa injection pressure, the second-stage combustion starts simultaneously just behind the leading regions of jets 1 and 2 penetrated along the bowl wall. OH is prevalent mainly in the middle to bottom portions of the bowl and not in the plane at 5 mm from the fire-deck. At 130 MPa injection pressure, by 10° CA aTDC (see Fig. 7.9), the second-stage combustion also starts in the jet-jet interaction zone over a large area. However, around the penetrated up-swirl side of jet 1, there is no second-stage combustion

going on. Another notable point is that the combustion also occurs in fuel-air mixture regions with $\phi < 1$ as highlighted with label ' D_1 ' whereas with 70 MPa injection pressure, the second-stage combustion occurs mainly around stoichiometric mixtures. By 13.5° CA aTDC with 70 MPa injection pressure and by 13° CA aTDC with 130 MPa injection pressure, the second-stage combustion goes on over a large area in all the three planes and in all the three regions of the bowl namely the trailing edge portions of jets 1 and 2 and the jet-jet interaction zone. As pointed out, with 130 MPa injection pressure, intermediate mixtures also undergo the second-stage combustion as highlighted with labels ' E_1 ' to ' E_3 ' and ' D_2 ' to ' D_4 '. Line of sight contours of OH^* show similar development of combustion for both the injection pressures.

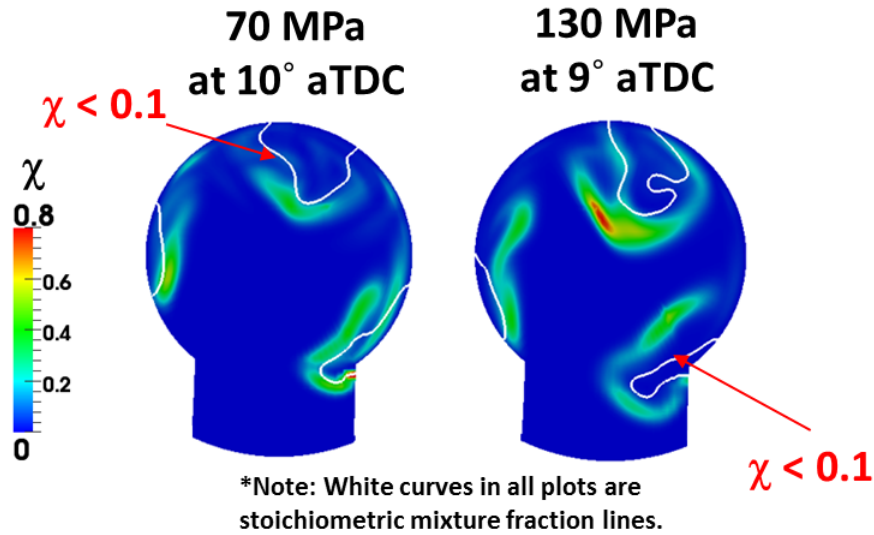


Figure 7.10: Scalar dissipation rate (χ) in a plane at 7 mm from fire-deck at 10° CA aTDC with 70 MPa injection pressure and at 9° CA aTDC with 130 MPa injection pressure.

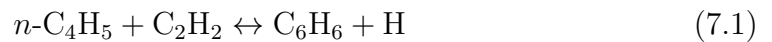
As a whole, around 1° crank angle after first observation of second-stage OH concentration for both the injection pressures, the second-stage combustion has started in the other two regions and a dip in heat release rate is not observed (see in Fig. 7.2), unlike was seen for the single jet cases for all the injection pressures (see in Fig. 6.1). In other words, the heat release rate steadily increased with

the occurrence of combustion in three different regions as opposed to two regions with single jet injection of fuel. This shows that the positive ignition dwell for the two jets cases has provided enough time for better mixing of evaporated fuel and air compared to the single jet cases, and thus lower scalar dissipation rate, causing less ignition delay on the up-swirl side.

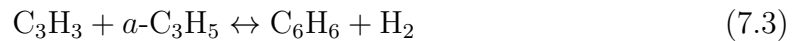
7.5 Formation and oxidation of soot precursors

Jet-jet interaction with both the injection pressures results in fuel rich mixtures in the interaction zone as shown in Figs. 7.5 and 7.6 with equivalence ratio (ϕ) around 1.7 with 70 MPa injection pressure and around 1.3 with 130 MPa injection pressure during the first-stage and the second-stage of combustion. As highlighted in [61], ϕ of around 1.4 is the critical sooting equivalence ratio for *n*-heptane or *iso*-octane. One of the key soot precursors is acetylene (C_2H_2). Acetylene is important in the formation and growth of large aromatic compounds, which eventually reach a size to be classed as soot. Blanquart et al. [29] in their development of a comprehensive hydrocarbon reaction mechanism with aromatic soot precursor reactions, identified two main reaction pathways that lead to the formation of aromatic soot precursors during combustion. The reactions are

In the first pathway:



and in second pathway:



where *n*-C₄H₅ is e-1,3-butadiene-1-yl, C₆H₆ is benzene, C₃H₃ is propargyl radical, *a*-C₃H₅ is allyl radical, H is hydrogen radical, and H₂ is molecular hydrogen. Even though species *n*-C₄H₅, C₆H₆ and *a*-C₃H₅ are not part of the considered skeletal mechanism of *n*-heptane for simulating diesel combustion, the presence of C₂H₂ and C₃H₃ in the rich regions can give an indication of formation of aromatic soot

precursors or soot in the region.

An experimental study by Genzale et al. [56] identified that in rich fuel-air mixture regions ($\phi \approx 1.4$) where formaldehyde (CH_2O) fluorescence disappears and OH fluorescence does not appear, soot precursors and soot are more likely to occur. In a similar way in the present study, as shown in Fig. 7.11, such rich fuel-air mixture regions in the jet-jet interaction zone are seen with 70 MPa injection pressure at 12° CA aTDC (labelled as ' F_1 ') and not seen with 130 MPa injection pressure at 10° CA aTDC in a plane at 7 mm from the fire-deck. Further analysis is done for both the injection pressures with the help of line of sight mass fraction contours of ($\text{C}_2\text{H}_2 + \text{C}_3\text{H}_3$) and mixture fraction (Z).

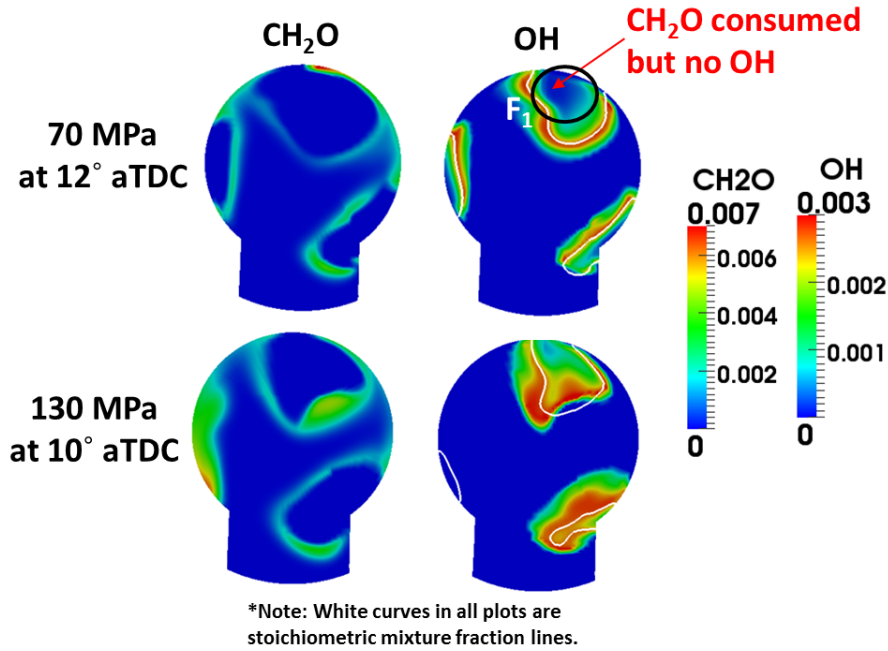


Figure 7.11: Mass fraction contours of formaldehyde (CH_2O) and OH in a plane at 7 mm from fire-deck. First row: 70 MPa injection pressure at 12° CA aTDC. Second row: 130 MPa injection pressure at 10° CA aTDC.

Line of sight mass fraction contours of ($\text{C}_2\text{H}_2 + \text{C}_3\text{H}_3$) and mixture fraction (Z) with 70 MPa injection pressure are shown in Fig. 7.12 at 10° , 12° and 16° CA aTDC, while Fig. 7.13 shows the case with 130 MPa injection pressure at 9° , 10° and 16° CA aTDC. For both the injection pressures, the plots are taken

from the start of second-stage of combustion and from where, if at all, soot or soot precursors can form in the rich regions. As can be seen, with 70 MPa injection pressure, high concentration of $(C_2H_2 + C_3H_3)$, which could lead to the formation of soot is seen in the rich jet-jet interaction zone, but by 16° CA aTDC, the concentrations reduced. This shows that the presence of high concentration of OH due to the second-stage of combustion around the high concentration of $(C_2H_2 + C_3H_3)$ as shown in Fig .7.11 led to oxidation of these species. In other words, the soot precursors formed in the rich regions oxidise eventually in the presence of OH radicals from the second-stage of combustion. Other thin bands of low concentrations of $(C_2H_2 + C_3H_3)$ in relatively lean regions may not lead to soot formation and instead may remain as part of un-burned hydrocarbons (UHC).

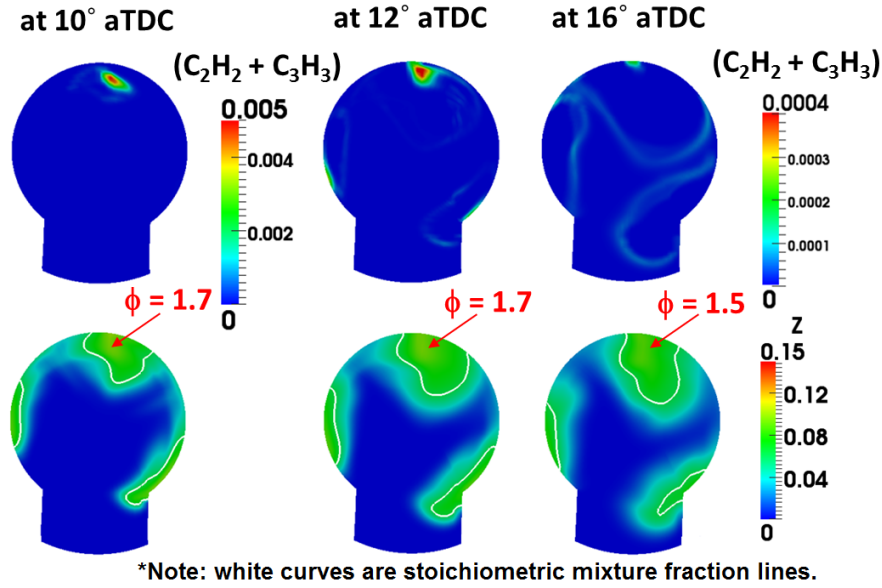


Figure 7.12: First row: Line of sight mass fraction contours of $(C_2H_2 + C_3H_3)$. Second row: Line of sight mixture fraction (Z) contours. Both the plots are taken at 10°, 12° and 16° CA aTDC with 70 MPa injection pressure.

In the case with 130 MPa injection pressure, rich fuel-air mixtures with ϕ in the order of 1.3 are seen in the jet-jet interaction region. As shown (see in Fig. 7.13), at 9° CA aTDC, very low concentration of $(C_2H_2 + C_3H_3)$ in the jet-jet

interaction region may not yield soot as still the first-stage combustion is going on (see in Fig. 7.6) and by 10° CA aTDC, the second-stage combustion starts in the region (see in Fig. 7.9) and appeared $(C_2H_2 + C_3H_3)$ is oxidised. Besides this, CH_2O consumed and no OH formed regions are not seen in this case. This shows that there is a very little chance of soot formation with 130 MPa injection pressure as mixtures are leaner and better mixed compared to the mixtures seen with 70 MPa injection pressure. Other thin bands of low concentrations of $(C_2H_2 + C_3H_3)$ in the lean mixture regions definitely will not lead to soot formation and remain as part of UHC if not consumed in the second-stage of combustion.

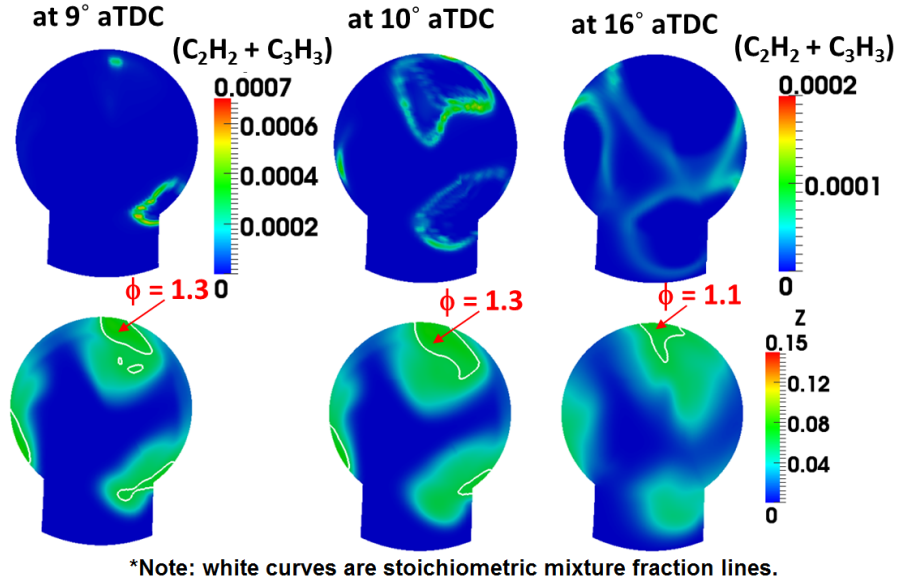


Figure 7.13: First row: Line of sight mass fraction contours of $(C_2H_2 + C_3H_3)$. Second row: Line of sight mixture fraction (Z) contours. Both the plots are taken at 9°, 10° and 16° CA aTDC with 130 MPa injection pressure.

7.6 Un-burned hydrocarbons (UHC) and CO emissions

To assess combustion efficiency in the two-jet cases, the transient development of UHC and CO is studied up to 80° CA aTDC along with iso-contours of UHC and

CO at 16° and 80° CA aTDC. Comparison of transient development of UHC and CO between the different injection pressures in the two-jet cases is shown in Fig. 7.14. 3-D mass fraction iso-contours of UHC and CO at 16° CA aTDC with 70 and 130 MPa injection pressure are shown in Fig. 7.15 and similar iso-contours at 80° CA aTDC are shown in Fig. 7.16. Finally, a comparison of transient development of UHC and CO with between the single and two-jet cases at both the injection pressures is presented in Fig. 7.17.

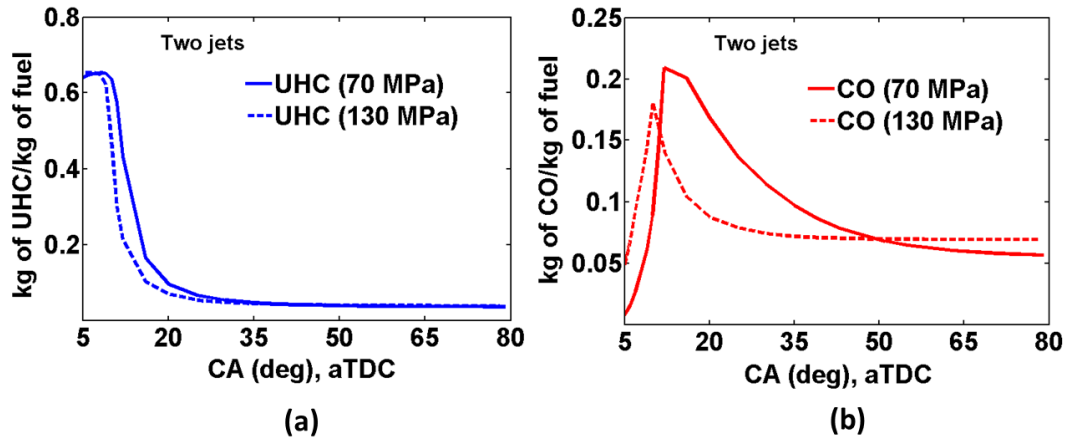


Figure 7.14: Comparison of transient development of UHC and CO with two jets at 70 and 130 MPa injection pressure from simulations.

As shown in Fig. 7.14, while the consumption rate of UHC is higher in the 130 MPa case than the 70 MPa case, the final value is about the same. The development of CO is somewhat different. It is well known that in two-stage combustion of *n*-heptane or diesel fuel that CO production reaches a peak at the onset of second-stage of combustion and is almost consumed during the second-stage [146]. With 130 MPa injection pressure, CO reaches peak at around 9° CA aTDC, where the second-stage combustion starts. In the 70 MPa case, the peak value is higher and the crank angle position of the peak value is delayed by around 1° CA due to the later start of the second-stage combustion starts at 10° CA aTDC (see in Figs. 7.8 and 7.9). After the summit, CO is consumed at faster rate and reaches flat levels earlier with 130 MPa injection pressure compared to 70 MPa injection pressure. This shows the mixing levels are better with 130 MPa

injection pressure, which was evident in line of sight mixture fraction contours shown in Figs. 7.12 and 7.13.

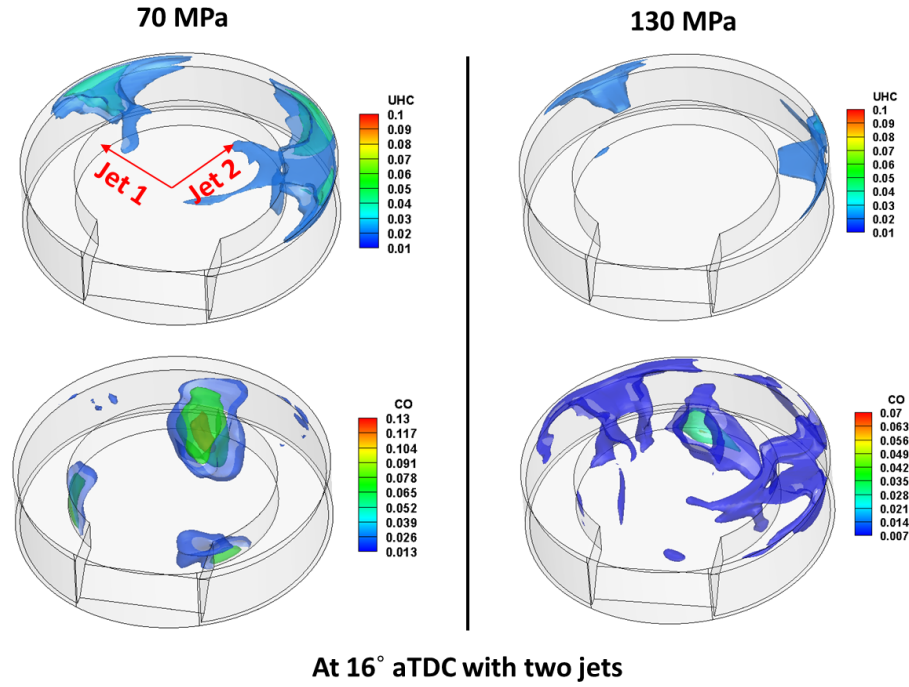


Figure 7.15: First column: Mass fraction iso-contours of UHC and CO at 16° CA aTDC with 70 MPa injection pressure. Second column: Mass fraction iso-contours of UHC and CO at 16° CA aTDC with 130 MPa injection pressure.

Furthermore, 3-D mass fraction iso-contours at 16° CA aTDC as shown in Fig. 7.15 show that UHC is seen in two weak combustion zones between the three active combustion zones (see in Figs. 7.8 and 7.9) for both the injection pressures, but concentration levels are less with 130 MPa injection pressure as seen in the transient development plots (see in Fig. 7.14). These two weak combustion zones exist around the point of impingement of fuel-jets on the bowl-wall, where mixtures are too lean to undergo complete combustion (see in Figs. 7.12 and 7.13). A higher concentration of CO (≈ 0.1 of mass fraction) is seen in the jet-jet interaction zone with 70 MPa injection pressure as the fuel-air mixture was rich in this region with ϕ around 1.7. CO is also seen in the rich regions of the trailing edges of jets 1 and 2. Another notable point is that the CO from

the jet-jet interaction zone is moving into the squish region due to the negative squish flow as the piston expands. Besides this, no appreciable CO is seen in the weak combustion zones. With 130 MPa injection pressure, since fuel-air mixture is better mixed and leaner compared to 70 MPa injection pressure, smaller mass fractions in the order of 0.01 are seen in the weak combustion zones while they are the order of 0.04 in the jet-jet interaction zone. Most of the observed CO is in the squish region for 130 MPa injection pressure, possibly explaining why the CO emissions are somewhat higher in this case. This could be because of a higher penetration rate of the jet while the piston is still moving up, thus resulting in more fuel penetrating over the bowl lip into the cool squish region where combustion does not go to completion.

At 80° CA aTDC, when chemical reactions have essentially ceased, 3-D iso-contours of mass fraction of UHC and CO are shown in Fig. 7.16 for both the injection pressures. On the top left of the figure, velocity vectors in a plane at 10 mm from fire-deck with 70 MPa injection pressure are shown. The vectors show that there is still a weak disturbed swirl in the flow with velocity in the order of 3 m/s. This can also be seen even with 130 MPa injection pressure (not shown). As can be seen, the left over UHC is seen almost entirely in the squish region for both the cases. Comparing with the earlier time, it has drifted from the weak combustion zones towards the jet 2 side due to the weak swirl flow, as seen at 16° CA aTDC (Fig. 7.15). The orders of magnitude are the same for both injection pressures. Coming to CO, with 70 MPa injection pressure, the high concentration of CO seen in the jet-jet interaction zone at 16° CA aTDC is almost consumed by 80° CA aTDC and the left-over has drifted towards jet 2. On the other hand, with 130 MPa injection pressure, the mass fractions in the order of 0.01 earlier observed in the weak combustion zones at 16° CA aTDC are largely intact and only a little consumed. These regions contributed the majority of the left-over CO with 130 MPa injection pressure. The comparison of transient development of UHC and CO for single and two jets is shown in Fig. 7.17. As shown, in the two jets cases, UHC and CO remained by the end of the combustion is more than observed in the single jet cases. This observation is line with the conclusions made in sections 7.3 and 7.4.

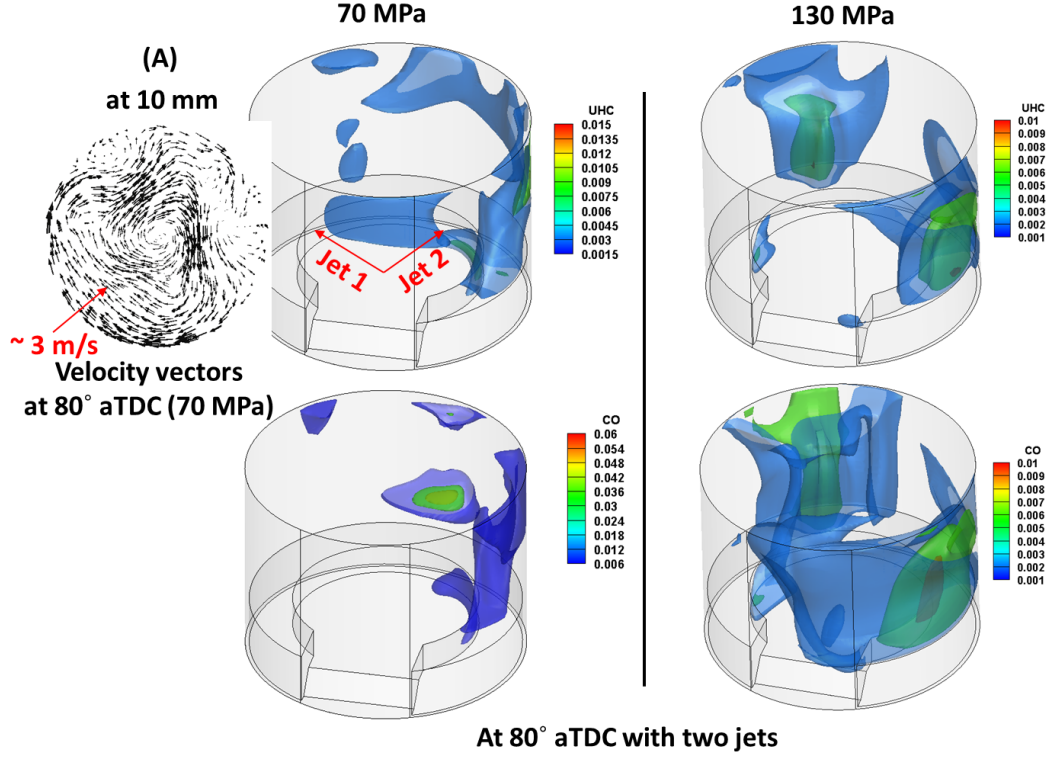


Figure 7.16: First column: Mass fraction iso-contours of UHC and CO at 80° CA aTDC with 70 MPa injection pressure. Second column: Mass fraction iso-contours of UHC and CO at 80° CA aTDC with 130 MPa injection pressure. (A): Velocity vectors in a plane at 10 mm from fire-deck at 80° CA aTDC with 70 MPa injection pressure (viewed from top).

7.7 Comparison with conventional and low temperature combustion (LTC)

The combustion development at 70 and 130 MPa injection pressure with two jets is compared to the conceptual model of the conventional, direct injection diesel combustion in a heavy-duty engine as proposed by Dec [45] and the conceptual model of light-duty, late-injection, EGR-diluted, partially premixed low-temperature combustion as proposed by Musculus et al. [115]. The two conceptual models are briefly described in section 2.1. Compared to the single jet cases, the combustion development for the two-jet cases follows more the LTC

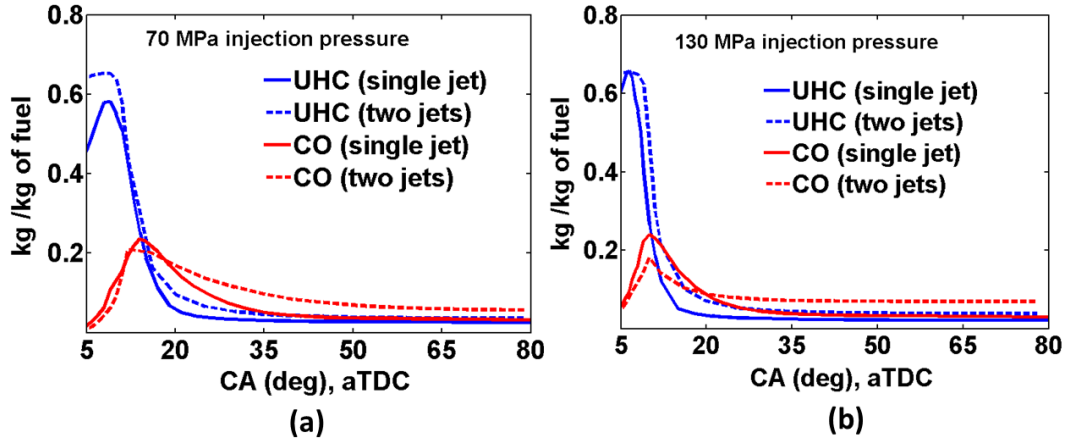


Figure 7.17: Comparison of transient development of UHC and CO with single and two jets configuration at 70 and 130 MPa injection pressure from simulations.

than the conventional combustion. The features that show similarity with LTC in a light-duty engine are:

- As seen in the LTC model, the first-stage combustion starts after the end of fuel injection, while the second-stage starts well after the end of injection, i.e. there is a positive ignition dwell. As a consequence, compared with the single-jet case that had a near-zero ignition dwell, the evaporated fuel has more time to mix with air before the combustion starts.
- The entire evaporated fuel undergoes the first-stage of combustion, but along the bowl-wall after impingement on the bowl-wall. In the LTC model, there exists an intact jet of evaporated fuel and the first-stage combustion occurs along the jet-axis also.
- Like in the LTC model, a clear two-stage heat release rate is observed with a dip in between due to ‘negative temperature coefficient’ in both the two-jet cases as almost all injected fuel is mixed to a degree sufficient to undergo first-stage combustion.
- The second-stage combustion is also seen in the regions with equivalence ratio (ϕ) less than 1.0 with 130 MPa injection pressure like in the low-temperature combustion.

-
- The unburned CO and UHC are seen in the squish region for both the cases like similar to what is observed in the LTC.

A key difference of the combustion development in the present two-jet cases with 70 and 130 MPa injection pressure is that the peak combustion temperature is not controlled by exhaust gas recirculation and therefore higher combustion temperatures in the order of 2600 K are observed, which can result in high NO_x .

7.8 Conclusions

The combustion development with two jets is different from that with a single jet at both the injection pressures during the both the cool-flame period and the main combustion period. The numerical simulations have provided useful insight into the combustion development. The following conclusions can be drawn:

- The distribution of same mass of total injected fuel to two jets reduced the fuel injection time compared to the single jet cases. This resulted in the start of ignition occurring after the end of fuel injection for both the considered injection pressures. This allowed additional time for mixing, as compared with the single jet fuel injection cases. Mixing caused relatively leaner mixtures to be formed, which resulted in a longer second stage ignition delay, thus allowing even more time for mixing. As a result, premixed burning was more prevalent in the two-jet cases, leading to higher peak heat release rates, shorter combustion duration, and higher peak pressures than in the single-jet cases.
- Redirection of fuel-air mixture from the jet-jet interaction zone towards the entrainment zone of jet 2 for both the cases was seen. However, as there was no combustion happening in the jet-jet interaction zone when the first-stage combustion started around jets 1 and 2, the entrained fluid was a fresh fuel-air mixture and not combustion products.
- After a while, the first-stage combustion spread over the entire evaporated fuel-air mixture regions along the bowl-wall except in a small region in

the jet-jet interaction zone with 70 MPa injection pressure. First-stage combustion also occurred along the jet-axes after the fuel injection period had ended.

- Second-stage combustion occurred in three different regions for both two-jet cases whereas it was only observed in two regions with the single jet cases. Moreover, with 130 MPa injection pressure, second-stage combustion occurred in the regions with $\phi < 1$. This resulted in steady increase of the heat release rate without the dip that was observed for the single jet cases due to the delayed start of the second-stage combustion on the up-swirl side compared to the down-swirl side.
- In the jet-jet interaction zone with 70 MPa injection pressure, fuel-air mixtures were rich with ϕ around 1.7 and resulted in the formation soot precursors, which eventually oxidised in the presence of OH radicals.
- The left-over UHC at 80° CA aTDC was almost the same for both two-jet cases and not much different from the left-over UHC in the single jet cases. The advantage gained from positive ignition dwell in the two-jet cases that could potentially have improved combustion efficiency was nullified by the generation of UHC from two weak combustion zones compared to one weak combustion zone with the single jet cases. On the other hand, more CO is observed in the two-jet cases because of presence of the rich jet-jet interaction region, which was absent in the single jet cases.

Chapter 8

Modelling of *n*-heptane aromatic hydrocarbon formation in an optically accessible heavy duty engine

Polycyclic aromatic hydrocarbons (PAH) are important precursor species for soot production in diesel engines, as well as being themselves a pollutant. Diesel fuel itself contains traces of aromatic hydrocarbons and during combustion additional formation of aromatics takes place. The combustion-triggered formation of PAHs and thereby soot is severe in conventional direct injection diesel engines. To reduce the severity of soot formation, various novel strategies of diesel combustion are being explored in the field of engine research. In this direction, important diesel combustion strategies include: homogenous charge compression ignition (HCCI), which is achieved by early injection of diesel fuel that allows considerable mixing of evaporated diesel fuel and air before combustion; low temperature combustion (LTC), achieved by a large amount of exhaust gas recirculation (EGR); premixed charge compression ignition (PCCI), achieved with dual injection of diesel fuel (one early and one conventional). To further develop and optimise these and other non-conventional combustion scenarios, the ability to predict aromatic species using simulations would be highly beneficial considering

the impact of aromatics on soot formation process.

Because of complexity of real fuels, engine simulations frequently consider surrogate fuels such as *n*-heptane [71]. However, most *n*-heptane chemical mechanisms, either reduced or detailed do not contain PAH reaction steps and can only predict acetylene (C_2H_2) as a soot precursor. The predicted C_2H_2 can only give qualitative indications for PAH observed in experiments [58]. In pursuit of aromatic reaction mechanisms, a detailed reaction mechanism of aromatic species was developed by Wang and Frenklach [166] in a study of benzene and PAH formation and oxidation in the context of acetylene and ethylene (C_2H_4) flames. Xi and Zhong [169] added the Wang and Frenklach [166] PAH mechanism to a detailed *nn*-heptane reaction mechanism of Curran et al. [40] and subsequently reduced this to a simple combined reaction mechanism using net reaction rate and sensitivity analysis. Blanquart et al. [29] developed a reaction mechanism suitable for high temperature combustion of a wide range of fuels ranging from methane to *iso*-octane fuels giving more emphasis on formation reactions of PAH soot precursors. Later Narayanaswamy et al. [117] extended the Blanquart et al. reaction mechanism to include oxidation of substituted aromatic species like toluene, styrene, ethylbenzene, 1,3-dimethylbenzene and 1-methylnaphthalene which are crucial components of engine fuels. More recently, Naranyanaswamy et al. [118] integrated their aromatic mechanism with a mechanism for low and high temperature *n*-dodecane combustion. All the mentioned reaction mechanisms with PAH reactions steps were not tested in actual diesel engine conditions and their predictive capability with respect to PAH species in 3-D diesel engine simulations is uncertain.

Some combined reaction mechanisms of primary reference fuel (PRF) and PAH were also developed to be used for soot modelling in engine simulations. Vishwanathan and Reitz [165] combined a PRF mechanism from Ra and Reitz [137] with a PAH mechanism from Xi and Zhong [169]. Pitsch et al. [131] used a combined reaction mechanism developed by Mauss [107] for soot prediction in diesel engines. Mosbach et al. [111] used a combined PRF mechanism from Bhave et al. [26] and PAH mechanism from Zhang et al. [172] for a detailed soot modelling in engines. These studies performed initial validation with simplified laboratory scale flames for important combustion products and soot precursors,

but when the models were applied to engines, only the final exhaust soot was compared.

Experimental techniques have come a long way in the study of effects of geometry and flow dynamics on formation of PAHs in engine conditions. To mention a few, Bruneaux [35] used PAH PLIF images to characterise low temperature combustion in a high pressure, high temperature constant volume combustion chamber in free and wall impingement jet configurations. Genzale et al. [56] conducted experiments using simultaneous planar laser-induced fluorescence (PLIF) of formaldehyde (CH_2O) and polycyclic aromatic hydrocarbons (PAH) in engine conditions with different bowl geometries. The experiments revealed that fuel jet-bowl and fuel jet-jet interactions play a role in determining the formation location and quantity of PAHs in diesel engines. PLIF of PAH also helped in conceptualising partially premixed low-temperature combustion in diesel engines [115]. Bobba and Musculus [30] utilised PAH PLIF combining with soot planar laser induced incandescence (PLII) in understanding evolution of soot precursors in the formation of soot in heavy duty engines under low-temperature combustion conditions. Further examples may be found in the review article [115].

In the present work, a combined *n*-heptane and aromatic species reaction mechanism was developed and validated for ignition delay time and different important species concentrations in laboratory scale premixed and counter-flow diffusion flames. To limit the overall computational expense, only aromatics species with a single ring were considered.

The small bore engine used for the other chapters was not employed in this chapter because experimental data for aromatic hydrocarbons was not available. Therefore, the new combined mechanism was used to simulate combustion in an optically accessible heavy duty diesel engine with two different bowl geometries. It was found that the predicted mono-aromatic hydrocarbon (MAH) concentration was qualitatively consistent with PLIF images of PAH from the experiment.

8.1 Chemical mechanism

A main objective of the present work was to develop a chemical mechanism for *n*-heptane that can predict formation of benzene and single aromatic ring com-

pounds. For this purpose, a semi-detailed *n*-heptane reaction mechanism from Lawrence Livermore National Laboratory (LLNL) [146] and single aromatic ring species formation reactions from the Blanquart et al. reaction mechanism [29] were systematically combined. This step was necessary because while Blanquart et al. [29] considered comprehensive kinetics for aromatics, only high temperature *n*-heptane kinetics were included, thus limiting the usefulness of the mechanism in engine simulations. An additional advantage of considering the LLNL reaction mechanism for *n*-heptane was that precursor hydrocarbons such as propyne (C_3H_4), propene (C_3H_6), propane (C_3H_8) and butadiene (C_4H_6) already exist in this mechanism. The reaction steps of the mentioned hydrocarbons leading to formation of radicals (propargyl C_3H_3 and allyl α - C_3H_5) involved in the formation of single ring aromatic compounds are also part of LLNL mechanism.

The starting mechanism was the LLNL mechanism, and all species and reactions from this mechanism were retained. The following reactions were added from [29]:

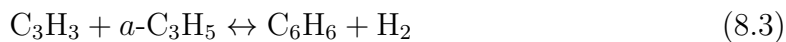
- 1,3-butadiene (C_4H_6) reaction steps that lead to the formation of e-1,3-butadiene-1-yl (n - C_4H_5) and i-1,3-butadiene-1-yl (i - C_4H_5) radicals. These radicals further participate in the formation of benzene and phenyl radical.
- 1-buten-3-yne (C_4H_4) reaction steps that produce i-1-butene-3-yne-2-yl (n - C_4H_3) and e-1-butene-3-yne-2-yl (i - C_4H_3).
- Fulvene ($C_5H_4CH_2$) formation steps. Benzene and phenyl radical formation steps from fulvene.
- Single-ring aromatic species formation reaction steps from H-abstraction- C_2H_2 -addition (HACA) reaction steps, toluene reaction steps and benzene oxidation reaction steps.

In the considered reaction steps, benzene formation takes place in two pathways as highlighted by Blanquart et al. [29].

In the first pathway:



and in second pathway:



The added single aromatic species reactions other than benzene are mostly from the H-abstraction-C₂H₂-addition (HACA) mechanism based on Ref. [55]. Finally, the combined reaction mechanism (LLNL-MAH) has 188 species and 1710 reactions including both forward and backward reactions. The thermodynamic and transport properties of all species in the resulting combined chemical mechanism (LLNL-MAH) were taken from the respective parent mechanisms [29; 146].

8.2 Validation of the mechanism

Combustion of diesel in direct injection compression ignition engines exhibits auto-ignition of the fuel with a time delay after the start of injection. Combustion occurs both in a diffusion flame mode and in a premixed combustion mode [45]. Therefore, it is necessary to validate the developed mechanism in both premixed and diffusion flame regimes.

8.2.1 Ignition delay time

The original LLNL mechanism was thoroughly validated for ignition delay times with experimental data obtained from shock tubes [37; 53] and rapid compression machines [110] at different pressures. It was necessary to check that the modified mechanism reproduced the behaviours. Therefore, the predicted ignition delay times using the LLNL-MAH were compared against those of the LLNL mechanism. The SENKIN code [104] was used to estimate the ignition delay time at a constant volume for a range of initial mixture equivalence ratios and temperatures. The point of ignition was defined as the time of maximum rate of temperature rise. The initial pressure of 40 bar was prescribed, as a pressure relevant to internal combustion engines. As can be seen in Fig. 8.1, the added aromatic reactions have not altered the ignition delay time as compared to the

original LLNL mechanism and experimental data from [37], as expected.

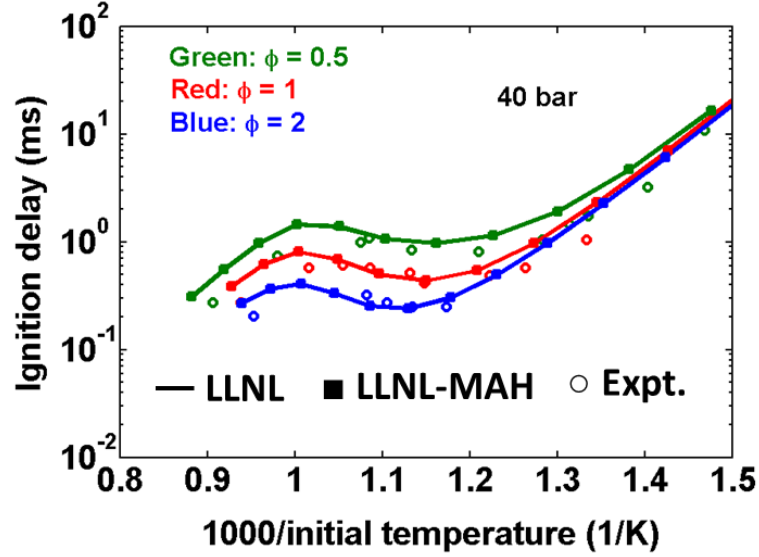


Figure 8.1: Comparison of predicted ignition delay times using LLNL-MAH and LLNL mechanisms with experimental data from Ciezki et al. [37].

8.2.2 Premixed flat flame

A rich *n*-heptane/air (equivalence ratio, $\phi = 1.9$) premixed laminar flame from experiments reported in Ref. [22] was considered for validation. The experiment was conducted at atmospheric pressure. In the experiment, liquid *n*-heptane was vaporised before mixing with oxygen and nitrogen. The gaseous mixture with a composition of O_2 : 23.16%, N_2 : 64.32% and C_7H_{16} : 12.52% by mass flowed from the burner exit with a velocity of 4.98 cm/s and at a temperature of 450 K. The PREMIX code [82] was used for the simulations. The temperature profile obtained from the experiment was prescribed in the simulations. This is an alternative to solving the energy equation, which is not feasible in this case due to unknown heat losses by conduction and radiation to the burner surface. The initial guess for the products and intermediate species mole fractions was taken from the experimental data.

As shown in Fig. 8.2, the consumption of fuel and oxidiser and formation of

the main combustion products (CO_2 , CO) are predicted well compared to the experimental data and Blanquart et al. [29] simulations, from which the MAH reaction steps were taken. This is as expected as the main *n*-heptane reaction steps from the LLNL mechanism are retained in LLNL-MAH mechanism. An important feature of the LLNL-MAH mechanism is the good prediction of soot precursors (benzene, C_6H_6) and acetylene (C_2H_2) compared with the experiment and Blanquart et al. [29] simulations. Other important combustion products such as allene ($\text{C}_3\text{H}_4\text{-A}$), butadiene (C_4H_6), and propene (C_3H_6) are also well predicted.

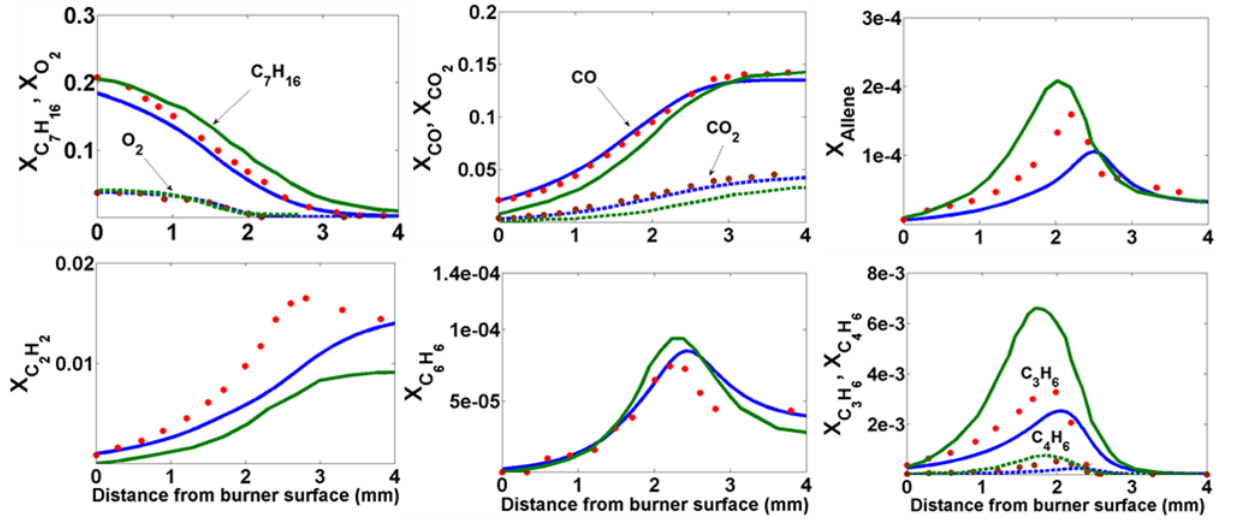


Figure 8.2: Mole fractions of important species and soot precursors for the rich *n*-heptane/air premixed flat flame (dots: experiment from Bakali et al. [22]; blue lines: simulations using LLNL-MAH; green lines: simulations from Blanquart et al. [29]).

8.2.3 Counter-flow diffusion flame

A counter-flow atmospheric *n*-heptane/air diffusion flame [24] with a very rich mixture of fuel and air ($\phi = 15$) on the fuel side was considered for validation of the LLNL-MAH mechanism. The experiment was designed to study the effect of partial premixing on the formation of NO_x , soot precursors such as acetylene,

benzene and other PAH species. A case with a global strain rate of 50 s^{-1} was chosen from the experiment and the velocities on fuel and oxidiser side were 12.2 cm/s and 13.5 cm/s respectively. The separation distance between the nozzles was 1 cm . The OPPDIF code was used for the simulations [103]. In this case, the energy equation was solved as the flame exists away from the burners and no significant heat loss by conduction to the burners takes place. The initial guess for the products and intermediate species mole fractions was taken from the experimental data.

As can be seen in Fig. 8.3, temperature, fuel and oxidiser consumption and important combustion products are predicted well compared to the experiment and simulations from Blanquart et al. [29]. Benzene concentration is over-predicted three fold. This may be due to over-prediction of ethylene (C_2H_4) in the diffusion flame, which further reacts to form C_2H_2 and $n\text{-C}_4\text{H}_5$ leading to formation of benzene, which is the first pathway as shown in Eq. 8.1. Also, experimental errors cannot be ruled out.

To assess possible effects of radiation heat loss, the simulations were also performed by considering an optically thin approximation. The radiative heat loss from CO_2 , H_2O and CH_4 species only was considered. Overall, little difference in the results was observed. The prediction of benzene did not improve compared to the experimental data (not shown here).

8.3 Engine simulation results

The validated LLNL-MAH reaction mechanism was used to simulate direct injection combustion in an optically accessible Cummins N-series heavy-duty engine installed in Sandia National Laboratories. The important engine operating conditions and geometry details for 70% and 80% are given in Table 8.1. The test conditions were taken from Ref. [56]. The fuel used was a blend of 79% *n*-heptane and 29% *iso*-octane. The engine has a low swirl ratio of 0.5. The low swirl of the engine has enabled us to consider a 45° periodic sector mesh of the engine covering a single fuel injector.

In the experiments, combustion and pollutant formation processes were studied using planar-laser-induced-fluorescence (PLIF) diagnostics which are fully de-

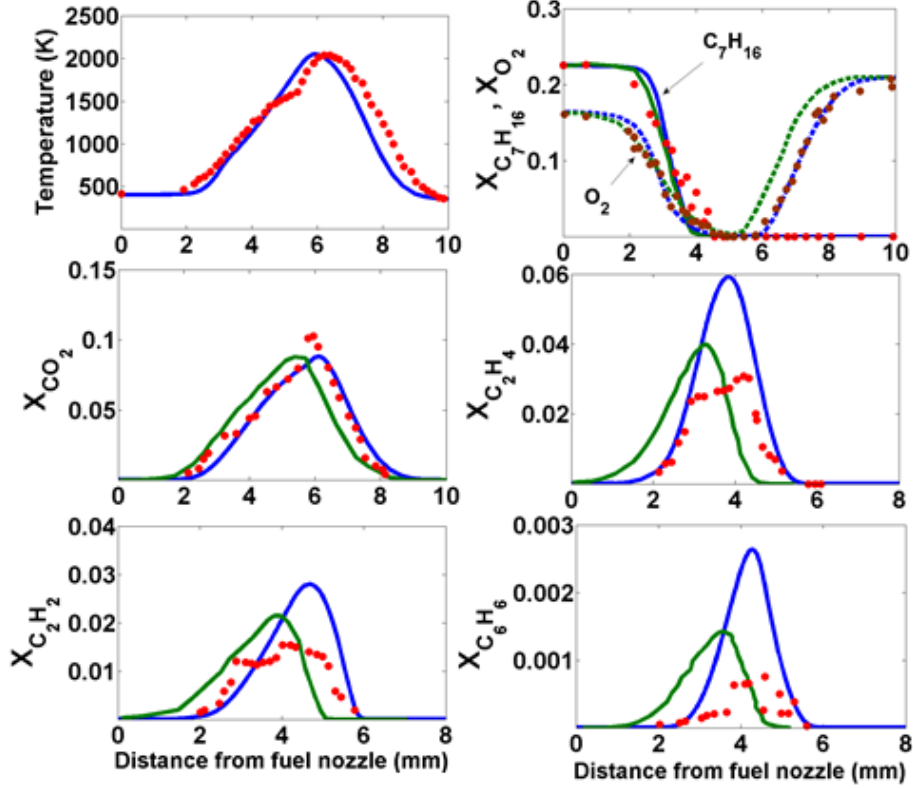


Figure 8.3: Mole fractions of important species and soot precursors for the n-heptane/air counter-flow diffusion flame (dots: experiment from Berta et al. [24]; blue lines: simulations using LLNL-MAH; green lines: simulations from Blanquart et al. [29]).

scribed in Ref. [56]. Local equivalence ratios were measured in a non-reacting case, achieved by substituting air for nitrogen, using PLIF of a 1 % toluene tracer excited at 266 nm and collected around 300 nm. Hydroxyl, a marker of high temperature reaction zones, was measured using OH PLIF, excited at 284 nm and collected around 312 nm. PLIF with excitation at 355 nm and collection around 408 nm was used to image formaldehyde (CH_2O) and PAH simultaneously. Formaldehyde is a product of the first stage cool-flame chemistry, and occurs early/upstream in the ignition sequence, while PAH forms much later and in more downstream locations. As such, these species do not significantly overlap; however, where the transition occurs is not known *a priori*. Therefore, to

help distinguish between regions of the jet where formaldehyde (CH_2O) and PAH occur, a part of the fluorescence signal was diverted to a spectrometer and cross-correlated with a reference spectrum for formaldehyde. The correlation coefficient for different slices along the jet axis will be displayed in a colour-bar at the bottom of the experimental images, where high values suggest a good correlation with formaldehyde at that axial location while low values suggest the observed signal is from PAH (and possibly, soot incandescence later in the cycle).

When the experimental results will be presented later in the chapter, ensemble-mean results will be presented for the equivalence ratio in non-reacting cases. However, ensemble-averaging of OH and CH_2O /PAH PLIF images is generally not preferred because it smears out turbulent features of combusting fuel jet. Therefore, in the considered experiment, instantaneous PLIF images were selected from a set of 20 images, acquired from 20 different engine cycles following a two-dimensional cross-correlation taken between an instantaneous image and the ensemble-average image. This cross-correlation gives an instantaneous image that is closely similar to the ensemble-average image [56].

Table 8.1: Engine operating conditions.

Engine speed	1200 rpm
Displacement (single-cylinder)	2340 cm^3
Bore	139.7 mm
Stroke	152.4 mm
Squish height	5.5 mm
Swirl ratio (nominal)	0.5
Bowl diameter x depth (70% bowl)	97.8 mm x 16 mm
Bowl diameter x depth (80% bowl)	111.8 mm x 12.3 mm
Intake valve closure (IVC) ¹	-165° CA aTDC
Exhaust valve closure (EVC)	140° CA aTDC
Injected fuel mass	56 mg
Start of fuel injection	0° CA aTDC
Injection duration	0.94 ms
Injector included angle (70% bowl)	152°
Injector included angle (80% bowl)	160°
Intake temperature	343 K
Intake pressure	202 kPa
Intake oxygen % (vol.)	12.7

8.3.1 Numerical setup

Simulations were performed using OpenFOAM [12]. Turbulence was modelled using the RNG $k - \epsilon$ model. A Lagrangian approach was used to model the evolution of the liquid fuel spray. The liquid fuel was injected as blobs with a diameter equal to the effective diameter of the nozzle. The rate of fuel injection profile was taken from [56]. The Kelvin-Helmholtz Rayleigh-Taylor (KH-RT) sub-model [139] was used to model the spray atomisation and break-up. The Kelvin-Helmholtz (KH) part of the KH-RT sub-model represents the break-up of initial blobs and then the Rayleigh-Taylor (RT) model predicts the secondary break-up of the droplets. The Ranz-Marshall correlation [39] was used to model the droplet evaporation. A detailed description of the spray model is given in section 3.2.5. The same direct-integration combustion model as used for the other studies with automotive-size optical diesel engine was used (see in section 3.2.7).

The simulations were started from intake valve closure (IVC) with a solid-body swirl of 0.5. The pressure and temperature at IVC were estimated from intake pressure and temperature assuming isentropic compression from BDC (Bottom Dead Centre) to IVC. A constant wall temperature of 500 K on the piston surface, 385 K on the cylinder head surface and 430 K on the cylinder wall were specified as suggested in Ref. [57] for the same engine geometry. A temperature wall function based on variable density as recommended in Ref. [67] was used for all walls.

8.3.2 In-cylinder pressure and heat release rate comparison

The in-cylinder pressure and apparent heat release rate (aHRR) obtained from the simulations for the 70% and the 80% bowl geometries using the LLNL-MAH reaction mechanism are compared with the experimental data in Fig. 8.4. The aHRR in the experiment and the simulations were calculated based on the pressure data and cylinder volume using Eq. 3.46 under adiabatic conditions. The

¹0 is taken at Top Dead Centre (TDC) in compression stroke.

simulated heat release rate in the first- and the second-stage start around 1° CA earlier in the 70% bowl geometry case compared to the 80% bowl geometry case. Similar observations were made in the experiment. As observed in the experiment, the simulated peak value of heat release rate in the second-stage combustion is lower in the 80% bowl geometry case than in the 70% bowl geometry case. Despite some small discrepancies, the overall trends observed in the experiment are captured well in the simulations for both the cases.

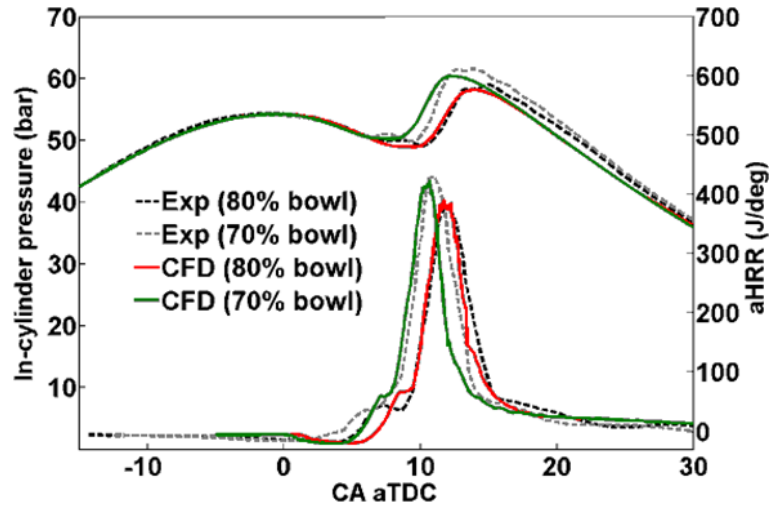


Figure 8.4: Comparison of in-cylinder pressure and aHRR with the experimental pressure trace [56] for 70% and 80% bowl geometries.

To investigate further the observed trends, the model results are compared with optical measurements in the engines. The comparisons include cases with combustion and non-reacting cases without combustion where the air was substituted with nitrogen. (In the simulations, the combustion model was switched-off to achieve the non-reacting condition.)

The 355nm PLIF images from firing cycles and equivalence ratio in non-reacting conditions from the experiment and the simulations are studied at 7° CA aTDC. At this time the first-stage combustion in the 70% bowl geometry case is in progress while it has just started in the 80% bowl geometry case. The crank angle 7° CA aTDC also marks the end of fuel injection in both cases. The equivalence ratio contours were ensemble-averaged over multiple cycles while the

355 nm PLIF images are selected from individual cycles that correlated well with the ensemble mean image. In Fig. 8.5, the top row corresponds to the 70% bowl geometry and the bottom row corresponds to the 80% bowl geometry. The dotted black arc in the equivalence ratio plots from the simulations is the field of view margin in the experiment and the continuous black line marks the edge of the bowl. The dotted and continuous white arcs in the CH_2O images represent the field of view margin in the experiment and the edge of the bowl respectively. In the 70% bowl geometry case, the comparison is done in a plane at 12 mm from the fire-deck whereas in the 80% bowl geometry case, the plane of study is at 10 mm from the fire-deck. The mentioned planes bisect the bowl vertically (as the 70% bowl is deeper) and the fuel impinges on the bowl surface [56] around the same location, which can give a better understanding about the start of combustion and fuel impingement on the wall.

As can be seen in Fig. 8.5, the simulated equivalence ratio contours in the non-reacting case compare well with the experimental contours and show the strong impingement of the jet on the bowl wall in the 70% bowl geometry whereas the jet is still freely propagating in the 80% bowl geometry since the diameter of the bowl is more.

In the reacting case, the 355 nm CH_2O /PAH PLIF at this early time certainly does not show PAH or soot, suggesting the image shows primarily CH_2O . The images from the experiment and CH_2O mass fraction contours from the simulations show that in the 70% bowl geometry case there is a strong concentration of CH_2O throughout the leading edge of the jet. This confirms that the first-stage combustion is in an advanced stage. In the 80% bowl geometry, the very low fluorescence in the experiment and low concentration of CH_2O from the simulations indicate the first-stage combustion has just started. The observation falls in line with the aHRR plots shown in Fig. 8.4. Overall there is a very good agreement for the location and timing of CH_2O .

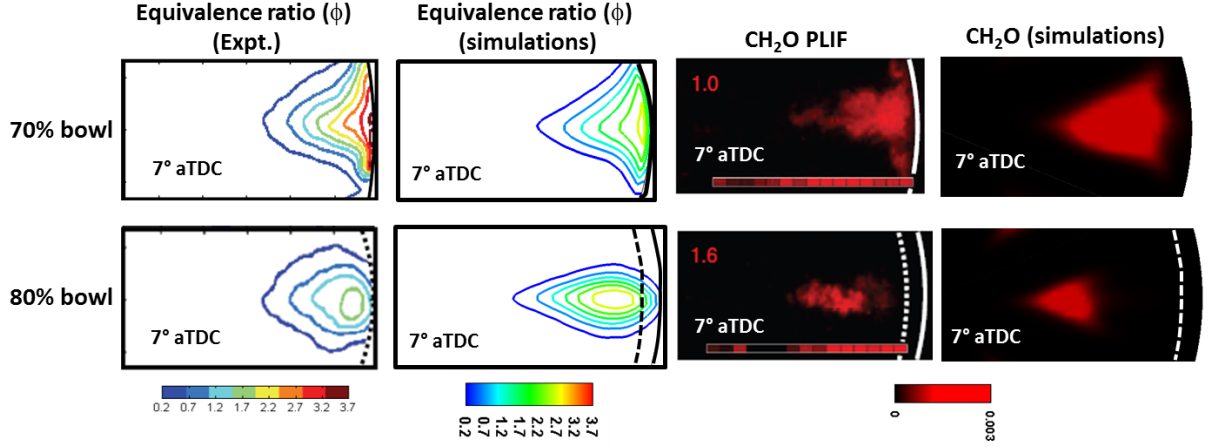


Figure 8.5: Top row: Formaldehyde (CH₂O) and equivalence ratio (non-combustion condition) comparison with the experiment [56] at 7° CA aTDC and in a plane at 12 mm from firedeck for the 70% bowl geometry. Bottom row: formaldehyde (CH₂O) and equivalence ratio (non-combustion condition) comparison with the experiment [56] at 7° CA aTDC and in a plane at 10 mm from firedeck for the 80% bowl geometry.

8.3.3 Effects of jet-wall and jet-jet interactions on PAH formation

The transient development of the predicted total mass of aromatic compounds in the cylinder for the two geometries is first shown in Fig. 8.6. It may be observed that MAH mass starts rising from 10° CA aTDC and peaks around 12° CA aTDC for both the geometries. Around this stage, second-stage high heat release combustion was going on in both the cases (see in aHRR in Fig. 8.4). During this time, the high temperature rich regions where soot precursors can form are prevalent. After the peak, the aromatic mass declines continuously as oxidation of MAH dominates over its formation. It reaches almost negligible levels by 40° CA aTDC. These trends are further discussed in relation to the optical measurements in the following.

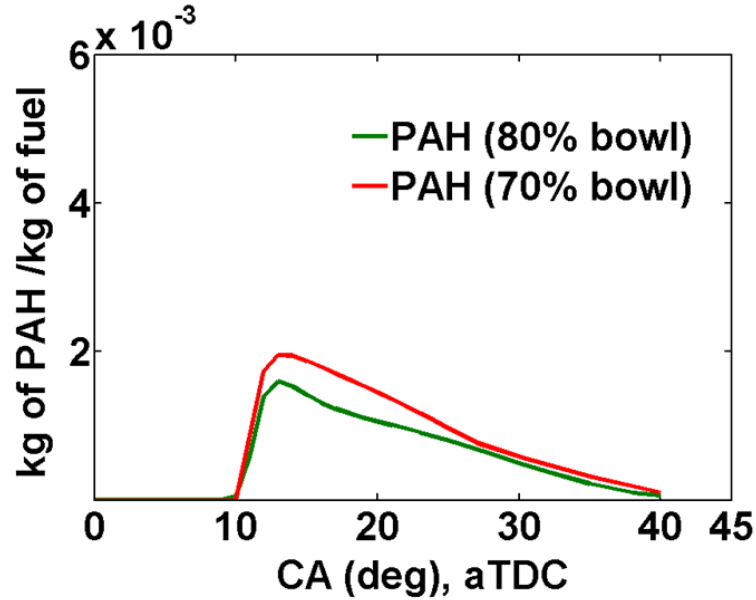


Figure 8.6: Transient formation of PAH from simulations for both 70% and 80% bowl geometries.

8.3.3.1 Interactions in the main combustion period

The fuel-air equivalence ratio distribution in the non-reacting condition and contours of mass fraction of simulated single ring aromatic compounds (MAH), CH_2O and OH are now compared with the corresponding PLIF images from the experiment during the main combustion period. The comparisons are shown for the 70% bowl geometry at 12° CA aTDC in Fig. 8.7 and for 14° CA aTDC in Fig. 8.8, while Fig. 8.9 shows the results in the 80% bowl geometry. As explained earlier, the PLIF images of $\text{CH}_2\text{O}/\text{PAH} + \text{OH}$ were selected from a single cycle whereas the equivalence ratio contours, derived from toluene PLIF, were ensemble-averaged from multiple cycles. At these early times, the experimental total soot luminosity was small suggesting that any 355 nm LIF signal not correlated with CH_2O was probably due to PAH.

Firstly, the comparison for the 70% bowl geometry is considered. The comparison is first done at 12° CA aTDC for the 70% bowl geometry, which marks the location of peak pressure (see Fig. 8.4). The comparison is shown in three different planes at 7, 12 and 18 mm from the fire deck. As shown in Fig. 8.7, the

white arc and the black arc in all the images represent the edge of the bowl in the experiment. The highlighted bright red spots with the letter b in the PLIF images of $\text{CH}_2\text{O}/\text{PAH} + \text{OH}$ (third column) at 18 mm are due to PAH fluorescence [56], as judged by the low correlation of the emission spectrum with the reference formaldehyde spectrum at the corresponding axial location (see the inset colour bar). In the images from the simulations (fourth column), the red contour lines are CH_2O mass fraction contours, the yellow contour lines are MAH contours and the green contours are of OH mass fraction. Similarly, red and green in the PLIF images in the third column represent CH_2O and OH fluorescence respectively.

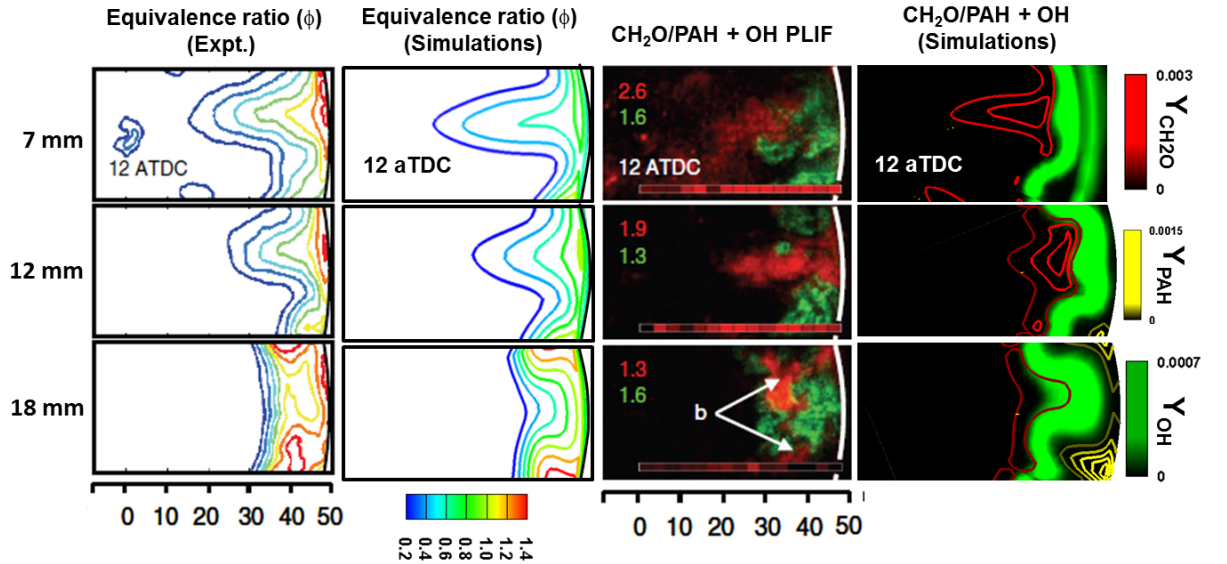


Figure 8.7: Comparison of equivalence ratio in non-combustion condition and $\text{CH}_2\text{O}/\text{PAH} + \text{OH}$ with combustion at 12° CA aTDC. The planes are taken at 7, 12 and 18 mm from fire-deck for the 70% bowl geometry.

It is again noted that the equivalence ratio contours from the simulations compare well those from the experiment in all the planes. The model seems to slightly underestimate the equivalence ratio near the bowl wall in planes 7 and 12 mm suggesting that a greater degree of mixing has occurred in the model. In the model, the maximum ϕ is around 1.0 whereas in the experiment the mixture is rich with $\phi \approx 1.4$. The fuel-air mixture is lean ($\phi \leq 0.2$) near the centre of the bowl and becomes richer near the wall after the wall-impingement in all

the planes in the experiment as well as in the simulations. This observation is consistent with the other fuel jet-wall impingement studies [34]. The equivalence ratio contours in the plane at 18 mm reveal that, in this smaller diameter bowl, the fuel jet interacts with the neighbour jets leading to the formation of rich pockets in the jet-jet interaction zones, which could lead to formation of PAH and soot.

Now, turning to the comparison of the experimental $\text{CH}_2\text{O}/\text{PAH} + \text{OH}$ PLIF and the corresponding mass fractions contours from the simulations, it is first noted that both model and simulations show significant OH near the bowl wall, which confirms the onset of high temperature combustion. The spatial extent of the high OH region is predicted well by the model in the 7 mm and 18 mm planes. In the 12mm plane, the model predicts high temperature combustion is occurring across the jet, while the experiments show a region of lower OH in the core of the jet. This could be connected with the relatively lower equivalence ratios seen in the model in this region. The model and experiment also agree quite well on the locations of formaldehyde in the upstream, leaner regions of the jet on the 7mm plane. The experiments show more formaldehyde in the jet core in the 12 mm, which corresponds with the earlier remark about OH. In the 18 mm plane, the experimental 355 nm PLIF signal near the bowl wall shows a low correlation with the formaldehyde reference spectrum, suggesting that the regions marked b in the images are due to PAH fluorescence. The model also shows significant PAH on this plane, and generally agrees with the experiment that aromatics mainly form in the rich jet-jet interaction regions on either side of the jet.

As shown in Fig. 8.8, a similar comparison of the experimental and model OH and $\text{CH}_2\text{O}/\text{PAH}$ is performed at a slightly later crank angle of 14° CA aTDC. In the simulations, the combined mass fraction contours of CH_2O , OH and MAH are shown in a complete 45° sector plane instead of clipping the plane to the 35 mm laser sheet width corresponding to the experimental imaging window. This is done to capture the entire MAH-forming region to know whether MAH formed is in the jet-jet interaction region or wall impingement region. As can be seen, in the left column, $\text{CH}_2\text{O}/\text{PAH}$ PLIF shows there is a consistent fluorescence due to PAH in all the planes. In the simulations, MAH is again observed in the jet-jet interaction region with increasing concentration from top to the bottom plane,

and these features agree with the experiments. However, in the experiments, PAH fluorescence is observed in a broader area compared to the model prediction. The experimental PAH also occurs in a broader region compared with the one seen at 12° CA aTDC, while in the simulations, the net mass of MAH decreased from 12° to 14° CA aTDC as shown in Fig. 8.6. Thus, overall there is a generally good agreement for this bowl geometry, although the extent of the aromatics in the model is smaller. One possible explanation for this is that the modelling only considered up to one aromatic ring. Obviously, much larger aromatics would be formed, which may oxidise more slowly thus leading to larger regions of total aromatics.

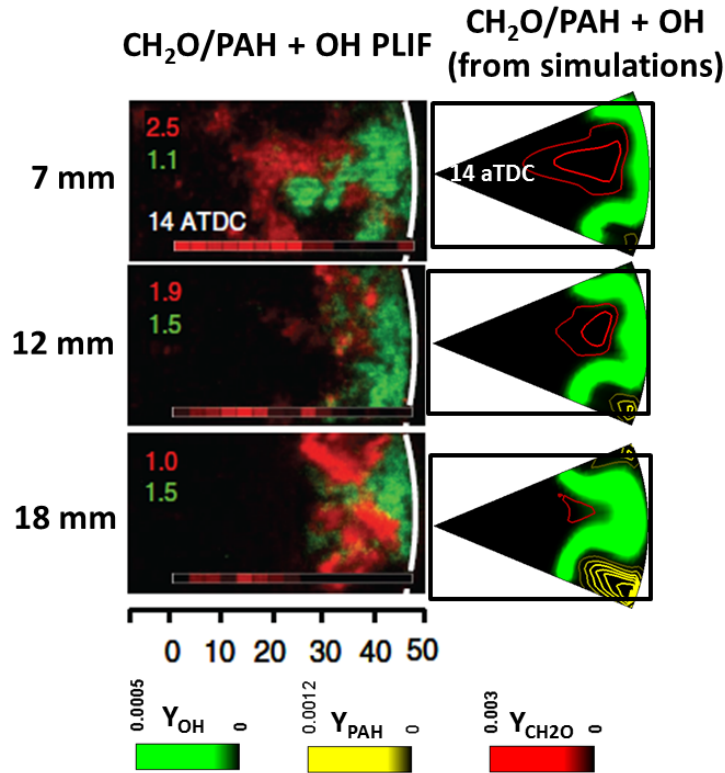


Figure 8.8: Comparison of CH₂O/PAH + OH at 14° CA aTDC. The planes are taken at 7, 12 and 18 mm from fire-deck for the 70% bowl geometry. Laser beam width is shown by black rectangle.

Fig. 8.9 makes similar comparisons for the 80% bowl geometry case. Contour

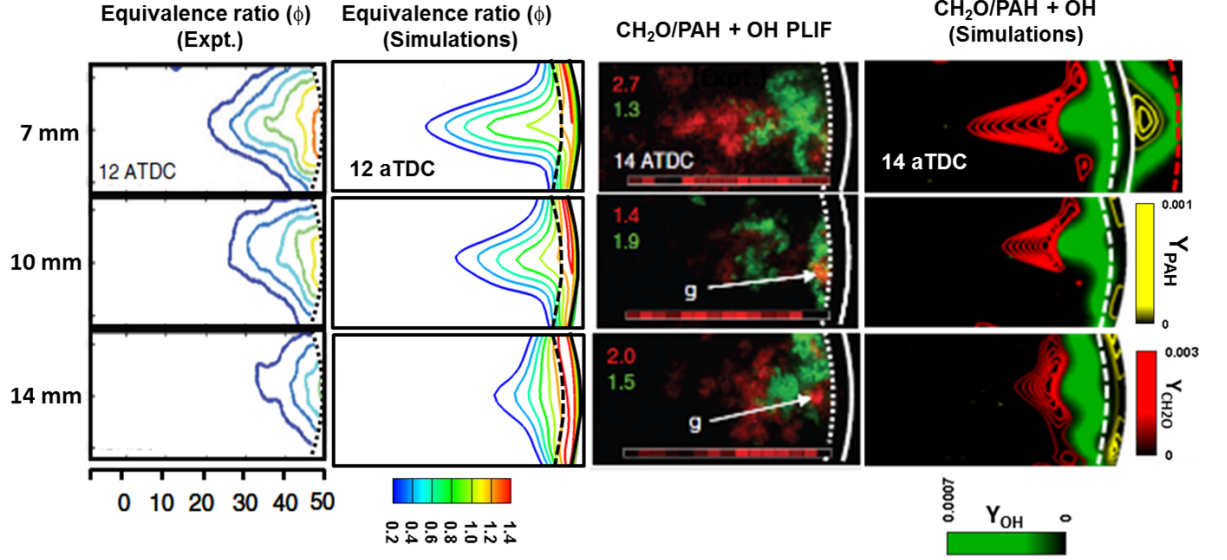


Figure 8.9: Comparison of equivalence ratio in non-combustion condition at 12° CA aTDC and CH₂O/PAH + OH with combustion at 14° CA aTDC. The planes are taken at 7, 10 and 14 mm from fire-deck for the 80% bowl geometry.

plots of CH₂O, OH (hydroxyl), and MAH mass fractions obtained from the simulations using the LLNL-MAH mechanism at 14° CA aTDC are compared with the corresponding PLIF images from the experiment at three different planes taken at 7, 10 and 14 mm from the fire deck. The equivalence ratio contours from the experiment and the simulations in the corresponding non-reacting case at 12° CA aTDC are also compared in the three planes. The dotted black arc in the equivalence ratio images represents the field of view margin in the experiment and the continuous black arc represents the edge of the bowl. The dotted white arc in PLIF of CH₂O/PAH + OH and images from the simulations represents the field of view margin in the experiment, the continuous white arc represents the edge of the bowl and the dotted red arc in the images from the simulations at 7 mm represents the edge of the cylinder. The highlighted bright red spots with the letter g in the PLIF images at 10 and 14mm are due to PAH fluorescence [56]. In the images from the simulations, the red contour lines are CH₂O contours whereas the yellow contour lines are MAH mass fraction contours.

As shown in Fig. 8.9, the simulated equivalence ratio contours once again

compare well with the experimentals. The contours in both the model and experiments show that within the window of view in the experiment, there is no jet-jet interaction in this larger bowl case, whereas in the 70% bowl geometry, a clear jet-jet interaction was seen (see Fig. 8.7). The simulated OH mass fraction contours (green) and formaldehyde (CH_2O) mass fraction contours are in qualitative agreement with the experimental OH and CH_2O fluorescence respectively in all the planes. Soot precursors are now considered. At 7 mm, MAH contours from the simulations are seen very close to the cylinder wall and well outside of the experimental field of view. At the 10 and 14 mm planes, MAH forms very near the edge of field of view, which coincides with the tiny spots of PAH fluorescence observed near the edge of the field of view in the experiment. Given the experimental images are instantaneous and the size of the PAH-containing regions small, it is speculated that the main PAH-containing region in the experiments was outside the field of view, as in the simulations.

Overall the comparison with the PLIF images at this stage during the main heat releasing events shows that the combined mechanism could predict well the formation locations and timing of first stage species such as CH_2O , combustion progress indicators such as OH and post-combustion aromatic soot precursors. The marked difference between the two geometries was captured well by the model, in that aromatics form earlier and most strongly in the jet-jet interaction region in the 70% bowl geometry, while the aromatics form later in the 80% geometry and the bias towards the jet edges is less significant.

8.3.3.2 Mixing-controlled period

Further comparisons of the PAH concentrations from the simulations and experiment are shown in Fig. 8.10 for 70% bowl geometry at 19° CA aTDC and for 80% bowl geometry at 24° CA aTDC in Fig. 8.11. All the dotted and continuous arcs in white and red colour represent the same boundaries as shown in Figs. 8.7 and 8.9. Once again, in the simulations, the combined mass fraction contours of CH_2O , OH and MAH are shown in a complete 45° sector plane in order to capture the entire MAH forming region. instead of clipping the plane to 35 mm laser sheet width as obtained from the experiment for PLIF images. This

is done to capture the entire MAH forming region mainly in 80% bowl geometry case to know whether MAH formed is in the jet-jet interaction region or wall impingement region.

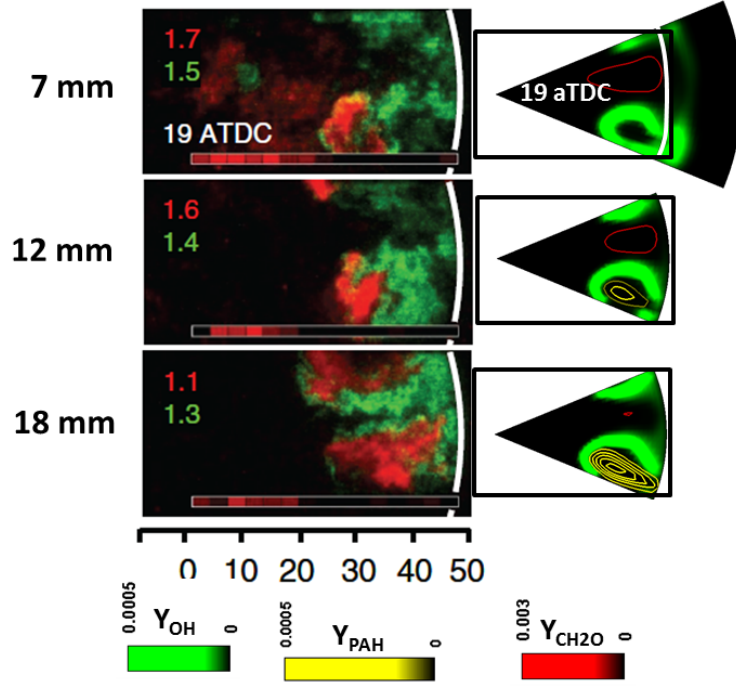


Figure 8.10: Comparison of $\text{CH}_2\text{O}/\text{PAH} + \text{OH}$ at 19° CA aTDC. The planes are taken at 7, 12 and 18 mm from fire-deck for the 70% bowl geometry. Laser beam width is shown by black rectangle.

As can be seen, in the left column of the figures, $\text{CH}_2\text{O}/\text{PAH}$ PLIF shows there is a consistent fluorescence that is not correlated with the CH_2O spectrum in all the planes for both the geometries. The interpretation of this signal in the experiments is not clear, because significant soot luminosity exists at this time, suggesting the signal could be soot incandescence. In the 70% bowl geometry, the observed MAH region at 19° CA aTDC coincides with the PAH fluorescence, which is in the jet-jet interaction region. In the 80% bowl geometry, the observed PAH fluorescence at 24° CA aTDC occurs around the jet-axis near the wall impingement region whereas in the simulations the high MAH region occurs off the jet-axis.

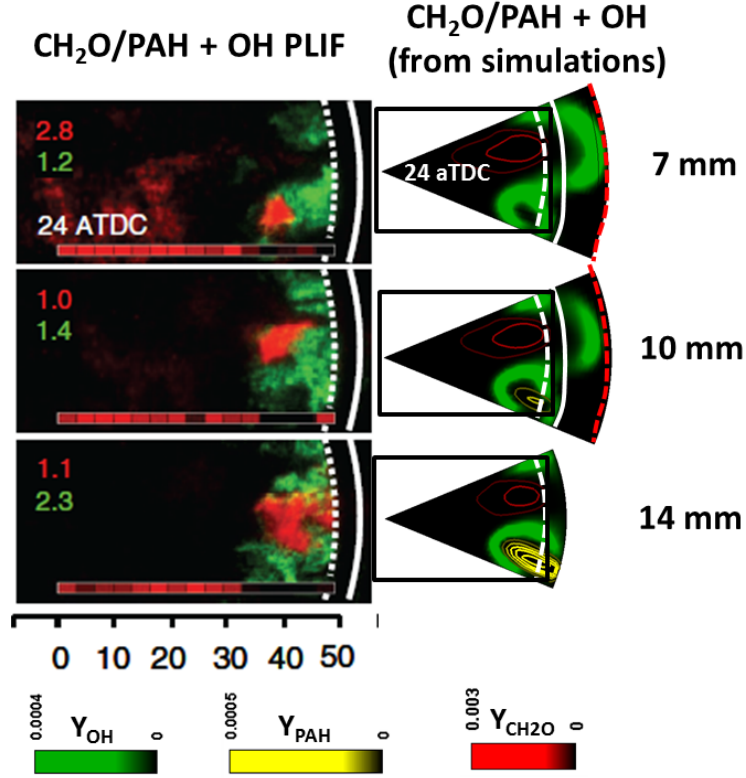


Figure 8.11: Comparison of $\text{CH}_2\text{O}/\text{PAH} + \text{OH}$ at 24°CA aTDC . The planes are taken at 7, 10 and 14 mm from fire-deck for the 80% bowl geometry. Laser beam width is shown by black rectangle.

8.3.3.3 Further discussion

To further understand the impact of jet-wall and jet-jet interactions on the location of PAH formation, contours of equivalence ratio in non-reacting conditions, temperature and MAH mass fraction with velocity vectors with combustion from the simulations for both the geometries are studied. All the contours are taken at 14°CA aTDC . The comparison is shown in Fig. 8.12. As can be seen, the first column corresponds to equivalence ratio with velocity vectors. The second column shows the temperature contours with combustion and the third column gives MAH mass fraction contours. The plane selected for comparison is the bottom most PLIF plane, which is at 18 mm from the fire deck for the 70% bowl geometry and 14 mm from the fire deck for the 80% bowl geometry. As mentioned

earlier, the fuel jet impinges almost at midpoint on the bowl wall vertically in both the geometries [56] and has to go down further along the bowl wall after the impingement. Therefore, the selected planes should give a better picture of the post bowl-wall impingement phenomenon. The equivalence ratio contours show that there are separate rich fuel-air mixture pockets ($\phi \geq 1.5$) in the 70% bowl geometry whereas in the 80% bowl geometry, the rich mixture exists as a thin belt near the bowl wall. The velocity vectors show that the flow effect is similar in both the geometries. The smaller diameter of the bowl in the 70% bowl geometry has provided a shorter radial distance for the jet to travel before impinging on the bowl wall and also a shorter arc length along the bowl wall for the jet to interact with the neighbouring jets. Even though the end of injection and jet velocity are same in the 80% bowl geometry case and the 70% bowl geometry case, because of increased bowl diameter in the 80% case, the jet could not interact with the neighbouring jets and the fuel-air mixture spreads around the jet axis after impinging on the bowl wall. These effects are clearly seen during the combustion in the respective geometries where the rich ϕ regions remain locked and inaccessible to oxygen which resulted in relatively low temperatures. It is confirmed from the simulations that there is no jet-jet interaction in the 80% bowl geometry, which could lead to less MAH formation and then soot as compared to the 70% bowl geometry in which strong jet-jet interaction exists.

8.4 Conclusions

A combined reaction mechanism of *n*-heptane and single aromatic ring species reactions was validated for ignition delay time and for important species concentrations from laboratory premixed and counter-flow diffusion flames. The mechanism was then used for simulating *n*-heptane combustion in a heavy duty direct injection diesel engine. The conclusions are as follows:

- The predicted important combustion products and benzene using the LLNL-MAH mechanism in a premixed flat flame were in agreement with the experimental data and the simulations from Blanquart et al. [29], whereas in the case of counter-flow diffusion flame, benzene was over-predicted.

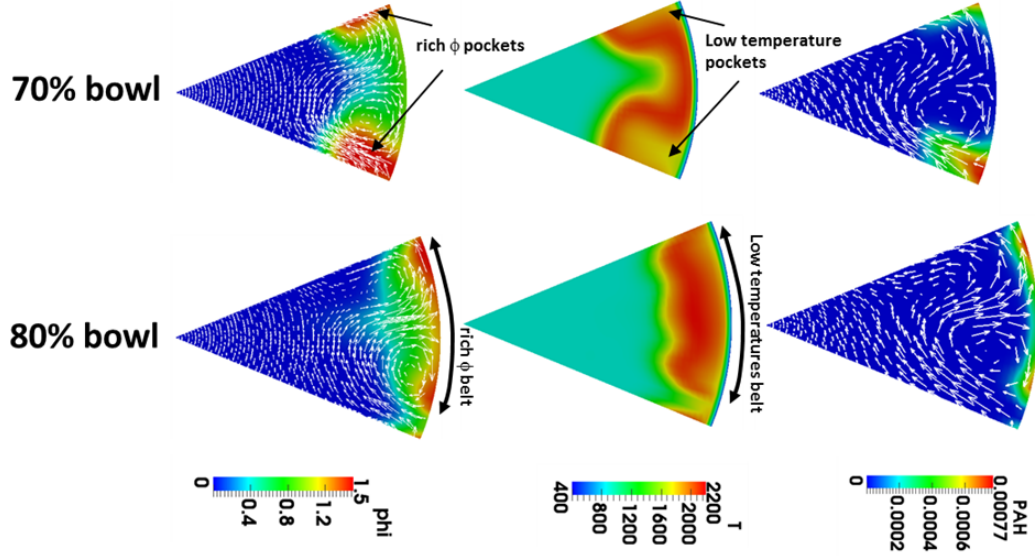


Figure 8.12: Comparison of simulated equivalence ratio (ϕ) with velocity vectors in non-combustion condition (first column), temperature with combustion (second column) and MAH mass fraction contours with velocity vectors (third column). The plane is taken at 18 mm from firedeck for the 70% bowl geometry and 14 mm from firedeck for the 80% bowl geometry. The crank angle position considered is 14° CA aTDC.

- The predicted apparent heat release rate and in-cylinder pressure in the diesel engine using the LLNL-MAH mechanism compare well with the experimental data for the two geometries considered. The smaller diameter of the bowl in the 70% bowl geometry case has played a major role in advancing the start of combustion compared to the 80% bowl geometry case. Similar observations were made in the experiment.
- In the 80% bowl geometry wall-jet interaction was observed whereas in the 70% bowl geometry both wall-jet and jet-jet interactions were seen because of the smaller axial distance to the wall and the shorter arc length along the bowl wall between the jets.
- The modelling and experiment showed a generally good agreement for the fuel equivalence ratio distributions, although they slightly under-predicted

equivalence ratios in some regions, and a generally good agreement for locations of formaldehyde and hydroxyl radical. These features suggest that the main features of the fuel-air mixing, low-temperature combustion, and high temperature combustion were reasonably well captured.

- As observed in the experiment, the modelling showed that rich pockets of fuel-air mixture ($\phi \geq 1.5$) were seen in the jet-jet interaction zones in the 70% bowl geometry. In the same locations relatively low temperatures were seen during the combustion because of restricted access to oxygen. This resulted in the formation of aromatic species in this region. The regions of formation of aromatics agreed quite well between the simulations and the experiments in the 70% bowl case.
- In the 80% bowl geometry, large regions of rich fuel-air mixtures were not seen at the time of the main heat release event within the field of view of the experiment in both experiment and modelling. The simulations provided better information about the location of rich mixtures ($\phi \geq 1.5$). As jet-jet interaction was absent in the 80% bowl case, the rich fuel-air mixture spreads along the bowl wall around the jet axis. As in the 70% bowl geometry, relatively low temperatures were seen in the rich region which resulted in the formation of aromatic species. The modelling predicted some features of the aromatic formation in the 80% bowl case, including the slightly later formation and lower total amount of aromatics, and the increasing amount of aromatics in towards the bottom of the bowl. At later timings during the mixing-controlled burn, the region of high aromatics was however observed to be off the jet axis in the modelling but on the jet axis in the experiments.

The below content has been added in response to comments from Examiner-1

Additional benefits from the present: The comparison of simulations for a 80% case from the present work with simulations and experiment from Genzale et. al. [58] is shown in Fig. 8.13. As mentioned in the comments, Genzale et. al. [58] compared PAH PLIF images with simulated C_2H_2 mass fraction (fourth column). In the present work, it is shown that C_2H_2 mass fraction contours (second column) look

similar to the one predicted by Genzale et. al. [58]. MAH mass fraction contours (third column) from the present prediction show that MAH forms slightly inside away from the field of view (dotted white arc) and close to the cylinder wall (continuous white arc). In the planes 10mm and 14mm from fire-deck, MAH mass fraction contours are close to the field of view as seen in PLIF images (marked as g). MAH mass fraction contours from the present work show that the concentration of PAH formed is relatively less whereas this information is not evident from C_2H_2 mass fraction contours. This is also shown from the temporal evolution of C_2H_2 simulated using LLNL mechanism [40] with and without MAH reaction steps (shown in Fig. 8.14).

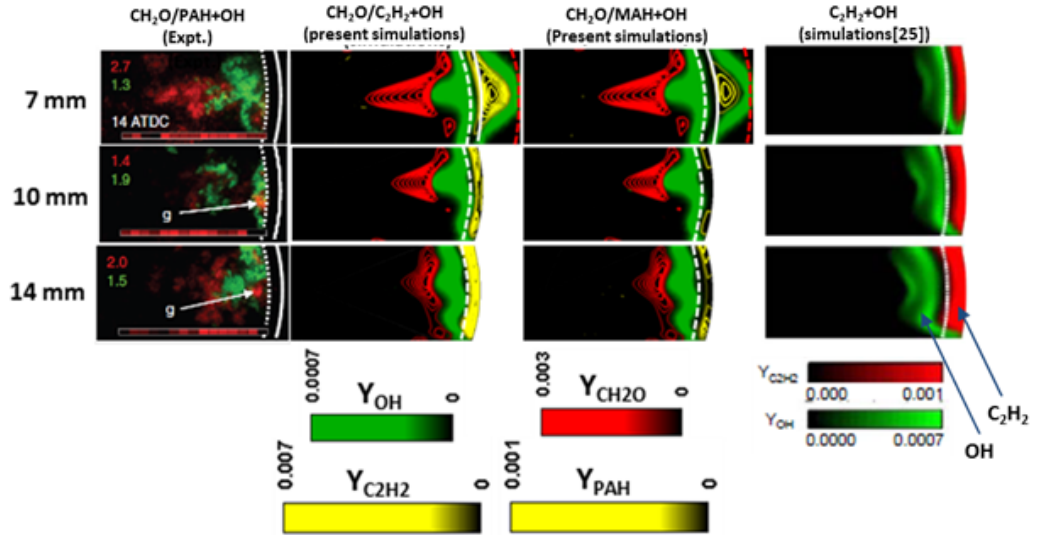


Figure 8.13: Comparison of model predicted mass fraction contours of $CH_2O/C_2H_2 + OH$ (second column) and $CH_2O/MAH + OH$ (third column) using LLNL-MAH mechanism at 14° aTDC with PLIF images (first column) from the experiment at 7 mm, 10 mm and 14 mm planes from the fire-deck and simulations (fourth column) from Ref. [58].

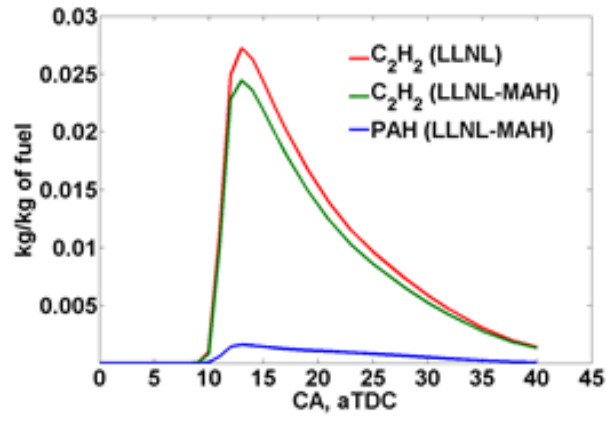


Figure 8.14: Model predicted temporal evolution of total mass of C₂H₂ in kg per kg of fuel using LLNL-MAH and LLNL mechanisms [40] and total mass of MAH in kg per kg of fuel using LLNL-MAH mechanism.

Chapter 9

Conclusions

9.1 Summary of the thesis

The thesis has considered numerical simulations of combustion in diesel engines. The emphasis was on predicting and understanding the effects of jet-wall and jet-jet interactions on mixture formation, combustion development, and emissions formation.

A pragmatic approach was taken to the modelling. Because these interactions are geometry-specific, it was considered important, where possible, to adopt a full cycle, realistic geometry model of the engine, which included modelling the flow in the intake and exhaust ports. Relatively detailed chemical kinetic models were also adopted in order to have a realistic treatment of the transient ignition and emissions formation processes involved.

Given the overall complexity of this problem, involving complex, moving geometry, sprays, complex turbulent flows, ignition in two stages, burning in pre-mixed and non-premixed combustion modes with slow and fast chemistry, it was necessary to simplify other aspects of the model. A standard and well understood RANS-based turbulence models was employed, while a similarly standard discrete phase model spray was adopted. A simple, direct-integration, well-mixed model of turbulence-chemistry interactions was employed.

One key goal was to determine how well the jet-jet and jet-wall interactions could be predicted by modelling. This required going beyond the typical comparisons of pressure traces and engine-out emissions to examine the phenomena in

detail as they happened inside the engine, which was achieved by comparisons to a suite of measurements in two optically accessible engines (one small-bore engine at UNSW and one heavy-duty engine at Sandia National Laboratories). After the usual comparisons of the heat release rate, comparisons of fuel-PLIF with modelled fuel mass fraction were used to understand the transient mixture formation process. Early-stage chemiluminescence and formaldehyde PLIF was compared with modelled fuel formaldehyde mass fraction to evaluate whether the simulations could predict cool flame, first-stage ignition. Chemiluminescence from OH* and OH-PLIF were compared with the modelled OH* and OH mass fractions, respectively, to assess the ability to predict the high temperature combustion regions. Finally PAH PLIF was compared with modelled single-ring aromatic mass fraction to evaluate the ability of the model to predict soot precursors. Thus, overall an extensive set of optical measurement modelling comparisons were performed that spanned the important processes involved in combustion development.

Overall, these comparisons were quite successful. In all the considered cases a good agreement was obtained for the heat release rate, demonstrating the capability of this relatively pragmatic modelling approach to capture the overall combustion behaviour. In-cylinder fuel-air mixing was generally well predicted, as was the timing and location of cool flame and high temperature combustion. The location and timing of aromatic species also agreed quite well, but left room for improvement.

The other main objective was to understand more about jet-jet and jet-wall interactions by further examination of the modelling results. Overall, this too was successful, revealing features that were not obvious from the experiments alone. In particular they highlighted that jet-wall and jet-jet interactions have a major and leading order influence on combustion in modern diesel engines. The flow-flame interactions involved during these phenomena are quite complex and quite geometry specific, highlighting the need for further development of conceptual models for diesel engine combustion affected by jet-jet and jet-wall interactions, which relative to older conceptual models of conventional diesel engine combustion are at a much less advanced stage.

- In Chapter 5, combustion development at a baseline injection pressure con-

dition (70 MPa injection pressure) was studied in the small bore engine. The model-predicted in-cylinder combustion pressure rise, heat release rate, jet-tip penetration length (under the influence of jet-wall impingement), and combustion during the first- and second-stages all compared well with the corresponding experimental data. Further numerical analysis revealed that under the influence of favouring swirl flow, the first- and second-stage combustion progressed relatively faster on the down-swirl side compared to the up-swirl side. It was proposed that the strain rate in the jet head region caused the delayed ignition on the up-swirl side. Analysis showed a value of $\chi > 0.1s^{-1}$ delayed the combustion. There was no initiation of combustion along the jet-axis during the injection period even though re-entrainment of the first-stage combustion products was observed. This was either because of high strain rate or insufficient residence time in this region. Left-over CO and UHC were observed in the squish region after combustion was almost frozen. Finally, the combustion development with the considered configuration was more similar to a conceptual model of light-duty EGR diluted diesel combustion as compared to a conceptual model of conventional, heavy-duty diesel combustion, except in the respect that ignition dwell was negative, albeit small.

- In Chapter 6, the same isolated single jet configuration was studied in the small bore engine with fuel injection pressures of 100, 130 and 160 MPa, keeping the total fuel mass fixed. Besides a very good comparison of predicted global parameters like in-cylinder pressure, heat release rate and jet-tip penetration length, the model captured very well the timing and locations of the first-stage and the second-stage combustion regions as seen in the experiments. The model correctly reproduced the effect of pressure on all the features. The simulations showed that with higher injection pressures, more evaporated fuel and mixed was available in the regions away from the jet-axis, where scalar dissipation rate was low enough ($\chi \approx 0.2s^{-1}$) for the combustion to start. The increased rate of progress of combustion with higher injection pressure reduced the net CO and UHC left unconsumed in the regions above bowl, even though almost same fraction of

fuel escaped into the squish region. Like in the baseline case, the combustion was more similar to the conceptual model of light-duty EGR diluted diesel combustion than it was to the heavy duty conventional model.

- Chapter 7 dealt with a numerical study of two isolated fuel jets with 70 and 130 MPa injection pressures in the small bore engine. The total injected fuel mass was once again held fixed. The shorter fuel injection period, as compared to the single jet cases, resulted in positive ignition dwell for both 70 and 130 MPa injection pressures. Due to the earlier end of injection, more time was available for mixing resulting in a leaner first stage ignition and thus a longer delay to the second stage, which allowed further mixing to take place before the main ignition. Unlike with the single jet cases, the entire evaporated fuel underwent the first-stage combustion before second stage ignition, including along the jet axis once fuel injection finished (see Figs. 7.5 and 7.6). The second-stage combustion occurred in three different regions whereas it was in two regions with the single jet cases. Overall, premixed combustion dominated over mixing-controlled combustion, leading to higher heat release rates and peak pressures in the two-jet cases. In the 70 MPa injection pressure case, soot precursors formed in the rich regions ($\phi \approx 1.7$) of the jet-jet interaction zone. These eventually oxidised in the presence of OH radicals from the second-stage. Despite the overall higher fuel-air mixedness in the two-jet cases, there was no net reduction in UHC compared to the single jet cases. In fact, more un-consumed CO was actually observed compared to the corresponding single jet cases in the region above the bowl, which despite the overall higher mixedness was locally rich due to jet-jet interactions. The combustion behaviour was quite similar to a conceptual model of light-duty EGR diluted diesel combustion, having features including positive ignition dwell, the entire evaporated fuel undergoing combustion, first-stage combustion along the jet-axis, and high temperature combustion in the mixtures with $\phi < 1$.
- Due to the unavailability of experimental PAH data from the small-bore engine, Chapter 8 investigated a heavy duty engine installed at Sandia National Laboratories, with the objective being to compare predictions of aro-

matic formation. A combined *n*-heptane and aromatic reaction mechanism was first developed and validated for ignition delay times, important combustion products and soot precursors in laboratory scale premixed and diffusion flames. The validated mechanism used for predicting aromatic species in the optical heavy-duty diesel engine with two different bowl geometries. Good predictions of the heat release rate, fuel distributions, formaldehyde distributions, and OH distributions were obtained. The predictions of aromatic species were encouraging and good qualitative results were obtained with one bowl geometry while in the other only some of the experimental features were reproduced.

9.2 Recommendations for future work

The numerical simulations demonstrated overall a surprisingly good agreement with the experiments. They also definitely provided more insight into the combustion development in diesel engines. More work in this direction would certainly be beneficial.

- Additional experimental data for comparison would be welcome. Velocity data would be helpful to understand how well the model can predict the in-cylinder flow, which is arguably a precursor to getting anything else right. In the small-bore engine, quantitative fuel distributions using a tracer would be useful as would qualitative 355 nm PLIF to image formaldehyde and PAH. OH PLIF without interference from fuel fluorescence by using a single component fuel would help in interpreting the results at the early stages of high temperature combustion. Soot PLII and laser extinction measurements would be very useful for future studies of soot. Space and time-resolved wall temperature measurements could help to better understand wall heat transfer effects.
- The combustion model can be improved in several ways. First, it would be interesting to add models for larger aromatic components and soot formation. It is suggested that recent work with *n*-dodecane chemistry based on

[118] is a good direction. However, this model needs to be reduced significantly to be computationally affordable. The Lu et al. model [171], which does not include aromatics and only models up to C7 species, is already very expensive. It is suggested that before moving to a soot model in the engine, the model is first verified against available data in simpler flow settings, foremost against single free jet sprays in constant volume chambers.

- The combustion model could also be improved by adding a model for turbulence-chemistry interactions (TCI). With present computational resources, highly accurate methods such as transported probability density function or conditional moment closure do not appear to be feasible for full geometry calculations, given they are much more expensive than the simple well-mixed model adopted here. Some form of combustion tabulation is probably required if a TCI model is to be considered. Large-eddy simulations are another interesting direction, but it is important to understand that unless the energy containing scales around the injector are not resolved, i.e. the grid around the injector is RANS-like, these computations will be extremely expensive.
- There is an urgent need to reduce the computational time for full cycle engine simulations. The approach taken here was computationally very intensive. An improved meshing strategy, for example based on the work of Lucchini [98] would help significantly. Improved approaches for model reduction will also help greatly. These steps would be necessary before moving for LES based engine simulations.
- The analysis highlighted that conceptual models for combustion in small bore diesel engines need further development. The present results made some useful remarks in this direction but the examined situations were somewhat artificial e.g. with just one or two jets, amongst other differences. A coordinated experimental and numerical study to develop such a conceptual model would be a valuable contribution. One way that numerical modelling can contribute is by performing a model-only study of a metal engine under more realistic operating conditions (with a more realis-

tic number of fuel jets, injection duration, ambient conditions, and across different loads). If the model is validated for the features of interest in the loads and conditions accessible to optical engines, and can reproduce the pressure trace of the metal engine, it would be reasonable to suggest that it could be used to contribute to developing such a conceptual model.

Appendix A

Numerical simulation of the impact of wall on the flame zone in an automotive-size diesel engine

This appendix reports results from a accepted paper submitted to the Proceedings of the Australian Combustion Symposium, The University Club of Western Australia (ISSN 1839-8162 online), 2013.

Authors: Pasunurthi, S. S., Hawkes, E. R., Talei, M., Kook, S., Lucchini, T., and D'Errico, G.

A.1 Abstract

A numerical study was conducted to understand interactions of wall-bounded flow and combustion in a small-bore, common-rail, direct injection diesel engine. The

piston bowl was modified by cutting out a section of the bowl wall and the spray was targeted at the corner of the cut-out such that one side of the jet was free (not impinging upon the bowl wall; free-jet side) while the other side of the jet impinged upon the bowl wall (wall-jet side). A reduced *n*-heptane reaction mechanism was used to simulate direct injected diesel combustion. The mechanism was appended with electronically excited hydroxyl radical (OH^*) reaction steps in order to qualitatively simulate chemiluminescence. The simulations showed that the combustion induced dilatation flow played a major role in the transport of hot combustion products towards the fuel-air mixture jet. As observed in the experiment, the simulations predicted shorter flame base height on wall-jet side compared with the height on free-jet side.

A.2 Introduction

Recent trends in diesel engine technology towards lower flame temperatures have resulted in flame lift-off lengths that are relatively longer than previous generations of engines. In the automotive sector, there have also been trends towards downsizing. Both factors lead to wall interactions becoming an important feature of the combustion and emissions formation processes.

Dec's conceptual model of diesel combustion in a situation free of walls [45] suggests that soot formation takes place in a rich premixed combustion region near the leading edge of the flame, which is enveloped by a diffusion flame. Experiments from Dec and Tree [48] showed that wall impingement of the reacting fuel-jet flattened the diffusion flame, which led after a short time to local extinction of the flame and soot deposition was observed. In another experiment on a confined jet, it was shown that re-entrained combustion products into the jet reduced the flame lift-off length and increased soot formation [128].

The effect of bowl-spray interactions on emissions was numerically studied in a premixed charge combustion mode [50] and in a conventional combustion mode [102]. In another numerical study, jet-jet and jet-wall interactions originating from a bowl-geometry effect were investigated [58]. In an attempt to better understand flame-wall interactions, a recent experimental study has been per-

formed in an optically accessible, automotive-sized diesel engine [144]. A novel piston bowl geometry was employed in which a section of the bowl wall was cut out (see Fig. A.1). A single fuel spray was then targeted at the edge of the cut-out region so that one side of the spray impinged upon the bowl wall while the other side was free to penetrate further downstream up to liner-wall. This bowl geometry modification has provided an opportunity to investigate the effects of two different scenarios of jet-wall interactions simultaneously. This was compared to a case where the single fuel jet was targeted away from the cut-out region, thus representing the normal situation of spray impingement onto the bowl wall. The study found that the length from the injector to the flame was greater on the free-jet side of the jet directed at the cut-out as compared with both that on the wall-jet side of that jet and that of the fully wall-directed jet. Also noted was a decrease in time of the length to the flame which was hypothesized to be due to entrainment of hot products into the jet. The present work complements this experimental work by modelling the case of the cut-out directed jet. Although the accuracy of a model is uncertain, a more complete data-set is available with three-dimensional, time-varying fields of all scalars and velocity, and this information may be valuable in interpreting the experimental results.

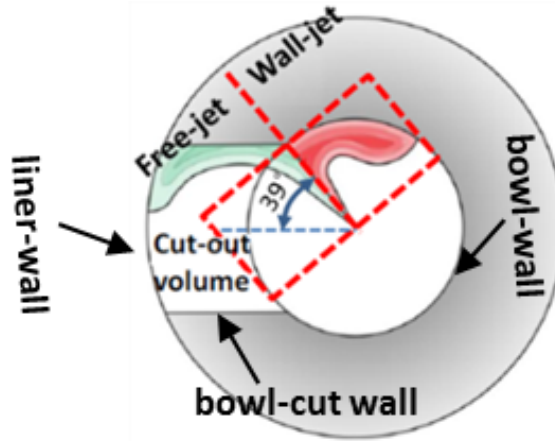


Figure A.1: A top view schematic of the modified piston and jet trajectory of a single jet bisecting into a simultaneous free-jet and wall-jet [144].

A.3 Experimental setup

A.3.1 Engine configuration

The experiments were conducted using a single-cylinder, direct-injection, automotive-size, diesel engine. The engine has quartz windows around the cylinder liner and on the piston head for optical access. The engine was operated using a conventional ultra-low sulphur diesel (ULSD) fuel with cetane number of 46 in compliance with the Fuel Quality Standards Act 2000, Australia. The important engine specifications are given in Table 4.1. The fuel injection system was composed of a Bosch made second-generation common-rail, 1-hole solenoid injector connected to an electronic signal generator (Zenobalti 5100). The 1-hole injector was obtained by closing the other six holes of the conventional 7-hole injector by laser welding.

A.3.2 Engine operating conditions

The experiments were performed at a fixed engine speed of 1200 rpm. The cylinder and the fire-deck wall temperatures were controlled by water circulation at 363 K. The intake air temperature was set at 303 K by means of two independent temperature control units with a feedback controller. The piston surface temperature was not controlled. The selected operating conditions are shown in Table 1.

A.4 Numerical setup

A.4.1 CFD code

Simulations were performed using the Lib-ICE code [101], which is a set of libraries and solvers for in-cylinder flow and combustion modelling based on the OpenFOAM technology [12]. Turbulence was modelled by an RNG k - ϵ model [66] and the Kelvin-Helmholtz Rayleigh-Taylor (KH-RT) sub-model [139] was used for spray atomisation and break-up.

An integrated chemistry model that solves a set of Ordinary Differential Equations (ODE) of chemical reactions was used for modelling combustion. This approach neglects turbulence-chemistry interactions assuming each cell as a well-stirred reactor. Obviously, this represents a considerable simplification; however, recent comparisons of similar models with diesel ignition in constant volume chambers demonstrate that this simple approach is at least capable of predicting general trends [69]. The combustion was modelled by using a 159 species and 1540 reactions *n*-heptane reaction mechanism (LLNL) [146]. The OH* reaction steps from Ref. [65] were added to the mechanism for qualitatively predicting OH* concentration in the flame region, thus enabling a more direct comparison with experimental OH* chemiluminescence images. The computational time for integration of the chemistry was reduced by a Dynamic Adaptive Chemistry (DAC) approach [92] that computes a reaction set that is valid for the local thermo-physical conditions.

A.4.2 Computational grids and initial conditions

The computational grids used for the simulations are shown in Fig. A.2. The mesh with valves and ports (see Fig. A.2a) contains a combination of hexahedral and tetrahedral cells with 2.5 million cells at Bottom Dead Centre (BDC) and 0.7 million cells at Top Dead Centre (TDC). This mesh was used for a motored simulation of two complete cycles to capture the asymmetric swirl induced by the intake ports. The mesh used for the spray and combustion simulations was a hexahedral mesh without valves and ports with 0.5 million cells at BDC and 10000 cells at TDC (see Fig. A.2b). The initial condition for the spray and combustion simulation was mapped from fields from the motored simulation after Intake Valve Closure (IVC) (-142° crank-angle (CA) after Top Dead Centre (aTDC)) in the third cycle. This approach provided a good quality hexahedral mesh and reduced computational time for the spray and combustion simulations. As temperature controlled water at 363 K was circulated, a fixed temperature of 363 K was specified for the walls of the cylinder and the fire-deck. The un-controlled piston hot-side surface temperature was specified using 1-D steady state heat transfer analysis considering heat transfer correlation suggested in Ref. [73]. A

temperature wall function based on variable density as suggested in Ref. [67] was used for all walls.

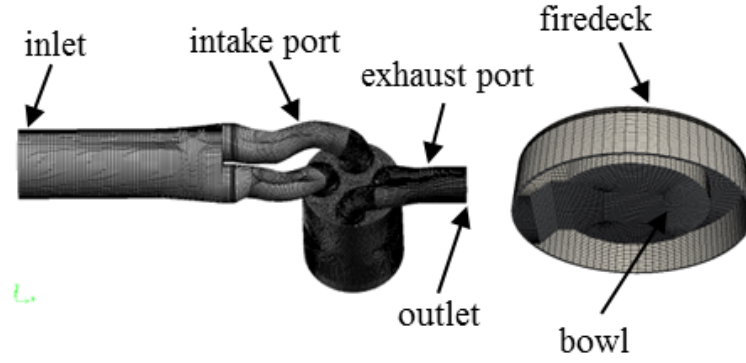


Figure A.2: Computational grids.

A.5 Results and Discussion

A.5.1 Pressure and heat release rate comparison

A comparison of the predicted in-cylinder pressure trace and apparent heat release rate (aHRR) with the experimental data is shown in Fig. A.3. The aHRR in the experiment and simulations were calculated based on the pressure data and cylinder volume by using the first law of thermodynamics with an adiabatic assumption [72].

As can be seen in Fig. A.3, the simulated pressure trace compares well with the experimental data. There is no net heat release observed in the experiment or in the simulation during the first stage of combustion, which could have been a result of the evaporative cooling of the injected fuel. The second stage combustion starts at around 6.5° CA aTDC, which is 3.5° CA before the end of injection.

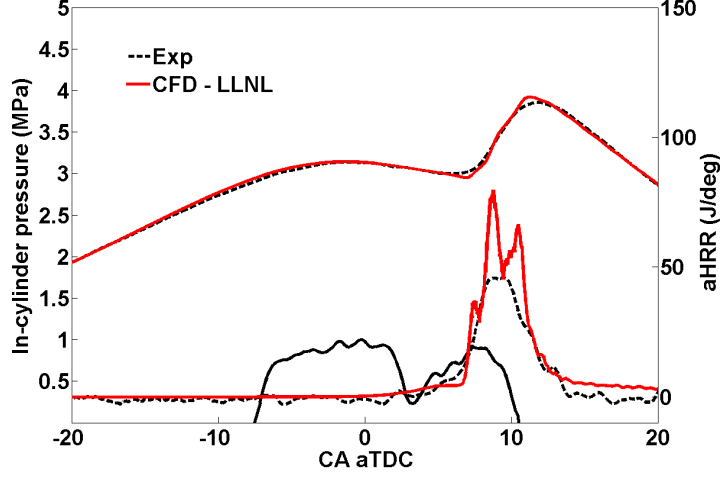


Figure A.3: In-cylinder pressure and apparent heat release rate comparison.

A.5.2 OH* chemiluminescence comparison

A comparison of the simulated OH* chemiluminescence against the experimental OH* images is shown in Fig. A.4. The experimental images are a line-of-sight measurement. Therefore, in the simulations, comparable images were obtained by summing-up equally-spaced planar data in the bowl region into a single plane. In the images from simulations, the approximate flame base height on the wall-jet side is marked by a continuous white line and on the free-jet side by a dotted white line. The flame base height is defined as the vertical distance to the marked lines from the nozzle centre-line is designated as OH_w on wall-jet side and OH_f on free-jet side. The dotted white circle in OH* contour images from simulations is the limit of the field of view for experimental images. Flame base heights from the simulations and the experiment are compared in Fig. A.5.

The simulated OH* contours replicate some features observed in the experiment at different crank angles from 8° aTDC to 11° aTDC. Importantly, the flame base height was distinctively shorter on the wall-jet side than on the free-jet side (see in Fig. A.5). As shown in Fig. A.5, the transient flame base height decreases gradually on both sides of the jet until the end of the injection at 10° aTDC. After the end of injection, from 11° CA aTDC onwards the heights remain

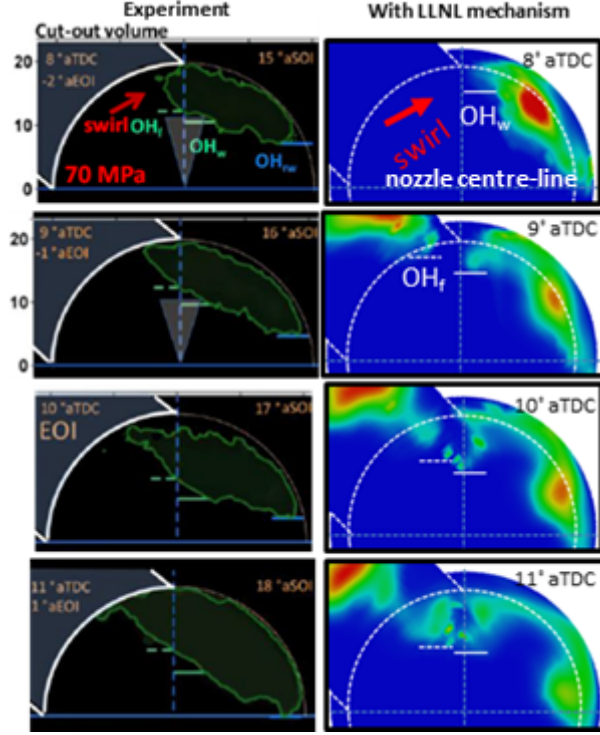


Figure A.4: OH* chemiluminescence comparison. Experiment (left), with the LLNL mechanism (right).

almost same as observed at 10° CA aTDC. A similar observation is also made in the experiment, but the heights are shorter compared with the respective heights from the simulations.

A.5.3 CFD based reasoning for flame base height reduction

To better understand the reason for gradual reduction of flame base heights, iso-surfaces of carbon mono-oxide (CO), unity equivalence ratio ($\phi = 1$) based on unburnt fuel and oxygen (O₂) and contours of temperature with velocity vectors from the simulations at 8, 9 and 10° CA aTDC are studied. The contours are shown in Fig. A.6 in three columns. For example, the first column corresponds

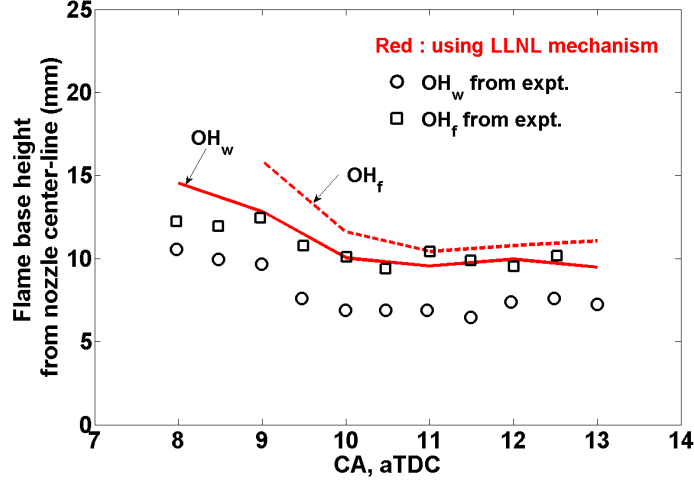


Figure A.5: Comparison of flame base heights.

to 8° CA aTDC with the iso-surfaces in the top row and the temperature contour with velocity vectors in the bottom row. The temperature contours are averaged contours generated from 6 equally-spaced planar data in the bowl region. In the similar way, velocity vectors were generated by averaging the components of the velocity vector. This averaging ensures that the contours give the information from the entire bowl region.

The temperature contour with velocity vectors at 8° CA aTDC (see in Fig. A.6) shows that the initial major combustion temperature rise takes place on wall-jet side and induces a dilatation flow towards the fuel jet. The iso-surfaces of CO and $\phi = 1$ at the same crank-angle show that on the wall-jet side, the hot combustion products move from the wall towards the trailing edge of the fuel-air mixture jet. At this crank-angle, as shown in Fig. A.7, the fuel-air mixture jet has velocity of around 45 m/s, which should also promote entrainment-however the flow into the jet, appears to be a dilatation-dominated. At 9° CA aTDC, the velocity vectors now show a strong dilatation-induced flow emanating now from the cut-out region. The region of combustion products, visualised here with CO has expanded along the wall and begins to overlap with the flammable mixture region. Once again, the dilatation flow appears to dominate over jet entrainment in its effect to transport products towards the flammable region. By

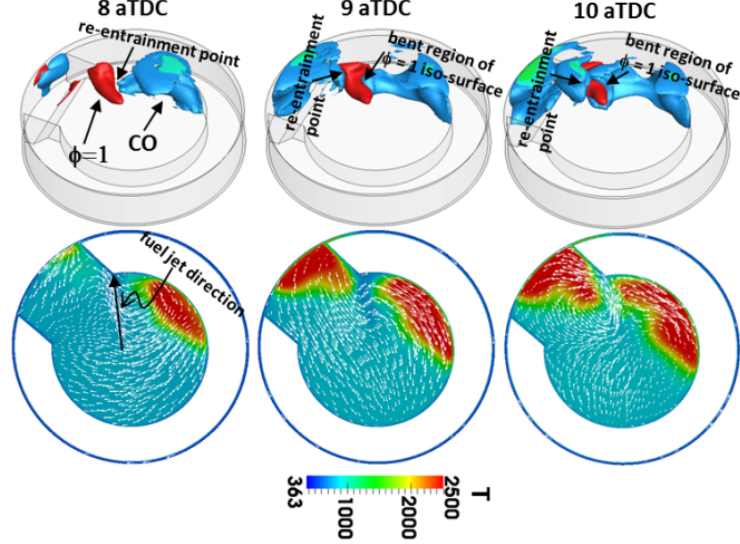


Figure A.6: Iso-surfaces of CO and $\phi = 1$ and temperature (K) contours with velocity vectors from the simulations at 8, 9 and 10° CA aTDC.

10° CA aTDC, dilatation-driven flows are less evident and a more conventional jet-like flow is observed. At this stage products fully envelop the jet of flammable mixtures, and local entrainment of products may be occurring near the flame base.

From 9° to 10° CA aTDC, the points of ignition on either side of the jet advanced towards the fuel injector from both the sides. This appears to be mainly a dilatation-induced phenomenon. As mentioned earlier, the flame base height on wall-jet side (OH_w) is distinctively shorter compared with the height (OH_f) on free-jet side. This appears to be simply because the combustion products on the free jet side have further to travel during their dilatation-dominated transport from the wall region back towards the flammable region.

A.6 Conclusions

In this paper, simulations of simultaneous free and wall jet effects of a single diesel jet were performed on a single-cylinder, small-bore, common-rail diesel engine.

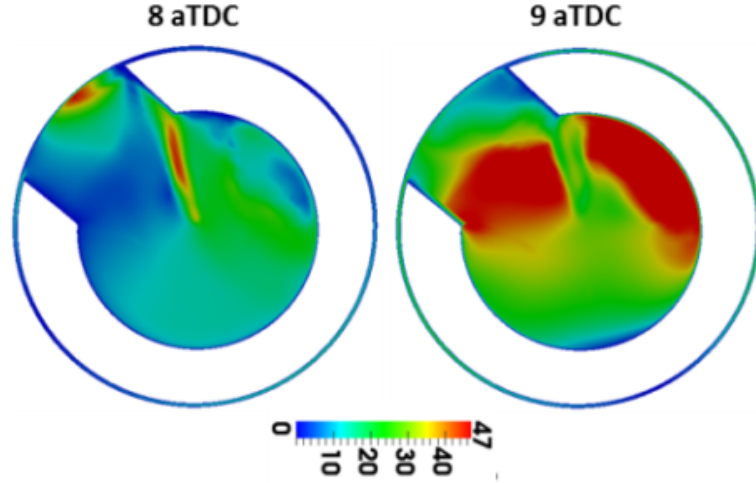


Figure A.7: Averaged velocity magnitude (m/s) contours from the simulations at 8 and 9° CA aTDC.

The OH* chemiluminescence data was compared with modelled OH* species. The following were achieved from the simulations.

- The combustion pressure trace and aHRR was predicted well.
- The modelled OH* captured the distinctively different flame lift-off lengths on the wall-jet side and free-jet side as observed in the experiment. Also, the model predicted the slow transient reduction of the lift-off lengths during the injection period as observed in the experiment.
- The combustion induced dilatation flow played a major role in the re-entrainment of hot combustion products towards the flammable fuel-air mixture. Jet entrainment flows may also contribute but these appear to have a lower magnitude until very close to the end of injection.

In general, the results highlight that in modern automotive-sized diesel engines, the effects of the wall are a leading order influence. The wall affects the fluid flows and the flame, in a manner which is complex and strongly interdependent. These interactions are expected to be highly dependent on geometry and operating conditions, emphasizing the continuing need for both experimental and computational research to shed light on the basic

phenomenology of combustion across a range of canonical situations representative of advanced CI engine technology.

References

- [1] STAR-CD methodology and documentation, version 3.26. 2005.
- [2] OpenFOAM programmer's guide, version 2.0.0. *www.openfoam.org*, 2010.
- [3] OpenFOAM user guide, version 2.0.0. *www.openfoam.org*, 2010.
- [4] Converge theory manual, version 2.1.0. 2013.
- [5] ansys website, <http://www.ansys.com>, 2014.
- [6] Converge website, <http://www.convergecd.com>, 2014.
- [7] DigAnaRS website, <http://www.cd-adapco.com/partner/diganars>, 2014.
- [8] Engine Combustion Network website, <http://www.sandia.gov/ecn/>, 2014.
- [9] ensight website, <http://www.ceisoftware.com>, 2014.
- [10] fieldview website, <http://www.ilight.com/en>, 2014.
- [11] OpenFOAM classes details website, <http://www.openfoam.org/docs/cpp/>, 2014.
- [12] Openfoam website, <http://www.openfoam.org>, 2014.
- [13] paraview website, <http://www.paraview.org>, 2014.
- [14] STAR-CD website, <http://www.cd-adapco.com/products/star-cd>, 2014.
- [15] STAR/KINetics website, <http://reactiondesign.com/news/48/95/star-kinetics-a-new-tool-for-reacting-flow-analysis/>, 2014.

REFERENCES

- [16] tecplot website, <http://www.tecplot.com>, 2014.
- [17] UNSW engine research group website, <http://www.engineering.unsw.edu.au/mechanical-engineering/engine-research>, 2014.
- [18] J. ABRAHAM, F. V. BRACCO, AND R. D. REITZ. Comparisons of computed and measured premixed charge engine combustion. *Combustion and Flame*, **60**[3]:309 – 322, 1985.
- [19] A. A. AMSDEN, P. J. O’ROURKE, AND T. D. BUTLER. KIVA-2: A computer program for chemically reactive flows with sprays. *Las Alamos National Laboratories*, **LA-11560-MS**, 1989.
- [20] A.A. AMSDEN. KIVA-3: Release 2, improvements to KIVA-3v. *Las Alamos National Laboratories*, **LA-13608-MS**, 1999.
- [21] A.A. AMSDEN, T.D. BUTLER, P.J. O’ROURKE, AND J.D. RAMSHAW. KIVA: A comprehensive model for 2-D and 3-D simulations. *SAE transactions*, **94**:850554, 1985.
- [22] A. E. BAKALI, J. L. DELFAU, AND C. VOVELLE. Experimental study of 1 atmosphere, rich, premixed n-heptane and iso-octane flames. *Combustion Science and Technology*, **140**[1-6]:69–91, 1998.
- [23] H. BARTHS, C. HASSE, AND N. PETERS. Computational fluid dynamics modelling of non-premixed combustion in direct injection diesel engines. *International Journal of Engine Research*, **1**:249 – 267, 2000.
- [24] P. BERTA, S. K. AGGARWAL, AND I. K. PURI. An experimental and numerical investigation of n-heptane/air counterflow partially premixed flames and emission of NO_x and PAH species. *Combustion and Flame*, **145**[4]:740 – 764, 2006.
- [25] S. BHATTACHARJEE AND D. C. HAWORTH. Simulations of transient n-heptane and n-dodecane spray flames under engine-relevant conditions using a transported PDF method. *Combustion and Flame*, **160**[10]:2083 – 2102, 2013.

REFERENCES

- [26] A. BHAVE, M. KRAFT, F. MAUSS, A. OAKLEY, AND H. ZHAO. Evaluating the EGR-AFR operating range of a HCCI engine. *SAE Technical Paper 2005-01-0161 (2005)*., 2005.
- [27] R. W. BILGER. The structure of turbulent nonpremixed flames. *Proc. Combust. Inst.*, **22**:475–488, 1988.
- [28] R. B. BIRD, W. E. STEWART, AND E. N. LIGHTFOOT. *Transport phenomena*. John Wiley and Sons, Inc, New York, second edition, 2001.
- [29] G. BLANQUART, P. PEPIOT-DESJARDINS, AND H. PITSCH. Chemical mechanism for high temperature combustion of engine relevant fuels with emphasis on soot precursors. *Combustion and Flame*, **156**[3]:588 – 607, 2009.
- [30] M. K. BOBBA AND M. P. B. MUSCULUS. Laser diagnostics of soot precursors in a heavy-duty diesel engine at low-temperature combustion conditions. *Combustion and Flame*, **159**[2]:832 – 843, 2012.
- [31] K. BOEHNE, W. AND HUMMEL. Common rail injection system for commercial diesel vehicles. *SAE Technical Paper 970345 (1997)*., 1997.
- [32] M. BOLLA, Y. M. WRIGHT, K. BOULOUCHOS, G. BORGHESI, AND E. MASTORAKOS. Soot formation modeling of n-heptane sprays under diesel engine conditions using the conditional moment closure approach. *Combustion Science and Technology*, **185**[5]:766–793, 2013.
- [33] K. N. C. BRAY AND N. PETERS. *Turbulent Reacting Flows by P. A. Libby and F. A. Williams*. Academic Press, London, 1994.
- [34] G. BRUNEAUX. Mixing process in high pressure diesel jets by normalized laser induced exciplex fluorescence part 2: Wall impinging versus free jet. *SAE Technical Paper 2005-01-2097 (2005)*., 2005.
- [35] G. BRUNEAUX. Combustion structure of free and wall-impinging diesel jets by simultaneous laser-induced fluorescence of formaldehyde, poly-aromatic hydrocarbons, and hydroxides. *International Journal of Engine Research*, **9**[3]:249–265, 2008.

REFERENCES

- [36] T. D. BUTLER, L. D. CLOUTMAN, J. K. DUKOWICZ, AND J. D. RAMSHAW. CONCHAS: An Arbitrary LagrangianEulerian computer code for multi-component chemically reactive fluid flow at all speeds. *Las Alamos National Laboratories*, **LA-8129-MA**, 1979.
- [37] H. K. CIEZKI AND G. ADOMEIT. Shock-tube investigation of self-ignition of n-heptane-air mixtures under engine relevant conditions. *Combustion and Flame*, **93**[4]:421 – 433, 1993.
- [38] W.F. COLBAN, P.C. MILES, AND S. OH. Effect of intake pressure on emissions from an automotive diesel engine operating in low temperature combustion regimes. *SAE Technical Paper 2007-01-4063 (2007)*., 2007.
- [39] C. T. CROWE, M. SOMMERFIELD, AND Y. TSUJI. *Multiphase flows with droplets and particles*. CRC Press LLC, Florida, second edition, 2011.
- [40] H.J. CURRAN, P. GAFFURI, W.J. PITZ, AND C.K. WESTBROOK. A comprehensive modeling study of n-heptane oxidation. *Combustion and Flame*, **114**[1-2]:149 – 177, 1998.
- [41] GORYNTSEV. D., A. SADIKI, AND J. JANICKA. Investigation of fuel-air mixing in disi engine using LES. *SAE transactions*, 2011-01-1886, 2011.
- [42] GORYNTSEV. D., A. SADIKI, AND J. JANICKA. Cycle-to-cycle variations based unsteady effects on spray combustion in internal combustion engines by using LES. *SAE transactions*, 2012-01-0399, 2012.
- [43] J. T. DAVID AND F. T. MARIO. KIVA-4: An unstructured ALE code for compressible gas flow with sprays. *Journal of Computational Physics*, **219**[2]:943 – 975, 2006.
- [44] J. T. DAVID, H. L. YUANHONG, AND S. C. KONG. Partitioning strategies for parallel KIVA-4 engine simulations. *Computers and Fluids*, **39**[2]:301 – 309, 2010.
- [45] J. E. DEC. A conceptual model of direct injection diesel combustion based on laser-sheet imaging. *SAE Technical Paper 970873 (1997)*., 1997.

REFERENCES

- [46] J. E. DEC AND C. ESPEY. Ignition and early soot formation in a direct injection diesel engine using multiple 2-d imaging diagnostics. *SAE Technical Paper 950456 (1995).*, 1995.
- [47] J. E. DEC AND C. ESPEY. Chemiluminescence imaging of autoignition in a direct injection diesel engine. *SAE Technical Paper 982685 (1998).*, 1998.
- [48] J. E. DEC AND D. R. TREE. Diffusion-flame / wall interactions in a heavy-duty direct injection diesel engine. *SAE Technical Paper 2001-01-1295 (2001).*, 2001.
- [49] R.E. DEC, J.E.AND CANAAN. Plif imaging of NO formation in a DI-diesel engine. *SAE Technical Paper 980147 (1998).*, 1998.
- [50] R. DIWAKAR AND S. SINGH. Importance of spray-bowl interaction in a diesel engine operating under pccci combustion mode. *SAE Technical Paper 2009-01-0711 (2009) .*, 2009.
- [51] SIEBERS D.L. Scaling liquid-phase fuel penetration in diesel sprays based on mixing-limited vaporization. *SAE Technical Paper 1999-01-0528 (1999).*, 1999.
- [52] N. DOCQUIER. Optical investigation of the effect of fuel jet wall impact position on soot emissions in a single cylinder common rail direct injection diesel engine. *SAE Technical Paper 2002-01-0495 (2002).*, 2002.
- [53] K. FIEWEGER, R. BLUMENTHAL, AND G. ADOMEIT. Self-ignition of s.i. engine model fuels: A shock tube investigation at high pressure. *Combustion and Flame*, **109**[4]:599 – 619, 1997.
- [54] S. FISCHER AND J. O. STEIN. Investigation on the effect of very high fuel injection pressure on soot-NO_x emissions at high load in a passenger car diesel engine. *SAE Int. J. Engines*, **2**:1737–1748, 06 2009.
- [55] M. FRENKLACH AND H WANG. Detailed modeling of soot particle nucleation and growth. *Symposium (International) on Combustion*, **23**[1]:1559 – 1566, 1991. Twenty-Third Symposium (International) on Combustion.

REFERENCES

- [56] C. L. GENZALE, R. D. REITZ, AND M. P. B. MUSCULUS. Effects of piston bowl geometry on mixture development and late-injection low-temperature combustion in a heavy-duty diesel engine. *SAE Int. J. Engines*, **1**:913–937, 04 2008.
- [57] C. L. GENZALE, R. D. REITZ, AND M. P. B. MUSCULUS. Optical diagnostics and multi-dimensional modeling of spray targeting effects in late-injection low-temperature diesel combustion. *SAE Int. J. Engines*, **2**:150–172, 11 2009.
- [58] C. L. GENZALE, R.D. REITZ, AND M. P. B. MUSCULUS. Effects of jet-bowl and jet-jet interactions on late-injection low-temperature heavy-duty diesel combustion. *THIESEL Proc. of the Conference on Thermo- and Fluid Dynamic Processes In Diesel Engines.*, 2008.
- [59] C.L. GENZALE, R.D. REITZ, AND D.D. WICKMAN. A computational investigation into the effects of spray targeting, bowl geometry and swirl ratio for low-temperature combustion in a heavy-duty diesel engine. *SAE Technical Paper 2007-01-0119 (2007).*, 2007.
- [60] M. GERMANO, U. PIOMELLI, P. MOIN, AND W. H. CABOT. A dynamic subgrid - scale eddy viscosity model. *Physics of Fluids A: Fluid Dynamics (1989-1993)*, **3**[7]:1760–1765, 1991.
- [61] I. GLASSMAN. *Combustion*. Academic Press, third edition, 1996.
- [62] I. GLASSMAN. Soot formation in combustion processes. *Proceedings of the Combustion Institute*, **22**:295–311, 1998.
- [63] A. D. GOSMAN. Progress on engine les using STAR-CD. *Japan STAR Conference 2012, Yokohama*, 2012.
- [64] J. D. GOSMAN AND D. CLERIDES. Diesel spray modelling: A review. *ILASS-Europe Annual Meeting*, 1997.
- [65] J. M. HALL AND E. L. PETERSEN. An optimized kinetics model for oh chemiluminescence at high temperatures and atmospheric pressures. *International Journal of Chemical Kinetics*, **38**[12]:714–724, 2006.

REFERENCES

- [66] Z. HAN AND R. D. REITZ. Turbulence modeling of internal combustion engines using RNG $k - \epsilon$ models. *Combustion Science and Technology*, **106**[4-6]:267–295, 1995.
- [67] Z. HAN AND R. D. REITZ. A temperature wall function formulation for variable-density turbulent flows with application to engine convective heat transfer modeling. *International Journal of Heat and Mass Transfer*, **40**[3]:613 – 625, 1997.
- [68] Z. HAN, A. ULUDOGAN, G. J. HAMPSON, AND R. D. REITZ. Mechanism of soot and nox emission reduction using multiple-injection in a diesel engine. *SAE transactions*, 960633, 1996.
- [69] E. R. HAWKES, M. BARDI, C. ANGELBERGER, AND Y. PEI. Engine combustion network 2 - ignition and lift-off session. *Second Workshop of the Engine Combustion Network (2012)*, 2012.
- [70] HAWORTH, D. C. Large-eddy simulation of in-cylinder flows. *Oil and Gas Science and Technology - Rev. IFP*, **54**[2]:175 – 185, 1999.
- [71] J.J. HERNANDEZ, J. SANZ-ARGENT, J. BENAÏES, AND S. MOLINA. Selection of a diesel fuel surrogate for the prediction of auto-ignition under HCCI engine conditions. *Fuel*, **87**[6]:655 – 665, 2008.
- [72] J. B. HEYWOOD. *Internal combustion engine fundamentals*. McGraw-Hill series in mechanical engineering, New York, second edition, 1988.
- [73] G. F. HOHENBERG. Advanced approaches for heat transfer calculations. *SAE Technical Paper 790825 (1979)*., 790825.
- [74] E. HOROWITZ AND S. SAHINI. *Fundamentals of data structures*. Computer Science Press, 1983.
- [75] L. P. HSIANG AND G. M. FAETH. Near-limit drop deformation and secondary breakup. *International Journal of Multiphase Flow*, **18**[5]:635 – 652, 1992.

REFERENCES

- [76] E. HUESTIS, P.A. ERICKSON, AND MUSCULUS M.P.B. In-cylinder and exhaust soot in low-temperature combustion using a wide-range of EGR in a heavy-duty diesel engine. *SAE Technical Paper 2007-01-4017 (2007)*., 2007.
- [77] H. JASAK. *Error Analysis and Estimation for the Finite Volume Method with Applications to Fluid Flows*. PhD thesis, Imperial College, UK, 1996.
- [78] H. JASAK AND Z. TUKOVIĆ. Automatic mesh motion for the unstructured finite volume method. *powerlab.fsb.hr*.
- [79] H JASAK, H. G. WELLER, AND N. NORDIN. In-cylinder cfd simulation using a c++ object-oriented toolkit. *SAE transactions, 2004-01-0110*, 2004.
- [80] R. JHAVAR AND C. J. RUTLAND. Using large eddy simulations to study mixing effects in early injection diesel engine combustion. *SAE transactions, 2006-01-0871*, 2006.
- [81] T.V. JOHNSON. Diesel emission control in review. *SAE Technical Paper 2009-01-0121 (2009)*., 2009.
- [82] R. J. KEE, J. F. GRACAR, M. D. SMOOKE, AND J. A. MILLER. A program for modeling steady, laminar, one-dimensional premixed flames. *Sandia Report No. SAND 85-8240*, 1985.
- [83] B. KERSCHGENS, M. GAUDING, C. FELSCH, N. PETERS, AND C. HASSE. A consistent flamelet model to describe the interaction of combustion chemistry and mixing in the controlled auto ignition regime. *SAE transactions, 2010-01-0181*, 2010-01-0181.
- [84] W. W. KIM AND S. MENON. A new dynamic one-equation subgrid-scale model for large eddy simulations. *33rd Aerospace Science Meeting and Exhibit, AIAA 95-0356*, 1995.
- [85] T. KITASEI, J. YAMADA, T. SHOJI, AND S. SHINO. Influence of the different fuel spray wall impingement angles on smoke emission in a DI-diesel engine. *SAE Technical Paper 2008-01-1791 (2008)*., 2008.

REFERENCES

- [86] A. Y. KLIMENKO AND R. W. BILGER. Conditional moment closure for turbulent combustion. *Progress in Energy and Combustion Science*, **25**[6]:595 – 687, 1999.
- [87] S. C. KONG, Z. HAN, AND R. D. REITZ. The development and application of a diesel ignition and combustion model for multidimensional engine simulation. *SAE transactions*, 950278, 1995.
- [88] S. C. KONG AND R. D. REITZ. Multidimensional modeling of diesel ignition and combustion using a multistep kinetics model. *Journal of Engineering for Gas Turbines and Power*, **115**[4]:781 – 789, 1993.
- [89] S. C. KONG AND R. D. REITZ. Multidimensional modeling of diesel ignition and combustion using a multistep kinetics model. *Journal of Engineering for Gas Turbines and Power*, **115**[4]:781 – 789, 1994.
- [90] S. C. KONG AND R. D. REITZ. Use of detailed chemical kinetics to study HCCI engine combustion with consideration of turbulent mixing effects. *Journal of Engineering for Gas Turbines and Power*, **124**[3]:702 – 707, 2002.
- [91] S. KOOK, C. BAE, P. C. MILES, D. CHOI, M. BERGIN, AND R. D. REITZ. The effect of swirl ratio and fuel injection parameters on CO emission and fuel conversion efficiency for high-dilution, low-temperature combustion in an automotive diesel engine, 2006.
- [92] L. LIANG, J. G. STEVENS, AND J. T. FARRELL. A dynamic adaptive chemistry scheme for reactive flow computations. *Proceedings of the Combustion Institute*, **32**[1]:527 – 534, 2009.
- [93] D. K. LILLY. A proposed modification of the Germano subgrid - scale closure method. *Physics of Fluids A: Fluid Dynamics (1989-1993)*, **4**[3]:633–635, 1992.
- [94] K. LIU AND D.C. HAWORTH. Large-eddy simulation for an axisymmetric piston-cylinder assembly with and without swirl. *Flow, Turbulence and Combustion*, **85**[3]:279 – 307, 2010.

REFERENCES

- [95] S. LIU, J. C. HEWSON, J. H. CHEN, AND H. PITSCH. Effects of strain rate on high-pressure nonpremixed n-heptane autoignition in counterflow. *Combustion and Flame*, **137**[3]:320 – 339, 2004.
- [96] PICKETT L.M., MANIN J., GENZALE C.L., SIEBERS D.L., MUSCULUS M.P.B., AND IDICHERIA C.A. Relationship between diesel fuel-jet vapour penetration/dispersion and local fuel mixture-fraction. *SAE Technical Paper 2011-01-0686 (2011)*., 2011.
- [97] T. LU AND C. K. LAW. A directed relation graph method for mechanism reduction. *Proceedings of the Combustion Institute*, **30**[1]:1333–1341, 2005.
- [98] T. LUCCHINI. A new meshing strategy for full engine meshes. *An internal communication from Politecnico di Milano*, 2014.
- [99] T. LUCCHINI AND G. D’ERRICO. Automatic mesh motion, topological changes and innovative mesh setup for I.C.E. CFD simulations. *power-lab.fsb.hr*.
- [100] T. LUCCHINI, G. D’ERRICO, AND D. ETTORRE. Numerical investigation of the spray - mesh - turbulence interactions for high pressure, evaporating sprays at engine conditions. *International Journal of Heat and Fluid Flow*, **32**[1]:285 – 297, 2011.
- [101] T. LUCCHINI, G. D’ERRICO, D. ETTORRE, AND G. FERRARI. Numerical investigation of non-reacting and reacting diesel sprays in constant-volume vessels. *SAE International Journal of Fuels and Lubricants*, **2**:966–975, 2009.
- [102] V. LUCKHCHOURA, F. ROBERT, N. PETERS, M. ROTTMANN, AND S. PISCHINGER. Investigation of spray-bowl interaction using two-part analysis in a direct-injection diesel engine. *SAE Technical Paper 2010-01-0182 (2010)* ., 2010.
- [103] A. E. LUTZ, R. J. KEE, J. F. GRGAR, AND F. M. RUPLEY. OPPDIF: A fortran program for computing opposed-flow diffusion flames. *Report No. SAND 96-8243*, 1996.

REFERENCES

- [104] A. E. LUTZ, R. J. KEE, AND J. A. MILLER. A program for predicting homogeneous gas-phase chemical kinetics in a closed system with sensitivity analysis. *Sandia Report No. SAND 87-8248, UC-4*, 1988.
- [105] B. F. MAGNUSSEN AND B. W. HJERTAGER. On the structure of turbulence and a generalised eddy dissipation concept for chemical reaction in turbulent flow. *19th AIAA Aerospace Meeting, St. Louis, USA*, 1981.
- [106] A. MATSUMOTO, W. R. MOORE, M. C. LAI, Y ZHENG, M. FOSTER, X. B. XIE, D. YEN, K CONFER, AND E HOPKINS. Spray characterization of ethanol gasoline blends and comparison to a cfd model for a gasoline direct injector. *SAE Int. J. Engines*, **3**:402–425, 04 2010.
- [107] F. MAUSS. *Development of a kinetic model of the soot formation with faster polymerization*. PhD thesis, RWTH, Aachen, 1998.
- [108] U. C. MÜLLER AND N. PETERS. Development of reduced reaction schemes for the ignition of diesel fuels in a non-premixed turbulent flow field. *IDEA Project, Periodic Report No. 3*, 1991.
- [109] S. MENDEZ, J. KASHDAN, G. BRUNEAUX, AND B. THIROUARD. Formation of unburned hydrocarbons in low temperature diesel combustion. *SAE Technical Paper 2009-11-02 (2009).*, 2009.
- [110] R. MINETTI, M. CARLIER, M. RIBAUOUR, E. THERSSEN, AND L. R. SOCHET. A rapid compression machine investigation of oxidation and auto-ignition of n-heptane: Measurements and modeling. *Combustion and Flame*, **102**[3]:298 – 309, 1995.
- [111] S. MOSBACH, M. S. CELNIK, A. RAJ, M. KRAFT, H. R. ZHANG, S. KUBO, AND K. O. KIM. Towards a detailed soot model for internal combustion engines. *Combustion and Flame*, **156**[6]:1156 – 1165, 2009.
- [112] M. P. B. MUSCULUS. Effects of the in-cylinder environment on diffusion flame lift-off in a di diesel engine. *SAE Technical Paper 2003-01-0074 (2003)* ., 2003.

REFERENCES

- [113] M. P. B. MUSCULUS. Multiple simultaneous optical diagnostic imaging of early-injection low-temperature combustion in a heavy-duty diesel engine. *SAE Technical Paper 2006-01-0079 (2006)*., 04 2006.
- [114] M. P. B. MUSCULUS, T. LACHAUX, L. M. PICKETT, AND C. A. IDICHERIA. End of injection over mixing and unburned hydrocarbon emissions in low temperature combustion diesel engines. *SAE Technical Paper 2007-01-0907 (2007)*., 2007.
- [115] M. P. B. MUSCULUS, P. C. MILES, AND L. M. PICKETT. Conceptual models for partially premixed low-temperature diesel combustion. *Progress in Energy and Combustion Science*, **39**:246 – 283, 2013.
- [116] J. D. NABER AND D. L. SIEBERS. Effects of gas density and vaporization on penetration and dispersion of diesel sprays. *SAE transactions*, 960034, 1996.
- [117] K. NARAYANASWAMY, G. BLANQUART, AND H. PITSCH. A consistent chemical mechanism for oxidation of substituted aromatic species. *Combustion and Flame*, **157**[10]:1879 – 1898, 2010.
- [118] K. NARAYANASWAMY, P. PEPIOT, AND H. PITSCH. A chemical mechanism for low to high temperature oxidation of n-dodecane as a component of transportation fuel surrogates. *Combustion and Flame*, **161**[4]:866 – 884, 2014.
- [119] P. A. N. NORDIN. *Complex chemistry modelling of diesel spray combustion*. PhD thesis, Chalmers University, 2001.
- [120] N. OTSU. A threshold selection method from gray-level histograms. *IEEE Transactions on Systems, Man and Cybernetics*, **9**[1]:62 – 66, 1979.
- [121] Y. PEI. *Transported PDF Modelling of Spray Combustion at Practical Diesel Engine Conditions*. PhD thesis, UNSW, Sydney, 2013.
- [122] Y. PEI, E. R. HAWKES, AND S. KOOK. A comprehensive study of effects of mixing and chemical kinetic models on predictions of n-heptane

REFERENCES

- jet ignitions with the PDF method. *Flow, Turbulence and Combustion*, **91**[2]:249–280, 2013.
- [123] Y. PEI, E. R. HAWKES, AND S. KOOK. Transported probability density function modelling of the vapour phase of an n-heptane jet at diesel engine conditions. *Proceedings of the Combustion Institute*, **34**[2]:3039 – 3047, 2013.
- [124] Y. PEI, E.R. HAWKES, S. KOOK, G.M. GOLDIN, AND T. LU. Modelling n-dodecane spray and combustion with the transported probability density function method. *Combustion and Flame*, **162**[5]:2006 – 2019, 2015.
- [125] N. PETERS. Local quenching of diffusion flamelets and non-premixed turbulent combustion. *Western States Section of the Combustion Institute, Spring Meeting, Irvine, CA*, 1980.
- [126] N. PETERS. Laminar flamelet concepts in turbulent combustion. *Twenty-First Symposium (International) on Combustion*, pages 1231–1250, 1986.
- [127] L. M. PICKETT, S. KOOK, AND T. C. WILLIAMS. Visualization of diesel spray penetration, cool-flame, ignition, high-temperature combustion, and soot formation using high-speed imaging, 04 2009.
- [128] L. M. PICKETT AND J. J. LÓPEZ. Jet-wall interaction effects on diesel combustion and soot formation. *SAE Technical Paper 2005-01-0921 (2005).*, 2005.
- [129] L. M. PICKETT AND D. L. SIEBERS. Soot in diesel fuel jets: effects of ambient temperature, ambient density, and injection pressure. *Combustion and Flame*, **138**[1-2]:114 – 135, 2004.
- [130] A PILCH AND C. A. ERDMAN. Use of breakup time data and velocity history data to predict the maximum size of stable fragments for acceleration-induced breakup of a liquid drop. *International Journal of Multiphase Flow*, **13**[6]:741 – 757, 1987.

REFERENCES

- [131] H. PITTSCH, E. RIESMEIER, AND N. PETERS. Unsteady flamelet modeling of soot formation in turbulent diffusion flames. *Combustion Science and Technology*, **158**[1]:389–406, 2000.
- [132] C. J. POLONOWSKI, C. J. MUELLER, C. R. GEHRKE, T. BAZYN, G. C. MARTIN, AND P. M. LILLO.
- [133] E. POMRANING. *Development of Large Eddy Simulation Turbulence Models*. PhD thesis, University of Wisconsin, Madison, 2000.
- [134] S. B. POPE. {PDF} methods for turbulent reactive flows. *Progress in Energy and Combustion Science*, **11**[2]:119 – 192, 1985.
- [135] S. B. POPE. Computationally efficient implementation of combustion chemistry using in situ adaptive tabulation. *Combustion Theory and Modelling*, **1**[1]:41–63, 1997.
- [136] S. B. POPE. *Turbulent flows*. Cambridge university press, London, 2000.
- [137] Y. RA AND R. D. REITZ. A reduced chemical kinetic model for IC engine combustion simulations with primary reference fuels. *Combustion and Flame*, **155**[4]:713 – 738, 2008.
- [138] B. V. RAJALINGAM AND P. V. FARRELL. The effect of injection pressure on air entrainment into transient diesel sprays. *SAE Technical Paper 1999-01-0523 (199)*., 1999.
- [139] R. D. REITZ AND J. C. BEALE. Modelling spray atomization with the Kelvin-Helmholtz/Rayleigh-Taylor hybrid model. *Atomization and Sprays*, **9**[6]:623–650, 1999.
- [140] R. D. REITZ AND R. DIWAKAR. Effect of drop breakup on fuel sprays. *SAE transactions*, 860469, 1986.
- [141] R. D. REITZ AND C. J. RUTLAND. Development and testing of diesel engine CFD models. *Progress in Energy and Combustion Science*, **21**[2]:173 – 196, 1995.

REFERENCES

- [142] C. M. RHIE AND W. L. CHOW. Numerical study of the turbulent flow past an airfoil with trailing edge separation. *AIAA Journal*, **21**[11]:1525 – 1532, 1983.
- [143] A. M. RUSLY. *The transiency of in-cylinder flame development in an automotive-size diesel engine*. PhD thesis, UNSW, Sydney, 2013.
- [144] A. M. RUSLY AND S. KOOK. Effect of injection pressure on transient behaviour of wall-interacting jet flame base in an automotive-size diesel engine. *SAE transactions*, 2013-01-2536, 2013.
- [145] A. M. RUSLY, R. ZHANG, S. KOOK, AND E. R. HAWKES. Diesel knock visualisation in a small-bore optical engine. *Proceedings of the Australian Combustion Symposium*, 2011, 2011.
- [146] R. SEISER, H. PITSCH, K. SESHADRI, W. J. PITZ, AND H. J. GURRAN. Extinction and autoignition of n-heptane in counterflow configuration. *Proceedings of the Combustion Institute*, **28**[2]:2029 – 2037, 2000.
- [147] P. K. SENEAL, E. POMRANING, K. J. RICHARDS, T. E. BRIGGS, C. Y. CHOI, R. M. MCDAVID, AND M. A. PATTERSON. Multi-dimensional modeling of direct-injection diesel spray liquid length and flame lift-off length using cfd and parallel detailed chemistry. *SAE transactions*, 2003-01-1043, 2003.
- [148] D. SIEBERS AND B. HIGGINS. Flame lift-off on direct-injection diesel sprays under quiescent conditions. *SAE Technical Paper 2001-01-0530 (2001)*., 2001.
- [149] S. SINGH. *Experimental investigation of multi-mode diesel engine combustion and validation of advanced combustion models*. PhD thesis, University of Wisconsin, Madison, 2006.
- [150] S. SINGH, M. P. B. MUSCULUS, AND R. D. REITZ. Mixing and flame structures inferred from oh-plif for conventional and low-temperature diesel engine combustion. *Combustion and Flame*, **156**[10]:1898 – 1908, 2009.

REFERENCES

- [151] S. SINGH, R. D. REITZ, AND M. P. B. MUSCULUS. Comparison of the characteristic time, representative interactive flamelet, and direct integration with detailed chemistry combustion models against optical diagnostic data for multi-mode combustion in a heavy-duty DI diesel engine. *SAE transactions 2006-01-0055*, 2006.
- [152] S. SINGH, R. D. REITZ, D. WICKMAN, D. STANTON, AND Z. TAN. Development of a hybrid, auto-ignition/flame-propagation model and validation against engine experiments and flame liftoff. *SAE transactions, 2007-01-0171*, 2007.
- [153] M. SJÖBERG AND J. E. DEC. Combined effects of fuel-type and engine speed on intake temperature requirements and completeness of bulk-gas reactions for hcci combustion. *SAE Technical Paper 2003-01-3173 (2003)*., 2003.
- [154] J. SMAGORINSKY. General circulation experiments with the primitive equations: I. The basis equations. *Monthly Weather Review*, **91**:99 – 164, 1963.
- [155] R. SOLSJÖ, M. JANGI, C. CHARTIER, Ö. ANDERSSON, AND X. S. BAI. Lift-off and stabilization of n-heptane combustion in a diesel engine with a multiple-nozzle injection. *Proceedings of the Combustion Institute*, **34**[2]:3031 – 3038, 2013.
- [156] S. SOM AND S. K. AGGARWAL. Effect of nozzle orifice geometry on spray, combustion, and emission characteristics of a compression ignition engine. *Proceedings of the 2010 Technical Meeting of the Central States Section of The Combustion Institute, USA*, 2010.
- [157] S. SOM, A. I. RAMIREZ, S. K. AGGARWAL, A. L. KASTENGREN, E. E. HANNOUNY, D. E. LONGMAN, C. F. POWELL, AND P. K. SENEAL. Development and validation of a primary breakup model for diesel engine applications. *SAE transactions, 2009-01-0838*, 2009.
- [158] J. STOER AND F. BULIRSCH. *Introduction to numerical analysis*. Springer-Verlag, 1980.

REFERENCES

- [159] B. STROUSTRUP. *The C++ Programming Language*. Addison-Wesley Professional, 1997.
- [160] T. F. SU, M. A. PATTERSON, R. D. REITZ, AND P. V. FARRELL. Experimental and numerical studies of high pressure multiple injection sprays. *SAE transactions*, 960861, 1996.
- [161] D. J. TORRES, P. J. O’ROURKE, AND A. A. AMSDEN. Efficient multi-component fuel algorithm. *Combustion Theory and Modelling*, 7[1]:66 – 86, 2003.
- [162] S. R. TURNS. *An Introduction to Combustion*. McGraw-Hill, New York, 2000.
- [163] R. VENUGOPAL AND J. ABRAHAM. A numerical investigation of flame lift-off in diesel jets. *Combustion Science and Technology*, 179[12]:2599–2618, 2007.
- [164] D. VEYNANTE AND L. VERVISCH. Turbulent combustion modeling. *Progress in Energy and Combustion Science*, 28[3]:193 – 266, 2002.
- [165] G. VISHWANATHAN AND R. D. REITZ. Development of a practical soot modeling approach and its application to low-temperature diesel combustion. *Combustion Science and Technology*, 182[8]:1050–1082, 2010.
- [166] H. WANG AND M. FRENKLACH. A detailed kinetic modeling study of aromatics formation in laminar premixed acetylene and ethylene flames. *Combustion and Flame*, 110[1-2]:173 – 221, 1997.
- [167] X. WANG, Z. HUANG, W. ZHANG, O. A. KUTI, AND K. NISHIDA. Effects of ultra-high injection pressure and micro-hole nozzle on flame structure and soot formation of impinging diesel spray. *Applied Energy*, 88[5]:1620 – 1628, 2011.
- [168] H. WEN, Y. SHI, R.D. REITZ, D.D. WICKMAN, AND W. WILLEMS. Engine development using multi-dimensional cfd and computer optimization. *SAE Technical Paper 2010-01-0360 (2010).*, 2010.

REFERENCES

- [169] J. XI AND B. J. ZHONG. Reduced kinetic mechanism of n-heptane oxidation in modeling polycyclic aromatic hydrocarbon formation in diesel combustion. *Chemical Engineering and Technology*, **29**[12]:1461–1468, 2006.
- [170] V. YAKHOT AND L. M. SMITH. The renormalization group, the ϵ - expansion and derivation of turbulence models. *Journal of Scientific Computing*, **7**[1]:35–61, 1992.
- [171] C. S. YOO, T. LU, J. H. CHEN, AND C. K. LAW. Direct numerical simulations of ignition of a lean n-heptane/air mixture with temperature inhomogeneities at constant volume: Parametric study. *Combustion and Flame*, **158**[9]:1727 – 1741, 2011.
- [172] H. R. ZHANG, E. G. EDDINGS, AND A. F. SAROFIM. Combustion reactions of paraffin components in liquid transportation fuels using generic rates. *Combustion Science and Technology*, **179**[1-2]:61–89, 2007.
- [173] W. ZHANG, K. NISHIDA, J. GAO, AND D. MIURA. An experimental study on flat-wall-impinging spray of microhole nozzles under ultra-high injection pressures. *Proceedings of the Institution of Mechanical Engineers, Part D: Journal of Automobile Engineering*, 2008.